The Pennsylvania State University

The Graduate School

College of Engineering

SEMI-ACTIVE CONTROL OF HELICOPTER VIBRATION USING CONTROLLABLE STIFFNESS AND DAMPING DEVICES

A Thesis in

Aerospace Engineering

by

Phuriwat Anusonti-Inthra

Submitted in Partial Fulfillment
of the Requirements
for the Degree of

Doctor of Philosophy

August 2002

We approve the thesis of Phuriwat Anusonti-Inthra.

Date of Signature

Farhan Gandhi
Associate Professor of Aerospace Engineering
Thesis Advisor
Chair of Committee

George A. Lesieutre
Professor of Aerospace Engineering

Edward C. Smith
Associate Professor of Aerospace Engineering

Christopher Rahn
Associate Professor of Mechanical Engineering

Dennis K. McLaughlin
Professor of Aerospace Engineering
Head of the Department of Aerospace Engineering

ABSTRACT

Semi-active concepts for helicopter vibration reduction are developed and evaluated in this dissertation. Semi-active devices, controllable stiffness devices or controllable orifice dampers, are introduced; *(i)* in the blade root region (rotor-based concept) and *(ii)* between the rotor and the fuselage as semi-active isolators (in the non-rotating frame). Corresponding semi-active controllers for helicopter vibration reduction are also developed. The effectiveness of the rotor-based semi-active vibration reduction concept (using stiffness and damping variation) is demonstrated for a 4-bladed hingeless rotor helicopter in moderate- to high-speed forward flight. The rotor blade is modeled as an elastic beam, which undergoes elastic flap-bending, lag-bending, and torsional deformations, and is discretized using finite element analysis. Aerodynamic loads on the blade are determined using blade element theory, with rotor inflow calculated using linear inflow or free wake analysis. The stiffness variation is introduced by modulating the stiffness of the root element or a discrete controllable stiffness device that connects the rotor hub and the blade. The damping variation is achieved by adjusting the damping coefficient of a controllable orifice damper, introduced in the blade root region. Optimal multi-cyclic stiffness/damping variation inputs that can produce simultaneous reduction in all components of hub vibrations are determined through an optimal semi-active control scheme using gradient and non-gradient based optimizations. A sensitivity study shows that the stiffness variation of root element can reduce hub vibrations when proper amplitude and phase are used. Furthermore, the optimal semi-active control scheme can determine the combination of stiffness variations that produce significant vibration reduction in all components of vibratory hub loads simultaneously. It is demonstrated that desired cyclic variations in properties of the blade root region can be practically achieved using discrete controllable stiffness devices and controllable dampers, especially in the flap and lag directions. These discrete controllable devices can produce 35-50% reduction in a composite vibration index representing all components of vibratory hub loads. No detrimental increases are observed in the lower harmonics of blade loads and blade response (which contribute to the dynamic stresses) and controllable device internal loads, when the optimal stiffness and damping variations are introduced. The effectiveness of optimal stiffness and damping variations in reducing hub vibration is retained over a range of cruise speeds and for variations in fundamental rotor properties. The effectiveness of the semi-active isolator is demonstrated for a simplified single degree of freedom system representing the semi-active isolation system. The rotor, represented by a lumped mass under harmonic force excitation, is supported by a spring and a parallel damper on the fuselage (assumed to have infinite mass). Properties of the spring or damper can then be controlled to reduce transmission of the force into the fuselage or the support structure. This semi-active isolation concept can produce additional 30% vibration reduction beyond the level achieved by a passive isolator. Different control schemes (i.e. open-loop, closed-loop, and closed-loop adaptive schemes) are developed and evaluated to control transmission of vibratory loads to the support structure (fuselage), and it is seen that a closed-loop adaptive controller is required to retain vibration reduction effectiveness when there is a change in operating condition.

TABLE OF CONTENTS

List of Tables……………………………………………………………………………..…. ix

List of Figures..……………………………………………………………………………...xii

List of Symbols ……………………………………………………………………………xix

Acknowledgements ……………………….....………………………………….………..xxv

Chapter 1 Introduction...…………………………………………………………...……1

- 1.1 Background and motivation……………………………………………………...…1
- 1.2 Overview of helicopter vibration…………………………………………………2
- 1.3 Passive helicopter vibration reduction……………….…………………………...3
- 1.4 Active helicopter vibration reduction…………………………….………………5
  - 1.4.1 Higher harmonic control……………..……………………………………..5
  - 1.4.2 Individual blade control……………………………………...……….……..7
  - 1.4.3 Active Control of Structural Response (ACSR)…………………….………12
- 1.5 Semi-active vibration reduction technology…………………….………………14
  - 1.5.1 Overview of semi-active vibration reduction concept………………….……14
  - 1.5.2 Comparison between active and semi-active concepts……………..……..15
  - 1.5.3 Semi-active vibration reduction applications…………………....………..15
  - 1.5.4 Helicopter vibration reduction using semi-active approach…..…………………18
- 1.6 Focus of the present research……………………………………………………20
- 1.7 Overview of dissertation…………………………………………………………21

Chapter 2 Analysis……………………………….…………………………………….30

- 2.1 Helicopter/Rotor modeling and response calculation……………………………...30
  - 2.1.1 Helicopter model……………………………………………………………..30
  - 2.1.2 Rotor blade model…………………………………………….………...31
  - 2.1.3 Coupled rotor response/trim calculation…………………………….……….33
  - 2.1.4 Blade root loads and hub loads calculation ……………………….…………34
- 2.2 Rotor blade stiffness variations……………………………………………………36
  - 2.2.1 Root element stiffness variations……………………………………...….36
  - 2.2.2 Stiffness variations of discrete devices…………………………….……...37
    - 2.2.2.1 Dual spring model……………………………………………..…38
    - 2.2.2.2 Single spring model……………………………………………....39
- 2.3 Rotor blade damping variations…………………………………………………42
  - 2.3.1 Controllable orifice damper model ………………………………………...42
  - 2.3.2 Inclusion of controllable dampers into blade equations……………………...45
  - 2.3.3 Blade root loads and hub loads calculation………………………………..48
- 2.4 Influence of semi-active stiffness and damping variation ..…….……………….…49

Chapter 3 Optimal Semi-Active Control Scheme ……….…………………………….61

- 3.1 Calculation of optimal semi-active inputs …………….………………………...61
  - 3.1.1 Gradient-based optimization……………..……………………………..62

3.1.2 Non-Gradient-based optimization ………………..…………………..………...63

Chapter 4 Sensitivity Study ………………………………………………………..……….64

4.1 Influence of root element stiffness variations on vibratory hub loads ………..…...64
4.1.1 Cyclic variation in flap stiffness ………………………………….…...……..64
4.1.2 Cyclic variation in lag stiffness ……………………………………………...66
4.1.3 Cyclic variation in torsion stiffness …………………………………………68
4.1.4 Summary of beneficial root element stiffness variations ……………………68
4.2 Mechanism for reduction of vibratory hub loads……………………….…………69
4.3 Influence of root element stiffness variation on blade root loads……...………..…71
4.3.1 Cyclic variation in flap stiffness …………………………………...…...72
4.3.2 Cyclic variation in lag stiffness ……………………………………………...72
4.3.3 Cyclic variation in torsion stiffness ……………………………………......74
4.4 Vibration reduction at different advance ratio ..…….……………..………………74
4.5 Summary on sensitivity of root element stiffness variation ..…………...…………75

Chapter 5 Optimal Control Study ………………………………………….…………92

5.1 Optimal 3/*rev* flap stiffness variation ……………………………..……..…...92
5.2 Optimal 2,3/*rev* flap & 3/*rev* lag stiffness variations……………………….………93
5.3 Optimal 2,3/*rev* Flap & Lag Stiffness Variations……...…………………….……..…93
5.4 Influence of Baseline Stiffness on Effectiveness of Vibration Control..…………..94
5.5 Effectiveness of Vibration Controller at Different Forward Speed ..………………96
5.6 Summary on optimal control of root element stiffness variation..…………………96

Chapter 6 Discrete Controllable Stiffness Devices ………….……………………………104

6.1 Baseline configuration …………………………………………...……..…...104
6.2 Optimal 2,3/*rev* flap stiffness variations……………………………….……….105
6.3 Optimal 2,3/*rev* lag stiffness variations ……...…………………………..…..…105
6.4 Optimal 3,4/*rev* torsion stiffness variations……………………...……….……105
6.5 Optimal 2,3/*rev* flap and lag stiffness variations...………………………….....…106
6.6 Influence of flexure stiffness on effectiveness of vibration control..…………..…106
6.7 Effectiveness of vibration controller at different forward speed ..………………..…107
6.8 Summary on discrete controllable stiffness device..…………………………...…107

Chapter 7 Discrete Controllable Stiffness Device Results – Model Refinements……..…115

7.1 Baseline configuration …………………………………………...……..…...115
7.2 Optimal 2,3/*rev* flap device stiffness variations …………….……………….....…116
7.3 Optimal 2,3/*rev* lag device stiffness variations …………...………………………116
7.4 Optimal 3,4/*rev* torsion device stiffness variations ………………………………117
7.5 Optimal 2,3/*rev* flap and lag device stiffness variations ..………….…………..…118
7.6 Influence of flexure stiffness on effectiveness of vibration control ..……………..…118
7.7 Effectiveness of vibration controller at different forward speeds ………………..…119
7.8 Summary on effectiveness of discrete controllable stiffness device ..……………119

Chapter 8 Discrete Controllable Orifice Dampers……………………………...………129

8.1 Baseline configuration……………………………………………………..…...129
8.2 Lag Damping Variation ……………………….……………………………….130
  8.2.1 Influence of optimal 2,3/*rev* lag damping variations ………………….………130
  8.2.2 Influence of lag damper sizing and configuration ………………...……...133
8.3 Simultaneous flap and lag damping variations..…….………….……….……135
  8.3.1 Influence of optimal 2,3/*rev* flap and lag damping variations………………135
  8.3.2 Effectiveness of flap and lag damping variations at different flight speeds ..138
8.4 Summary on controllable orifice dampers..……………………...…………138

Chapter 9 Semi-Active Isolator ………………………………………….….……153

9.1 System description……………………………………………………..…...153
  9.1.1 System with controllable stiffness device…………………….……….……154
  9.1.2 System with controllable damper………………………………………...154
9.2 Fundamentals of Controller Design ………………….…………….……..……155
  9.2.1 Optimal semi-active control scheme……………..………………….……155
  9.2.2 Semi-active device saturation consideration ………………….……...…...156
  9.2.3 Frequency content of the semi-active input ……………………...………157
  9.2.4 Identification of the system transfer matrix, *T* …………………....……...158
9.3 Semi-active controller schemes..…….…………….…………………..……160
  9.3.1 Open-loop controller …………………………………………..…………160
  9.3.2 Closed-loop controller……………………………………………………...160
  9.3.3 Closed-loop adaptive controller ………………………………...……...161
9.4 Effectiveness of semi-active controllers for vibration reduction..………….….…161
  9.4.1 Baseline System ………………………………………………………….…161
  9.4.2 Vibration reduction using open-loop controller…………………………..……162
    9.4.2.1 Controllable stiffness device……………………………..…...…162
    9.4.2.2 Controllable damper…………………………..……....…164
  9.4.3 Vibration reduction using closed-loop controller…………………...………164
    9.4.3.1 Closed-loop controller with controllable stiffness device…...…165
    9.4.3.2 Closed-loop controller with controllable damper……………..…166
  9.4.4 Closed-Loop Adaptive Control Scheme…………………………….……166
9.5 Summary of semi-active isolator ..………………………………………....…167

Chapter 10 Concluding Remarks and Recommendations…….………………………179

10.1 Concluding remarks ……………………………………………………...179
10.2 Recommendations for future work …………………………………….……...182

References………………..………………………….……………………….….184

Appendix A Loads on Helicopter Fuselage……………………………….….…….195

A.1 Loads from fuselage…………………………………….…………..……...…...195
A.2 Lift from horizontal tail……………………………………….……….…….195
A.3 Thrust from tail rotor ……...……………………………………….……….…196

Appendix B Elemental Structural Matrices and Load Vector…..………………………….197

B.1 Elemental structural mass matrix……………………….……………………...197
B.2 Elemental structural stiffness matrix…………………………..…….…….…….197
B.3 Elemental structural damping matrix……..……………..…………………..…198
B.4 Elemental structural force vector……..…………………..……………………198

Appendix C Rotor Inflow Models ……………………………………….…….……….200

C.1 Linear inflow model…………………………….……………..……..…...200
C.2 Rotor inflow using free wake analysis……………………………………...….200

Appendix D Elemental Aerodynamic Load Vector…..……………………………………201

D.1 Resultant incident velocity……………………….…………………..…………...201
D.2 Blade sectional loads from circulatory effects..…………………………..………201
D.3 Blade sectional loads from non-circulatory effects ...…...………..…………..……202
D.4 Elemental aerodynamic force vector ……...……………………..…….…………202

Appendix E Blade Response Calculation …..……………...……………………………203

Appendix F Vehicle Trim Calculation…...………………...……………………………205

Appendix G Fluid Dynamic Model of Controllable Damper…..…………………….…206

Appendix H Helicopter and Rotor Properties…..……………………………………..…207

Appendix I Convergence Study: Numbers of Finite Elements and Modal Representation.208

I.1 Number of finite elements along the blade span………………...………………..208
I.2 Number of blade modes in modal transformation ……………….……………….209

LIST OF TABLES

Table 4.1a: 4/*rev* vibratory hub loads for baseline rotor, no root element stiffness variation..88

Table 4.1b: Harmonics of blade root loads for baseline rotor, no root element stiffness variation………………………………………………………………...88

Table 4.2: Summary of beneficial effects of stiffness variations on vibratory hub loads…...88

Table 4.3a: Change in harmonics of blade root loads due to 2/*rev* variation in flap stiffness $\left\{ EI_\beta = \overline{EI_\beta} + \Delta EI_\beta^{2p}\sin(2\psi+\phi),\ \Delta EI_\beta^{2p} = 0.15\overline{EI_\beta},\ \phi = 240^\circ \right\}$…......89

Table 4.3b: Change in harmonics of blade root loads due to 3/*rev* variation in flap stiffness $\left\{ EI_\beta = \overline{EI_\beta} + \Delta EI_\beta^{3p}\sin(3\psi+\phi),\ \Delta EI_\beta^{3p} = 0.15\overline{EI_\beta},\ \phi = 45^\circ \right\}$……....89

Table 4.4a: Change in harmonics of blade root loads due to 2/*rev* variation in lag stiffness $\left\{ EI_\zeta = \overline{EI_\zeta} + \Delta EI_\zeta^{2p}\sin(2\psi+\phi),\ \Delta EI_\zeta^{2p} = 0.15\overline{EI_\zeta},\ \phi = 90^\circ \right\}$………89

Table 4.4b: Change in harmonics of blade root loads due to 3/*rev* variation in lag stiffness $\left\{ EI_\zeta = \overline{EI_\zeta} + \Delta EI_\zeta^{3p}\sin(3\psi+\phi),\ \Delta EI_\zeta^{3p} = 0.05\overline{EI_\zeta},\ \phi = 135^\circ \right\}$……...90

Table 4.4c: Change in harmonics of blade root loads due to 3/*rev* variation in lag stiffness $\left\{ EI_\zeta = \overline{EI_\zeta} + \Delta EI_\zeta^{3p}\sin(3\psi+\phi),\ \Delta EI_\zeta^{3p} = 0.05\overline{EI_\zeta},\ \phi = 225^\circ \right\}$…......90

Table 4.4d: Change in harmonics of blade root loads due to 5/*rev* variation in lag stiffness $\left\{ EI_\zeta = \overline{EI_\zeta} + \Delta EI_\zeta^{5p}\sin(5\psi+\phi),\ \Delta EI_\zeta^{5p} = 0.05\overline{EI_\zeta},\ \phi = 200^\circ \right\}$……...90

Table 4.5a: Change in harmonics of blade root loads due to 3/*rev* variation in torsion stiffness $\left\{ GJ = \overline{GJ} + \Delta GJ^{3p}\sin(3\psi+\phi),\ \Delta GJ^{3p} = 0.15\overline{GJ},\ \phi = 320^\circ \right\}$……...91

Table 4.5b: Change in harmonics of blade root loads due to 4/*rev* variation in torsion stiffness $\left\{ GJ = \overline{GJ} + \Delta GJ^{4p}\sin(4\psi+\phi),\ \Delta GJ^{4p} = 0.15\overline{GJ},\ \phi = 100^\circ \right\}$…...91

Table 5.1: Change in harmonics of blade root loads due to optimal 3/*rev* flap stiffness variation…………………………………………………………………102

Table 5.2: Optimal 2, 3/*rev* flap and 3/*rev* lag stiffness variations (J_z = 8.92)……………..102

Table 5.3a: Optimal 2, 3/*rev* flap and lag stiffness variations using gradient based optimization, without input penalty (W_k = 0), (J_z = 7.34)……………….……..102

Table 5.3b: Optimal 2, 3/*rev* flap and lag stiffness variations using non-gradient based optimization, without input penalty (W_k = 0), (J_z = 3.55)……………….……..103

Table 5.3c: Optimal 2, 3/*rev* flap and lag stiffness variations using gradient based optimization with input penalty (W_k = I)……………………………….....……..103

Table 5.4: Change in harmonic of blade root loads due to the optimal 2,3/*rev* flap and lag stiffness variation (W_k = I)…………………...…………………………………103

Table 6.1: Discrete controllable stiffness device and blade flexure properties…………......112

Table 6.2a: 4/*rev* vibratory hub loads for baseline rotor - no stiffness variation (Drees inflow, μ = 0.3)…………………...……………………………………….…112

Table 6.2b: Harmonics of blade root loads for baseline rotor - no stiffness variation (Drees inflow, μ = 0.3)…………………...……………………………………….…112

Table 6.2c: 4/*rev* vibratory hub loads for baseline rotor -no stiffness variation (Drees inflow, μ = 0.35)…………………...……………………….…….…113

Table 6.2d: Harmonics of blade root loads for baseline rotor - no stiffness variation (Drees inflow, μ = 0.35)…………………...……………………….…….…113

Table 6.3: Optimal 2, 3/*rev* flap device stiffness variations (J_z = 24.2)…………….......…113

Table 6.4: Optimal 2, 3/*rev* lag device stiffness variations (J_z = 60.8) ……………...….....113

Table 6.5: Optimal 2, 3/*rev* torsion device stiffness variations (J_z = 91.3)…………..….....114

Table 6.6: Optimal 2, 3/*rev* flap and lag device stiffness variations (J_z = 14.28) ……….....114

Table 6.7: Change in harmonics of blade root loads due to the optimal 2,3/*rev* flap and lag spring stiffness variations …………………...…………………………………114

Table 7.1: Discrete controllable stiffness device and blade flexure properties……………....126

Table 7.2a: 4/*rev* vibratory hub loads for baseline rotor – no cyclic stiffness variation (Free-wake, μ = 0.3)…………………...……………………………………….…126

Table 7.2b: Harmonics of blade root loads for baseline rotor – no cyclic stiffness variation (Free-wake, μ = 0.3)…………………...……………………………………….…126

Table 7.3: Optimal 2,3/*rev* flap device stiffness variations (J_z = 69.25)………………......127

Table 7.4: Optimal 2,3/*rev* lag device stiffness variations (J_z = 84.23) ………………….......127

Table 7.5: Optimal 3,4/*rev* torsion spring stiffness variations, with varying input weights (W_u) and baseline torsion spring stiffness ($\overline{K}_\phi$ and $2\overline{K}_\phi$)……………….127

Table 7.6: Optimal 2,3/*rev* flap and lag devices stiffness variations (J_z = 67.23)……….....128

Table 7.7: Change in harmonics of blade root loads due to the optimal 2,3/*rev* flap and lag device stiffness variations…………………...…………………………………128

Table 8.1: Discrete controllable damper properties and blade frequencies…………..….....149

Table 8.2a: 4/*rev* vibratory hub loads for baseline rotor, no cyclic damping variation……..149

Table 8.2b: Harmonics of blade root loads for baseline rotor, no cyclic damping variation..149

Table 8.2c: Harmonics of flexbeam root loads for baseline rotor, no cyclic damping variation……………………………………………………………...…..149

Table 8.2d: Harmonics of damper loads for baseline rotor, no cyclic damping variation..…150

Table 8.2e: Harmonics of blade tip response for baseline rotor, no cyclic damping variation ……………………………………………………………..…..150

Table 8.3: Optimal 2,3/*rev* lag damping variation (J_z = 64.55) ……………….……….…......150

Table 8.4: Change in harmonics of damper loads, due to optimal lag damping variation (from Table 8.3)…………………………..…………150

Table 8.5: Change in harmonics of blade root loads, due to optimal lag damping variation (from Table 8.3)…………………………..…………151

Table 8.6: Change in harmonics of flexbeam root loads, due to optimal lag damping variation (from Table 8.3)…………………………..…………151

Table 8.7: Change in harmonics of blade tip lag response, due to optimal lag damping variation (from Table 8.3)…………………………..…………151

Table 8.8: Optimal 2, 3/*rev* flap and lag damping variations (J_z = 52.87)…………..……......151

Table 8.9: Change in harmonics of damper loads, due to optimal flap and lag damping variations (from Table 8.8)………………...……………152

Table 8.10: Change in harmonics of blade root loads, due to optimal flap and lag damping variations (from Table 8.8)…………………...…………152

Table 8.11: Change in harmonics of flexbeam root loads, due to optimal flap and lag damping variations (from Table 8.8)………………...……………152

Table 8.12: Change in harmonics of blade tip flap and lag responses, due to optimal flap and lag damping variations (from Table 8.8)………...……………………152

Table 9.1: Numerical values of system parameters for single degree of freedom system....178

Table H.1: Rotor and fuselage properties………………………………...……….……......207

Table I.1: Optimal stiffness variations predicted using 2 flap, 2 lag, and 2 torsion modes (Drees inflow, μ = 0.35)……………………………...……….....……………215

Table I.2: 4/*rev* vibratory hub loads (predicted using 2 flap, 2 lag, and 2 torsion modes), with and without stiffness variations (Drees inflow, μ = 0.35)……………...….215

LIST OF FIGURES

Figure 1.1: Helicopter vibration profile at various forward speeds……………….……….22

Figure 1.2: Blade Vortex Interaction (BVI) schematic…………………….……..………...22

Figure 1.3: Angle of attack variation at a high-speed forward flight ……………….……..22

Figure 1.4: Frequency analysis of normalized vibration of a four-bladed helicopter in (a) the blade [rotating frame] and (b) the fuselage [non-rotating frame]…...23

Figure 1.5: Frequency response of a dynamic system with and without an absorber ….…..24

Figure 1.6: Hub mounted in-plane bifilar absorber ………………………………..….24

Figure 1.7: Blade mounted mass pendulum absorber ……………………………..….24

Figure 1.8: Helicopter vibration isolators; (a) Isolation platform with elastomeric pads and (b) Nodal beam…………………………………………………….25

Figure 1.9: Schematic of a Higher Harmonic Control (HHC) system ……………………..25

Figure 1.10: Schemetics of Individual Blade Control (IBC) systems using (a) blade pitch, (b) active flap, and (c) blade twist controls…………….……..26

Figure 1.11: Schematics of Active Control of Structural Response (ACSR) systems using force actuators located in (a) engine platform and (b) cabin…………….27

Figure 1.12: Schematics of (a) a semi-active suspension model and (b) a semi-active controllable damper……………………………………….27

Figure 1.13: Schematics of (a) a building model for sesmic testing and (b) a semi-active controllable orifice damper, and (c) calibration curve of the controllable damper…………………………………………………………28

Figure 1.14: Schematics of (a) a building model for sesmic testing and (b) a semi-active MR damper, and (c) MR damper characteristic…………………………29

Figure 2.1: Forces and moments exert on a helicopter in a level forward flight…………...51

Figure 2.2: Spatial discretization of a rotor blade using Finite Element Method…………..52

Figure 2.3: Global mass matrix of a rotor blade with 5 spatial elements…………………..52

Figure 2.4: Discretization of azimuthal position for blade response calculation using Finite Element in time method…………………………………………..52

Figure 2.5: Flowchart of coupled rotor/trim response calculation procedure………………53

Figure 2.6: Nodal blade shear forces in vertical and chordwise directions………………...54

Figure 2.7: Nodal blade moments in flapwise direction……………………………………54

Figure 2.8: Blade root shear forces and moments ………………………………………….54

Figure 2.9: Transformation between Hub loads and Blade Root Loads……………………55

Figure 2.10: Stiffness variation of the root element……………………………………………55

Figure 2.11: Schematic sketch of discrete controllable stiffness devices……………………55

Figure 2.12: Mathematical idealization of discrete controllable stiffness devices using dual spring model in (a) flap and (b) lead-lag directions………………...56

Figure 2.13: Mathematical idealization of discrete controllable stiffness devices using single spring model in (a) flap, (b) lead-lag, and (c) torsional directions……...56

Figure 2.14: Configuration and attachment geometry of controllable stiffness devices, (a) flap device and (b) lag device………………………………………………57

Figure 2.15: (a) Deformation of the flap device due to blade bending, and (b) Loads exerted on the blade at attachment point by the flap device………...57

Figure 2.16: Schematic of a semi-active controllable damper……………….……………58

Figure 2.17: Force/Displacement hysteresis loops for different bypass orifice settings (valve voltages); (a) experiment, (b) fluid dynamic model simulations (from Ref. 103)……………………………………………………………58

Figure 2.18: Force/Displacement hysteresis cycles produced by the fluid dynamics based damper model and an equivalent damping coefficient model (at a specified orifice command voltage V_o)…………………………………...58

Figure 2.19: Calibration curve for equivalent viscous damping coefficient as a function of orifice voltage……………………………………………………59

Figure 2.20: Damper hysteresis loops for prescribed damper motion at frequency Ω and cyclically varying orifice voltage (a) $V=V_o+\Delta V\sin(\Omega t)$ and (b) $V=V_o+\Delta V\sin(2\Omega t)$ ………………………………………………………59

Figure 2.21: Schematic of rotor blade with controllable flap and lag dampers……………...59

Figure 2.22: (a) Deformation of the flap damper due to blade bending, and (b) loads exerted on the blade at attachment point by the flap damper ………..60

Figure 2.23a: Blade root vertical shear, S_z, with contributions from the flexbeam, S_z^{flex} (obtained by summing vertical shear forces, f_z^i, along blade Finite Element DOF's), and the flap damper, S_z^{damper} …………………………60

Figure 2.23b: Blade root drag shear, S_x, with contributions from the flexbeam, S_x^{flex} (obtained by summing drag shear forces, f_x^i, along blade Finite Element DOF's), and the lag damper, S_x^{damper} ……………………………………..60

Figure 4.1: Influence of phase, ϕ, of 1/*rev* variation in flap stiffness on 4/*rev* hub forces (a) and moments (b), $\left\{ EI_\beta = \overline{EI_\beta} + \Delta EI_\beta^{1p}\sin(\psi+\phi),\ \ \Delta EI_\beta^{1p} = 0.15\overline{EI_\beta} \right\}$…..76

Figure 4.2: Influence of phase, ϕ, of 2/*rev* variation in flap stiffness on 4/*rev* hub forces (a) and moments (b), $\left\{ EI_\beta = \overline{EI_\beta} + \Delta EI_\beta^{2p}\sin(2\psi+\phi),\ \ \Delta EI_\beta^{2p} = 0.15\overline{EI_\beta} \right\}$...77

Figure 4.3: Influence of phase, ϕ, of 3/*rev* variation in flap stiffness on 4/*rev* hub forces (a) and moments (b), $\left\{ EI_\beta = \overline{EI_\beta} + \Delta EI_\beta^{3p} \sin(3\psi + \phi),\ \ \Delta EI_\beta^{3p} = 0.15\overline{EI_\beta} \right\}$…78

Figure 4.4: Influence of phase, ϕ, of 2/*rev* variation in lag stiffness on 4/*rev* hub forces (a) and moments (b), $\left\{ EI_\zeta = \overline{EI_\zeta} + \Delta EI_\zeta^{2p} \sin(2\psi + \phi),\ \ \Delta EI_\zeta^{2p} = 0.15\overline{EI_\zeta} \right\}$…79

Figure 4.5: Influence of phase, ϕ, of 3/*rev* variation in lag stiffness on 4/*rev* hub forces (a) and moments (b), $\left\{ EI_\zeta = \overline{EI_\zeta} + \Delta EI_\zeta^{3p} \sin(3\psi + \phi),\ \ \Delta EI_\zeta^{3p} = 0.05\overline{EI_\zeta} \right\}$….80

Figure 4.6a: Influence of magnitude of 3/*rev* variations in lag stiffness on vibratory hub torque……………………………………………………………………81

Figure 4.6b: Influence of magnitude of lag stiffness variations on vibratory hub torque…...81

Figure 4.7: Influence of phase, ϕ, of 5/*rev* variation in lag stiffness on 4/*rev* hub forces (a) and moments (b), $\left\{ EI_\zeta = \overline{EI_\zeta} + \Delta EI_\zeta^{5p} \sin(5\psi + \phi),\ \ \Delta EI_\zeta^{5p} = 0.05\overline{EI_\zeta} \right\}$…82

Figure 4.8: Influence of phase, ϕ, of 3/*rev* variation in torsion stiffness on 4/*rev* hub forces (a) and moments (b), $\left\{ GJ = \overline{GJ} + \Delta GJ^{3p} \sin(3\psi + \phi),\ \ \Delta GJ^{3p} = 0.15\overline{GJ} \right\}$..83

Figure 4.9: Influence of phase, ϕ, of 4/*rev* variation in torsion stiffness on 4/*rev* hub forces (a) and moments (b), $\left\{ GJ = \overline{GJ} + \Delta GJ^{4p} \sin(4\psi + \phi),\ \ \Delta GJ^{4p} = 0.15\overline{GJ} \right\}$..84

Figure 4.10: Change in 4/*rev* hub loads, F_z^{4p}, due to 2/*rev* variation in flap stiffness $\left\{ EI_\beta = \overline{EI_\beta} + \Delta EI_\beta^{2p} \sin(2\psi + \phi),\ \Delta EI_\beta^{2p} = 0.15\overline{EI_\beta},\ \phi = 240^\circ \right\}$………………85

Figure 4.11: Change in contributions of hub load, F_x^{4p}, due to 3/*rev* variation in flap stiffness $\left\{ EI_\beta = \overline{EI_\beta} + \Delta EI_\beta^{3p} \sin(3\psi + \phi),\ \ \Delta EI_\beta^{3p} = 0.15\overline{EI_\beta},\ \ \phi = 45^\circ \right\}$….....85

Figure 4.12: Change in 4/*rev* hub loads, F_z^{4p}, due to due to 3/*rev* variation in flap stiffness $\left\{ EI_\beta = \overline{EI_\beta} + \Delta EI_\beta^{3p} \sin(3\psi + \phi),\ \ \Delta EI_\beta^{3p} = 0.15\overline{EI_\beta},\ \ \phi = 45^\circ \right\}$….....86

Figure 4.13: Change in 4/*rev* hub loads, F_z^{4p}, due to 3/*rev* variation in lag stiffness $\left\{ EI_\zeta = \overline{EI_\zeta} + \Delta EI_\zeta^{3p} \sin(3\psi + \phi),\ \ \Delta EI_\zeta^{3p} = 0.05\overline{EI_\zeta},\ \ \phi = 225^\circ \right\}$……………..86

Figure 4.14: Change in 4/*rev* hub loads, F_z^{4p}, due to 4/*rev* variation in torsion stiffness $\left\{ GJ = \overline{GJ} + \Delta GJ^{4p} \sin(4\psi + \phi),\ \ \Delta GJ^{4p} = 0.15\overline{GJ},\ \ \phi = 100^\circ \right\}$…………...87

Figure 4.15: Reduction in M_z^{4p} at different advance ratios, due to 3/*rev* lag stiffness variation $\left\{ EI_\zeta = \overline{EI}_\zeta + \Delta EI_\zeta^{3p} \sin(3\psi + \phi),\ \ \Delta EI_\zeta^{3p} = 0.05\overline{EI}_\zeta,\ \ \phi = 135^\circ \right\}$….87

Figure 5.1: Contour plot of performance index, *J*, (% Baseline) due to 3/*rev* flap stiffness variation…………………………………………….97

Figure 5.2: Hub vibration reduction due to optimal 3/*rev* flap stiffness variation………...97

Figure 5.3: Hub vibration reduction due to optimal 2,3/*rev* flap and 3/*rev* lag stiffness variations……………………………………………………………..98

Figure 5.4: Hub vibration reduction due to optimal 2,3/*rev* flap and lag stiffness variations with gradient based (G) and non-gradient based (NG) optimizations …………98

Figure 5.5: Hub vibration reduction due to optimal 2,3/*rev* flap and lag stiffness variations with (W_u = I) and without (W_u = 0) input penalty…………………...99

Figure 5.6: Effectiveness of optimal 2,3/*rev* flap and lag stiffness variations for different values of blade flap stiffness (flap natural frequency) ……………….99

Figure 5.7: Effectiveness of optimal 2,3/*rev* flap and lag stiffness variations for different values of blade lag stiffness (lag natural frequency)………………..100

Figure 5.8: Effectiveness of optimal 2,3/*rev* flap and lag stiffness variations for different values of blade torsion stiffness (torsion natural frequency)….…….100

Figure 5.9: Effectiveness of optimal 2,3/*rev* flap and lag stiffness variations for different advance ratios…………………………………………………….101

Figure 6.1: Hub vibration reduction due to optimal 2,3/*rev* discrete flap stiffness variations…………………………………………………………….108

Figure 6.2: Hub vibration reduction due to optimal 2,3/*rev* discrete lag stiffness variations…………………………………………………………….108

Figure 6.3: Hub vibration reduction due to the optimal 3,4/*rev* discrete torsion stiffness variations…………………………………………………….109

Figure 6.4: Hub vibration reduction due to the optimal 2,3/*rev* discrete flap and lag spring stiffness variations……………………………………..109

Figure 6.5: Effectiveness of optimal 2,3/*rev* discrete flap and lag spring stiffness variations for different value of flap flexure stiffness ………………110

Figure 6.6: Effectiveness of optimal 2,3/*rev* discrete flap and lag spring stiffness variations for different value of lag flexure stiffness………………..110

Figure 6.7: Effectiveness of optimal 2,3/*rev* discrete flap and lag spring stiffness variations for different value of torsional flexure stiffness…………111

Figure 6.8: Effectiveness of the optimal 2,3/*rev* discrete flap and lag spring stiffness variations for different advance ratios ………………………………111

Figure 7.1: Hub vibration reduction due to optimal 2,3/*rev* flap device stiffness variations…………………………………………………………….121

Figure 7.2: Optimal flap device stiffness variation over one rotor revolution, (with 2, 3/*rev* inputs from Table 7.3)………………………………………121

Figure 7.3: Hub vibration reduction due to optimal 2,3/*rev* lag device stiffness variations…………………………………………………………….122

Figure 7.4: Hub vibration reduction due to optimal 3,4/*rev* torsion device stiffness variations (W_u = 0.02[I], baseline torsion device stiffness = $\overline{K}_\phi$)……………122

Figure 7.5: Hub vibration reduction due to the optimal 3,4/*rev* torsion device stiffness variations, with varying input weights (W_u) and baseline torsion spring stiffness ($\overline{K}_\phi, 2\overline{K}_\phi$)………………………………………………………...123

Figure 7.6: Hub vibration reduction due to optimal 2,3/*rev* flap and lag device stiffness variations……………………………………………………………123

Figure 7.7: Effectiveness of optimal 2,3/*rev* flap and lag device stiffness variations for different values of flap flexure stiffness……………………………………..124

Figure 7.8: Effectiveness of optimal 2,3/*rev* flap and lag device stiffness variations for different values of lag flexure stiffness …………………………………...124

Figure 7.9: Effectiveness of optimal 2,3/*rev* flap and lag device stiffness variations for different values of torsion flexure stiffness……………………………….125

Figure 7.10: Effectiveness of optimal 2,3/*rev* flap and lag device stiffness variations for different advance ratios………………………………………………………125

Figure 8.1: Optimal lag damping variation over one rotor revolution (with 2/*rev* and 3/*rev* inputs from Table 8.3)…………………………………139

Figure 8.2: Hub vibration reduction due to optimal 2, 3/*rev* lag damping variation……...139

Figure 8.3: Lag damper force variation over one rotor revolution (with optimal semi-active lag damping variation from Table 8.3)…………………………..140

Figure 8.4: Blade root loads over one rotor revolution (with optimal semi-active lag damping variation from Table 3), (a) blade root drag shear, S_x, and (b) blade root radial shear, S_r…………………………………………………141

Figure 8.5: Flexbeam root loads over one rotor revolution (with optimal semi-active lag damping variation from Table 8.3), (a) flexbeam root drag shear, S_x^{flex}, and (b) flexbeam root radial shear, S_r^{flex}……………………………………….142

Figure 8.6: Blade flap, lag, and torsional tip responses over one rotor revolution (with optimal semi-active lag damping variation from Table 8.3) …………...143

Figure 8.7: Effectiveness of lag damping variation in reducing vibration for different damper mounting angles……………………………………………143

Figure 8.8: Effectiveness of lag damping variation in reducing vibration for different damper offsets ……………………………………………………144

Figure 8.9: Effectiveness of lag damping variation in reducing vibration for different damper attachment points…………………………………………...144

Figure 8.10: Effectiveness of lag damping variation in reducing vibration for different damper sizes…………………………………………………………145

Figure 8.11: Optimal flap and lag damping variations over one rotor revolution (with 2/*rev* and 3/*rev* inputs from Table 8.8)……………………………………145

Figure 8.12: Hub vibration reduction due to optimal 2, 3/rev flap and lag damping variations……………………………………………………………146

Figure 8.13: Lag damper force variation over one rotor revolution (with optimal semi-active flap and lag damping variations from Table 8.8)………………...146

Figure 8.14: Flap damper force variation over one rotor revolution (with optimal semi-active flap and lag damping variations from Table 8.8)………………...147

Figure 8.15: Blade flap, lag, and torsional tip responses over one rotor revolution (with optimal semi-active flap and lag damping variations from Table 8.8)…147

Figure 8.16: Effectiveness of optimal 2, 3/rev flap and lag damping variations for different advance ratios…………………………………………………………148

Figure 9.1: Schematics of single-degree-of-freedom system for vibration reduction using (a) semi-active controllable stiffness device, and (b) controllable damper…..169

Figure 9.2: Frequency-to-Time domain conversion (F/T) unit…………………………...169

Figure 9.3: Block diagram of open-loop control system……………………………..…...169

Figure 9.4: Block diagram of closed-loop control system………………………………...170

Figure 9.5: Block diagram of closed-loop adaptive control system…………………….....170

Figure 9.6: (a) Time history and (b) corresponding frequency content of disturbance force, F, and support force, F_s, of the baseline uncontrolled system…………171

Figure 9.7: Frequency content of disturbance force, F, and support force, F_s, due to optimal stiffness variation input (no input limits)……………………..172

Figure 9.8: Frequency content of disturbance force, F, and support force, F_s, due to optimal semi-active stiffness variation (input “scaled-down”)………..172

Figure 9.9: Frequency contents of support force, F_s, for increasing stiffness variation input amplitudes.…………………………………………………………173

Figure 9.10: Frequency contents of support force, F_s, for increasing semi-active damping variation input amplitudes (with “input scaling”).……………………173

Figure 9.11: Time history of disturbance force, F, and support force, F_s, for closed-loop controller with controllable stiffness device, with change in phase of excitation force ($\phi = 45°$)…………………………..174

Figure 9.12: Amplitude of support force, F_s, at disturbance frequency, Ω, for open-loop and closed-loop controller with controllable stiffness device, with change in phase of excitation force ($\phi = 45°$)…………………..174

Figure 9.13: Amplitude of support force, F_s, at excitation frequency, Ω, for open-loop and closed-loop controllers with controllable stiffness device, with change in phase of excitation force ($\phi = 90°$)…………………..175

Figure 9.14: Variation in steady state support force, F_s, at Ω for closed-loop and open-loop controllers with controllable stiffness device as a function of change in phase of excitation force……………………………..175

Figure 9.15: Variation in steady state support force, F_s, at Ω for closed-loop and open-loop controllers with controllable damper as a function of change in phase of excitation force……………………………..176

Figure 9.16: Amplitude of support force, F_s, at excitation frequency, Ω, for closed-loop adaptive controller using controllable stiffness device, with change in phase of excitation force (ϕ = 45°)…………………………..176

Figure 9.17: Amplitude of support force, F_s, at excitation frequency, Ω, for closed-loop adaptive controller using controllable stiffness device, with change in phase of excitation force (ϕ = 90°)…………………………..177

Figure 9.18: Variation in steady state support force, F_s, at Ω for open-loop, closed-loop and closed-loop adaptive controllers with controllable stiffness device as a function of change in phase of excitation force…………177

Figure I.1: Rotor blade finite element discretization used in the convergence study…….211

Figure I.2: Blade rotating natural frequencies for increasing number of finite elements...211

Figure I.3: Blade flap mode shapes for increasing number of finite elements…………...212

Figure I.4: Blade lag mode shapes for increasing number of finite elements…………….212

Figure I.5: Blade torsional mode shapes for increasing number of finite elements………213

Figure I.6: Variation in 4/*rev* vibratory hub load predictions with increasing number of flap modes, when a 2,3/*rev* flap stiffness variation is used (Drees inflow, μ = 0.35)……………………………………………………213

Figure I.7: Variation in 4/*rev* vibratory hub load predictions with increasing number of lag modes, when a 2,3/*rev* lag stiffness variation is used (Drees inflow, μ = 0.35)……………………………………………………214

Figure I.8: Variation in 4/*rev* vibratory hub load predictions with increasing number of torsion modes, when a 3,4/*rev* torsion stiffness variation is used (Drees inflow, μ = 0.35)……………………………………………214

LIST OF SYMBOLS

a	Blade section lift-curve slope
a_{ht}	Horizontal tail section lift-curve slope
a_{tr}	Tail rotor blade section lift-curve slope
A	Rotor disk area
A_p, A_f, A_r	Piston, accumulator, and rod area
A_{pri}, A_{con}	Primary and controllable orifice area
b	Blade half chord
c	Blade chord
C	Damping matrix
$[C]_\mathrm{i}$	Structural damping matrix of the ith element
C_{vv}, C_{vw}, $C_{v\phi}$	Damping matrix associated with lag degree of freedom
C_{wv}, C_{ww}, $C_{w\phi}$	Damping matrix associated with flap degree of freedom
$C_{\phi v}$, $C_{\phi w}$, $C_{\phi\phi}$	Damping matrix associated with torsion degree of freedom
c_{tr}	Tail rotor blade chord
C_d	Sectional drag coefficient
C_l	Sectional lift coefficient
C_m	Sectional pitching moment coefficient
C_T	Thrust coefficient
C_{Ttr}	Tail rotor thrust coefficient
C_w , C_v	Damping coefficient of controllable flap and lag dampers
C_o	Baseline damping coefficient of controllable damper
C_1	Maximum damping variation of controllable damper
C_{yf}, C_{mxf}, C_{myf}, C_{mzf}	Fuselage side force, rolling, pitching, and yawing moment coefficients
D	Sectional drag
D_f	Fuselage drag
e_d	Chordwise offset of blade center-of mass (ahead of elastic axis)
e_w , e_v	offset of controllable flap, lag stiffness devices (dampers)

e_g	Chordwise offset of aerodynamic center (behind elastic axis)
EI_y , EI_z	Blade flapwise, chordwise stiffness
EB_1 , EB_2	Section stiffness constants
EC_1	Warping rigidity
EC_2	Section warping constant
f	Equivalent drag area of helicopter fuselage and hub
f_x , f_z	Nodal blade drag, vertical force
F	Force vector
F^A	Aerodynamic load vector
F_A	Blade axial force
F_D	Damper force
F_i	Structural load vector of the ith element
F_v, F_w, F_ϕ	Load vector associated with lag, flap, and torsion degree of freedom, respectively
F_v^A, F_w^A, F_ϕ^A	Aerodynamic load vector associated with lag, flap, and torsion degree of freedom, respectively
F_s	Support force
F_o	Excitation force
F_x , F_y , F_z	Rotor drag, side, and vertical forces
G	Controller gain
GJ	Blade torsional stiffness
h	Hub offset above center of gravity
H	Spatial modeshape vector (flap and lag degree of freedoms)
H_t	Temporal modeshape vector
$H_{\hat{\phi}}$	Spatial modeshape vector (torsion degree of freedom)
J	Jacobian matrix
J_z , J_u	Vibration index and semi-active input index
k_m	Blade cross sectional mass radius of gyration
k_{m1} , k_{m2}	Blade cross sectional mass radius of gyration in the flap and lag directions, respectively

k_{pri}, k_{con}	Primary and controllable orifice discharge coefficient
K	Stiffness matrix
K_a	Equivalent accumulator stiffness
$[K]_i$	Structural stiffness matrix of the ith element
K_w , K_v , K_ϕ	Stiffness of controllable flap, lead-lag, and torsion stiffness devices
K_{vv}, K_{vw}, $K_{v\phi}$	Stiffness matrix associated with lag degree of freedom
K_{wv}, K_{ww}, $K_{w\phi}$	Stiffness matrix associated with flap degree of freedom
$K_{\phi v}$, $K_{\phi w}$, $K_{\phi\phi}$	Stiffness matrix associated with torsion degree of freedom
K_o	Baseline stiffness of controllable stiffness device
K_1	Maximum stiffness variation of controllable stiffness device
l, l_i	Element length
L	Sectional lift
L_{ht}	Lift of horizontal tail
L_u, L_v, L_w	Blade forces in undeformed frame
$\overline{L}_u$, $\overline{L}_v$, $\overline{L}_w$	Blade forces in deformed frame
L_u^A, L_v^A, L_w^A	Blade forces in deformed frame including non-circulatory effect
L_w^{NC}	Non-circulatory blade lift
m	Mass, blade mass per unit length
m_o	Elemental mass
m_β , m_ζ , m_ϕ	Nodal blade flap, lag, and torsional moment
M	Mass matrix
$[M]_i$	Structural mass matrix of the ith element
M_x , M_y , M_z	Rotor rolling, pitching moment and torque
M_{xf} , M_{yf} , M_{zf}	Fuselage aerodynamic rolling, pitching moment and torque
M_β, M_ζ, M_ϕ	Blade root flapping, lead-lag, and pitching moment
M_{vv}, M_{vw}, $M_{v\phi}$	Mass matrix associated with lag degree of freedom
M_{wv}, M_{ww}, $M_{w\phi}$	Mass matrix associated with flap degree of freedom
$M_{\phi v}$, $M_{\phi w}$, $M_{\phi\phi}$	Mass matrix associated with torsion degree of freedom

$M_{\hat{\phi}}$	Blade pitching moment in deformed frame
$M_{\hat{\phi}}^{A}$	Blade pitching moment in deformed frame including non-circulatory effect
$M_{\hat{\phi}}^{NC}$	Non-circulatory blade pitching moment
N	Number of main rotor blades
N_{tr}	Number of tail rotor blades
p	Modal coordinates
P	Pressure
q	Normalized coordinates
r	Radial position
R	Rotor radius
R_{tr}	Tail rotor radius
s	Local coordinate of spatial element
S	Blade nodal load vector
S_{ht}	Horizontal tail area
S_r , S_x , S_z	Blade root radial, drag, and vertical shear force
t	Time, non-dimensional time
T	Rotor thrust
T_{tr}	Tail rotor thrust
T_{DU}	Transformation matrix from blade undeformed from to blade deformed frame
u	control input
u_c	control input (frequency domain)
U	Section resultant velocity
U_P, U_R, U_T	Air velocity of blade; perpendicular, radial, tangential components
U_x, U_y, U_z	x, y, z components of blade sectional velocity
V	Helicopter forward velocity
W	Helicopter gross weight,
W_z, W_u	Vibration and input penalty weighting matrix

x	Blade non-dimensional radial coordinate; body-fixed coordinate; displacement
x_{cg}	Hub offset from center of gravity in x direction
x_{ht}	Horizontal tail offset from center of gravity in x direction
x_{tr}	Tail rotor offset from center of gravity in x direction
y	body-fixed coordinate, state vector
y_{cg}	Hub offset from center of gravity in y direction
Y_f	Fuselage aerodynamic side force
z	body-fixed coordinate
z_{tr}	Tail rotor offset from center of gravity in z direction
α	Blade section angle of attack
α_s	Longitudinal shaft tilt
α_w , α_v	Mounting angle of controllable flap and lag stiffness device (dampers)
β	Fluid bulk modulus
β_p	Blade precone angle
δT	Variational kinetic energy
δU	Variational strain energy
δT	Virtual work
$\delta \Pi$	Variational Hamiltonian
ε	Error
γ	Blade lock number
γ_{tr}	Tail rotor blade lock number
η	Solution vector for helicopter trim
η_r	Distance from blade elastic axis to blade ¾ chord
θ	Pitch angle
θ_o, θ_{1c}, θ_{1s}	Collective, cosine, and sine components of blade pitch
θ_{tr}	Tail rotor collective
λ	Main rotor inflow ratio
λ_i	Induced inflow

λ_{tr}	Tail rotor inflow ratio
λ_o	Main rotor mean induced velocity
λ_{1c}	Cosine component of rotor inflow
λ_{1s}	Sine component of rotor inflow
μ	Main rotor advance ratio
μ_{tr}	Tail rotor advance ratio
ρ	Air density
σ	Rotor solidity
ϕ	Section inflow angle; phase angle
Φ	Eigenvectors representing mode shapes
ϕ_s	Lateral shaft tilt
ψ	Azimuth position
Ω	Main rotor rotational speed; excitation frequency
Ω_{tr}	Tail rotor rotational speed
$\dot{(\;)}$	$\partial(\;)/\partial t$
$(\;)'$	$\partial(\;)/\partial x$

ACKNOWLEDGEMENTS

I would like to express my sincere appreciation to my advisor, Dr. Farhan Gandhi, who has dedicated his years to teach and assist me in almost every aspect of life throughout my graduate study. I am also grateful to members of my advisory committee, Drs. Smith, Lesieutre, and Rahn, all of whom have shown interest in this work and provided countless advice and discussion. I would like to thank Dr. Lane Miller of Lord Corp. for his valuable guidance and suggestions.

The financial support for this research, which is provided by the Department of Aerospace Engineering and the Rotorcraft Center of Excellence, is gratefully acknowledged. I am thankful for the RCOE for awarding me many years of the Rotorcraft Center fellowships that presented me with both financial as well as moral support.

I am grateful for many of my colleagues at the Rotorcraft Center for their friendship, support, and help over the years. In particular, I appreciate Martin Sekula, Eric Hathaway, and Brendon Malovrh for shearing their life, numerous stories, and laughter while we had some spare time mostly on friday afternoon. Thanks also to Lionel Tauszig for his dedicated assistance with a free wake analysis, which is used extensively in this research.

Most of all I am indebted to my parents, Viroj and Chumpee Anusonti-Inthra, half way around the world for their unconditional love, support, and encouragement which guided me through the years. I would like to express my gratitude to my brothers, Phurithat and Jackchai, who make me feel loved and supported always. A special thank is dedicated to my future wife, Jirin Palanuwech, for her kindness, care, and love.

Chapter 1

Introduction

1.1 Background and motivation

Helicopters play an essential role in today's aviation with unique abilities to hover and take off/land vertically. These capabilities enable helicopters to carry out many distinctive tasks in civilian and military operations. Despite these attractive abilities, helicopter trips are usually unpleasant for passengers and crew because of high vibration level in the cabin. This vibration is also responsible for degradation in structural integrity as well as reduction in component fatigue life. Furthermore, the high vibration environment may decrease the effectiveness of onboard avionics or computer systems that are critical for aircraft primary control, navigation, and weapon systems. Consequently, significant efforts have been devoted over the last several decades for developing strategies to reduce helicopter vibration.

To develop a new helicopter vibration reduction method, it is essential to first understand the origin and fundamental mechanics of helicopter vibration, which are summarized in Section 1.2. A comprehensive review of previous helicopter vibration reduction schemes using both passive and active strategies is also conducted and presented in Sections 1.3 and 1.4, respectively. This suggests that passive vibration reduction concepts can produce modest performance (no power is required), while incurring considerable weight penalty, and the designs are generally fixed with no ability to adapt to any changes. Even though active vibration reduction methods can produce relatively better performance and can adapt to changes in configuration or operating condition, they usually require significant power to operate. This leads to an effort to combine the advantages of passive and active vibration reduction strategies into a recently developed "semi-active" approach, which is reviewed thoroughly in Section 1.5. Generally, the semi-active method can produce better performance than purely passive approach, while using relatively small power. However, most of the recent semi-active concepts are developed for broadband vibration reduction applications, which are not directly applicable for helicopter use since helicopter vibration is tonal or narrow-band in nature (helicopter vibration is concentrated at some specific frequencies). This motivates the development of a new helicopter vibration reduction scheme using the semi-active concept.

1.2 Overview of helicopter vibration

Helicopter vibration generally originates from many sources; for example, transmission, engine, and tail rotor, but most of the vibration comes primarily from the main rotor system, even with a perfectly tracked rotor. Figure 1.1, which shows a typical vibration profile of a helicopter, as a function of cruise speeds, demonstrates that severe vibration usually occurs in two distinct flight conditions; low speed transition flight and high-speed flight. In the low-speed transition flight (generally during approach for landing), the severe vibration level is primarily due to impulsive loads induced by interactions between rotor blades and strong tip vortices dominating the rotor wake (see Fig. 1.2). This condition is usually referred to as Blade Vortex Interaction (BVI). In moderate-to-high speed cruise, the BVI-induced vibration is reduced since vortices are washed further downstream from the rotor blades, and the vibration is caused mainly by the unsteady aerodynamic environment in which the rotor blades are operating. This highly periodic aerodynamic environment creates large periodic variations in blade velocity and angle of attack, and corresponding large periodic vibratory loads on the blades. Figure 1.3 shows, for example, a typical variation in blade angle of attack around the azimuth for a high-speed forward flight. For an extremely high-speed cruise, the vibration can be even more severe since the blades can encounter shock on the advancing side (which generates large blade drag and pitching moment) or stall on the retreating side (which results in sudden loss of lift) over every revolution. This severe high vibration level and associated increases in rotor power generally limits the maximum helicopter cruise speed.

Once the blade loads are generated, they are further transmitted into the non-rotating frame as vibratory hub loads and then into the cabin as cabin vibration. Normally, sectional blade loads are comprised of both aerodynamic and inertial contributions at harmonics of the rotor speed, Ω. The aerodynamic component of blade loads is generated by periodic flow field around the rotating blades, while the inertial component of blade loads is created by blade rotation (gyroscopic effect) and blade motion in flap, lag and torsion directions. The sectional inertial and aerodynamic blade loads can be integrated along the blade length to obtain the blade root loads, also at harmonics of Ω, as seen in Fig. 1.4a. These blade root loads from every blade are summed at the rotor hub to yield hub loads. Since the rotor blades are assumed identical, implying identical blade root loads with the phase shifted properly, most of the harmonics of hub loads will be filtered (cancelled) out, except components at the frequencies of; 0, NΩ, 2NΩ, 3NΩ, etc., where N is the number of blades, (see Fig. 1.4b). The most significant component of the vibratory hub loads is the NΩ or N/*rev* component, and the amplitudes of the higher harmonic are progressively smaller. These hub loads are then transmitted through the helicopter cabin via the transmission platform. The amount of vibration throughout the helicopter cabin may vary, depending on the vibration characteristics of the fuselage itself.

1.3 Passive helicopter vibration reduction

Passive strategies have been employed extensively for reducing helicopter vibration. Most of the passive strategies produce moderate vibration reduction in certain flight conditions, and only at some locations in the fuselage (such as, pilot seats or avionics compartments). The major advantage of the passive concepts is that they require no external power to operate. However, they generally involve a significant weight penalty and are fixed in design, implying no ability to adjust to any possible change in operating conditions (such as changes in rotor RPM or aircraft forward speed). Examples of these passive vibration reduction strategies include tuned-mass absorbers, isolators, and blade design optimizations.

Tuned-mass vibration absorbers can be employed for reducing helicopter vibration both in the fuselage and on the rotor system. The absorbers are generally designed using classical spring-mass systems tuned to absorb energy at a specific frequency [1], for example at N/*rev*, thus reducing system response or vibration at the tuned frequency (see Fig. 1.5). In the fuselage, the absorbers are usually employed to reduce vibration levels at pilot seats or at locations where sensitive equipment is placed. Without adding mass, an aircraft battery may be used as the mass in the absorber assembly [2]. Vibration absorbers can also be integrated into the rotor hub system (Fig. 1.6) or can be located on the blades themselves (Fig. 1.7). The absorbers are often designed using a pendulum like configuration, with stiffness provided by centrifugal force. Various configurations have been developed; for example blade-mounted vertical plane pendulum absorbers [3], dual-frequency pendulum absorbers [4], hub-mounted inplane bifilar absorbers [5], dual frequency monofilar inplane absorbers [6], and single-frequency inplane roller absorbers [7]. Many design tradeoffs have to be considered when using these absorbers on helicopters for vibration reduction. Generally a sizable absorber mass is required for a good performance. Furthermore, the effectiveness of the absorbers is highly dependent on frequency, thus changes in rotor RPM may even produce increases in the vibration levels. Also, some power is lost due to the additional aerodynamic drag produced by the absorbers in the rotor system.

Vibration isolators typically are used in helicopters for reducing transmission of vibration from the rotor to the fuselage. Normally the isolator and load-carrying member are designed as an integrated unit for mounting the rotor/transmission assembly to the fuselage, as seen in Fig. 1.8. These isolators are designed specifically to reduce transmission of vibration at specific frequency close to N/*rev* [8]. Isolator designs range from using simple elastomeric material [9] to using more complicated strategies such as a nodal beam configuration [10]. Extensive usage of the passive isolators in helicopters has been limited due to many concerns. The most important issue is the load-carrying capacity of the isolator unit, because the unit has to be able to withstand the weight of the entire helicopter as well as its payload with some safety margin. For the nodal beam concepts, the vibration reduction performance is restricted when allowable deflection of the isolators is small [11].

Blade design optimization is another effective alternative for reducing helicopter vibration. Rotor blade fundamental properties (such as structural and aerodynamic) are chosen optimally to reduce overall vibration in the designing phase [12]-[16]. Examples of the design parameters used are rotor tip sweep, taper, and anhedral, nonstructural mass distribution, structural stiffness, elastic tailoring, and spar cross-sectional geometry. Other variations to classical structural design optimization strategies include dynamically tuned pushrods [17] and dynamically tuned swashplates [18]. An advantage of using structural design optimization (over other passive methods) is that no significant added mass is necessary for the resulting vibration reduction. However, the vibration characteristic of the rotor blade and airframe may change during operation depending on; the amount of fuel left in the fuel tank, the weight and location of payloads, rotor RPM, and aircraft speeds. Therefore, the optimized configuration in one condition may not produce vibration reduction in other conditions. This problem, though, is common to all passive vibration reduction strategies.

1.4 Active helicopter vibration reduction

Active vibration reduction concepts have been introduced with the potential to improve vibration reduction capability and to overcome the fixed-design drawback of the passive designs. The majority of the active vibration reduction concepts aim to reduce the vibration in the rotor system, and some active methods intend to attenuate the vibration only in the fuselage. In general, an active vibration reduction system consists of four main components; sensors, actuators, a power supply unit, and a controller. Based on the current vibration levels measured by sensors, the controller calculates output action required to minimize the vibration. The output action is carried out by actuators, with the power supplied by an external power supply unit. Also, the controller can be configured to adjust itself for any possible change in operating conditions using an adaptive control scheme.

In principle, this active strategy can be very effective in reducing helicopter vibration for most operating conditions. However, many of the active vibration reduction techniques have never been applied to production helicopters because of several reasons. Safety is one of the main concerns because some methods utilize the primary control system of the aircraft (pitch links or swash plate) for vibration reduction purpose. Also, some active concepts require electrical or hydraulic slip rings, which are relatively bulky and are susceptible to failure, to transfer significant amount of power to actuators located on the rotor system. Additional drawbacks include requirement of high force actuators and considerable amount of power, a significant weight penalty, stability issues pertaining to the active control system, and the very high pitch link loads in some approaches. The most commonly examined active vibration reduction strategies include Higher Harmonic Control (HHC), Individual Blade Control (IBC), and Active Control of Structural Response (ACSR).

1.4.1 Higher Harmonic Control (HHC)

The HHC concept has been explored extensively in many helicopter vibration reduction studies. The main objective of this concept is to generate higher harmonic unsteady aerodynamic loads on the rotor blades that cancel the original loads responsible for the vibration. The unsteady aerodynamic loads are introduced by adding higher harmonic pitch input through actuation of the swash plate at higher harmonics [19], [20]. Conventionally, the swash plate is used to provide rotor blade collective and first harmonic cyclic pitch inputs (1/*rev*), which are controlled by the pilot to operate the aircraft. In addition to the pilot pitch inputs, the HHC system provides higher harmonic pitch inputs (for example; 3/*rev*, 4/*rev*, and 5/*rev* pitch inputs for a 4-bladed rotor) through hydraulic or electromagnetic actuators, attached to the swash plate in the non-rotating frame (see Fig. 1.9). The concept was examined extensively in many analytical studies (see Refs. [21]-[28]). With promising results obtained from some analytical studies, the HHC concept was then examined experimentally and its effectiveness demonstrated in both wind tunnel scale [29]-[33] as well as full scale helicopters [34]-[36]. Some of the key studies are described in greater detail below:

In Ref. [23], Nguyen used 3, 4, and 5/*rev* pitch inputs to successfully suppress vibratory hub shears for a 4-bladed hingeless rotor helicopter. In this analysis, the rotor blade was discretized using finite element method. The aerodynamic loads were calculated using a nonlinear unsteady aerodynamic model. A free wake model was considered for rotor inflow calculation. The vehicle orientations/controls and blade responses were solved iteratively in a coupled trim procedure. The vibration control scheme was based on minimization of a quadratic performance index in which hub loads were included. The controller was a fixed-gain frequency-domain controller whose gain was calculated based on a transfer matrix, which related HHC inputs to vibratory hub loads. The results showed that the HHC controller was effective in reducing the vibratory hub shears for most operating conditions. However, Nguyen observed that the required HHC actuator amplitudes and power increased significantly at high forward speeds (above 100 knots), and the blade torsional loads and control system loads were increased considerably.

A successful wind tunnel demonstration of the HHC system was conducted by Shaw et al. [30]. The experiment was conducted in the Boeing Helicopter Wind Tunnel using a 3-bladed dynamically scaled model rotor of the CH-47D helicopter. The rotor was instrumented to measure blade loads through blade-mounted strain gauges. 2, 3, and 4/*rev* pitch inputs were applied to reduce the 3/*rev* vertical, and 2, 4/*rev* in-plane root shears. Open-loop tests were performed at several flight conditions to obtain the transfer matrices required for calculating gains of a frequency-domain controller. Both fixed- and scheduled-gain controllers were considered. Again, the control scheme was based on minimization of a quadratic vibration index. Closed-loop test results showed that the HHC system produced more than 90% reduction in the 3 measured vibrations. The vibration reduction was demonstrated over a range of flight conditions, up to a forward speed of 188 knots. However, small-to-moderate increases in blade and control system fatigue loads were observed. The HHC input requirement for the reduction was relatively large, with 2 and 3 degree peak pitch input requirements for the forward speeds of 135 and 188 knots, respectively.

A full-scale flight demonstration of the HHC system was carried out on a modified Sikorsky S-76A helicopter [36]. All passive vibration reduction devices; for example the bifilars and fuselage absorbers, were removed for the flight tests. HHC inputs (3, 4, and 5/*rev*) were employed to reduce the 4/*rev*-fuselage vibration. Electro-hydraulic actuators were used to provide the HHC inputs. The vibration was measured using accelerometers located throughout the aircraft. Open-loop test results showed significant reduction in fuselage vibration, while moderate increases in blade and control system fatigue loads were observed. The vibration reduction at forward speed above 100 knots was limited because of actuator constraints.

Even though HHC is shown to be highly effective in reducing helicopter vibration, there are many associated drawbacks that have impeded the implementation of the HHC concept on production helicopters. First of all, the HHC system uses the primary control system (swashplate and pitch links) to transfer higher harmonic pitch inputs to the rotor blades. In the event of failure of the HHC system, the pilot may not have full control of the aircraft. Also the HHC system requires the use of hydraulic or electromagnetic actuators with sufficiently high force output and high bandwidth to provide desired swashplate motion. Thus, considerable power is required to operate the actuators. With the movement of the swash plate, causing the pitch link to push or pull the blade to a desired pitch angle, it is easy to see that the pitch links are subjected to large dynamic loadings that can be structurally detrimental.

1.4.2 Individual Blade Control (IBC)

IBC is another active strategy that has been widely explored for helicopter vibration reduction. The main idea of IBC is similar to that of HHC (generating unsteady aerodynamic loads to cancel the original vibration), but with a different implementation method. Instead of placing the actuators in the non-rotating frame (HHC concept), the IBC approach uses actuators located in the rotating frame to provide, for example, blade pitch, active flap, and blade twist inputs for vibration reduction

IBC concept using the blade pitch control can be implemented using electromagnetic or hydraulic actuators connecting blade pitch horn and swash plate, replacing conventional pitch links (Fig. 1.10a). Several studies on this approach were conducted at MIT, and are well summarized in Ref. [37]. Full-scale wind tunnel tests of this system were conducted at the NASA Ames Research Center [38]-[40]. Several flight tests of the IBC system for vibration reduction have been conducted successfully [41], [42]. Detailed reviews of some of the studies are presented below:

Full-scale wind tunnel demonstrations of the IBC system using blade pitch control were conducted by Jacklin et al. in the NASA Ames 40- by 80-Foot Wind Tunnel [38]-[40]. The rotor system was a 4-bladed BO-105 hingeless rotor. The rotor was instrumented to measure blade loads through strain gauges. The pitch links were replaced by servo-actuators to provide IBC pitch inputs. Results obtained for the open-loop tests showed that the hub vibration was sensitive to IBC inputs. However, the pitch link loads were always higher than those without IBC inputs, and increased with increasing IBC amplitude and frequency. Closed-loop test results demonstrated that reductions in the dominant 4/*rev* hub vibration could be obtained simultaneously using multi-harmonic IBC inputs.

Results of Full-scale flight tests of IBC system with blade pitch control for vibration reduction were reported by Kube and Van Der Wall [41]. The tests were conducted with a modified BO105 helicopter, using blade root pitch actuation system. The aircraft was instrumented extensively with pressure gauges, accelerometers, and strain gauges to determine blade pressure and displacement. The tests were carried out at various advance ratios. IBC pitch input was limited to 0.5° and 1° for the 2/*rev* and 3/*rev* components, respectively. The results illustrated that an appropriate 2/*rev* IBC input could produce 50% reduction in all fuselage vibrations, while the 3/*rev* IBC input could only produce 40% reduction in vertical vibration.

Despite the promising performance of the IBC concept using blade pitch control for vibration reduction, many practical concerns have to be addressed before this IBC system can be used in a production helicopter. First and foremost, the system must be again fail-safe, which implies minimal effect on primary aircraft control system in the event of system failure. Secondly this concept requires the use of electrical or hydraulic slip rings to transfer a significant amount of power to actuators in the rotating frame [43], and these have a high risk of failure if not properly maintained

Another IBC concept using flap actuation is explored extensively for vibration reduction. This concept uses a small flap on each blade to generate the desired unsteady aerodynamic loads for vibration reduction (see Fig. 1.10b). This concept can be equally effective, but uses less power than IBC system using blade pitch control [44],[45]. Also the location and size of the flaps can be chosen optimally to increase efficiency of the flap system [46]. Another attractive feature of the active flap is that the failure of the flap system does not compromise the aircraft primary flight control system [45]. In general, deflection of the flaps can be provided by many types of on-blade actuation using mechanical linkages [47], as well as modern smart materials actuators (for example, Piezoelectric actuators [48]- [56] and Magnetostrictive actuators [57]-[59]). The effectiveness of the Trailing Edge flaps for vibration reduction has been demonstrated both on a hover stand [60] and in a wind tunnel [61]-[63], and is in a development phase for a future flight demonstration [64]. A brief description of some key studies on the use of active flaps for vibration reduction is provided below:

Millott conducted a thorough analytical investigation of vibration reduction using Actively Controlled trailing edge Flaps (ACF) [44]. The analysis was conducted for a 4-bladed helicopter. Two blade models fitted with ACF were considered; *(i)* fully coupled flap-lag-torsion rigid blade model, and *(ii)* fully flexible elastic blade model using three flap modes, two lead-lag modes, and two torsional modes. The aerodynamic loads were calculated using a quasi-steady aerodynamic model incorporating reverse flow effect. The coupled trim and blade responses were solved using the Harmonic Balance method. Again, the control scheme was based on minimization of a quadratic vibration index, and the controller was a frequency-domain controller with gain calculated using a transfer matrix relating ACF inputs to vibratory hub loads. The results showed substantial reduction in vibration using the ACF controller, and the power requirement was between 4-16% of that required by a conventional IBC system. Some of the results suggested that location of the flap had a strong influence on vibration reduction effectiveness as well as power requirements. Also the flap size, span and chord length, showed minor impact on effectiveness of ACF, but had a strong effect on power and input amplitude requirements.

Another comprehensive vibration reduction study using trailing edge flaps was conducted by Milgram [46]. This investigation considered a 4-bladed Sikorsky S-76 main rotor. The analysis used a nonlinear aeroelastic rotor model, and unsteady compressible aerodynamic model. Blade response was calculated using finite element method, with coupled wind tunnel trim. Once again, a quadratic vibration index was minimized to yield the optimal flap control inputs, and a frequency-domain controller was considered. The controller gain was calculated using a transfer matrix relating multi-cyclic flap inputs to hub vibrations. The flap inputs consisted of components at 3, 4 and 5/*rev*. The results showed that either vibratory hub shears or hub moments could be reduced using the active flap concept. The vibration reduction effectiveness, which was dependent on flap parameters such as; flap length, flap location, and chord length, could be compensated by appropriately adjusting flap inputs, provided that the flap had sufficient deflection authority.

A wind tunnel demonstration of an active flap system was conducted by Dawson et al. [61]. An active flap model rotor, used by McDonnell Douglas Helicopter Systems, was tested in the NASA Langley 14- by 22-foot Subsonic Wind Tunnel open jet test section. The main objectives were to examine the reduction of BVI noise and vibration. The flap actuation mechanism was operated by a pretension cable attached between the hub and the active flap assembly. The blades were instrumented with strain gauges to measure blade loads. The active flap inputs included components at 3, 4, and 5/*rev*. Open-loop test results showed that the 5/*rev* flap input produced significant reduction in vibratory pitch moment.

Although the flap actuation approach offers an excellent potential for vibration reduction, many practical issues have to be addressed before the system can be used commercially. Power transfer to the rotating blade is still an unavoidable challenge for the flap system. Also the actuation mechanism has to be sufficiently powerful to provide the required authority, yet small enough to fit within blade the cavity, and strong enough to withstand immense centrifugal force.

Another IBC concept [65], similar to trailing edge flaps, is an actively controlled blade tip. By varying the pitch of the blade tip at higher harmonics, unsteady aerodynamic loads that cancel vibrations can again be generated. In Ref. [65], actuation of the blade tip was provided by a piezoelectric beam that utilized bending-torsion coupling effect to generate pure torsion deflection at the blade tip. A Froude-scaled blade model was fabricated and tested on a hover stand. The results demonstrated that the blade tip could undergo pitch rotations of 2° in the range of 2/*rev* to 5/*rev* (for 100 Volts actuation), and could provide corresponding vibratory blade shear (vertical) of 10-20% of the nominal lift. This vibratory blade shear could then be used for hub vibration reduction if the blade tip deflection was phased properly.

IBC concept using blade twist for vibration reduction has also been investigated recently. The idea is to actively introduce elastic blade twist to generate unsteady aerodynamic loads for vibration reduction. The entire blade can be twisted actively using smart materials embedded in the rotor blades (Fig. 1.10c). There are many studies on the active blade twist concept conducted jointly between NASA/ARMY/MIT [66]-[69]. An active-twist prototype blade was tested recently on a hover stand at the NASA Langley Research Center by Wilbur et al. [68]. The Active Twist Rotor (ATR) was an aeroelastically-scaled model rotor that was designed and fabricated to incorporate piezoelectric Active Fiber Composites (AFC) into the blade composite structure for providing active twist deformation. The hover tests showed good performance and endurance characteristics of the ATR prototype. An analysis conducted using CAMRAD II successfully predicted general trends of the ATR prototype. The active twist response of the ATR prototype was estimated, using CAMRAD II, to be 0.75°-1.5° (depending on frequency) when applying 1000-Volt sinusoidal input. The ATR blades have been tested recently at the NASA Langley Transonic Dynamics Tunnel [69]. It was demonstrated that active twist control could produce 60% to 95% reductions in fixed-frame vibration (using 1.1° to 1.4° active twist), depending on flight conditions. Similar efforts to elastically twist the blade were conducted at the University of Maryland [70]-[71] using embedded piezoceramic elements.

While the active twist rotor technology can produce significant reduction in vibration, as in the case of all IBC concepts it is impossible to avoid transfer of power to the rotor system through slip ring. Power requirements are expected to be higher than those for active pitch links or trailing edge flaps. An additional concern includes shielding of all electronic parts from moisture, to which the blades are exposed in normal operation.

1.4.3 Active Control of Structural Response (ACSR)

Unlike the HHC and IBC techniques that are intended to reduce the vibration in the rotor system, ACSR approach is designed to attenuate the N/*rev* vibration in the fuselage, and is one of the most successful helicopter vibration reduction methods at the present time. Vibration sensors are placed at key locations in the fuselage, where minimal vibration is desired (for example, pilot and passenger seats or avionic compartments). Depending on the vibration levels from the sensors, an ACSR controller will calculate proper actions for actuators to reduce the vibration. The calculated outputs will be fed to appropriate actuators, located throughout the airframe, to produce the desired active forces (see Fig. 1.11). Commonly used force actuators include electro-hydraulic, Piezoelectric, and inertial force actuators. Extensive studies on ACSR system have been conducted analytically [72]-[74] and experimentally [75]-[78]. Successful flight tests demonstrating the effectiveness of the ACSR concept have been conducted on a Westland 30 helicopter [79] and an UH-60 Black Hawk helicopter [80]. Recently, the ACSR technology has been incorporated in modern production helicopters such as the Westland EH101 [81] and the Sikorsky S-92 Helibus [82]. Some of the key studies on the ACSR approach for vibration reduction are described briefly below:

Chui and Friedmann conducted an analytical investigation of helicopter vibration reduction using the ACSR technique [74]. A coupled rotor/flexible fuselage model was developed to represent a helicopter with a 4-bladed hingeless rotor. An ACSR platform, equipped with 4 force actuators, was used to mount the rotor assembly into the fuselage. The elastic fuselage was represented by a three-dimensional finite element model. The rotor blades were assumed to be fully flexible, with coupled flap-lag-torsion dynamics. The aerodynamic loads were calculated using a quasi-steady aerodynamic model, with inclusion of the reverse flow effect. Blade response and vehicle trim solutions were obtained using Harmonic Balance method. The control scheme was based on a time-domain controller designed to reject disturbance. The vibration was modeled as a single frequency disturbance to be rejected by the controller. The incoming disturbance (vibration) was estimated, and the controller calculated an appropriate action to cancel it. The results showed substantial reduction in the fuselage vibration. In particular, fuselage accelerations were reduced to the vibration level below 0.05g. However, substantial amounts of control force were required to achieve the reduction.

An experimental investigation of ACSR system was conducted by Welsh et al. on a modified Sikorsky S-76B helicopter [77]. The ACSR system accommodated up to 10 accelerometers, monitoring airframe vibrations, and up to 4 servo force actuators. An adaptive controller was used to calculate the ACSR actuator force outputs that minimized a quadratic vibration index. A controller gain was calculated based on a transfer matrix (obtained off-line) relating ACSR outputs to the sensed vibrations. The results demonstrated that the ACSR system was effective in reducing airframe vibration, even with variations in the rotor RPM. Also, power consumption of the system was significantly lower than that of HHC systems.

A flight test of an ACSR system was carried out on a Sikorsky S-92 helicopter [82]. The system used 10 vibration sensors to measure vibrations throughout the fuselage, and several inertial force generating devices provided active forces to the airframe. The force generating devices were designed to operate using difference in centrifugal force of two counter-rotating wheels with eccentric masses. The controller was an adaptive optimal controller, whose gain was calculated based on a transfer matrix relating ACSR outputs to the sensed vibrations. The transfer matrix was estimated on-line using a modified Kalman filter. Flight test results showed that the ACSR system was effective in reducing fuselage vibration over ranges of forward speed up to 150 knots.

While the ACSR approach offers significant vibration reduction performance for modern helicopters, some concerns still exist. In order to reach satisfactory vibration reduction results, ACSR system has to exert large forces (at frequency of N/*rev*) on the fuselage. The combination of the large force with high frequency poses a threatening issue of local structural failure, near the actuation points. Thus, the actuation locations have to be designed specially to accommodate the large force without compromising structural integrity. Further, they also have to be chosen appropriately for maximum overall vibration reduction in the fuselage. This increases system weight penalty (due to weight of the sensors, actuators, control system, and structural re-enforcements). Also the ACSR system may require a large amount of power to operate its actuators. In addition, the vibration reductions obtained may be localized at the sensor locations, regardless of vibration levels elsewhere in the airframe, and the vibration levels in the rotor system are left unaltered.

1.5 Semi-active vibration reduction technology

Semi-active vibration reduction concepts are developed to combine the advantages of both purely active as well as purely passive concepts. Like purely active concepts, semi-active concepts have the ability to adapt to changing conditions, avoiding performance losses seen in passive systems in "off-design" conditions. In addition, like passive systems, semi-active systems are considered relatively reliable and fail-safe, and require only very small power (compared to active systems). Semi-active vibration reduction concepts have already been investigated in several engineering applications but only very recently has there been any focus on using them to reduce helicopter vibration. In the following sections, a brief description of the semi-active vibration reduction concept is first provided (Section 1.5.1), followed by comparison between semi-active and purely active systems (Section 1.5.2) and examples of semi-active vibration reduction in other engineering applications (Section 1.5.3). Finally, application of semi-active concepts to the helicopter vibration reduction problem is addressed (Section 1.5.4).

1.5.1 Overview of semi-active vibration reduction concept

Semi-active strategies achieve vibration reduction by modifying structural properties, stiffness or damping, of semi-active actuators. Examples of these semi-active actuators include controllable orifice dampers, controllable magneto-rheological (MR) or electro-rheological (ER) devices, and friction controllable bearings [83]-[84]. Power required to change properties of these devices is usually very small, since the property modification process incurs very little or no mechanical resistance. By modulating properties of such devices, "semi-active forces" can be generated across the semi-active actuators. These semi-active forces are generally proportional to a product between the change in structural properties and system responses; for example, ΔKx and $\Delta C\dot{x}$ for stiffness and damping variation respectively, and are sometimes called bilinear forces.

With a proper controller to calculate the semi-active inputs (ΔK or ΔC), the semi-active force can be exploited for vibration reduction. However, the semi-active control algorithms tend to be more complex, since the semi-active control system is now non-linear because of the controllable bilinear forces.

1.5.2 Comparison between active and semi-active concepts

Both active and semi-active vibration reduction systems are comprised of similar basic components; sensors, actuators, and a controller. The fundamental concept of active and semi-active approaches is virtually identical. The controller calculates required action for minimizing the vibration measured by sensors. The corresponding action is then carried out by actuators. Major differences between active and semi-active concepts are their actuators and associated controllers. Active actuators generally provide *direct* active force, while semi-active actuators generate *indirect* semi-active force through property modification. Correspondingly, the controllers for both active and semi-active systems have to be different, because of the differences in the required output actions. The semi-active controller is definitely more complex, since it has to cope with the bilinear semi-active forces.

There are several advantages for using the semi-active concepts over the active concepts. First of all, power requirement of the semi-active approaches is typically smaller than that of the active methods. This is because active actuators generate direct force to overcome the external loads acting on the system, while semi-active actuators only modify the structural properties of the system. Secondly, control system stability is almost guaranteed for the semi-active concepts, since virtually no external power is introduced into the semi-active control system. Lastly, there may be less concern for actuator saturation in semi-active systems than the active systems, when the vibration level increases. This is due to corresponding increases in system response and thus the bilinear semi-active forces, without increasing the semi-active inputs.

1.5.3 Semi-active vibration reduction applications

With the advantages of the semi-active concepts, there has been much interest in using the semi-active approach for vibration reduction in recent years, especially in automobile suspensions and earthquake protection applications. This section describes some of the studies on these subjects.

In the automobile industry, the semi-active suspension system has been developed for enhancing suspension performance to reduce effect of road vibration on the passengers [85]. The system usually employs controllable damper devices in the suspension system for generating semi-active force. Several analytical studies on this subject have been conducted with satisfactory results [86]-[92]. There are also numerous experimental studies on the semi-active suspension system [93]-[97]. In addition, many automobile companies such as Ford Motor Co. [98], Toyota Motor Co. [99], and Nissan Motor Co. [100] are interested in semi-active suspension systems.

One successful study of the semi-active suspension system was conducted by Yi, Wargelin, and Hedrick [88]. A quarter car semi-active suspension model was considered (see Fig. 1.12). The semi-active suspension was modeled as a controllable damper that can produce a bilinear semi-active force dependent on the product of the suspension velocity, $\dot{x}$, and control input, v. Using a transformation, $u = v\dot{x}$ (such that the semi-active force is now proportional to the new control variable, u), the system equations of motion were now linear. For this resulting linear system, the controller gain, G, was calculated by solving a conventional optimal control problem. Having found the controller gain, the temporary control variable, u, was computed by multiplying the gain and the system state vector ($u = G\cdot\underline{x}$). Then the actual semi-active control input was calculated as;

$$v = u/\dot{x} = G\cdot\underline{x} / \dot{x} \tag{1.1}$$

However, this optimal semi-active control action required very large control inputs when the suspension velocity was close to zero. For practical purposes, control input limitations were imposed by clipping at prescribed upper and lower limits. This control algorithm was often referred to as a clip-optimal controller. The controller was then extended to incorporate an observer, since all system states could not be measured. The numerical and experimental results suggested that the semi-active suspension system showed good performance in reducing dynamic tire force.

In earthquake protection applications, the semi-active system has been designed to reduce the effect of huge seismic energy induced by ground movement on a civil structure. Generally the system uses controllable orifice and MR devices for absorbing significant amount of energy that otherwise would have destroyed the structure. Another concept includes the use of special variable stiffness members, which can be engaged or disengaged depending on a control signal [101]. Since power failure is likely to occur during a seismic event, many of the earthquake protection systems are purposely designed to operate on battery power. Many studies on this subject have been conducted analytically [102]-[106] as well as experimentally [107]-[110].

One of the experimental investigations of semi-active seismic protection systems was conducted by Symans and Constantinou [109]. The experiment used semi-active controllable orifice fluid dampers to control seismic response of a three-storey scale-model building. Shaking table tests were performed to simulate seismic excitations. The structure model building was modified to add semi-active dampers in the lateral bracing located in the first storey (Fig. 1.13a). The semi-active fluid damper was a modified conventional monotube damper with accumulator (Fig. 1.13b). The piston head orifices were designed specially to yield force output that was proportional to the relative velocity of the piston head and the damper casing. An external control valve was added for adjusting the damping characteristic of the semi-active damper. This semi-active damper was tested experimentally to yield linear damping behavior with an adjustable damping coefficient. The highest damping was associated with a fully closed external valve position, while the lowest damping was related to a fully opened external valve position. The intermediate valve positions were tested to yield a calibration curve that linearly related the valve position (semi-active command input) to damping coefficient (Fig. 1.13c). Two controller algorithms were examined; *(i)* optimal control algorithm, and *(ii)* nonlinear sliding mode control algorithm. The optimal control approach followed the clipped-optimal approach described earlier in the study of semi-active suspension system by Yi et al [88]. The results obtained from this study showed that the semi-active damper control system improved structural response of the building dramatically. The reduction in response obtained using this semi-active system was similar to that achieved by a well-designed passive damping system. An improvement could be made if the semi-active control algorithm were designed to incorporate control action limitations at the outset, rather than clipping the optimal control inputs that did not consider actuator limitations.

Another experimental study on seismic protection using semi-active approach was conducted by Dyke et al. [110]. The experiment was set up to demonstrate the effectiveness of MR dampers for semi-active structural response control of a three-storey model building. In the experiment, a

MR damper was installed between the ground and first floor (see Fig. 1.14a and Fig. 1.14b). Many sensors were used to measure necessary variables for the system. Accelerometers were located on all floors to provide response measurements, a linear variable differential transformer (LVDT) was used to measure displacement of the MR damper, and a force transducer was employed to determine the control force applied to the structure. Again, the clipped-optimal control algorithm based on H_2/LQG strategy was considered to obtain desired output force from the MR damper. Using the force transducer, another subsystem would control the MR damper force to match the desired output force. To control the damper force, the subsystem used an electrical signal to increase or decrease the magnetic field applied to the damper so that the output damper force would increase or decrease, respectively (see also Fig. 1.14c). The results showed that the MR damper effectively reduced both the peak as well as the RMS response of the structure due to seismic excitations. In all cases, the semi-active system outperformed passive systems in reducing the structural response.

The above discussions clearly demonstrate the success of semi-active vibration reduction strategies in several practical applications. In addition, several semi-active controllers for vibration reduction were developed, but only for broadband applications. Detailed analyses of various semi-active actuators (including MR fluid devices and variable orifice dampers) were also conducted. These analyses are essential in applying the semi-active technology to helicopter application.

1.5.4 Helicopter vibration reduction using semi-active approach

There have been only a few studies focused on semi-active vibration reduction of helicopters. The approach can be implemented by using semi-active actuator to modifying structural properties of the rotor blade. Such an approach was first examined using variation in effective root torsion stiffness of the rotor blade to reduce the N/*rev* blade root vertical shear force [111]-[113].

First, Nitzsche introduced the concept of stiffness variation by analytically modifying blade root boundary condition from hinged (zero stiffness) to flexible (finite stiffness) to cantilever (infinite stiffness) in flap and torsion directions [111]. In this analysis, a BO-105 type dynamically scaled model rotor was considered and the rotor properties were experimentally obtained at the

German-Dutch Wind Tunnel (DNW). The rotor blade was assumed to undergo flap-bending and elastic torsion deformation, without any coupling between the flap and torsion modes. Blade aerodynamic loads were calculated using blade element theory, and the effect of compressibility and Blade Vortex Interaction was neglected. Based on a parametric study, the 1, 3, and 5/*rev* variations in blade torsion stiffness were effective in reducing the 4/*rev* blade torsion response.

In Ref. [112], Nitzsche analytically applied 3/*rev* variation in blade effective torsion stiffness to reduce the 4/*rev* blade flapwise bending and torsional responses of a 4-bladed rotor. The rotor was similar to that considered in Ref. [111]. A low speed descent flight condition was considered. The rotor pitch input was obtained from the wind tunnel tests. Elastic flap bending and torsion deformations of the blade were considered. Blade aerodynamic loads were calculated from two sources; *(i)* motion-dependent loads, and *(ii)* loads that were not motion dependent. The motion-dependent aerodynamic loads were calculated using quasi-steady blade element theory. The aerodynamic loads that were not dependent on blade motion, including BVI, dynamic stall, and compressibility effects, were calculated using rigid blade assumption. The steady state blade responses were obtained using numerical integration. The open loop results showed that the 3/*rev* torsion stiffness variation produced significant reduction in the 4/*rev* blade flap bending and torsional responses.

Subsequently, Nitzsche conducted another study to develop a frequency domain controller for vibration reduction using variations in flap and torsion stiffness [113]. The rotor model considered was similar to that in his previous study [112]. However, an improved aerodynamic model was considered. Blade aerodynamic loads were obtained again from motion and non-motion dependent contributions. The motion-dependent aerodynamic loads were calculated using a modified unsteady aerodynamic theory that accounted for reverse flow, compressibility, and finite span effects. The aerodynamic loads that were not dependent on blade motion, including BVI and dynamic stall effects, were calculated using a rigid blade assumption, as before. The steady state blade responses were computed using harmonic balance method. A frequency domain controller was set up for the disturbance (vibration) rejection problem. However, no detailed information about controller design or its effectiveness in reducing vibration was presented.

1.6 Focus of the present research

The focus of this dissertation is to develop, and evaluate the effectiveness of, semi-active approaches (through the use of controllable stiffness and controllable damping devices) in reducing helicopter vibration in moderate- to high-speed flight. To achieve this, several specific tasks are conducted;

The first task involves evaluating sensitivity of hub vibration to cyclic changes in stiffness of the blade root region. The rotor blades are spatially discretized using Finite Element Method. Stiffness variation input is introduced by analytically modifying the effective flap/lag/torsion stiffness of the entire root element of the blade. The influence of single harmonic stiffness variation (flap, lag, and torsion) on hub vibrations is examined extensively. The effect of phase and amplitude of the stiffness variation on hub vibration are also investigated. In addition, several issues are also considered; such as, identifying vibration reduction mechanism, changes in blade root loads, and changes in vibration reduction effectiveness with forward speed.

The second task focuses on the development and evaluation of a semi-active controller (open-loop) for helicopter vibration reduction using multi-cyclic stiffness or damping variations. The semi-active control scheme is formulated using optimal control theory in the frequency domain. Both gradient- and non-gradient-based optimizations are applied to determine optimal semi-active inputs that minimize all components of hub vibration simultaneously. The effectiveness of the semi-active controller is also evaluated when rotor fundamental properties and forward speeds are varied.

The third task takes a step toward practical implementation of this concept with introduction of discrete controllable stiffness as well as damping devices into the root region of the rotor blades. The controllable dampers are introduced because of several reasons – *(i)* extensive availability of the controllable dampers and *(ii)* large controllable damping authority. There is additional appeal for using controllable dampers since almost all helicopters already have passive lag dampers installed for aeromechanical stability augmentation, and replacing them with semi-active controllable dampers may be a relatively simple proposition. It should be noted that the introduction of these discrete devices in the blade root region creates multiple load paths for transfers of loads to the rotor hub. The effectiveness of multi-cyclic variation in stiffness and damping of these discrete semi-active devices on hub vibration reduction is determined. The corresponding changes in blade root loads, damper loads, and blade responses are also examined. The effectiveness of the discrete semi-active devices is also evaluated when rotor fundamental properties, device attachment geometry and sizing, and forward speeds are varied.

The final task in this present research involves the development and evaluation of another possible application using semi-active devices for helicopter vibration reduction by introducing the devices as isolators to reduce transmission of vibratory loads to the fuselage. A single degree of freedom system is used to represent the semi-active isolation system, which consists of a lumped mass (representing the rotor), under harmonic excitation, supported by a spring and a parallel damper on fixed support (representing the fuselage). Properties of the spring or damper can be varied to reduce transmission of the harmonic force into the support structure. The proper variation in the properties (stiffness or damping) is determined using; *(i)* open loop, *(ii)* closed-loop, and *(iii)* closed-loop adaptive control schemes. Effectiveness of the semi-active isolation system is examined even when there is change in the phase of excitation force.

1.7 Overview of dissertation

The remainder of this dissertation is organized into four parts. The first portion describes the analysis methods used to simulate helicopter vibration and development of an open-loop semi-active vibration controller. Chapter 2 outlines basic formulation of blade and helicopter equations in the presence of stiffness and damping variation devices, and procedure for solving the equations. The development of an optimal semi-active controller is provided in Chapter 3. The second part presents the vibration reduction results achieved using – *(i)* blade root stiffness variation, with preliminary study presented in Chapter 4 and optimal control study presented in Chapter 5, *(ii)* discrete controllable stiffness devices (Chapter 6-7), and *(ii)* discrete controllable dampers (Chapter 8). The third part presents development and results of semi-active isolation system (Chapter 9). In the final chapter, conclusions and recommendations for future work are discussed.

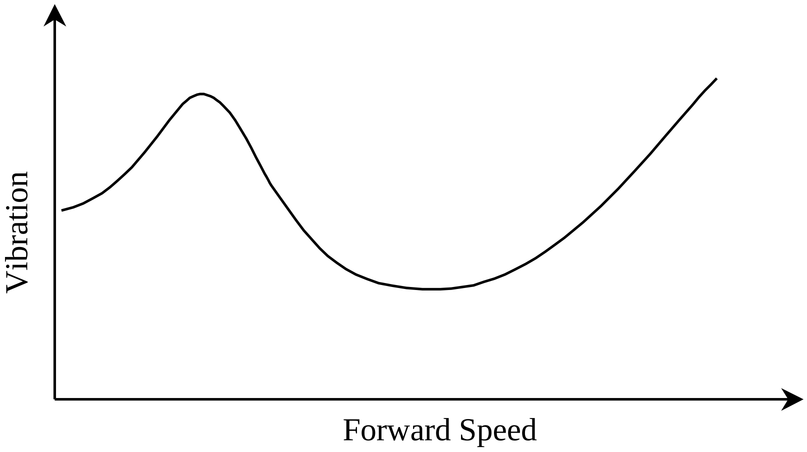

Figure 1.1: Helicopter vibration profile at various forward speeds

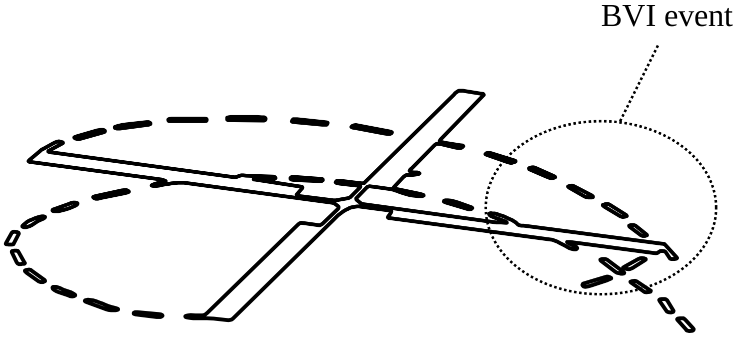

Figure 1.2: Blade Vortex Interaction (BVI) schematic

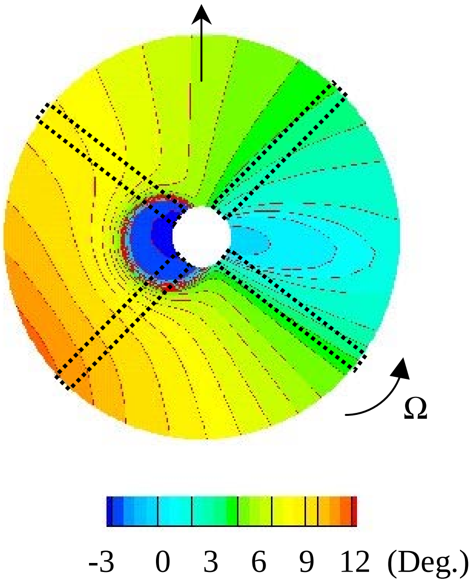

Figure 1.3: Angle of attack variation at a high-speed forward flight

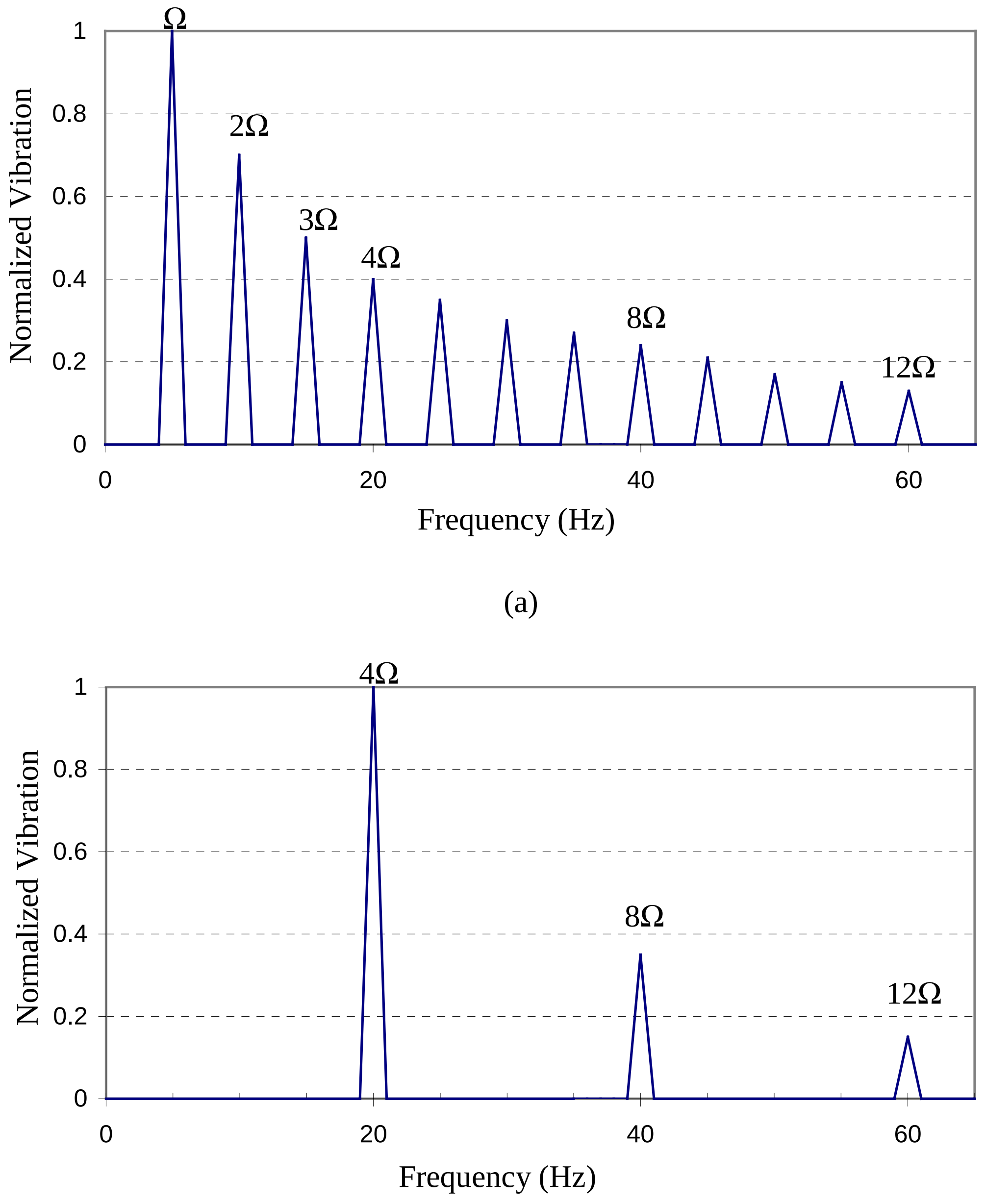

(a)

(b)

Figure 1.4: Frequency analysis of normalized vibration of a four-bladed helicopter in (a) the blade [rotating frame] and (b) the fuselage [non-rotating frame]

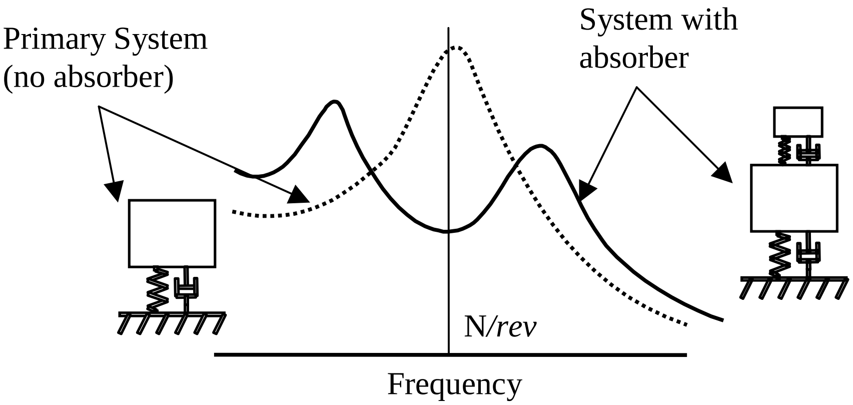

Figure 1.5: Frequency response of a dynamic system with and without an absorber

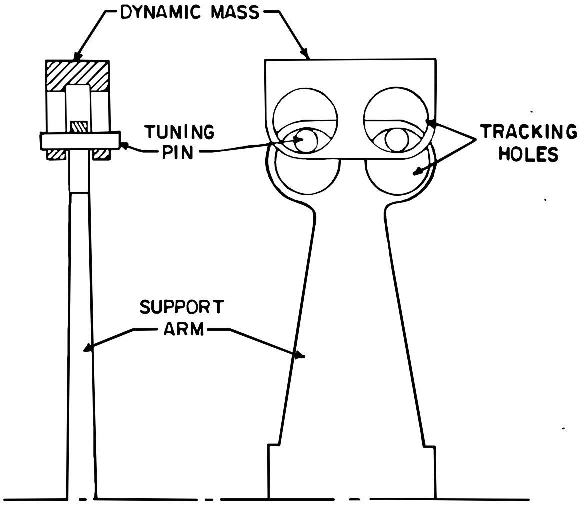
DYNAMIC MASS
TUNING
PIN
TRACKING
HOLES
SUPPORT
ARM

Figure 1.6: Hub mounted in-plane bifilar absorber (from Ref. [5])

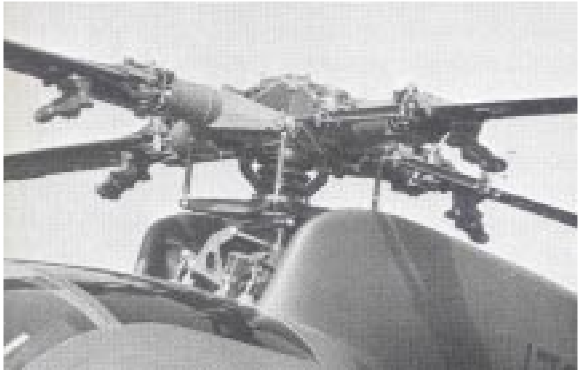

Figure 1.7: Blade mounted mass pendulum absorber (from Ref. [3])

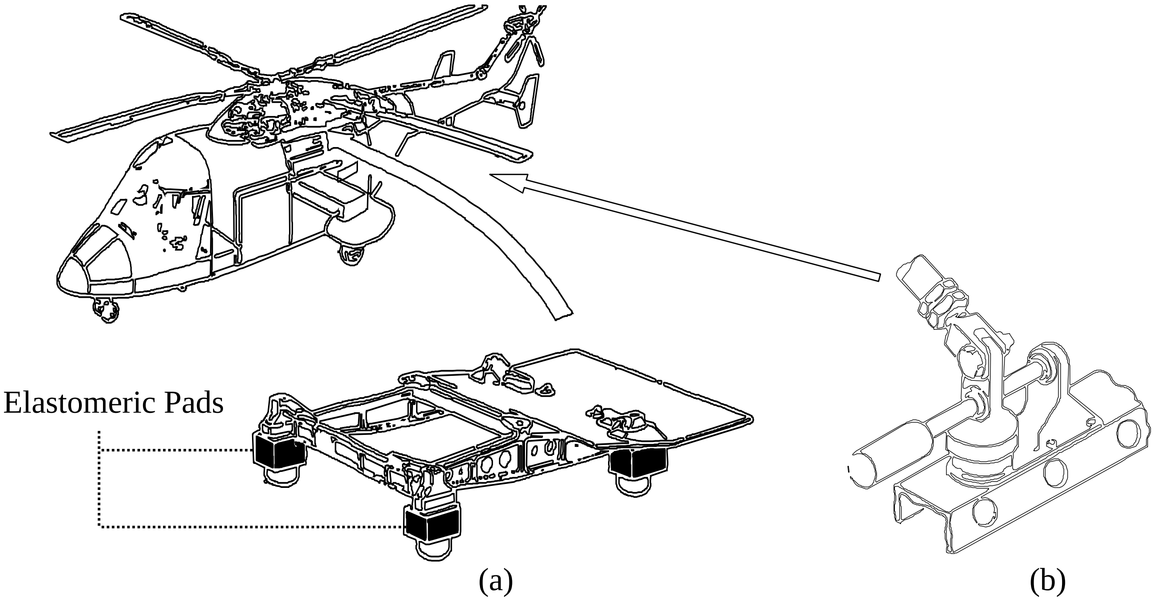
Elastomeric Pads
(a)
(b)

Figure 1.8: Helicopter vibration isolators; (a) Isolation platform with elastomeric pads and (b) Nodal beam (from Ref. [10])

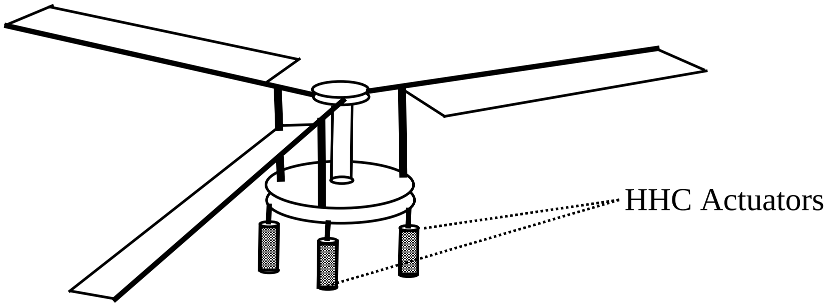
HHC Actuators

Figure 1.9: Schematic of a Higher Harmonic Control (HHC) system

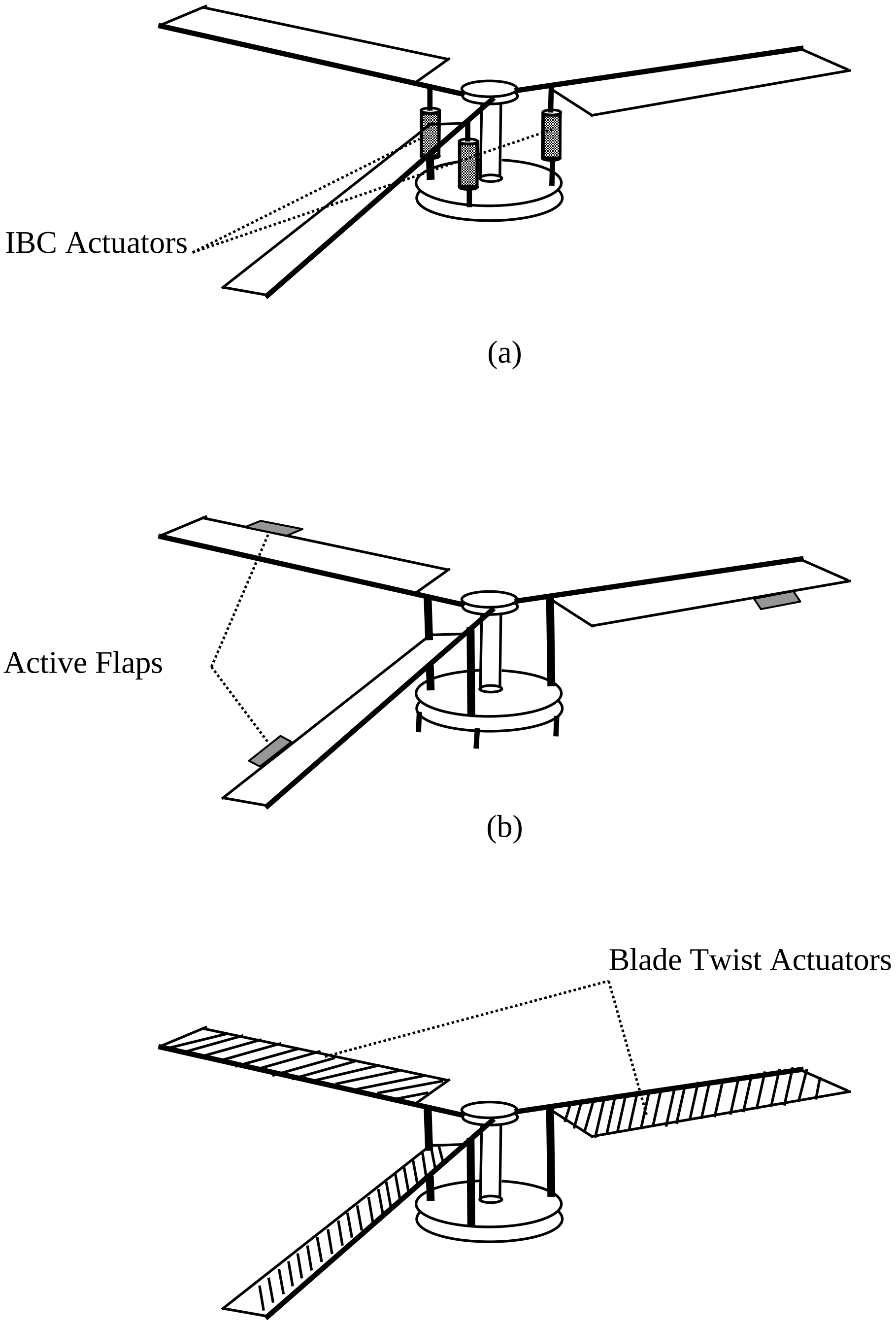
IBC Actuators
(a)
Active Flaps
(b)
Blade Twist Actuators
(c)

Figure 1.10: Schemetics of Individual Blade Control (IBC) systems using (a) blade pitch, (b) active flap, and (c) blade twist controls

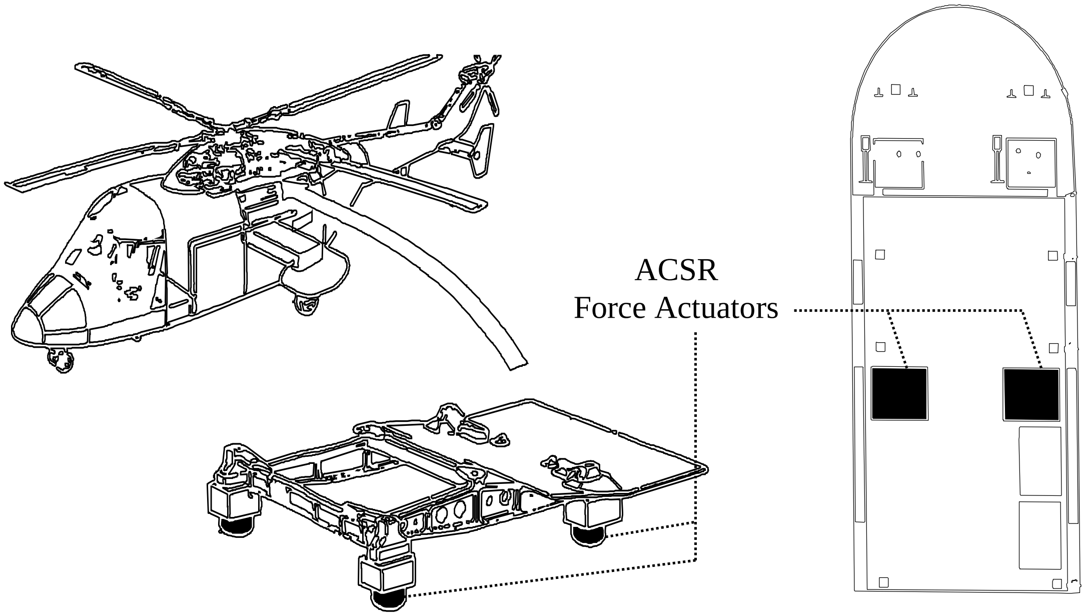
ACSR
Force Actuators

(a) (b)

Figure 1.11: Schematics of Active Control of Structural Response (ACSR) systems using force actuators located in (a) engine platform and (b) cabin (from Ref. [82])

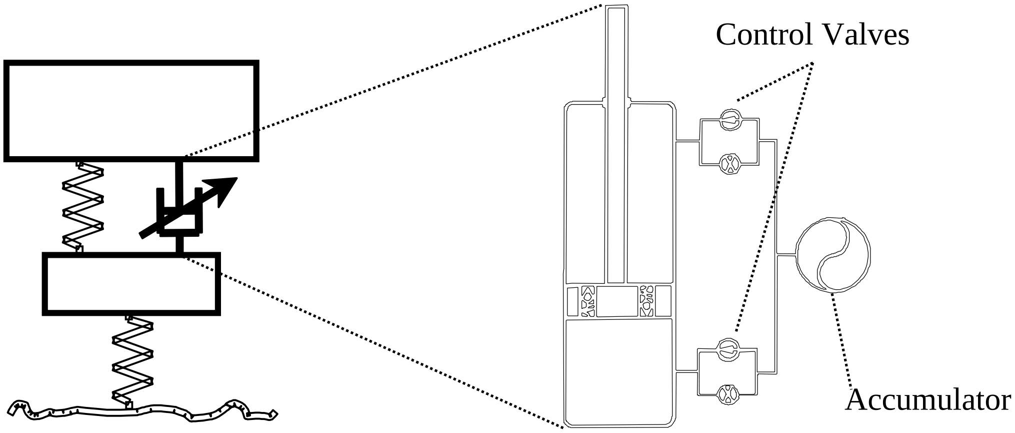
Control Valves
Accumulator

(a) (b)

Figure 1.12: Schematics of (a) a semi-active suspension model and (b) a semi-active controllable damper (from Ref. [88])

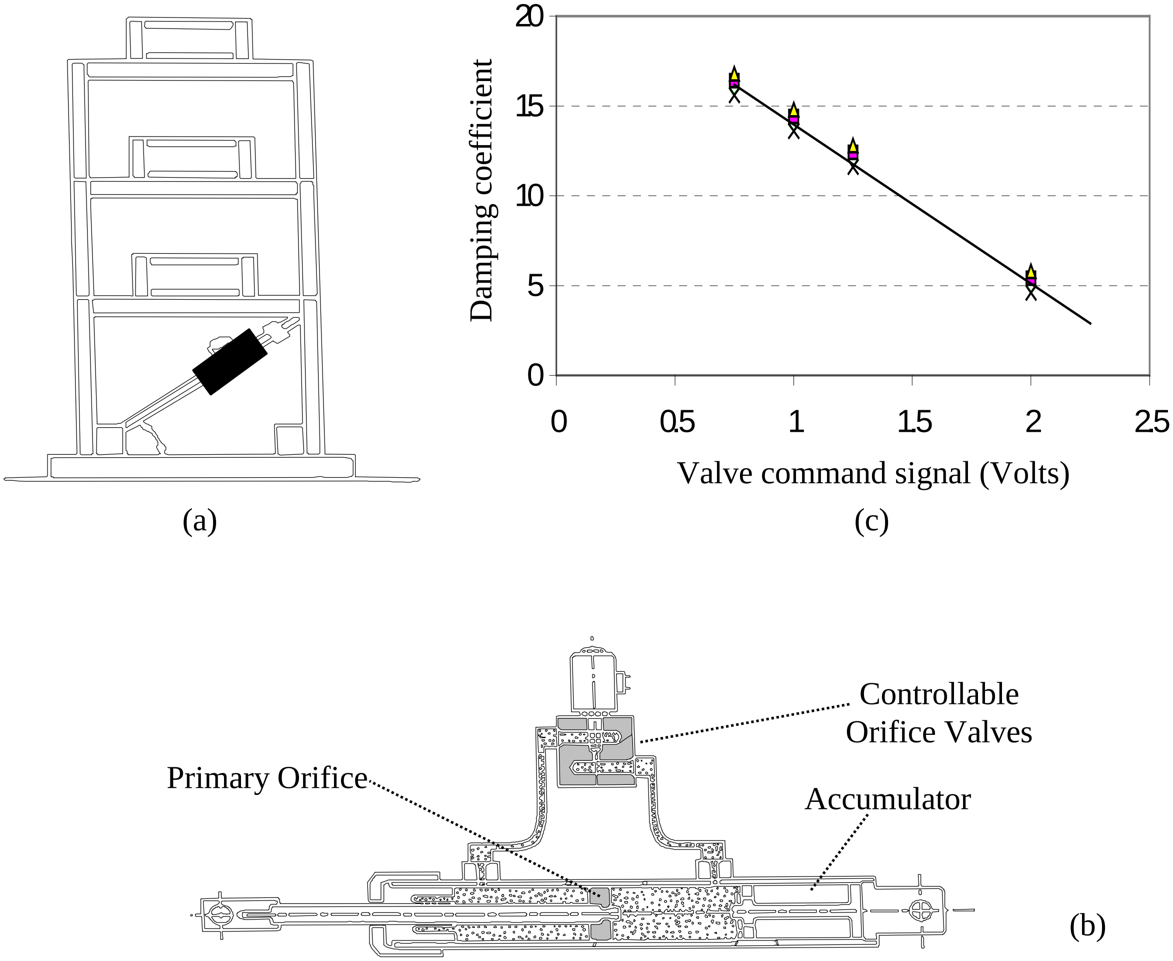
20
15
10
5
0
Damping coefficient
0
0.5
1
1.5
2
2.5
Valve command signal (Volts)
Controllable
Orifice Valves
Primary Orifice
Accumulator

(a)

(c)

(b)

Figure 1.13: Schematics of (a) a building model for sesmic testing and (b) a semi-active controllable orifice damper, and (c) calibration curve of the controllable damper (from Ref. [107])

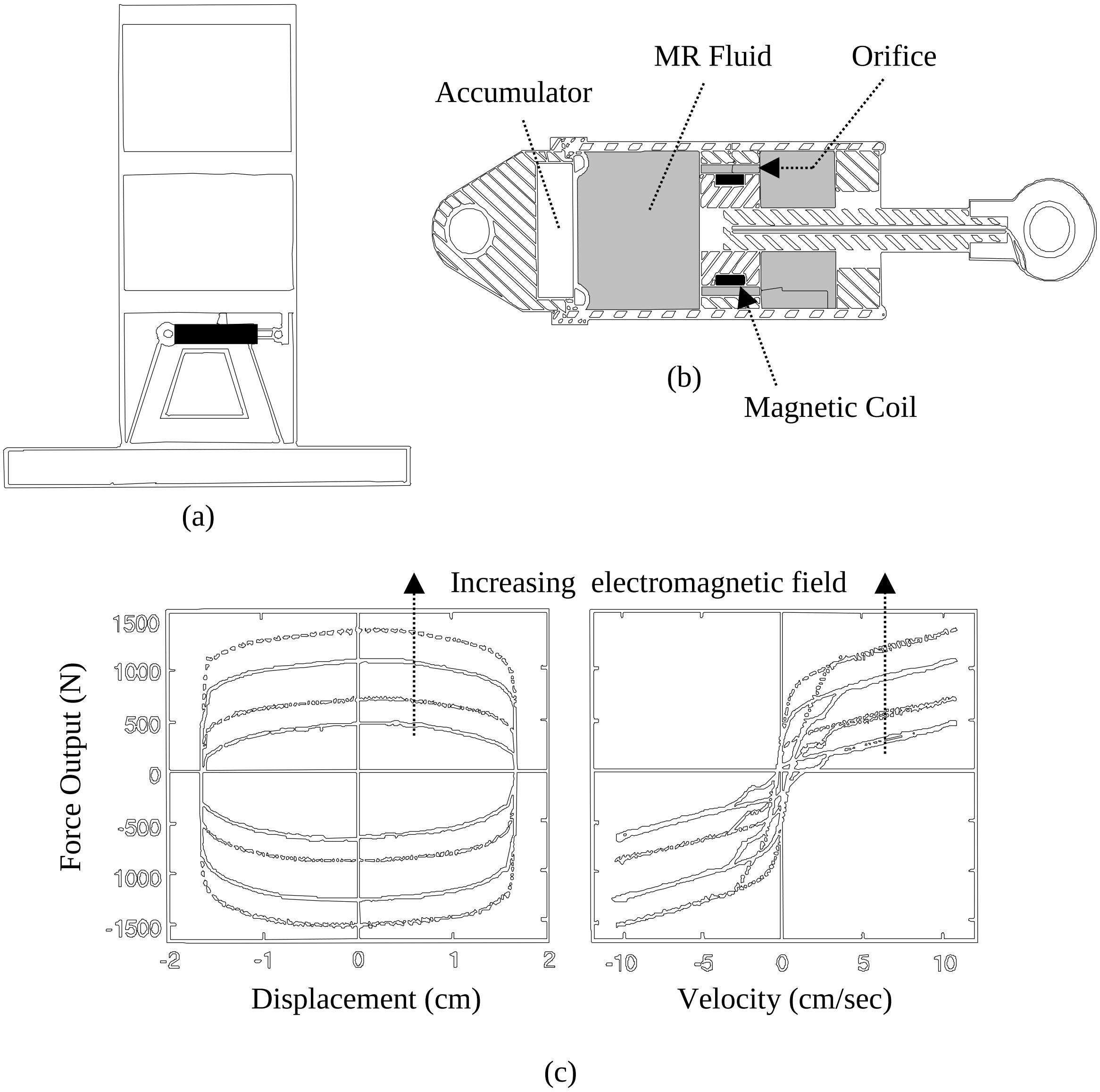

(a)
MR Fluid
Orifice
Accumulator
(b)
Magnetic Coil
Increasing electromagnetic field
Force Output (N)
1500
1000
500
0
-500
1000
-1500
-2
-1
0
1
2
Displacement (cm)
-10
-5
0
5
10
Velocity (cm/sec)
(c)

Figure 1.14: Schematics of (a) a building model for sesmic testing and (b) a semi-active MR damper, and (c) MR damper characteristic (from Ref. [110])

Chapter 2

Analysis

This chapter describes mathematical models used in this dissertation to represent a 4-bladed rotor helicopter with controllable stiffness and damping devices. Fundamental helicopter and rotor equations (without any controllable semi-active devices) and associated solution procedure are discussed in Section 2.1. Modifications of the basic rotor equations and blade root load calculation with the introduction of stiffness and damping variations are presented in Section 2.2 and Section 2.3, respectively. Section 2.4 explains the underlying influence of the semi-active stiffness and damping variation on blade response, blade root loads, and hub vibration.

2.1 Helicopter/Rotor modeling and response calculation

The analytical model used in this dissertation is based on the University of Maryland Advanced Rotorcraft Code (UMARC) formulation [114]. A four-bladed helicopter is simulated, with the blades assumed to undergo elastic flap, lag bending and elastic torsion deformations. The following sections explain briefly the basic formulation of helicopter and blade equations and the corresponding methods for solving the equations.

2.1.1 Helicopter model

In this dissertation, a four-bladed BO-105 type hingeless rotor helicopter model is used. The fuselage is modeled as a rigid body in a level flight with associated loads from the rotor system, horizontal tail, tail rotor, and the fuselage itself (see Figure 2.1). Hub loads from the rotor system are discussed in greater detail in Section 2.1.4. The other loads on the fuselage are presented in Appendix A for completeness. In a level flight, it can be deduced that all forces and moments exerted on the helicopter are in equilibrium. Helicopter equilibrium equations at the rotor hub are presented in Eq. 2.1.

$$\left\{\begin{matrix} F_x^H \\ F_y^H \\ F_z^H \\ M_x^H \\ M_y^H \\ M_z^H \end{matrix}\right\} = \begin{bmatrix} D_f + F_x \cos\alpha_s - F_z \sin\alpha_s \\ Y_f + F_y \cos\phi_s + F_z \sin\phi_s + T_{tr} \\ F_z \cos\phi_s \cos\alpha_s + F_x \sin\alpha_s - F_y \sin\phi_s - W - L_{ht} \\ M_x + M_{xf} + Y_f (h\cos\phi_s + y_{cg} \sin\phi_s) + W(h\sin\phi_s - y_{cg} \cos\phi_s) + T_{tr} (h - z_{tr}) \\ M_y + M_{yf} + W(h\sin\alpha_s - x_{cg} \cos\alpha_s) - D_f (h\cos\alpha_s + x_{cg} \sin\alpha_s) + L_{ht} x_{ht} \\ M_z + M_{zf} - D_f y_{cg} \cos\alpha_s + T_{tr} x_{tr} - Y_f x_{cg} \cos\phi_s \end{bmatrix} \tag{2.1}$$

This set of equations is then solved for equilibrium state (all forces and moments at the rotor hub are zero), with the solution procedure presented in Section 2.1.3.

2.1.2 Rotor blade model

All four blades are assumed to be identical with uniform properties along the blade length, and are assumed to undergo elastic flap-bending, lag-bending, and torsional deformations. Each blade is spatially discretized using Finite Element Method, and the blade equations are transformed into modal space using modal reduction method. A brief description of the derivation of the blade equations is given below:

The blade governing equations are derived using the Hamilton's principle in conjunction with Finite Element Method. The formulation starts with generalized Hamilton's principle (Eq. 2.2);

$$\delta\Pi = \int_{t_1}^{t_2} (\delta U - \delta T - \delta W) dt = 0 \tag{2.2}$$

where δU is the variation of strain energy, δT is the variation of kinetic energy, and δW is the virtual work done by external forces. A complete detail derivation of the strain energy, kinetic energy, and virtual work can be found in Ref. [114]. In this study, the blade elastic extension is neglected, since the blade extension stiffness is extremely high.

Using the Finite Element Method, the blade is discretized into a number of beam elements (see Fig. 2.2). Each beam element has eleven Degree of Freedoms (DoF's); 4 flap, 4 lag, and 3 torsional DoF's. These elements assure physical continuity of blade displacement and slope for flap and lag bending, and continuity of blade elastic twist. Within the element, bending moments and torsional moment are assumed to vary linearly. The displacement field within the element can be obtained through interpolations using FEM modeshapes and the nodal DoF's. Using this in Eq. 2.2, the variations in kinetic and strain energy of an ith element can be written in a matrix form as

$$\left(\delta U-\delta T\right)_i=\delta q_i^T\left(M\ddot{q}+C\dot{q}+Kq-F\right)_i \tag{2.3}$$

where M_i, C_i, K_i, and F_i are structural mass, damping, stiffness matrices, and load vector of the ith element, respectively, and $q_i^T=\left\{v_1,v_1',v_2,v_2',w_1,w_1',w_2,w_2',\hat{\phi}_1,\hat{\phi}_2,\hat{\phi}_3\right\}$ is the elemental DoF vector for the ith element. These elemental structural matrices and load vector are summarized in Appendix B.

To calculate the virtual work of the ith element, aerodynamic forces and moments on the blade element are determined using a quasi-steady aerodynamic model. In this model the airloads are functions of the instantaneous angle of attack of the blade section. The sectional angle of attack is determined based on the local blade pitch angle, the blade and wind velocities, which includes rotor inflow calculated using either a linear inflow model [115] or a Free Wake analysis [116]. A brief description of both inflow models is presented in Appendix C. The effect of fluid compressibility is accounted for by using the Prandl-Glauert factor. In reverse flow region, the aerodynamic center of the airfoil is shifted from the quarter chord to three-quarter chord. Using this method the variation in virtual work of the ith element can be written as

$$\left(-\delta W\right)_i=\delta q_i^T\left(-F^A\right)_i \tag{2.4}$$

where F^A is the aerodynamic load vector, and it is summarized in Appendix D.

After obtaining the elemental matrices and load vectors for every element on the blade, using the Gaussian numerical integration method, the global non-linear equations of motion are assembled as follows:

$$\delta\Pi=\int_{t_1}^{t_2}\delta q^T\left(M\ddot{q}+C\dot{q}+Kq-F-F^A\right)\,dt=0 \tag{2.5}$$

where $q=\sum_{i=1}^{N}q_i$, $M=\sum_{i=1}^{N}M_i$, $C=\sum_{i=1}^{N}C_i$, $K=\sum_{i=1}^{N}K_i$, $F=\sum_{i=1}^{N}F_i$, and $F^A=\sum_{i=1}^{N}F_i^A$. In the assembling process, compatibility of the global DoF, q, between adjacent elements must be insured, and the geometric constraints are enforced. The procedure is shown graphically in Fig. 2.3 for the global mass matrix.

In Eq. 2.5, since the virtual displacements, δq, are arbitrary, the integrand must be zero. This gives the blade governing equations of motion as follows:

$$\mathrm{M}\ddot{\mathrm{q}} + \mathrm{C}\dot{\mathrm{q}} + \mathrm{K}\mathrm{q} = \mathrm{F} + \mathrm{F}^{\mathrm{A}} \tag{2.6}$$

In general, this set of equations involves many DoFs (30 DoFs to represent a rotor with 5 beam elements). To reduce computational time, the blade equations are transformed into modal space using the eigenvectors of Eq. 2.7.

$$\mathrm{M}\ddot{\mathrm{q}} + \mathrm{K}\mathrm{q} = 0 \tag{2.7}$$

A number of fundamental flap, lag, and torsional modes (with the total number of 6 or 10 modes) are chosen to represent the rotor blade. Using the eigenvectors associated with the selected modes, Φ, the blade equations of motion in modal space can be written as

$$\overline{\mathrm{M}}\ddot{\mathrm{p}} + \overline{\mathrm{C}}\dot{\mathrm{p}} + \overline{\mathrm{K}}\mathrm{p} = \overline{\mathrm{F}} \tag{2.8}$$

where $q = \Phi p$, $\overline{\mathrm{M}} = \Phi^{\mathrm{T}}\mathrm{M}\Phi$, $\overline{\mathrm{C}} = \Phi^{\mathrm{T}}\mathrm{C}\Phi$, $\overline{\mathrm{K}} = \Phi^{\mathrm{T}}\mathrm{K}\Phi$, and $\overline{\mathrm{F}} = \Phi^{\mathrm{T}}(\mathrm{F} + \mathrm{F}^{\mathrm{A}})$.

2.1.3 Coupled rotor response/trim calculation

Rotor response and vehicle trim (vehicle orientation and controls) are obtained in an iterative process. First, with an initial guess value of vehicle trim, the rotor response is calculated. From this initial response, steady rotor forces and moments can be obtained (see Section 2.1.4 for detail). These rotor loads are used in vehicle equilibrium equations (Eq. 2.1) to determine whether the helicopter is in an equilibrium state or not. If not, the vehicle trim will be updated accordingly, and the rotor response will be calculated again with the updated trim. The whole process repeats until vehicle equilibrium is satisfied. The procedure for evaluation of the coupled trim–rotor response problem is summarized in a flowchart presented in Fig. 2.5.

Rotor blade response is calculated using Finite Element in time method based on the Hamilton's principle, and the detailed procedure of blade response calculation is summarized in Appendix E. Blade equations are transformed into first order form and discretized using Finite Element in time method (see Fig. 2.4). The blade response is solved using the Newton's method for solving non-linear equations.

Vehicle trim is obtained using again the Newton's method, which is outlined in detail in Appendix F. Rotor responses, hub loads, and equilibrium equations (Eq. 2.1) are first evaluated for an initial guess value of vehicle trim. If the vehicle is not in equilibrium state, the vehicle trim will be updated based on the residual of the equilibrium equations. The new responses and hub loads are again calculated using the updated trim. This process is repeated until a vehicle trim that satisfies the equilibrium equations is determined.

2.1.4 Blade root loads and hub loads calculation

Once the blade responses are known, the blade root loads can be determined using a force summation method. Then rotor hub loads are obtained by summing blade root loads from every blade in the rotor system.

Blade root shear forces and moments can be obtained by integrating blade aerodynamic and inertial loads along the length of the blade. Most of the blade aerodynamic and inertial loads are already calculated for the blade equations (Eq. 2.6). In fact, Eq. 2.6 may be used to calculate blade root loads with some adjustment, since it includes terms related to elastic strain energy, as well. After removing the elastic strain energy related terms, all remaining terms (which are related to only aerodynamic or inertial loads), are combined to yield the blade nodal load vector

$$S = M\ddot{q} + C\dot{q} + \overset{*}{K} q - \overset{*}{F} - F^{A} \tag{2.9}$$

where $\overset{*}{K}$ and $\overset{*}{F}$ are the modified stiffness matrix and structural load vector, respectively (with all elastic strain energy related terms removed). This nodal blade load vector contains integrated aerodynamic and inertial loads for all degree of freedoms ($w, w', v, v',$ and $\hat{\phi}$) at every finite element node. Examples of these nodal force and moment are shown in Figure 2.6 and Figure 2.7, respectively. The blade root loads can be calculated by summing contributions from the blade nodal forces and moments along the blade span as

$$
\begin{aligned}
S_x &= \sum_{k=1}^{\#\ of\ nodes} f_x^k \\
S_z &= \sum_{k=1}^{\#\ of\ nodes} f_z^k \\
M_\phi &= \sum_{k=1}^{\#\ of\ nodes} m_\phi^k \\
M_\beta &= \sum_{k=1}^{\#\ of\ nodes} m_\beta^k + \sum_{k=1}^{\#\ of\ nodes} f_z^k \left(\sum_{n=1}^{k-1} l^n\right) \\
M_\zeta &= \sum_{k=1}^{\#\ of\ nodes} m_\zeta^k + \sum_{k=1}^{\#\ of\ nodes} f_x^k \left(\sum_{n=1}^{k-1} l^n\right)
\end{aligned}
\tag{2.10a}
$$

The blade root radial shear, S_r, is calculated separately by integrating aerodynamic and inertial radial forces along the blade as

$$
S_r = \int_o^1 \{-m[\ddot{u} - 2\dot{v} - x + e_g(v' - \ddot{v}')\cos\theta_1 + e_g(w' - \ddot{w}' + 2\dot{\theta}_1)\sin\theta_1] + L_u\}dx \tag{2.10b}
$$

where the aerodynamic radial force, L_u, is defined in Eq. D.2a. All components of the blade root loads are shown graphically in Figure 2.8.

Once blade root loads are calculated, hub forces and moments can be obtained (using a proper transformation shown in Fig. 2.9) by summing the root loads from every blade as follows;

$$
\begin{aligned}
F_x &= \sum_{i=1}^{N} S_r^i \cos\psi^i + S_x^i \sin\psi^i \\
F_y &= \sum_{i=1}^{N} S_r^i \sin\psi^i - S_x^i \cos\psi^i \\
F_z &= \sum_{i=1}^{N} S_z^i \\
M_x &= \sum_{i=1}^{N} M_\phi^i \cos\psi^i + M_\beta^i \sin\psi^i \\
M_y &= \sum_{i=1}^{N} M_\phi^i \sin\psi^i - M_\beta^i \cos\psi^i \\
M_z &= -\sum_{i=1}^{N} M_\zeta^i
\end{aligned}
\tag{2.11}
$$

where N is the number of blades. Using Fourier transformation, these hub loads are then expressed as steady hub loads (which are required in vehicle trim calculation) and vibratory hub loads.

2.2 Rotor blade stiffness variations

In this dissertation, harmonic variations in effective flap/lag/torsion stiffness of rotor blade are introduced for hub vibration reduction. The variations in the effective stiffness are examined in two different ways; *(i)* varying the stiffness of the entire root element of the blade and *(ii)* varying stiffness of discrete controllable stiffness devices attached near the blade root.

2.2.1 Root element stiffness variations

The effective stiffness of the entire root element is assumed to vary cyclically (see Fig. 2.10), about their baseline values, as follows:

$$\begin{aligned} EI_{\beta}^{Root}(\psi) &= \overline{EI}_{\beta}^{Root} + \sum_{n=1}^{N}\left[\Delta EI_{\beta}^{np}\sin(n\psi + \phi_n)\right] \\ EI_{\zeta}^{Root}(\psi) &= \overline{EI}_{\zeta}^{Root} + \sum_{n=1}^{N}\left[\Delta EI_{\zeta}^{np}\sin(n\psi + \phi_n)\right] \\ GJ^{Root}(\psi) &= \overline{GJ}^{Root} + \sum_{n=1}^{N}\left[\Delta GJ^{np}\sin(n\psi + \phi_n)\right] \end{aligned} \tag{2.12}$$

In the above relations, "*n*" represents the frequency of the cyclic variations in stiffness (n = 1 implies 1*/rev* variations in stiffness, n = 2 implies 2*/rev* variations, etc); and ϕ_n, represents the phase angle of the cyclic variations in stiffness at *n/rev*. The amplitudes of the stiffness variations, ΔEI_{β}^{np}, ΔEI_{ζ}^{np}, and ΔGJ^{np}, are expressed in percentage of their baseline values ($\overline{EI}_{\beta}^{Root}$, $\overline{EI}_{\zeta}^{Root}$, and $\overline{GJ}^{Root}$, respectively).

These root stiffness variations are then incorporated into the blade equations (Eq. 2.6), which are solved for the corresponding blade responses. In the response calculation process, it is seen that the blade equations (Eq. 2.6) are evaluated at various azimuthal positions. At any azimuthal position, ψ, the stiffness of the root element of the blade is calculated using Eq. 2.12. With these stiffness variations, the elemental stiffness matrix (Eq. B.2) of the root element is modified as

$$[K(\psi)]_{Root} = [\overline{K}]_{Root} + [\Delta K(\psi)]_{Root} \tag{2.13}$$

where $[\overline{K}]_{Root}$ is the baseline elemental stiffness matrix of the root element and $[\Delta K(\psi)]_{Root}$ is the stiffness matrix of the root element associated with the stiffness variation. This modified root element stiffness matrix is assembled to yield modified blade equations, Eq. 2.14.

$$M\ddot{q} + C\dot{q} + \{\overline{K} + \Delta K(\psi)\}q = F + F^{A} \tag{2.14}$$

where $\Delta K(\psi)$ represents the component of the stiffness matrix with periodically varying terms due to the root element stiffness variation. The modified blade equations are then solved to yield the corresponding blade response using the procedure described in Appendix E.

Blade root loads and hub loads are calculated correspondingly from the modified blade response. The procedure outlined in Section 2.1.4 is directly applicable, since blade stiffness is not required in calculating blade root loads and hub loads.

2.2.2 Stiffness variations of discrete devices

In practice, variations in the effective stiffness of the blade root region can be achieved through discrete controllable stiffness devices introduced near the root region of the blade (see schematic sketch, Fig. 2.11). Examples of these discrete devices are controllable orifice devices and controllable frictional bearing. The stiffness of these devices is assumed to vary as follows:

$$\begin{aligned}
K_{w}(\psi) &= \overline{K}_{w} + \sum_{i=1}^{n}\left[\Delta K_{w}^{np}\sin(n\psi + \phi_{n}^{w})\right] \\
K_{v}(\psi) &= \overline{K}_{v} + \sum_{i=1}^{n}\left[\Delta K_{v}^{np}\sin(n\psi + \phi_{n}^{v})\right] \\
K_{\phi}(\psi) &= \overline{K}_{\phi} + \sum_{i=1}^{n}\left[\Delta K_{\phi}^{np}\sin(n\psi + \phi_{n}^{\phi})\right].
\end{aligned} \tag{2.15}$$

Again, "*n*" represents the frequency of the stiffness variations, and "ϕ_n" represents the phase angle of the stiffness variation at *n*/*rev*. The amplitudes of flap, lag, and torsion spring stiffness variations, ΔK_w, ΔK_v, and ΔK_ϕ are expressed as percentages of their baseline values ($\overline{K}_w$, $\overline{K}_v$, and $\overline{K}_\phi$ respectively). It can be deduced from Fig. 2.11 that the flap controllable stiffness device contributes significantly to both translational and rotational stiffness of the blade in the vertical direction (due to device attachment geometry). Similarly, both blade chordwise translational and rotational stiffnesses are affected by the lag device, while the controllable torsion stiffness device only influence the blade torsional stiffness. The discrete devices are mathematically modeled using translational and rotational springs. Two separate models are used: *(i)* dual spring model and *(ii)* single spring model.

2.2.2.1 Dual spring model

The controllable flap and lag stiffness devices can be modeled using a dual spring model to reflect the dependency of translational and rotational stiffness of the blade incurred by the configuration geometry of the devices. The flap device can be mathematically represented by two simultaneous controllable translational and rotational springs: K_w and $K_{w'}$, respectively (as shown in Fig. 2.12a), since the stiffnesses are derived from a single flap device. Similarly, the lag device can be modeled by simultaneous controllable springs K_v, and $K_{v'}$ (see Fig. 2.12b). The relationship between the translational and rotational springs is summarized as:

$$\begin{aligned} K_{w'}(\psi) &= \upsilon_w K_w(\psi) \\ K_{v'}(\psi) &= \upsilon_v K_v(\psi) \end{aligned} \tag{2.16}$$

where υ_w and υ_v are constants that depend on device configuration.

These simultaneous controllable springs are integrated into the blade equations (Eq. 2.6), and the corresponding blade response is calculated. The instantaneous stiffnesses of the controllable springs are calculated using Eq. 2.15 and Eq. 2.16. Using these instantaneously varying stiffnesses, the elemental stiffness matrix for flap and lag DoFs (Eq. B.2) of the root element is modified as follows:

$$\lfloor K_{ww}(\psi) \rfloor_{Root} = \lfloor K_{ww} \rfloor_{Root} + \lfloor K_{ww}(\psi) \rfloor_{Device} \tag{2.17}$$

$$\lfloor K_{vv}(\psi) \rfloor_{Root} = \lfloor K_{vv} \rfloor_{Root} + \lfloor K_{vv}(\psi) \rfloor_{Device}$$

where $\lfloor K_{ww} \rfloor_{Root}$ and $\lfloor K_{vv} \rfloor_{Root}$ are defined in Eq. B.2, and $\lfloor K_{ww}(\psi) \rfloor_{Device}$ and $\lfloor K_{vv}(\psi) \rfloor_{Device}$ are defined in Eq. 2.18.

$$\left[K_{ww}(\psi)\right]_{Device} = \begin{bmatrix} 0 & 0 & 0 & 0 \\ 0 & 0 & 0 & 0 \\ 0 & 0 & \overline{K}_w + \Delta K_w(\psi) & 0 \\ 0 & 0 & 0 & \upsilon_w \left\{\overline{K}_w + \Delta K_w(\psi)\right\} \end{bmatrix} \tag{2.18a}$$

$$\left[K_{vv}(\psi)\right]_{Device} = \begin{bmatrix} 0 & 0 & 0 & 0 \\ 0 & 0 & 0 & 0 \\ 0 & 0 & \overline{K}_v + \Delta K_v(\psi) & 0 \\ 0 & 0 & 0 & \upsilon_v \left\{\overline{K}_v + \Delta K_v(\psi)\right\} \end{bmatrix} \tag{2.18b}$$

These modified elemental stiffness matrices are assembled, and the modified blade equations again can be represented using Eq. 2.14, without loss of generality. Then these blade equations are solved to obtain blade response through the procedure outlined in Appendix E.

2.2.2.2 Single spring model

The flap, lag and torsion controllable stiffness devices can also be modeled as single controllable springs attached on the blade (see Fig. 2.13). For the flap and lag controllable stiffness devices, configuration and attachment geometry is shown in Fig. 2.14. While one end of the device is attached to the rotor hub the other end is attached to the rotor blade at a finite element node so that the motion of that point (required to determine the device forces) is directly available, and semi-active forces and moments exerted on the blade are easily accounted for. The semi-active force generated depends on both the instantaneous stiffness of the devices as well as the blade motion at the attachment point, which governs the relative displacement of the controllable springs. Figure 2.15a shows the deformation of the flap device due to flap bending motion of the blade. From the geometry and kinematics it can be shown that the flap spring deformation due to flap displacement, w, and slope, w', at the attachment point is given by:

$$\Delta L_w = -w \sin\alpha_w - e_w w' \cos\alpha_w \tag{2.19}$$

Similarly, if *v* and *v'* are the lag bending displacement and slope at the point the controllable lag spring is attached to the blade, the deformation of the lag spring can be shown to be:

$$\Delta L_v = -v \sin \alpha_v - e_v v' \cos \alpha_v \tag{2.20}$$

In Eqs. 2.19 and 2.20, α_w and α_v are the attachment angles of the flap and lag devices, and e_w and e_v are the attachment offsets (as seen in Figs. 2.14). The semi-active flap device force, F_w, and lag device force, F_v , are then expressed as:

$$\begin{aligned} F_w &= -K_w \Delta L_w \\ F_v &= -K_v \Delta L_v \end{aligned} \tag{2.21}$$

with K_w and K_v representing the instantaneous stiffness of the controllable flap and lag devices, respectively. The devices exert both forces and bending moments on the blade at the point of attachment, in the flap and lag directions (see Fig. 2.15b for the force and moment on the blade due to the flap device). The resulting loads at the blade finite element nodes (flap bending shear force, F_w^K, and moment, M_w^K, lag bending shear force, F_v^K, and moment, M_v^K) can be represented as:

$$\begin{Bmatrix} F_w^K \\ M_w^K \end{Bmatrix} = -K_w \begin{bmatrix} \sin^2 \alpha_w & e_w \sin \alpha_w \cos \alpha_w \\ e_w \sin \alpha_w \cos \alpha_w & (e_w \cos \alpha_w)^2 \end{bmatrix} \begin{Bmatrix} w \\ w' \end{Bmatrix} \tag{2.22a}$$

$$\begin{Bmatrix} F_v^K \\ M_v^K \end{Bmatrix} = -K_v \begin{bmatrix} \sin^2 \alpha_v & e_v \sin \alpha_v \cos \alpha_v \\ e_v \sin \alpha_v \cos \alpha_v & (e_v \cos \alpha_v)^2 \end{bmatrix} \begin{Bmatrix} v \\ v' \end{Bmatrix} \tag{2.22b}$$

Further, the torsion moment acting on the blade at the attachment point of the torsion stiffness device is expressed as:

$$M_\phi^K = -K_\phi \phi \tag{2.22c}$$

Since the blade loads in Eqs. 2.22 are dependent on the blade response at the attachment point (w, w', v, v', and ϕ), they will result in a modification of the blade elemental stiffness matrices of the root element as:

$$
\begin{aligned}
\lfloor K_{ww}(\psi)\rfloor_{Root} &= \lfloor K_{ww}\rfloor_{Root} + \lfloor K_{ww}(\psi)\rfloor_{Device} \\
\lfloor K_{vv}(\psi)\rfloor_{Root} &= \lfloor K_{vv}\rfloor_{Root} + \lfloor K_{vv}(\psi)\rfloor_{Device} \\
\lfloor K_{\phi\phi}(\psi)\rfloor_{Root} &= \lfloor K_{\phi\phi}\rfloor_{Root} + \lfloor K_{\phi\phi}(\psi)\rfloor_{Device}
\end{aligned}
\tag{2.23}
$$

where $\lfloor K_{ww}\rfloor_{Root}$, $\lfloor K_{vv}\rfloor_{Root}$, and $\lfloor K_{\phi\phi}\rfloor_{Root}$ are defined in Eq. B.2, and $\lfloor K_{ww}(\psi)\rfloor_{Device}$, $\lfloor K_{vv}(\psi)\rfloor_{Device}$, and $\lfloor K_{\phi\phi}(\psi)\rfloor_{Device}$ are defined in Eq. 2.24.

$$
\left[K_{ww}(\psi)\right]_{Device} = K_w(\psi)\begin{bmatrix} 0 & 0 & 0 & 0 \\ 0 & 0 & 0 & 0 \\ 0 & 0 & \sin^2\alpha_w & e_w \sin\alpha_w \cos\alpha_w \\ 0 & 0 & e_w \sin\alpha_w \cos\alpha_w & \left(e_w \cos\alpha_w\right)^2 \end{bmatrix} \tag{2.24a}
$$

$$
\left[K_{vv}(\psi)\right]_{Device} = K_v(\psi)\begin{bmatrix} 0 & 0 & 0 & 0 \\ 0 & 0 & 0 & 0 \\ 0 & 0 & \sin^2\alpha_v & e_v \sin\alpha_v \cos\alpha_v \\ 0 & 0 & e_v \sin\alpha_v \cos\alpha_v & \left(e_v \cos\alpha_v\right)^2 \end{bmatrix} \tag{2.24b}
$$

$$
\left[K_{\phi\phi}(\psi)\right]_{Device} = \begin{bmatrix} 0 & 0 & 0 \\ 0 & 0 & 0 \\ 0 & 0 & K_\phi(\psi) \end{bmatrix} \tag{2.24c}
$$

The instantaneous stiffness of the discrete devices ($K_w(\psi)$, $K_v(\psi)$, and $K_\phi(\psi)$) are defined earlier in Eq. 2.15. With these modified elemental stiffness matrices, the blade equations are obtained by assembling matrices from other beam elements. The modified blade equations can also be represented by Eq. 2.14, and can be solved to yield blade response via the method presented in Appendix E.

Comparing Eq. 2.24 to Eq. 2.18 suggests that the single spring model is representing the controllable stiffness devices more accurately than the dual spring model. The single spring model includes translation and rotational coupling effect (seen as off-diagonal terms in Eq. 2.24), while the dual spring model does not account for the coupling effect.

2.3 Rotor blade damping variations

Due to limited availability of controllable stiffness devices and extensive work with controllable dampers, it is natural to consider whether controllable dampers could be used in practice to achieve helicopter vibration reduction, through cyclic variations of their properties. In addition, all helicopters already employ passive lag dampers for aeromechanical stability augmentation, and replacing them with semi-active controllable dampers may be relatively simple. The controllable damper considered is a controllable orifice damper whose damping coefficient can be modified by simply opening or closing an orifice valve. The following sections explain damper modeling, incorporation of the controllable damper model, and blade root load calculation.

2.3.1 Controllable orifice damper model

This section presents the development and verification of a mathematical model representing a semi-active controllable orifice damper. A schematic sketch of the damper considered is shown in Fig. 2.16. It comprises of a standard linear viscous damper augmented with a bypass, which has a controllable valve. By varying the area of the controllable orifice through the application of a voltage, the damper force or the equivalent damping coefficient can be controlled. The change in damper characteristics with variation in orifice setting was experimentally demonstrated in Ref. [107], and a fluid dynamics based model for the damper behavior was also developed and validated in that study. The fluid dynamics based model involves computing the instantaneous pressures developed in each chamber of the damper due to fluid flow through the primary and bypass valves (see Fig. 2.16). The damper force can then be calculated from pressure difference between the two chambers as follows:

$$F_D = P_1 A_p - P_2 (A_p - A_r) + F_f \operatorname{sgn}(\dot{u}) \tag{2.25}$$

where A_p is the piston area, A_r is the rod area, F_f is the static frictional force between the piston and the damper casing, and $\dot{u}$ is the piston velocity. Although Eq. 2.25 looks simple, the fluid dynamics based model requires the solution of coupled differential equations governing the pressures developed in each chamber. These equations (from Ref. [107]) are provided in Appendix G for completeness. The controllable orifice area, A_{con}, as a function of applied voltage, V, was reported to vary in the following manner:

$$A_{con}(V) = A_{\max}\left[1 - \exp(-\gamma V^{\varsigma})\right] \tag{2.26}$$

where $A_{\max}$ is the maximum orifice area, and γ and ζ are parameters obtained through calibration of the valve. Varying the area of the controllable orifice changes the pressures developed in the chambers (see Eqs. G.1 and G.2), and consequently, changes the damper behavior. From Eq. 2.26 it is seen that for zero voltage the controllable orifice is completely shut (A_{con} = 0), and for increasing values of voltage the orifice starts to open.

Figure 2.17 shows the force versus displacement damper hysteresis curves for various values of orifice voltage (or orifice area). It is observed that the fluid dynamics model matches the experimental data very well. Maximum damping is available for zero voltage when the bypass valve is completely shut, and the available damping progressively reduces (hysteresis loop area decreases) as the bypass valve opens with the application of a voltage. It is also seen that for a specified orifice voltage, or orifice area, A_{con}, the hysteresis loop closely resembles that of a linear viscous damper. Thus, in principle, an equivalent viscous damping coefficient,

$$C = \frac{\mathit{Energy\ Dissipated}\ (\mathit{area\ under\ hysteresis\ cycle})}{\pi\, \Omega\, x_o^2} \tag{2.27}$$

can be assigned to each hysteresis cycle, corresponding to a specified applied voltage. Figure 2.18 shows that the damper hysteresis cycle obtained using the full fluid dynamics based model compares very well with that generated assuming a linear viscous damper with equivalent damping coefficient from Eq. 2.27. This process can be repeated for different orifice voltages, and a viscous damping coefficient determined for each case. A calibration curve of equivalent damping coefficient as a function of bypass orifice voltage (or orifice area) can then be obtained, as shown in Fig. 2.19. From the figure it is encouraging to note that – *(i)* the range of damping variation available is very large, providing up to almost ±80% change from the mean damping coefficient, and *(ii)* the calibration curve has a large linear range, which is beneficial from a controller design standpoint.

Based on Fig. 2.19, the damping coefficient in the present study is assumed to vary linearly as:

$$C(V) = \overline{C} + \frac{dC}{dV}(V - V_o) \qquad \text{or} \qquad C(V) = \overline{C} + \frac{dC}{dV}\Delta V = \overline{C} + \Delta C(V) \qquad (2.28)$$

which provides an accurate description of the damping behavior over a large range of variation in input voltage. In Eq. 2.28, $\overline{C}$ is the nominal damping, V_o is the nominal voltage, and ΔC is the variation in damping due to the voltage change ΔV. Such a reduced order controllable damper model (Eq. 2.28) avoids the complexity of the full fluid dynamic based model, and can be easily introduced in the rotor blade finite element equations.

However, before using the reduced order model in Eq. 2.28, additional verification is necessary. In developing the reduced order model based on the calibration curve in Fig. 2.19, hysteresis cycles for a series of different orifice settings were considered (Fig. 2.17); but the orifice area (voltage) was never varied *cyclically*. In the present study, cyclic variations in the orifice voltage are to be introduced at harmonics of the rotor frequency. It is necessary to verify that the reduced order model is valid (produces damper force predictions, or hysteresis cycles, very similar to those obtained using the full fluid dynamics based model) even when the orifice is controlled cyclically, at harmonics of the damper motion frequency.

Figures 2.20a and 2.20b, respectively, show the hysteresis cycles predicted when cyclic variation in the orifice voltage is introduced at the damper motion frequency and at twice the motion frequency. In both figures, the results from the reduced order model (Eq. 2.28) are practically identical to those from the full fluid dynamics model (Eqs. G.1, G.2 and 2.25), thus establishing the validity of the reduced order model, even for cyclically varying orifice voltages. It should be noted that a cyclic variation in orifice voltage, of amplitude ΔV about a mean voltage of V_o, produces a change in the shape of the hysteresis cycle but no change in the area enclosed (which remains the same as that when a constant voltage V_o is applied) – cycles in Figs. 2.18, 2.20a, and

2.20b all have the same enclosed area. This suggests that while cyclic variation in voltage will produce higher harmonic forces that could be exploited to reduce hub vibrations, it is unlikely to compromise the energy dissipation characteristics of the damper (which are determined only by the mean orifice voltage, V_o, or, in effect, the mean damping coefficient, $\overline{C}$). In addition, a change in the phase of the cyclic voltage input would result in the hysteresis curves shown in Figs. 2.20 undergoing a corresponding rotation, but again, the area enclosed is unchanged.

In the present study controllable orifice dampers are introduced in the rotor blade root region, and the voltage varied cyclically with time, or with azimuthal position, ψ (since the system is periodic). Thus the reduced order model in Eq. 2.28 can be represented in the following form

$$C(\psi) = \overline{C} + \Delta C(\psi) \tag{2.29}$$

where the variation in damping, ΔC, about the mean value, $\overline{C}$, is expressed in terms of the independent variable, ψ, rather than the dependent variable, $V(\psi)$.

2.3.2 Inclusion of controllable dampers into blade equations

Controllable dampers are introduced in the blade root region in the flap and lag directions (see schematic in Fig. 2.21) to produce semi-active forces that modify the blade response and reduce hub vibrations. Flap and lag controllable dampers are introduced because preliminary studies (presented later in Chapters 6 and 7) showed that semi-active stiffness variations particularly with the flap and lag devices are effective in reducing hub vibrations. Using the reduced order damper model (Eq. 2.29), cyclic variations in the flap and lag damping coefficients are represented, without loss of generality, in the following form:

$$\begin{aligned} C_w(\psi) &= \overline{C}_w + \Delta C_w(\psi) = \overline{C}_w + \sum_{n=1}^{N}\left[\Delta C_w^n \sin(n\psi + \phi_n^w)\right] \\ C_v(\psi) &= \overline{C}_v + \Delta C_v(\psi) = \overline{C}_v + \sum_{n=1}^{N}\left[\Delta C_v^n \sin(n\psi + \phi_n^v)\right] \end{aligned} \tag{2.30}$$

Again, "n" represents the frequency of the cyclic damping variations and "ϕ_n" represents the phase angle corresponding to damping variation at *n*/*rev*. The amplitudes of flap and lag damping variations, ΔC_w and ΔC_v are expressed as percentages of their baseline values ($\overline{C}_w$ and $\overline{C}_v$, respectively). It should be noted that from a practical standpoint there is a limit to the maximum variations in damping coefficient achievable with the controllable orifice dampers, and this was taken to be $\pm 80\%$ of the baseline damping coefficients ($\overline{C}_w$, or $\overline{C}_v$), based on Fig. 2.19. Equations 2.30 can be written in a compact form as:

$$C_D(\psi) = \overline{C}_D + \Delta C_D(\psi) = \overline{C}_D + \sum_{n=1}^{N} \left[\Delta C_D^n \sin(n\psi + \phi_n)\right] \tag{2.31}$$

The damper configuration and attachment geometries are similar to that shown in Fig. 2.14, except that the controllable stiffness devices are replaced with controllable dampers. Again, the flap and lag dampers are attached to the rotor blade at a finite element node so that the semi-active forces and moments exerted on the blade are easily accounted for, since blade velocity at the node is readily available. The semi-active damper force generated depends on the instantaneous damping coefficient of the controllable dampers as well as the blade flap and lag velocities at the attachment point, which determines the piston velocities of the controllable dampers. Figure 2.22a shows the change in the flap damper length due to flap bending deformations of the blade. From the geometry and kinematics it can be shown that the flap damper deformation due to flap displacement, *w*, and slope, *w'*, at the attachment point is given by Eq. 2.19, and the piston velocity of the flap damper can be written as:

$$\Delta\dot{L}_w = -\dot{w}\sin\alpha_w - e_w\dot{w}'\cos\alpha_w \tag{2.32a}$$

Similarly, if *v* and *v'* are the lag bending displacement and slope at the point of attachment of the lag damper to the blade, the piston velocity of the lag damper can be shown to be:

$$\Delta\dot{L}_v = -\dot{v}\sin\alpha_v - e_v\dot{v}'\cos\alpha_v \tag{2.32b}$$

Again, α_w and α_v are the attachment angles of the flap and lag dampers, and e_w and e_v are the attachment offsets (as seen in Figs. 2.14). The semi-active flap damper force, F_w, and lag damper force, F_v, are then expressed as:

$$\begin{aligned} F_w &= -C_w \Delta \dot{L}_w \\ F_v &= -C_v \Delta \dot{L}_v \end{aligned} \tag{2.33}$$

with C_w and C_v representing the instantaneous damping coefficients of the controllable flap and lag dampers, respectively. The dampers exert forces and bending moments on the blade at the point of attachment in both the flap and lag directions (see Fig. 2.22b for the force and moment due to the flap damper). The resulting loads at the blade finite element nodes (flap bending shear, F_w^D, and moment, M_w^D, and lag bending shear, F_v^D, and moment, M_v^D) can be expressed as:

$$\begin{Bmatrix} F_w^D \\ M_w^D \end{Bmatrix} = -C_w \begin{bmatrix} \sin^2 \alpha_w & e_w \sin \alpha_w \cos \alpha_w \\ e_w \sin \alpha_w \cos \alpha_w & (e_w \cos \alpha_w)^2 \end{bmatrix} \begin{Bmatrix} \dot{w} \\ \dot{w}' \end{Bmatrix} \tag{2.34}$$

$$\begin{Bmatrix} F_v^D \\ M_v^D \end{Bmatrix} = -C_v \begin{bmatrix} \sin^2 \alpha_v & e_v \sin \alpha_v \cos \alpha_v \\ e_v \sin \alpha_v \cos \alpha_v & (e_v \cos \alpha_v)^2 \end{bmatrix} \begin{Bmatrix} \dot{v} \\ \dot{v}' \end{Bmatrix}$$

Since the blade loads contain velocity-dependent terms, they will result in a modification of the blade elemental damping matrices of the root element as follows.

$$\begin{aligned} \lfloor C_{ww}(\psi) \rfloor_{Root} &= \lfloor C_{ww} \rfloor_{Root} + \lfloor C_{ww}(\psi) \rfloor_{Damper} \\ \lfloor C_{vv}(\psi) \rfloor_{Root} &= \lfloor C_{vv} \rfloor_{Root} + \lfloor C_{vv}(\psi) \rfloor_{Damper} \end{aligned} \tag{2.35}$$

where $\lfloor C_{ww} \rfloor_{Root}$ and $\lfloor C_{vv} \rfloor_{Root}$ are defined in Eq. B.3, and $\lfloor C_{ww}(\psi) \rfloor_{Damper}$ and $\lfloor C_{vv}(\psi) \rfloor_{Damper}$ are defined in Eq. 2.36.

$$\left[C_{ww}(\psi) \right]_{Damper} = C_w(\psi) \begin{bmatrix} 0 & 0 & 0 & 0 \\ 0 & 0 & 0 & 0 \\ 0 & 0 & \sin^2 \alpha_w & e_w \sin \alpha_w \cos \alpha_w \\ 0 & 0 & e_w \sin \alpha_w \cos \alpha_w & (e_w \cos \alpha_w)^2 \end{bmatrix} \tag{2.36a}$$

$$\left[C_{vv}(\psi) \right]_{Damper} = C_v(\psi) \begin{bmatrix} 0 & 0 & 0 & 0 \\ 0 & 0 & 0 & 0 \\ 0 & 0 & \sin^2 \alpha_v & e_v \sin \alpha_v \cos \alpha_v \\ 0 & 0 & e_v \sin \alpha_v \cos \alpha_v & (e_v \cos \alpha_v)^2 \end{bmatrix} \tag{2.36b}$$

The instantaneous damping coefficient of the flap and lag dampers, $C_w(\psi)$ and $C_v(\psi)$, are given in Eq. 2.30. Then the modified blade equations are obtained by assembling all the other matrices with the modified elemental damping matrix. The modified blade equations can be represented by Eq. 2.37.

$$M\ddot{q} + \left\{\overline{C} + \Delta C(\psi)\right\}\dot{q} + Kq = F + F^A \tag{2.37}$$

where $\Delta C(\psi)$ represents the component of the damping matrix with periodically varying terms due to the controllable orifice dampers. The blade responses are obtained by solving these blade equations using the method described in Appendix E.

2.3.3 Blade root loads and hub loads calculation

It should be noted that introduction of the controllable flap and lag dampers, as shown in Figs. 2.21, creates multiple paths for transfer of loads to the rotor hub. Blade root loads calculation outlined in Section 2.1.4 can still be used, but the semi-active forces generated by the controllable dampers have to be considered. The shear forces and moments at the root of the flexbeam are denoted with the superscript "flex". In addition, the superscript "damper" is used to denote the shear forces and moments appearing at the root of the damper. See Figures 2.23a and 2.23b, respectively, for the root vertical shear and the drag shear forces due to the flexbeam and the damper. The "total" blade root shear forces (S_z and S_x in Figs. 2.23a and 2.23b), then, are summations of the flexbeam and damper contributions ($S_z = S_z^{flex} + S_z^{damper}$ and $S_x = S_x^{flex} + S_x^{damper}$). It is these "total" shear forces that are considered when calculating the vibratory hub forces. Thus, the vertical shear force, S_z^{flex}, and the drag shear force, S_x^{flex}, at the root of the flexbeam can be expressed as,

$$\begin{aligned} S_z^{flex} &= \sum_{k=1}^{\#\,of\ nodes} f_z^{\,k} - F_w \sin\alpha_w \\ S_x^{flex} &= \sum_{k=1}^{\#\,of\ nodes} f_x^{\,k} - F_v \sin\alpha_v \end{aligned} \tag{2.38}$$

The vertical shear force, S_z^{damper}, and the drag shear force, S_x^{damper}, at the root of the flap and lag dampers are simply

$$
\begin{aligned}
S_z^{damper} &= F_w \sin\alpha_w \\
S_x^{damper} &= F_v \sin\alpha_v
\end{aligned}
\tag{2.39}
$$

Thus, from Eqs. 2.38 and 2.39, the total blade root shear forces (S_z and S_x) are obtained as,

$$
\begin{aligned}
S_z &= S_z^{flex} + S_z^{damper} = \sum_{k=1}^{\#\,of\ nodes} f_z^{\,k} \\
S_x &= S_x^{flex} + S_x^{damper} = \sum_{k=1}^{\#\,of\ nodes} f_x^{\,k}
\end{aligned}
\tag{2.40}
$$

It is interesting to note that the total blade root shears (S_z and S_x) used in the calculation of the hub forces have only aerodynamic and inertial contributions (contained in the $f_z^{\,k}$'s and $f_x^{\,k}$'s), and the damper loads cancel out (see Eq. 2.40). These equations for blade root shears are the same as the equations presented in Eq. 2.10a. In a similar manner it could be shown that any direct damper contributions to the root radial shear force, and the blade root moments, cancel out as well. The damper, however, has modified the blade response, and the inertial and aerodynamic loads (which are dependent on the blade response). Further, the loads at the flexbeam root are modified due to the presence of the controllable damper (see Eq. 2.38). After blade root loads are obtained, hub loads can be calculated using the method in Section 2.1.4.

2.4 Influence of semi-active stiffness and damping variation

From previous sections, it is seen that the blade equations are modified when semi-active stiffness or damping variations are introduced as presented in Eq. 2.14 and 2.37, respectively.

$$M\ddot{q} + C\dot{q} + \overline{K}q = F + F^A - \Delta K(\psi)q \tag{2.14a}$$

$$M\ddot{q} + \overline{C}\dot{q} + Kq = F + F^A - \Delta C(\psi)\dot{q} \tag{2.37a}$$

where $\Delta K(\psi)$ represents the stiffness variations and $\Delta C(\psi)$ represents the damping variations. Clearly, the $\Delta K(\psi)q$ (due to cyclic stiffness variations) and $\Delta C(\psi)\dot{q}$ (due to cyclic damping variations) terms can be regarded as unsteady semi-active loads that can be used to modify the blade response as desired. Traditionally for a 4-bladed rotor helicopter, HHC or IBC uses higher harmonic pitch input at 3/*rev*, 4/*rev*, and 5/*rev* to produce higher harmonic unsteady aerodynamic forces of those frequencies, and change blade response and reduce vibration. With the present semi-active approach, even lower harmonic variations in stiffness, $\Delta K(\psi)$, or damping, $\Delta C(\psi)$, at 2/*rev* and 3/*rev*, are able to generate the desired higher harmonic semi-active loads, $\Delta K(\psi)q$ or $\Delta C(\psi)\dot{q}$, at 3/*rev*, 4/*rev*, and 5/*rev*, for vibration reduction, since the blade response and velocity, q and $\dot{q}$, themselves already contain harmonics of rotor frequency (1/*rev*, 2/*rev*, 3/*rev*, etc.). This will be demonstrated in the result sections that 2/*rev* and 3/*rev* stiffness or damping variations are particularly effective in reducing 4/*rev* hub vibrations.

Calculation of blade root loads and hub loads are unchanged with the introduction of stiffness and damping variations, since all direct contributions of the semi-active loads (from the stiffness and damping variations) to blade root loads are canceled out. In other words, influence of the stiffness and damping variations has to be taken into account in the calculation of the blade response, but its effect on the blade root loads is only to the extent that the changed response of the blade affects the aerodynamic and inertial loading. This suggests that the stiffness and damping variations generate semi-active loads that change blade response, and indirectly influence the blade root loads, which in turn can be used to reduce the hub vibrations.

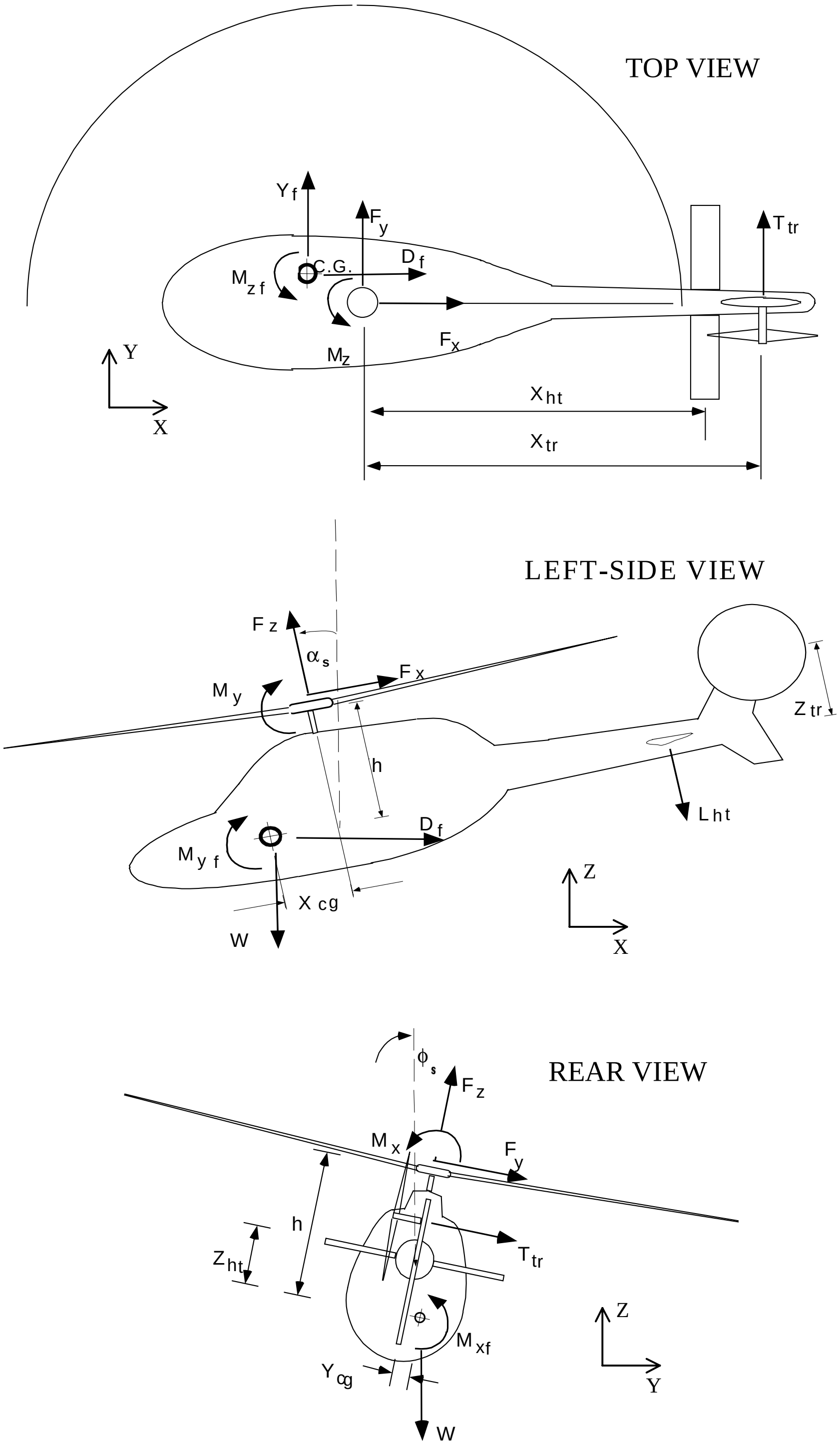
TOP VIEW
Y f
F y
T tr
D f
C.G.
M z f
M z
F x
Y
X
X ht
X tr
LEFT-SIDE VIEW
F z
α s
F x
M y
Z tr
h
D f
L ht
M y f
X cg
W
Z
X
REAR VIEW
φ s
F z
M x
F y
h
Z ht
T tr
Z
Y
M xf
Y cg
W

Figure 2.1: Forces and moments exert on a helicopter in a level forward flight

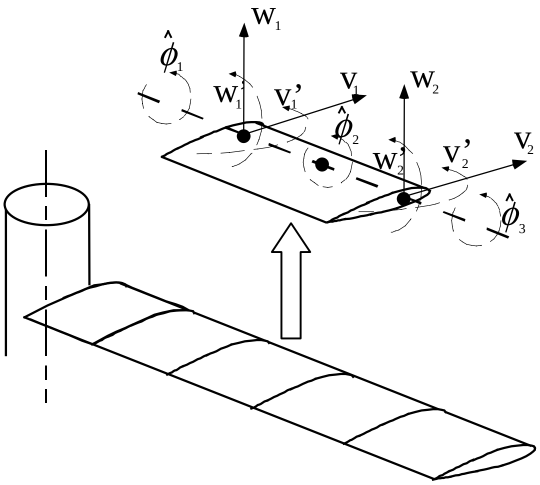
w_1
$\hat{\phi}_1$
w_1'
v_1'
v_1
w_2
$\hat{\phi}_2$
w_2'
v_2'
v_2
$\hat{\phi}_3$

Figure 2.2: Spatial discretization of a rotor blade using Finite Element Method

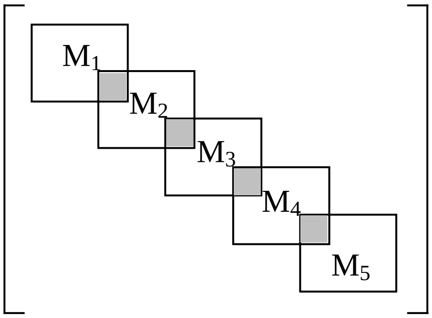
M_1
M_2
M_3
M_4
M_5

Figure 2.3: Global mass matrix of a rotor blade with 5 spatial elements

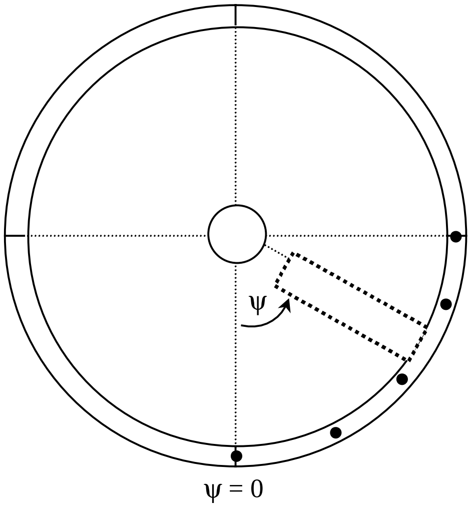

Figure 2.4: Discretization of azimuthal position for blade response calculation using Finite Element in time method

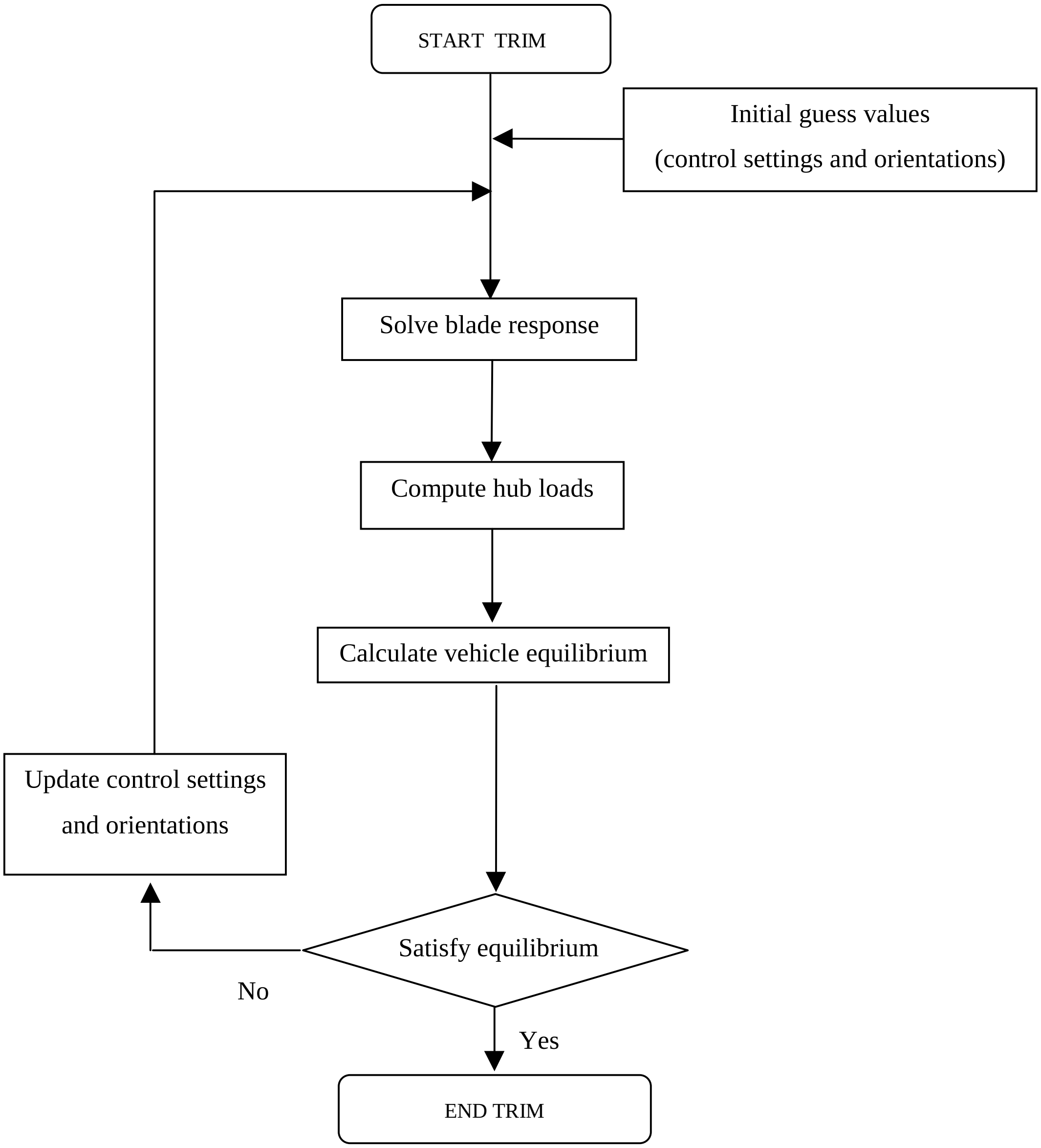
START TRIM
Initial guess values
(control settings and orientations)
Solve blade response
Compute hub loads
Calculate vehicle equilibrium
Update control settings
and orientations
Satisfy equilibrium
No
Yes
END TRIM

Figure 2.5: Flowchart of coupled rotor/trim response calculation procedure

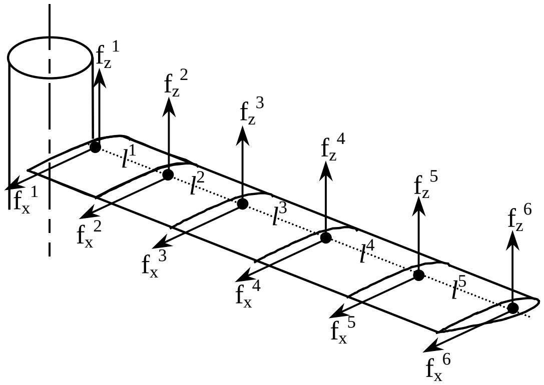
f_z^1
f_z^2
f_z^3
f_z^4
f_z^5
f_z^6
l^1
l^2
l^3
l^4
l^5
f_x^1
f_x^2
f_x^3
f_x^4
f_x^5
f_x^6

Figure 2.6: Nodal blade shear forces in vertical and chordwise directions

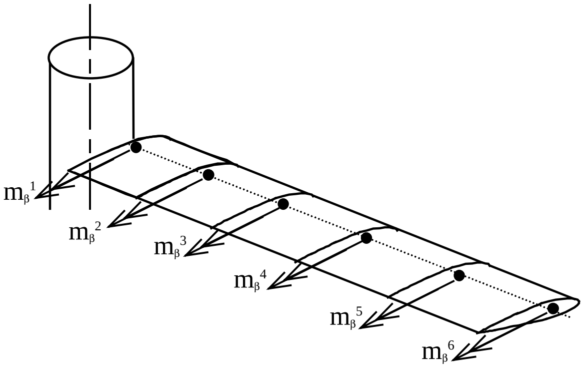
m_β^1
m_β^2
m_β^3
m_β^4
m_β^5
m_β^6

Figure 2.7: Nodal blade moments in flapwise direction

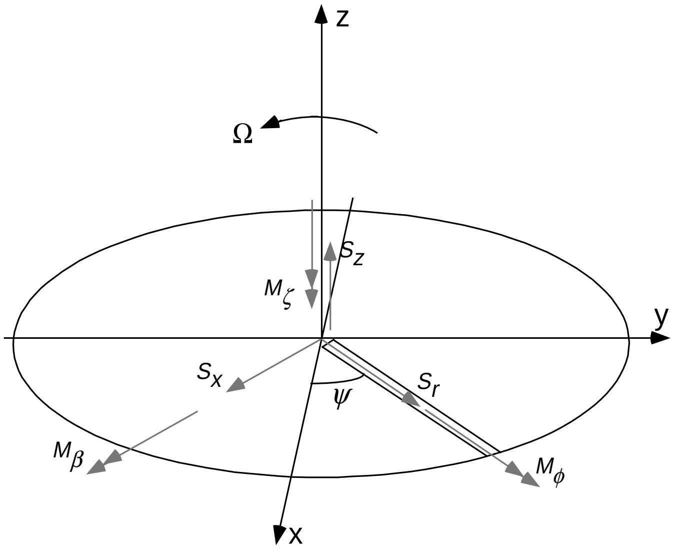
z
Ω
S_z
M_ζ
y
S_x
S_r
ψ
M_β
M_ϕ
x

Figure 2.8: Blade root shear forces and moments

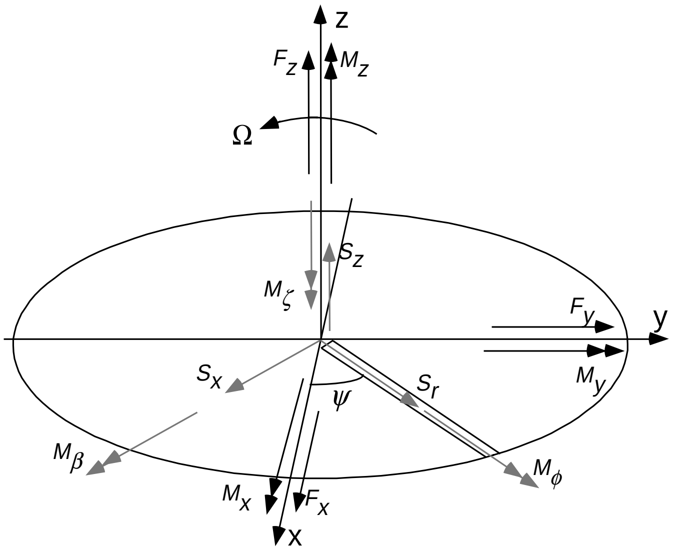
z
F_z
M_z
Ω
S_z
M_ζ
F_y
y
S_x
S_r
M_y
ψ
M_β
M_φ
M_x
F_x
x

Figure 2.9: Transformation between Hub loads and Blade Root Loads

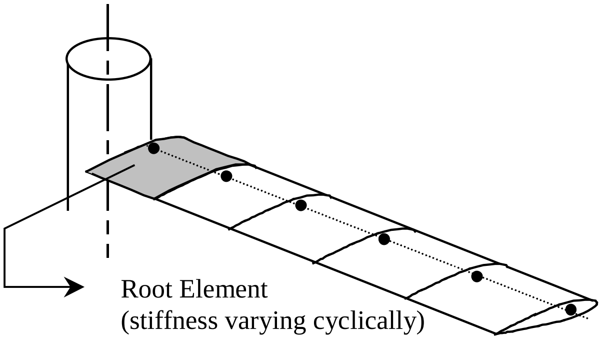
Root Element
(stiffness varying cyclically)

Figure 2.10: Stiffness variation of the root element

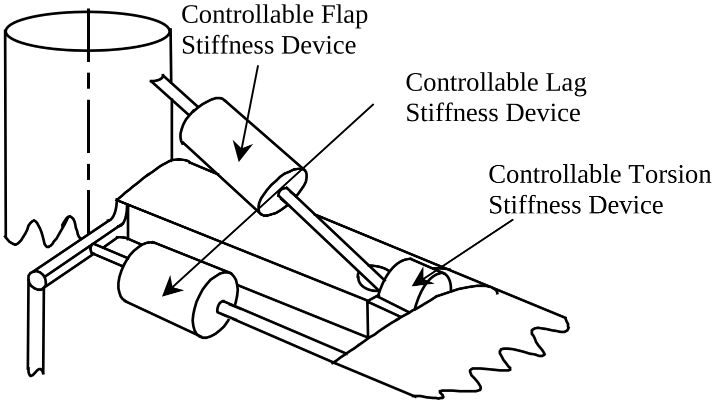
Controllable Flap
Stiffness Device
Controllable Lag
Stiffness Device
Controllable Torsion
Stiffness Device

Figure 2.11: Schematic sketch of discrete controllable stiffness devices

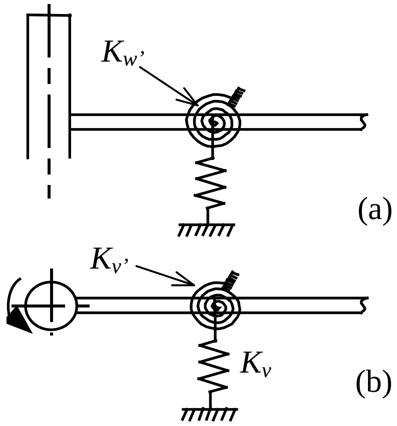

Figure 2.12: Mathematical idealization of discrete controllable stiffness devices using dual spring model in (a) flap and (b) lead-lag directions.

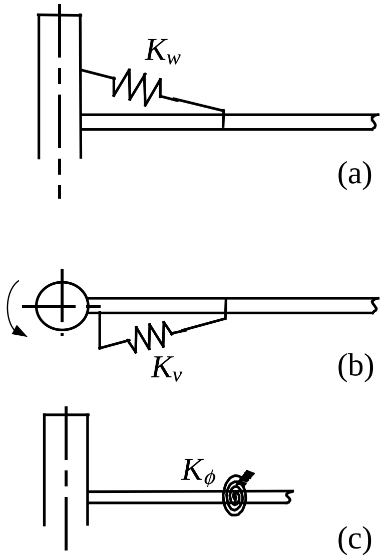

Figure 2.13: Mathematical idealization of discrete controllable stiffness devices using single spring model in (a) flap, (b) lead-lag, and (c) torsional directions.

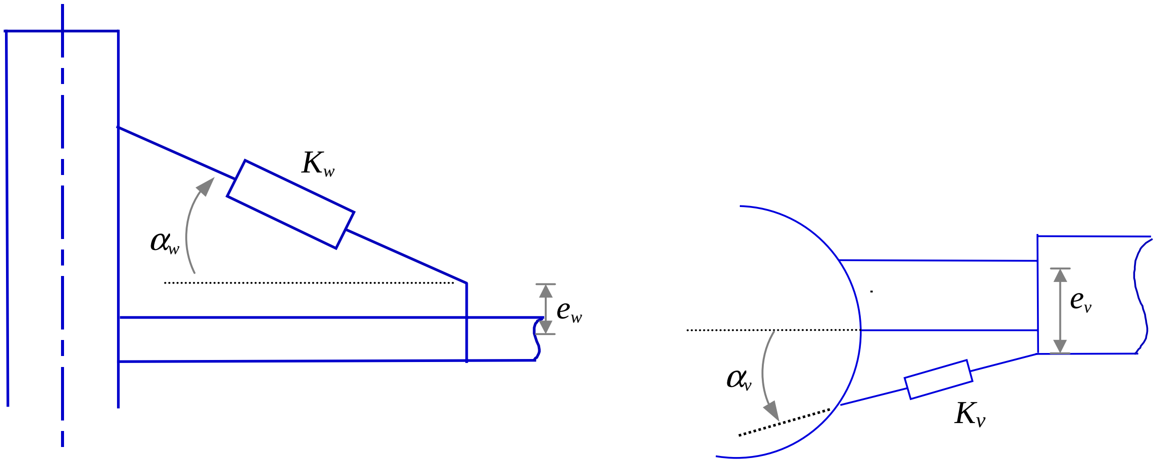
Kw
αw
ew
ev
αv
Kv

(a) (b)

Figure 2.14: Configuration and attachment geometry of controllable stiffness devices, (a) flap device and (b) lag device

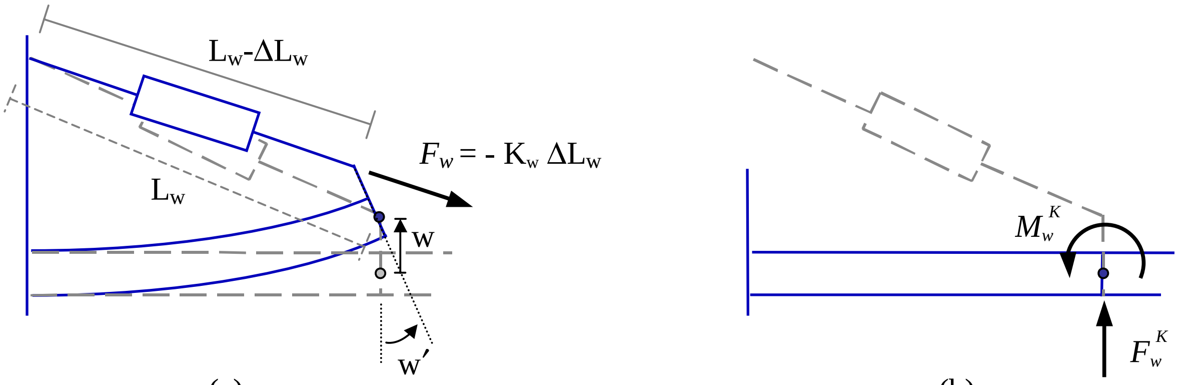
Lw-ΔLw
Lw
Fw = - Kw ΔLw
w
w′
Mw K
Fw K

(a) (b)

Figure 2.15: (a) Deformation of the flap device due to blade bending, and (b) Loads exerted on the blade at attachment point by the flap device

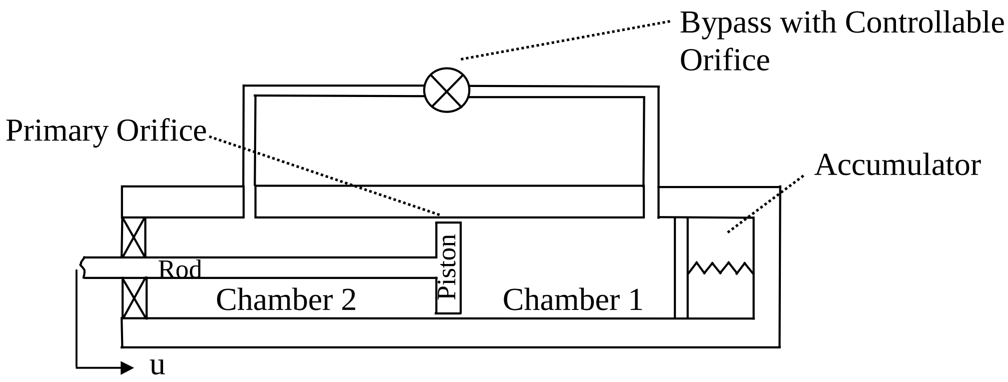
Bypass with Controllable Orifice
Primary Orifice
Accumulator
Piston
Rod
Chamber 2
Chamber 1
u

Figure 2.16: Schematic of a semi-active controllable damper

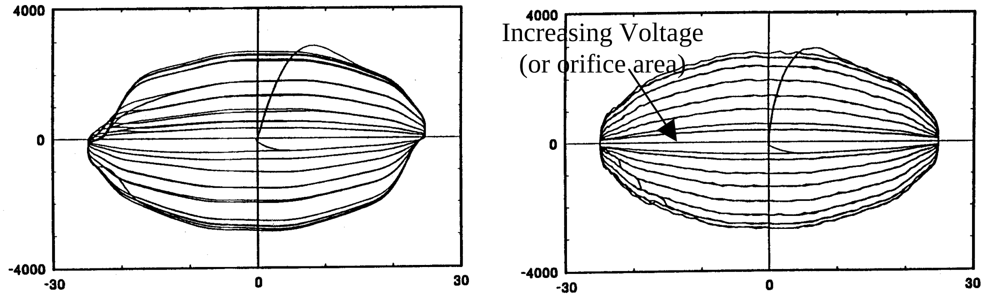

(a) (b)

Figure 2.17: Force/Displacement hysteresis loops for different bypass orifice settings (valve voltages); (a) experiment, (b) fluid dynamic model simulations (from Ref. 103)

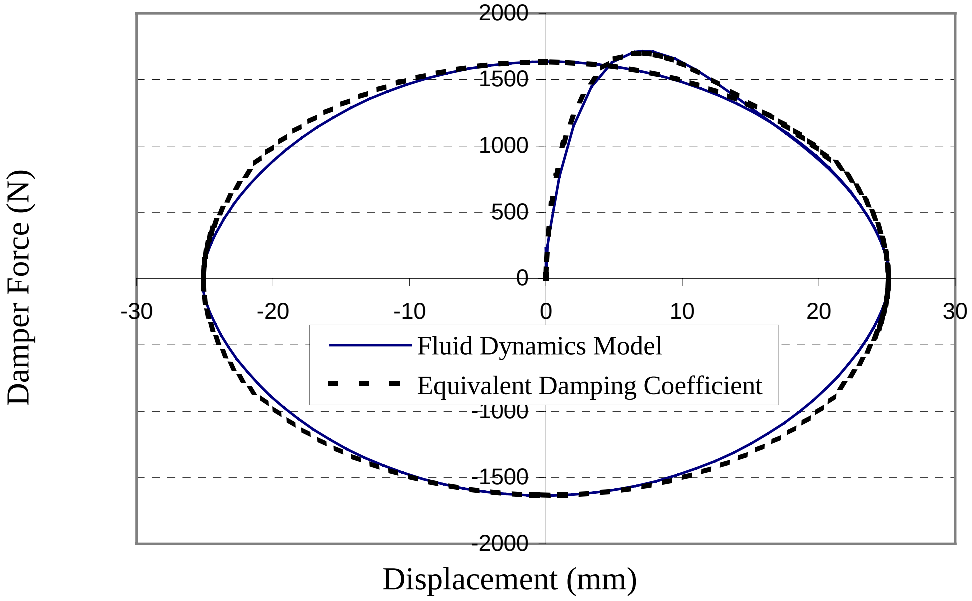

Figure 2.18: Force/Displacement hysteresis cycles produced by the fluid dynamics based damper model and an equivalent damping coefficient model (at a specified orifice command voltage V_o)

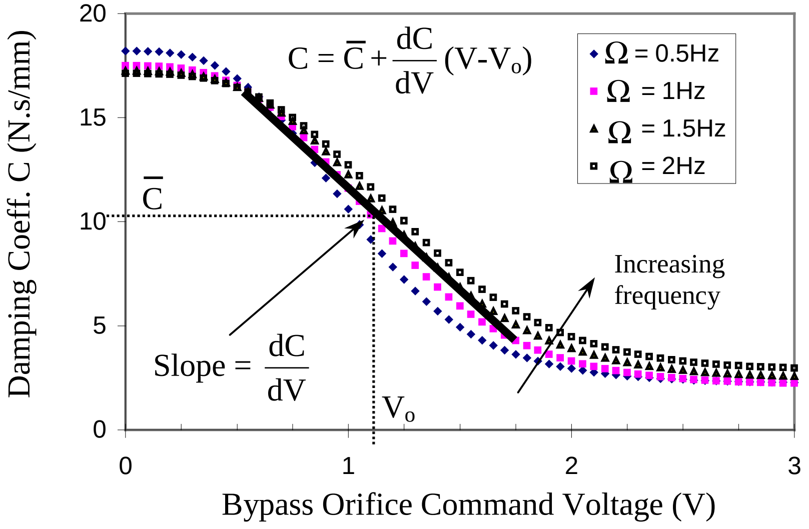

Figure 2.19: Calibration curve for equivalent viscous damping coefficient as a function of orifice voltage

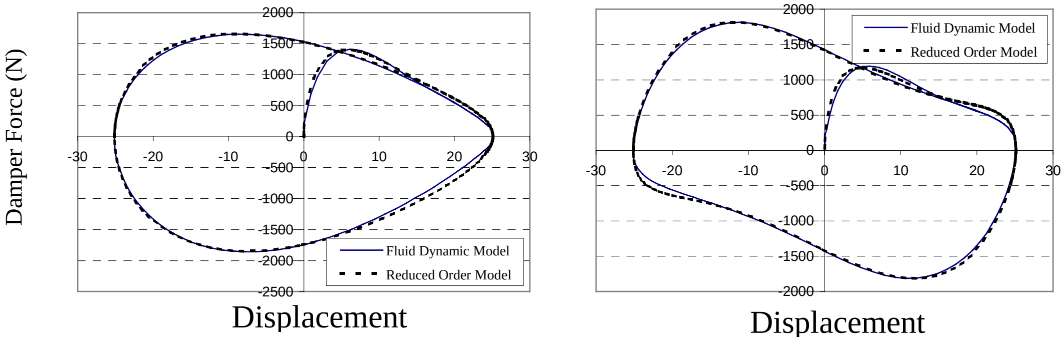

(a) (b)

Figure 2.20: Damper hysteresis loops for prescribed damper motion at frequency Ω and cyclically varying orifice voltage (a) $V=V_o+\Delta V\sin(\Omega t)$ and (b) $V=V_o+\Delta V\sin(2\Omega t)$

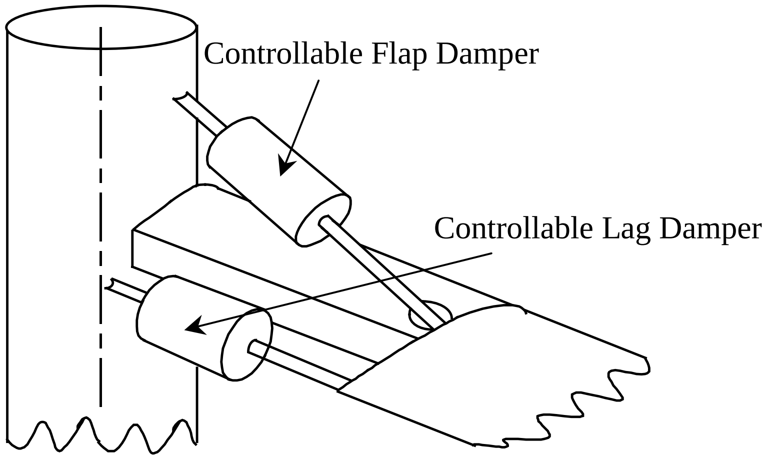

Controllable Flap Damper
Controllable Lag Damper

Figure 2.21: Schematic of rotor blade with controllable flap and lag dampers

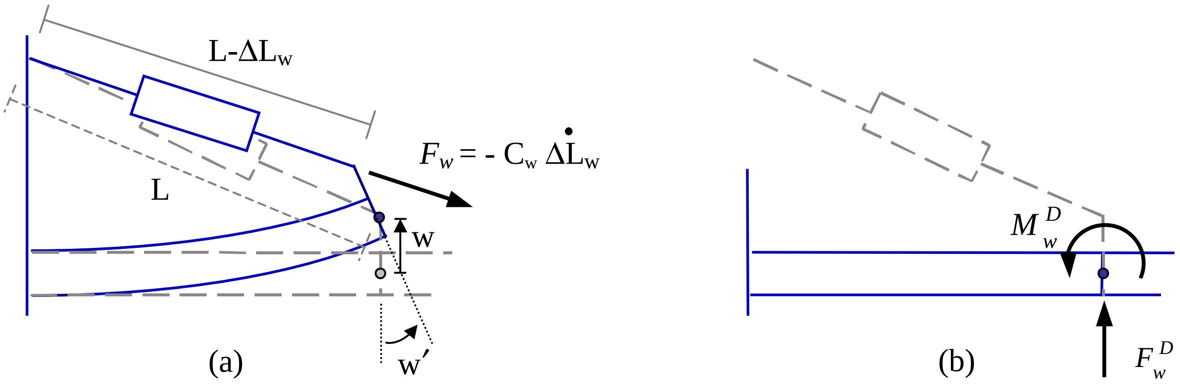
$L-\Delta L_w$
$F_w = -C_w \Delta\dot{L}_w$
L
w
w′
(a)
M_w^D
F_w^D
(b)

Figure 2.22: (a) Deformation of the flap damper due to blade bending, and (b) loads exerted on the blade at attachment point by the flap damper

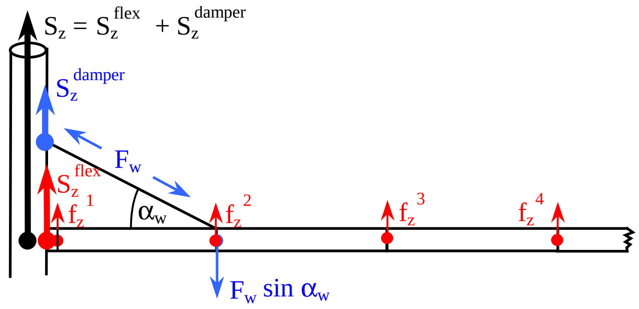
$S_z = S_z^{flex} + S_z^{damper}$
S_z^{damper}
F_w
S_z^{flex}
f_z^1
α_w
f_z^2
f_z^3
f_z^4
$F_w \sin \alpha_w$

Figure 2.23a: Blade root vertical shear, S_z, with contributions from the flexbeam, S_z^{flex} (obtained by summing vertical shear forces, f_z^i, along blade Finite Element DOF’s), and the flap damper, S_z^{damper}

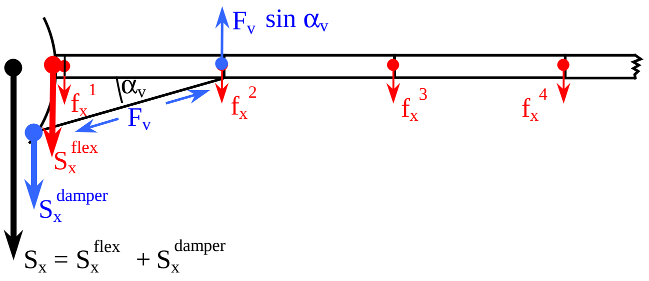
$F_v \sin \alpha_v$
α_v
f_x^1
f_x^2
f_x^3
f_x^4
F_v
S_x^{flex}
S_x^{damper}
$S_x = S_x^{flex} + S_x^{damper}$

Figure 2.23b: Blade root drag shear, S_x, with contributions from the flexbeam, S_x^{flex} (obtained by summing drag shear forces, f_x^i, along blade Finite Element DOF’s), and the lag damper, S_x^{damper}

Chapter 3

Optimal Semi-Active Control Scheme

3.1 Calculation of optimal semi-active inputs

A frequency-domain approach is considered in determining optimal semi-active input, Δ*U*, (which can represent either stiffness variation, $\Delta K(\psi)$, or damping variation, $\Delta C(\psi)$). This frequency domain method is similar to that developed in Ref. 117 and widely employed in previous active vibration reduction studies. The semi-active input, Δ*U*, is expressed in frequency-domain and comprises of amplitudes of sine and cosine components of stiffness or damping variations (at harmonics of rotational speed). Examples of the semi-active inputs are shown in Eq. 3.1a and 3.1b for stiffness and damping variations, respectively.

$$\Delta U = [\underbrace{\Delta K_w^{2c} \quad \Delta K_w^{2s} \quad \Delta K_w^{3c} \quad \Delta K_w^{3s}}_{\substack{2,3/rev\ stiffness\ \mathrm{var}iations \\ of\ the\ flap\ device}} \quad \underbrace{\Delta K_v^{2c} \quad \Delta K_v^{2s} \quad \Delta K_v^{3c} \quad \Delta K_v^{3s}}_{\substack{2,3/rev\ stiffness\ \mathrm{var}iations \\ of\ the\ lag\ device}}]^T \qquad (3.1a)$$

$$\Delta U = [\underbrace{\Delta C_w^{2c} \quad \Delta C_w^{2s} \quad \Delta C_w^{3c} \quad \Delta C_w^{3s}}_{\substack{2,3/rev\ damping\ \mathrm{var}iations \\ of\ the\ flap\ damper}} \quad \underbrace{\Delta C_v^{2c} \quad \Delta C_v^{2s} \quad \Delta C_v^{3c} \quad \Delta C_v^{3s}}_{\substack{2,3/rev\ damping\ \mathrm{var}iations \\ of\ the\ lag\ damper}}]^T \qquad (3.1b)$$

where superscript "*nc*" represents the cosine component at *n*/*rev* and superscript "*ns*" represents sine component at *n*/*rev*. The rotor hub vibration is expressed in frequency domain as, *z*, which consists of sine and cosine components of all vibratory hub loads, and is defined in Eq. 3.2.

$$z = \left[F_x^{4c} \quad F_x^{4s} \quad F_y^{4c} \quad F_y^{4s} \quad F_z^{4c} \quad F_z^{4s} \quad M_x^{4c} \quad M_x^{4s} \quad M_y^{4c} \quad M_y^{4s} \quad M_z^{4c} \quad M_z^{4s}\right]^T \qquad (3.2)$$

where superscripts "*4c*"and "*4s*" denote cosine and sine components of the *4*/*rev* vibratory hub loads, respectively. It is assumed that the semi-active input, Δ*U*, and hub vibration, *z,* are related through a transfer matrix, *T*, as follows:

$$z = z_o + T\,\Delta U \tag{3.3}$$

where "z_o" is the baseline 4/*rev* hub vibration (without any semi-active input). The transfer matrix, *T*, is numerically calculated by perturbation of individual semi-active input components, about the baseline configuration.

The control algorithm, adapted from Ref. 117, is based on the minimization of a composite quadratic objective function, *J*, defined as:

$$J = J_z + J_u = \underbrace{z^T W_z z}_{J_z} + \underbrace{\Delta U^T W_u \Delta U}_{J_u} \tag{3.4}$$

where "W_z" represents the weighting on hub vibration ($W_z = \frac{100}{6}\left\lfloor z_o z_o^T \right\rfloor^{-1}$), and "$W_u$" represents the penalty weighting on semi-active input (W_u is usually set to an identity matrix, unless otherwise stated). In the result Chapters, $J_z = z^T W_z z$ (which is a measure of the vibration level) is used as a performance index; with smaller values of J_z indicating more vibration reduction due to semi-active inputs. The semi-active input index, J_u, can represent the amount of semi-active input required for vibration reduction. The optimal semi-active input (stiffness or damping variations) can be determined using both gradient and non-gradient based methods.

3.1.1 Gradient-based optimization

The optimal semi-active input can be obtained using a gradient-based optimization approach. An optimal input is obtained by substituting Eq. 3.3 into Eq. 3.4 and setting the derivative of the objective function with respect to semi-active inputs to zero ($\partial J/\partial \Delta U = 0$). The resulting optimal semi-active input is presented in Eq. 3.5.

$$\Delta U = -(T^T W_z T + W_u)^{-1} T^T W_z z_o \tag{3.5}$$

Equation 3.5 suggests that the calculation of semi-active input requires prior knowledge of the baseline hub vibration, z_o (measured or calculated), and transfer matrix, *T*. This semi-active control scheme is equivalent to an open-loop scheme, which might produce non-optimal inputs when there is a change in operating condition or rotor configuration. If the change occurs, the semi-active input would have to be re-evaluated since the baseline hub vibration and/or transfer matrix may change.

3.1.2 Non-Gradient-based optimization

The optimal semi-active input can also be determined using a non-gradient-based optimization method. The optimization method considered is based on Genetic Algorithm (GA) approach [118]. An optimal input is determined through an evolutionary process replicating natural selection. Any possible semi-active input, ΔU, is coded into a binary string called an individual. Initially, several individuals are generated randomly to make up the first generation. For every individual in the generation, a "fitness function" is evaluated based on the same objective function defined in Eq. 3.4. The "most fit" individuals in that generation, or the ones that produce the minimum objective function, will be chosen to produce individuals in the next generation through a mating and mutation process. After repeating this process for several generations, the procedure will produce the individual with the highest fitness, which can be decoded back to yield optimal semi-active input that minimizes the objective function. For the genetic algorithm simulations conducted in the present study, the number of individuals in each generation is 20, and the number of generations is 50-200. In general, the amount of time involved in calculating an optimal input using this GA approach is a lot longer than that used by the gradient based approach.

Chapter 4

Sensitivity Study

This Chapter presents preliminary vibration reduction results using root element stiffness variations, described in Section 2.2.1. The effectiveness of root element stiffness variations on reducing hub vibration is examined at a nominal advance ratio of 0.3, using Drees inflow model. The helicopter considered is a 4-bladed hingeless rotor helicopter whose rotor-fuselage properties are given in Appendix H (Table H.1). Stiffnesses of the root elements of the blades are varied cyclically to produce hub vibration reduction (see Eq. 2.12 and Fig. 2.10). Five beam elements are used to model the rotor blade, and 6 modes (2 flap, 2 lag, and 2 torsion modes) are used in modal transformation. The baseline hub vibrations and blade root loads, without any root element stiffness variations, are given in Table 4.1a and Table 4.1b, respectively. Section 4.1 shows sensitivity of vibratory hub loads to root element flap, lag, and torsion stiffness variations at various frequencies, amplitudes, and phases. Underlying mechanism of hub vibration reduction is presented in Section 4.2. Influence of the root element stiffness variations on blade root loads is shown in Section 4.3. Further, Section 4.4 illustrates effectiveness of the root stiffness variation in reducing hub vibration at different advance ratios. A brief summary of the results in this chapter is presented in Section 4.5.

4.1 Influence of root element stiffness variations on vibratory hub loads

The Influence of individual variations in root element flap, lag, and torsion stiffness on hub vibration is examined. The influence of different harmonics (1/*rev*, 2/*rev*, 3/*rev*, 4/*rev*, and 5/*rev*) of the stiffness variations is also considered. For each harmonic of the stiffness variations, the associated phase angle (see Eq. 2.12) is varied to demonstrate sensitivity of vibratory hub loads to the stiffness variation.

4.1.1 Cyclic variation in flap stiffness

The effects of cyclic variations in flapwise stiffness of the root element (flap stiffness) are examined in this section. For a 1/*rev* variation in flap stiffness, Figs. 4.1a and 4.1b show the vibratory hub forces and moments, respectively, as a function of phase angle, ϕ, of the flap stiffness variation. The amplitude of the stiffness variation considered is 15% of the baseline flap stiffness ($\Delta EI_{\beta}^{1p} = 0.15\,\overline{EI}_{\beta}$). The vibratory forces and moments are non-dimensionalized by their respective baseline values (denoted as 100%). From Fig. 4.1a it can be seen that while the hub in-plane shear forces, F_x^{4p} and F_y^{4p}, are virtually insensitive to 1/*rev* flap stiffness variations, the hub vertical shear force, F_z^{4p}, can be reduced by roughly 20% at an "optimal" phase angle of about 225°. Figure 4.1b indicates that the hub moments are mildly sensitive to 1/*rev* flap stiffness variations. At the phase angle, $\phi = 225^{\circ}$, small reductions in hub moments (of no more than 10%) can be obtained in addition to the reduction in F_z^{4p}.

Figure 4.2 shows the influence of 2/*rev* variations in flap stiffness on the vibratory hub loads. The amplitude of the variation, ΔEI_{β}^{2p}, is 15% of the baseline flap stiffness, $\overline{EI}_{\beta}$. It is seen from Fig. 4.2a that at an "optimal" phase angle of around 240°, a 70% reduction in hub vertical shear force, F_z^{4p}, can be achieved. The hub in-plane shears, F_x^{4p} and F_y^{4p}, show very little sensitivity to a 2/*rev* variation in flap stiffness. Figure 4.2b indicates that the hub moments are moderately sensitive to 2/*rev* flap stiffness variations, with a 15-20% increase in the hub in-plane moments, M_x^{4p} and M_y^{4p}, observed at $\phi = 240^{\circ}$.

Figure 4.3 shows the influence of 3/*rev* variations in flap stiffness on the vibratory hub loads. The amplitude of the variation, ΔEI_{β}^{3p}, is 15% of the baseline flap stiffness, $\overline{EI}_{\beta}$. All vibratory hub forces and moments show large sensitivity to 3/*rev* variations in flap stiffness. Figure 4.3a indicates that a substantial 70% reduction in the hub in-plane shear forces, F_x^{4p} and F_y^{4p}, and a 40% reduction in the hub vertical shear, F_z^{4p}, can be achieved at a phase angle of around 0°. At this phase angle, the hub torque, M_z^{4p}, is unchanged and the pitching moment, M_y^{4p}, is decreased by 15%, but the rolling moment, M_x^{4p}, is increased by 20% (Fig. 4.3b). Alternatively, if a phase angle of around 45° is selected, 60% and 85% reductions in hub in-plane moments, M_x^{4p} and M_y^{4p}, and an approximately 30% reduction in all hub forces can be achieved. This phase angle, though, produces a 25% increase in the vibratory hub torque, M_z^{4p}.

A 4/*rev* flap stiffness variation with an amplitude as low as 5% of the baseline flap stiffness ($\Delta EI_{\beta}^{4p} = 0.05\overline{EI}_{\beta}$) produced a more than 200% increase in vibratory hub vertical shear, F_z^{4p}, over the entire range of phase angles. The system appears to be "overdriven" with the stiffness variations actually producing significant vibrations rather than merely canceling the original vibrations. Conceivably, the amplitude of stiffness variation could be further reduced, but smaller amplitudes would require high precision in stiffness variation. A 5/*rev* flap stiffness variation had the greatest influence on the in-plane vibratory hub moments. For an amplitude of variation of 5% of the baseline flap stiffness ($\Delta EI_{\beta}^{5p} = 0.05\overline{EI}_{\beta}$), up to 60% reductions in the in-plane hub moments were possible. However, the phase angles that produced a decrease in the rolling moment, M_x^{4p}, increased the pitching moment, M_y^{4p}, by a comparable amount, and vice-versa. Thus, 4/*rev* and 5/*rev* variations in flap stiffness are not considered as candidates for reduction of vibratory hub loads.

4.1.2 Cyclic variation in lag stiffness

The effects of cyclic variations in chordwise stiffness of the root element (lag stiffness) are examined in this section. A 1/*rev* variation in lag stiffness, of amplitude 15% of the baseline lag stiffness ($\Delta EI_{\zeta}^{1p} = 0.15\overline{EI}_{\zeta}$), was first considered. The vibratory hub forces and moments were found to be relatively insensitive to 1/*rev* lag stiffness variations, with reductions in vibratory hub loads of no more than 5-7%, relative to the baseline values.

The influence of 2/*rev* lag stiffness variations on the vibratory hub loads is shown in Fig. 4.4. The amplitude of variation, ΔEI_{ζ}^{2p}, is 15% of the baseline lag stiffness, $\overline{EI}_{\zeta}$. The vibratory in-plane hub forces and the hub torque are most sensitive to the 2/*rev* lag stiffness variations. From Fig. 4.4a it is seen that at an "optimal" phase angle of about 90°, the in-plane shear forces, F_x^{4p} and F_y^{4p}, are reduced by about 20% and 30%, respectively. At the same phase angle, the hub torque, M_z^{4p}, is simultaneously reduced by about 20%.

Figure 4.5 shows the influence of 3/*rev* variations in lag stiffness on the vibratory hub loads. The amplitude of the variation, ΔEI_{ζ}^{3p}, is 5% of the baseline lag stiffness, $\overline{EI}_{\zeta}$. In Fig. 4.5a it is seen that at a phase angle of 225°, the hub vertical shear, F_z^{4p}, can be reduced by 40% without adversely affecting any of the other hub forces or moments. Alternatively, Fig. 4.5b indicates that a phase angle of 135° produces an 85% reduction in hub torque, M_z^{4p}, without adversely affecting any other hub forces or moments. Any phase angle between 135° and 225° produces simultaneous reductions in F_z^{4p} and M_z^{4p}. The in-plane hub forces and moments are relatively insensitive to 3/*rev* lag stiffness variations. At a phase of 135°, if larger amplitudes of stiffness variation are considered, the vibratory hub torque starts to increase since the system is "overdriven" and the stiffness variations are producing the vibrations rather than merely cancelling them. Figure 4.6a clearly illustrates this principle. It is seen in the figure that as ΔEI_ζ^{3p} increases from $0.02\,\overline{EI}_\zeta$ to $0.05\,\overline{EI}_\zeta$, larger reductions in M_z^{4p} can be achieved. However, an increase in ΔEI_ζ^{3p} to $0.10\,\overline{EI}_\zeta$ produces smaller reductions in M_z^{4p}, and for $\Delta EI_\zeta^{3p} = 0.15\,\overline{EI}_\zeta$, the vibrations actually increase, at any phase angle. Figure 4.6b shows the maximum reduction in M_z^{4p} versus magnitude of stiffness variation (at the optimal phase angle) for 2/*rev* as well as 3/*rev* lag stiffness variations. It is seen from the figure that for 2/*rev* variations, more vibration reduction is achieved as ΔEI_ζ increases. However, the hub vibrations are more sensitive to 3/*rev* lag stiffness variations, so small amplitudes are able to produce large reductions. If the amplitude is further increased, the system is "overdriven" and the stiffness variations produce the vibrations.

A 4/*rev* lag stiffness variation (of amplitude $\Delta EI_\zeta^{4p} = 0.05\,\overline{EI}_\zeta$) produced about 40% variations in all the vibratory hub forces and the hub torque. However, the phase angles that produced a decrease in the vibratory hub drag, F_x^{4p}, produced a corresponding increase in the side-force, F_y^{4p}, and vice-versa. Thus, 4/*rev* variations in lag stiffness are not considered as a candidate for reduction of vibratory hub loads.

Figure 4.7 shows the influence of 5/*rev* variations in lag stiffness on the vibratory hub loads. The amplitude of the variation, ΔEI_ζ^{5p}, is 5% of the baseline lag stiffness, $\overline{EI}_\zeta$. From Fig. 4.7b it is seen that the hub torque, M_z^{4p}, is virtually eliminated at a phase of about 180°, but components of hub forces are simultaneously increased by 10-20% (Fig. 4.7a). However, a phase angle of about 200° can reduce the hub torque, M_z^{4p}, by over 85% without adversely affecting the hub forces. The in-plane moments, M_x^{4p} and M_y^{4p}, are insensitive to 5/*rev* lag stiffness variations.

4.1.3 Cyclic variation in torsion stiffness

The effects of cyclic variations in torsional stiffness of the root element are examined in this section. 1/*rev* and 2/*rev* variations in torsion stiffness, of amplitude 15% of the baseline torsion stiffness, were found to have relatively little influence on the vibratory hub forces and moments (with hub vibration reductions of no more than 5-7% of the baseline values). Hence 1/*rev* and 2/*rev* variations in torsion stiffness are not considered for reduction of vibratory hub loads.

The effect of 3/*rev* torsion stiffness variation on the vibratory hub loads is shown in Fig. 4.8. The amplitude of variation, ΔGJ^{3p}, is 15% of the baseline torsion stiffness, $\overline{GJ}$. Figure 4.8a indicates that while the vibratory in-plane hub forces are insensitive to 3/*rev* torsion stiffness variations, a 15% reduction in hub vertical shear, F_z^{4p}, can be achieved if a phase angle of 315° - 360° is selected. For these values of phase angle, the vibratory hub moments show no significant change (Fig. 4.8b).

Figure 4.9 shows the influence of 4/*rev* variations in torsion stiffness on the vibratory hub loads. The amplitude of variation, ΔGJ^{4p}, is again 15% of the baseline torsion stiffness, $\overline{GJ}$. Figure 4.9a indicates that while the in-plane vibrations, F_x^{4p} and F_y^{4p}, are insensitive to the stiffness variations, a 20% reduction in vertical shear, F_z^{4p}, can be achieved for an "optimal" phase angle of around 90° - 135°. The influence of 4/*rev* torsion stiffness variations on vibratory hub moments is fairly insignificant (Fig 4.9b).

5/*rev* variations in torsion stiffness (with $\Delta GJ^{5p} = 0.15\overline{GJ}$) were able to produce reductions in F_z^{4p} of no more than 8%. Other vibratory hub loads showed even lower sensitivity. Hence 5/*rev* torsion stiffness variations are not considered for reduction of hub vibrations.

4.1.4 Summary of beneficial root element stiffness variations

Harmonic variations in flap, lag, and torsion stiffness of the root element that produced significant reductions in vibratory hub loads are summarized in Table 4.2. Listed in the table are the amplitudes of stiffness variation required (as a percentage of the baseline stiffness), the "optimal" phase, and the corresponding changes in the components of vibratory hub loads. A

1/*rev* flap stiffness variation is not considered, since significantly larger reductions in the hub vertical force, F_z^{4p}, can be achieved using 2/*rev* variations in flap stiffness. Although torsion stiffness variations produce reductions in F_z^{4p} that are comparable to those achieved using a 1/*rev* flap stiffness variation, these are retained to assess comparison between the flap stiffness versus torsion stiffness variations. In general, it can be observed from Table 4.2 that torsion stiffness variations produce only moderate reductions in F_z^{4p}. Lag stiffness variations can produce reductions in all hub forces and the hub torque. Flap stiffness variations are probably the most versatile, and have the potential to reduce all hub forces and the in-plane hub moments.

4.2 Mechanism for reduction of vibratory hub loads

In the previous section, stiffness variations that produced reductions in vibratory hub loads were identified (Table 4.2). For these stiffness variations, the present section examines the mechanism by which the vibration reduction is achieved. Specifically, since inertial and aerodynamic components of the various blade root loads contribute significantly to the hub loads, this section seeks to understand the individual change or the combination of changes, in these components that leads to the reduction of the vibratory hub loads.

The following comments can be made about all the reductions in vibratory hub moments. The hub roll and pitch moments, M_x^{4p} and M_y^{4p}, have contributions from the blade root flapping moment, M_β, and the blade root pitching moment, M_ϕ. However, for the symmetric airfoil considered in the present study, the root pitching moments in the absence of stall are considerably smaller than the blade root flapping moment. Further, the blade root flapping moment contribution to M_x^{4p} and M_y^{4p} is dominated by the inertial component and it is reductions in the inertial component of M_β (due to stiffness variations) that produce reductions in M_x^{4p} and M_y^{4p}. The blade root lag moment contributes to the vibratory hub yaw moment, M_z^{4p}. The blade root lag moment is also dominated by the inertial contribution, and reduction in M_z^{4p} is achieved when stiffness variation reduces this component. The mechanisms for reduction of the vibratory hub forces are more varied, and are discussed below.

For the 2/*rev* flap stiffness variation, Fig. 4.10 depicts, vectorially, the inertial and aerodynamic components of F_z^{4p}. Compared to the baseline rotor (no stiffness variations) the aerodynamic component increases slightly. The inertial component decreases somewhat in magnitude (by no more than 20%) but undergoes a phase change. This phase change in the inertial component results in a significantly reduced vectorial sum (of the inertial and aerodynamic components), so that there is a 70% net reduction in the total F_z^{4p} load.

For the 3/*rev* flap stiffness variation, a phase angle of 45° produced 30% reductions in vibratory hub forces, and 60% and 85% reductions, respectively, in the hub roll and pitch moments, M_x^{4p} and M_y^{4p}. The blade root radial shear force, S_r, and drag shear force, S_x, contribute to the in-plane hub forces. Figure 4.11 shows the contributions of S_r and S_x to F_x^{4p}, vectorially. It clearly indicates that although the individual contributions of S_r and S_x to F_x^{4p} have not changed in magnitude, an increase in the relative phase angle results in a smaller net F_x^{4p}. The reduction in F_y^{4p} occurs in a similar manner. Figure 4.12 depicts, vectorially, the inertial and aerodynamic components of F_z^{4p}. Compared to the baseline rotor, the aerodynamic component decreases slightly and the inertial component decreases to a larger extent (by about 40%). While both components individually undergo a change in phase, there is little change in the relative phase angle. Thus it can be concluded that the 30% reduction in the total F_z^{4p} load is due to the decrease in the magnitude of the contributing aerodynamic and inertial components.

The 2/*rev* lag stiffness variation produced 20%-30% reductions in the hub in-plane forces, which was due to decreases in both the blade root radial shear and drag shear contributions to F_x^{4p} and F_y^{4p}. These decreases, specifically, occurred due to reductions in the magnitude of the inertial components of the loads. The magnitude of the aerodynamic components and the phase of both components was unchanged.

For a 3/*rev* lag stiffness variation, a phase angle of 135° produced an 85% reduction in vibratory hub yaw moment. This was again due to a corresponding reduction in the blade root lag moment (inertial component). Alternatively, a phase angle of 225° produced a 40% reduction in F_z^{4p}. Figure 4.13 depicts, vectorially, the inertial and aerodynamic components of F_z^{4p}. Compared to the baseline rotor both the aerodynamic and inertial components show fairly significant increases. However, the change in phase angles of both these components results in an increase in the relative phase and produces a significantly reduced vectorial sum of the total F_z^{4p} load.

3/*rev* and 4/*rev* torsion stiffness variations reduced F_z^{4p} by approximately 15%-20%. Figure 4.14 depicts, vectorially, the inertial and aerodynamic components of F_z^{4p}, for 4/*rev* torsion stiffness variations. Both aerodynamic and inertial components increase in magnitude, compared to the baseline rotor. However, both components undergo changes in phase, so that the resultant F_z^{4p} load (vectorial sum of inertial and aerodynamic components) is reduced. When 3/*rev* torsion stiffness variations are used, reductions in F_z^{4p} are obtained in a similar manner.

4.3 Influence of root element stiffness variation on blade root loads

For the stiffness variations identified in Table 4.2 (that produced reductions in vibratory hub loads), the present section examines the corresponding blade root loads in the rotating system. For a reduction in the hub in-plane vibratory forces or moments, reductions are generally expected in the 3/*rev* components of blade root radial shear, drag shear, flapping moment, and pitching moment. Similarly, for a reduction in the hub vibratory vertical shear force and torque, corresponding reductions are expected in the 4/*rev* components of blade root vertical shear and lag moment. However, it is important to ascertain that a stiffness variation that produces a reduction in a particular vibratory hub force or moment does not simultaneously produce excessive increases in other harmonics of blade root loads (that do not contribute to the fixed-system hub loads). This is an important consideration since increased blade root dynamic stresses could result in premature fatigue. As a benchmark, the harmonics of blade root loads for the baseline configuration (without stiffness variations) are presented in Table 4.1b. It should be noted that the fifth harmonics are generally one-to-two orders of magnitude lower than the third and fourth harmonics. Thus, increases in fifth harmonics (even by factors of 2-5) are generally of lesser concern than increases in third, fourth, and lower harmonics. Additionally, for the symmetric airfoil considered in the present study, harmonics of blade root torsion moment are generally 1-2 orders of magnitude lower than those of the blade root flap or lag moments. Thus, increases in blade root torsion moment (even by factors of 2-3) are also of relatively lower importance, although it is recognized that such increases would lead to an increase in vibratory pitch-link loads.

4.3.1 Cyclic variation in flap stiffness

This section examines the blade root loads in the presence of flap stiffness variations that resulted in reductions in hub vibrations (Table 4.2). Shown in Table 4.3a are changes in harmonics of blade root loads due to a 2/*rev* variation in flap stiffness ($\Delta EI_\beta^{2p} = 0.15\overline{EI}_\beta$, ϕ = 240°). The shaded areas in Table 4.3a denote harmonics of blade root loads contributing to hub vibrations. A 73% reduction is observed in the 4/*rev* component of blade root vertical shear, S_z, consistent with the approximately 70% reduction in F_z^{4p} achieved with 2/*rev* flap stiffness variation (see Table 4.2). An 18% increase in M_β^{3p} contributes to the increases in vibratory hub rolling moment, M_x^{4p} and pitching moment, M_y^{4p}. The most significant increase in blade root loads is a 42% increase in the 2/*rev* component of blade root flapping moment, M_β.

Shown in Table 4.3b are changes in harmonics of blade root loads due to a 3/*rev* variation in flap stiffness ($\Delta EI_\beta^{3p} = 0.15\overline{EI}_\beta$, ϕ = 45°). Although only very modest 9% and 6.5% reductions are observed in the 3/*rev* components of S_r and S_x, changes in relative phase are responsible for the net reduction in hub loads (as discussed in Section 4.2, see Fig. 4.11). The reduction observed in the 4/*rev* component of S_z, is consistent with the reduction in hub vertical shear, F_z^{4p}. The significant 73% reduction in the 3/*rev* component of M_β contributes to the large reductions in hub rolling and pitching moments, M_x^{4p} and M_y^{4p}, respectively. The increase in M_ζ^{4p} is consistent with the corresponding increase in the vibratory hub yaw moment indicated in Table 4.2. There are no significant increases in 1/*rev*, 2/*rev*, and 3/*rev* components of blade root loads. Of some concern are increases of 88% in S_r^{4p} and 36% in S_x^{4p}. Although large percentage increases are also observed in the 5/*rev* components of S_z and M_β, their baseline values are very small.

4.3.2 Cyclic variation in lag stiffness

This section examines the blade root loads in the presence of lag stiffness variations that resulted in reductions in hub vibrations (Table 4.2). Shown in Table 4.4a are changes in harmonics of blade root loads due to a 2/*rev* variation in lag stiffness ($\Delta EI_\zeta^{2p} = 0.15\overline{EI}_\zeta$, ϕ = 90°). Reductions of 15% in S_r^{3p} and 44% in S_x^{3p} contribute to the reductions in the in-plane hub shears, F_x^{4p} and F_y^{4p}, indicated in Table 4.2. A nearly 20% reduction is observed in the 4/*rev* component of blade root lag moment, M_ζ, consistent with the corresponding reduction in hub torque, M_z^{4p} (see Table 4.2). Although a 200% increase in the 3/*rev* component of M_ζ is of concern, it should be noted that the baseline value of M_ζ^{3p} was very low (about 25% of the magnitude of M_ζ^{4p}, as seen in Table 4.1b).

The changes in blade root load harmonics due to the 3/*rev* variation in lag stiffness ($\Delta EI_\zeta^{3p} = 0.05\overline{EI}_\zeta$, $\phi = 135^\circ$) are presented in Table 4.4b. An approximately 86% reduction is observed in the 4/*rev* component of blade root lag moment, M_ζ^{4p}, consistent with the reduction obtained in the vibratory hub torque seen in Table 4.2. Additional large decreases in 4/*rev* components of in-plane blade root shears are obtained. Although large increases in the 4/*rev* and 5/*rev* component of blade root pitching moment, M_ϕ, are obtained, the baseline values for blade root pitching moment harmonics were very small. Table 4.4c shows the resulting changes in harmonics of blade root loads when a phase angle of $\phi = 225^\circ$ is considered (with the amplitude, ΔEI_ζ^{3p}, retained at 5% $\overline{EI}_\zeta$). A 40% reduction is observed in the 4/*rev* component of blade root vertical shear, S_z, consistent with the 40% decrease in hub vertical shear, F_z^{4p}. The most significant increase in blade root loads is a 57% increase in S_r^{4p}. The 75% increase in M_ϕ^{4p} is of less significance due to the baseline value being very small. Similarly, increases in fifth harmonics are of less significance.

A 5/*rev* variation in lag stiffness ($\Delta EI_\zeta^{5p} = 0.05\overline{EI}_\zeta$, $\phi = 200^\circ$) produced a 75% reduction in the 4/*rev* component of blade root lag moment, M_ζ (Table 4.4d), consistent with the reduction in vibratory hub yaw moment obtained (see Table 4.2) due to this stiffness variation. No increases were obtained in the first, second, and third harmonics of the blade root loads. In addition to the reduction in M_ζ^{4p}, reductions of 23% in S_r^{4p}, and 60% in S_x^{4p}, are also obtained. However, very large percentage increases are obtained in the 5/*rev* components of S_r, and S_x, (500-600%), M_ζ, (800%), and M_ϕ (300%).

4.3.3 Cyclic variation in torsion stiffness

This section examines the blade root loads in the presence of torsion stiffness variations that resulted in reductions in hub vibrations (Table 4.2). Shown in Table 4.5a are changes in harmonics of blade root loads due to 3/*rev* variation in torsion stiffness ($\Delta GJ^{3p} = 0.15\overline{GJ}$, $\phi = 320^{o}$). The 15% reduction observed in the 4/*rev* component of blade root vertical shear, S_z, is consistent with the corresponding reduction in vibratory hub vertical force, F_z^{4p}, seen in Table 4.2. Shown in Table 4.5b are the changes in harmonics of blade root loads due to 4/*rev* variation in torsion stiffness ($\Delta GJ^{4p} = 0.15\overline{GJ}$, $\phi = 100^{o}$). Again, the 20% reduction observed in the 4/*rev* component of blade root vertical shear, S_z^{4p}, is consistent with the corresponding decrease in vibratory hub vertical shear, F_z^{4p}, seen Table 4.2. For both 3/*rev* as well as 4/*rev* torsion stiffness variations, very large percentage increases are obtained in the 4/*rev* and 5/*rev* components of pitching moment, M_ϕ. These may not be insignificant even though the baseline values of these components were very small. No increases of any significance are observed in any of the other harmonics of blade root loads.

4.4 Vibration reduction at different advance ratio

In Section 4.1.2 it was shown that 3/*rev* lag stiffness variations ($\Delta EI_\zeta^{3p} = 0.05\overline{EI}_\zeta$, $\phi = 135^{o}$) produced about 85% reductions in M_z^{4p} at $\mu = 0.3$. Figure 4.15 shows reductions in M_z^{4p} (due to 3/*rev* lag stiffness variations) at three different advance ratios. At $\mu = 0.35$, only a 66% reduction could be achieved in M_z^{4p}, since the baseline vibrations are higher. Larger amplitudes of stiffness variation ($\Delta EI_\zeta^{3p} > 0.05\overline{EI}_\zeta$) would be required to produce additional vibration reductions. At $\mu = 0.25$, the vibration reduction achieved using $\Delta EI_\zeta^{3p} = 0.05\overline{EI}_\zeta$, $\phi = 135^{o}$, was negligible. However, further investigation revealed that the optimal phase angle at $\mu = 0.25$ was 100° (and not 135°). A phase of 100° did produce slightly larger reductions in M_z^{4p}, but the system was "overdriven" at $\mu = 0.25$ since the baseline vibrations were lower. Smaller stiffness variation amplitudes could be used at lower advance ratios, or alternatively, no stiffness variation may be used at moderate advance ratios, and stiffness variations could be introduced when the advance ratio increases beyond a prescribed value, say $\mu = 0.3$.

The above observations were found to be equally true for other stiffness variations and components of vibratory hub loads, and may be generalized as follows. The amplitude of stiffness variation required for vibration reduction increases with advance ratio. If moderate vibration reduction is achieved at $\mu = 0.3$, the same amplitude of stiffness variation is likely to produce larger reductions at lower advance ratios. However, if substantial vibration reduction is achieved at $\mu = 0.3$, the same amplitude of stiffness variation is likely to produce smaller reductions (or even increases) at lower advance ratios, since the system will be “overdriven”. At $\mu = 0.35$, the amplitudes of stiffness variation required would always be greater (for a similar reduction in vibration). The optimal phase angle may change with advance ratio.

4.5 Summary on sensitivity of root element stiffness variation

From the results presented in this chapter, it is clearly shown that components of vibratory hub loads could be modified using specific harmonic variations in root element flap, lag, and torsion stiffness. With a proper amplitude and phase angle, harmonic stiffness variation can be employed to reduce some components of hub vibration. In particular, lag stiffness variations can produce substantial reductions in all vibratory hub forces and hub yaw moment, while flap stiffness variations have the potential to significantly reduce all hub forces and the hub roll and pitch moments. Torsion stiffness variations, on the other hand, produce only moderate reductions in only 4/*rev* vertical hub forces. The reduction in vibrations are obtained by one of two mechanisms - *(i)* reduction in magnitude of the inertial component of the blade root loads that contribute to hub vibrations; *(ii)* change in relative phase of the contributing components. The cyclic stiffness variations that produce reductions in vibratory hub loads may produce increases in certain blade root load harmonics.

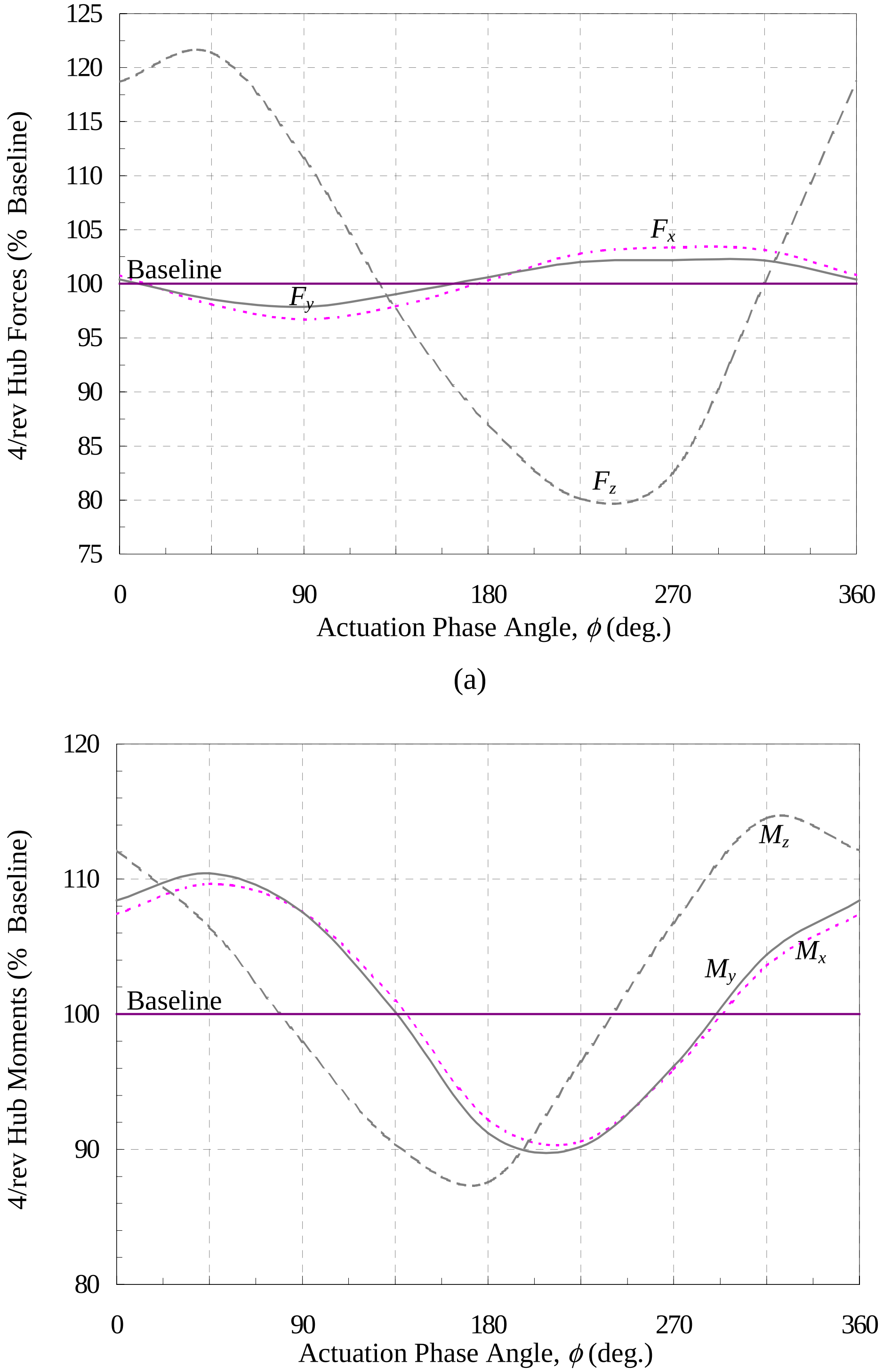

(a)

(b)

Figure 4.1: Influence of phase, ϕ, of 1/*rev* variation in flap stiffness on 4/*rev* hub forces (a) and moments (b), $\left\{ EI_\beta = \overline{EI_\beta} + \Delta EI_\beta^{1p} \sin(\psi + \phi),\ \ \Delta EI_\beta^{1p} = 0.15\overline{EI_\beta} \right\}$

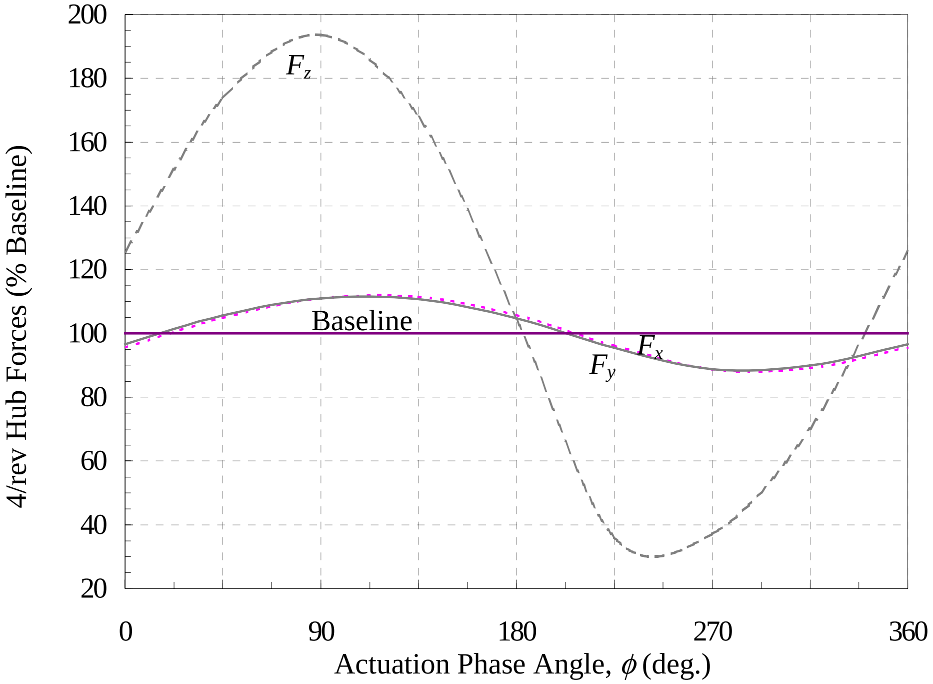

(a)

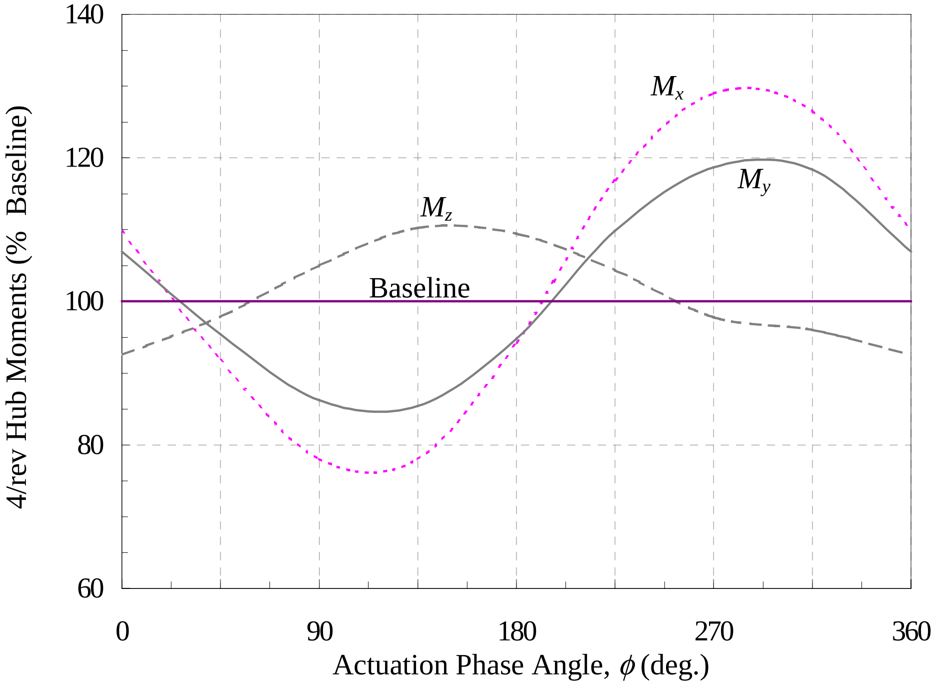

(b)

Figure 4.2: Influence of phase, ϕ, of 2/*rev* variation in flap stiffness on 4/*rev* hub forces (a) and moments (b), $\left\{ EI_\beta = \overline{EI_\beta} + \Delta EI_\beta^{2p}\sin(2\psi + \phi),\ \ \Delta EI_\beta^{2p} = 0.15\overline{EI_\beta} \right\}$

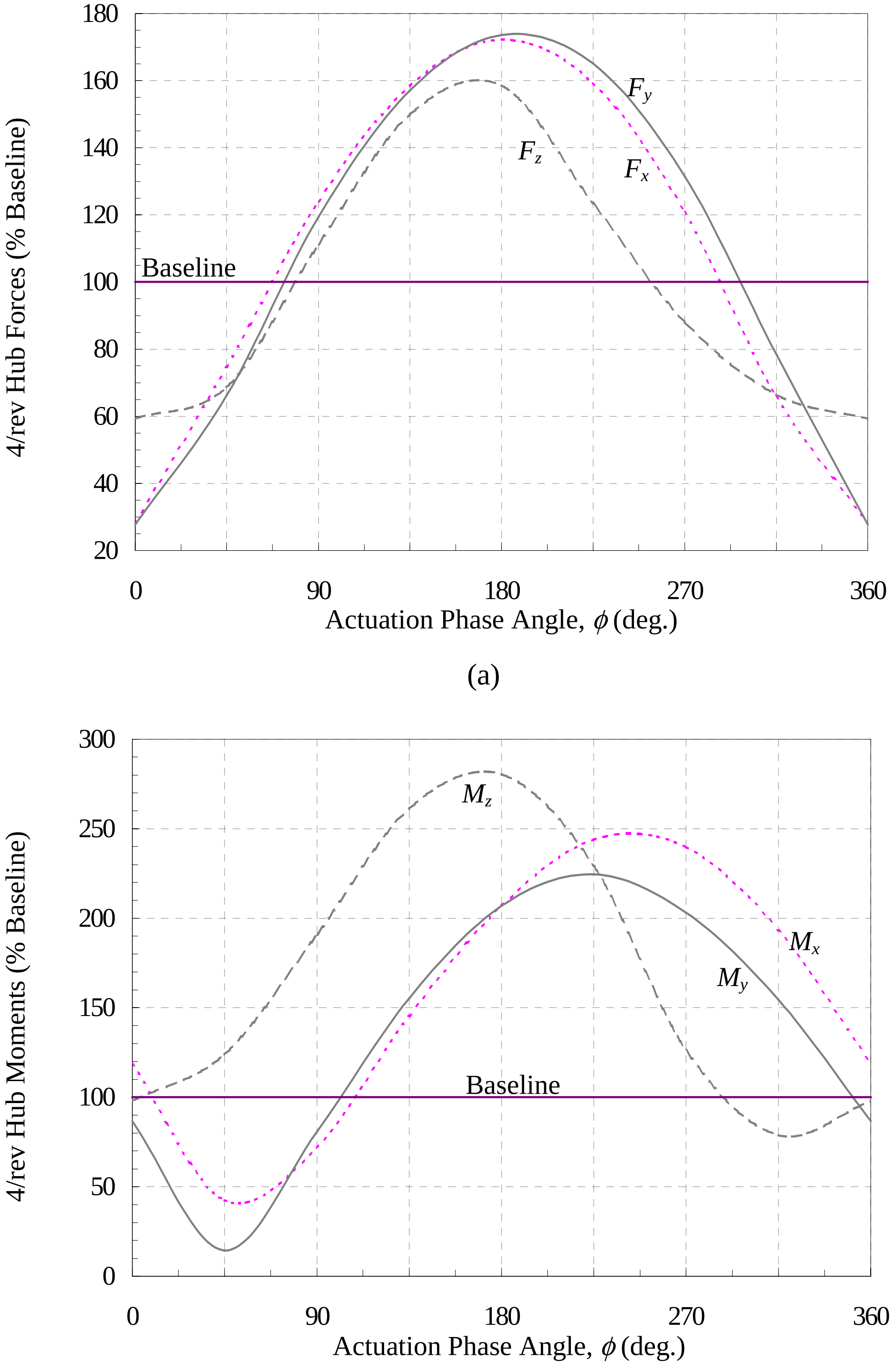

(a)

(b)

Figure 4.3: Influence of phase, ϕ, of 3/*rev* variation in flap stiffness on 4/*rev* hub forces (a) and moments (b), $\left\{ EI_\beta = \overline{EI_\beta} + \Delta EI_\beta^{3p} \sin(3\psi + \phi),\ \ \Delta EI_\beta^{3p} = 0.15\overline{EI_\beta} \right\}$

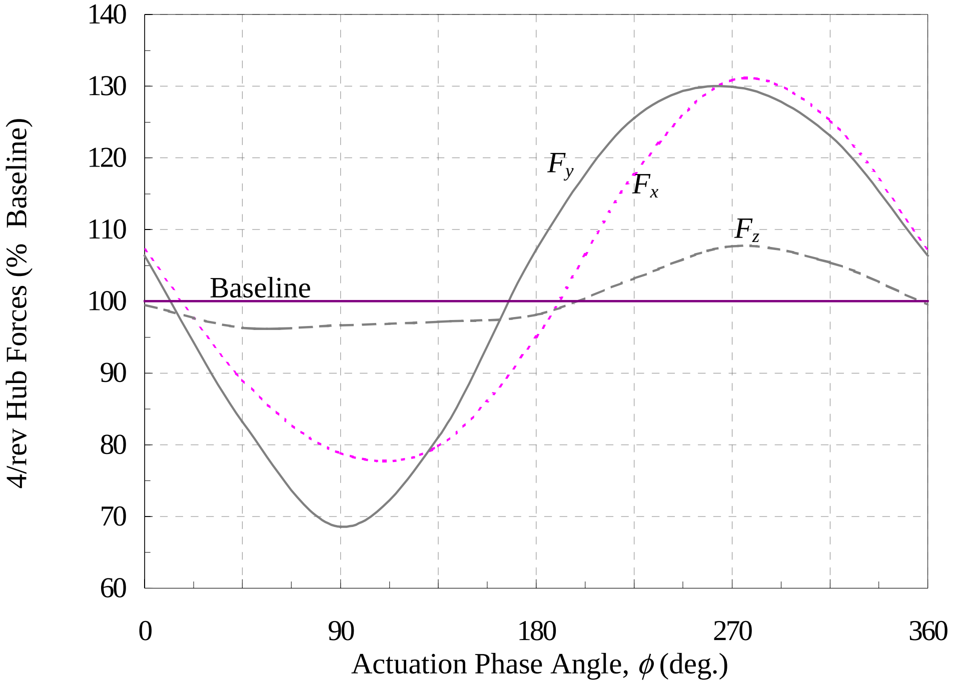

(a)

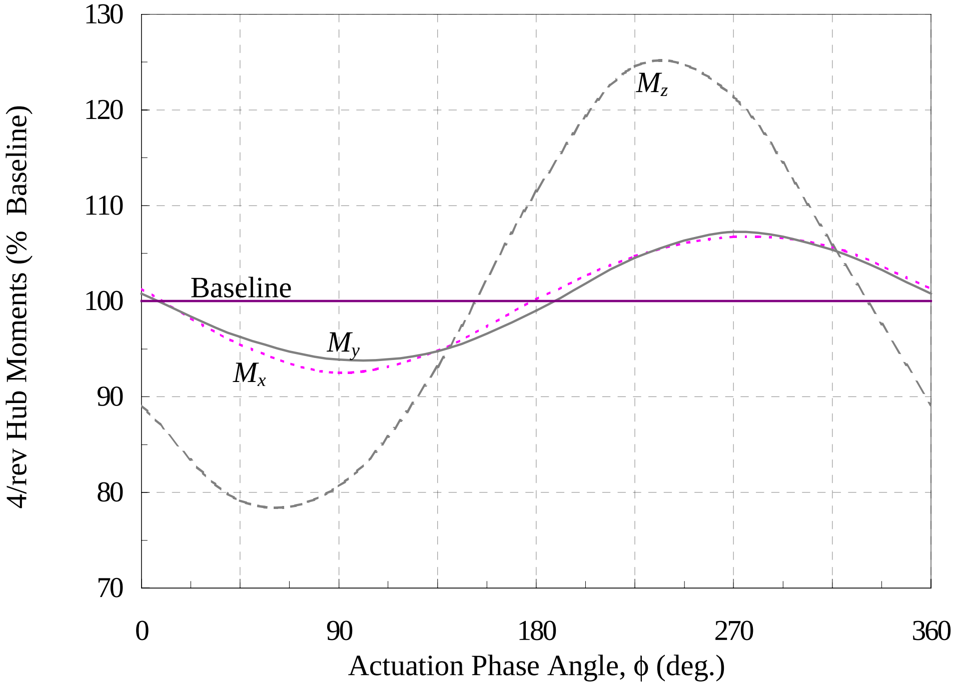

(b)

Figure 4.4: Influence of phase, ϕ, of 2/*rev* variation in lag stiffness on 4/*rev* hub forces (a) and moments (b), $\left\{ EI_\zeta = \overline{EI_\zeta} + \Delta EI_\zeta^{2p}\sin(2\psi+\phi),\ \ \Delta EI_\zeta^{2p} = 0.15\overline{EI_\zeta} \right\}$

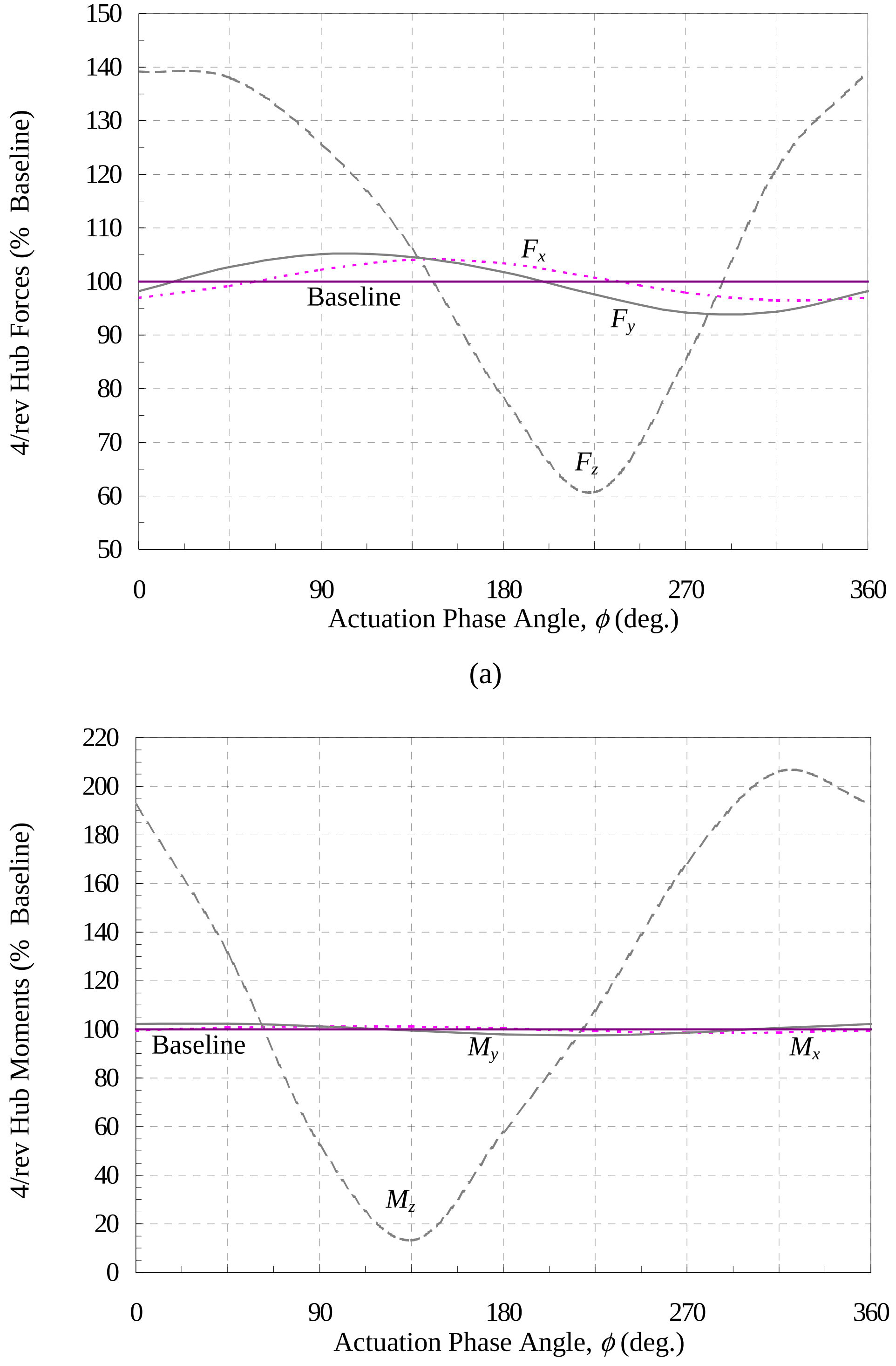

(a)

(b)

Figure 4.5: Influence of phase, ϕ, of 3/*rev* variation in lag stiffness on 4/*rev* hub forces (a) and moments (b), $\left\{ EI_\zeta = \overline{EI_\zeta} + \Delta EI_\zeta^{3p} \sin(3\psi + \phi),\ \ \Delta EI_\zeta^{3p} = 0.05\overline{EI_\zeta} \right\}$

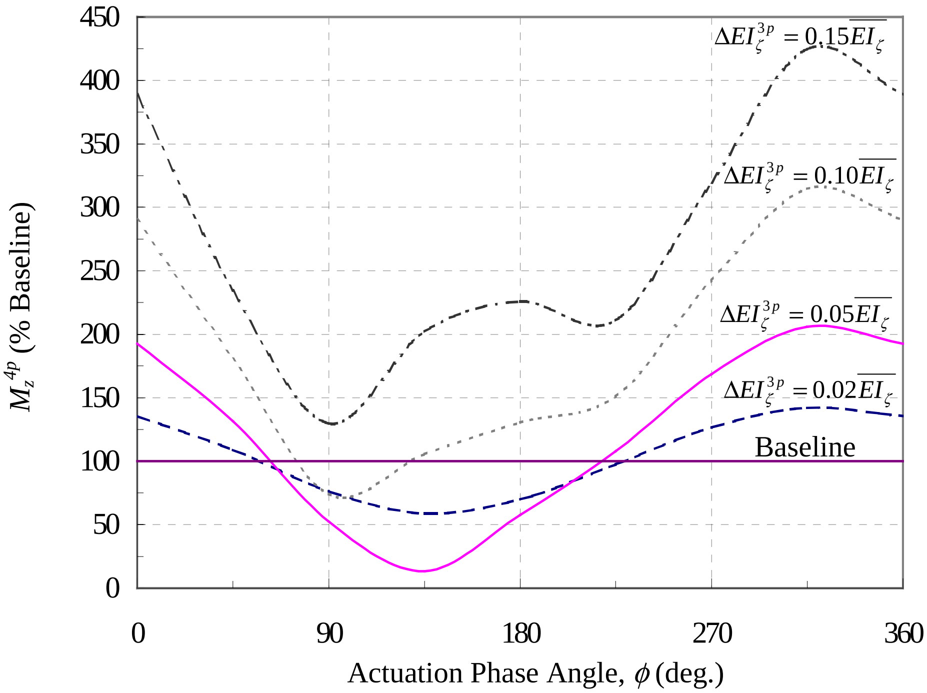

Figure 4.6a: Influence of magnitude of 3/*rev* variations in lag stiffness on vibratory hub torque

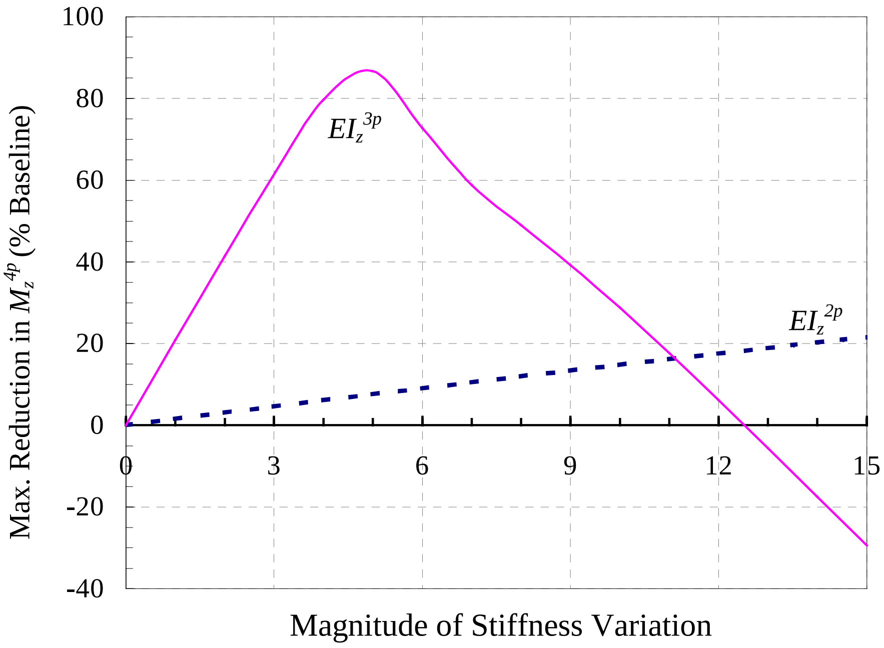

Figure 4.6b: Influence of magnitude of lag stiffness variations on vibratory hub torque

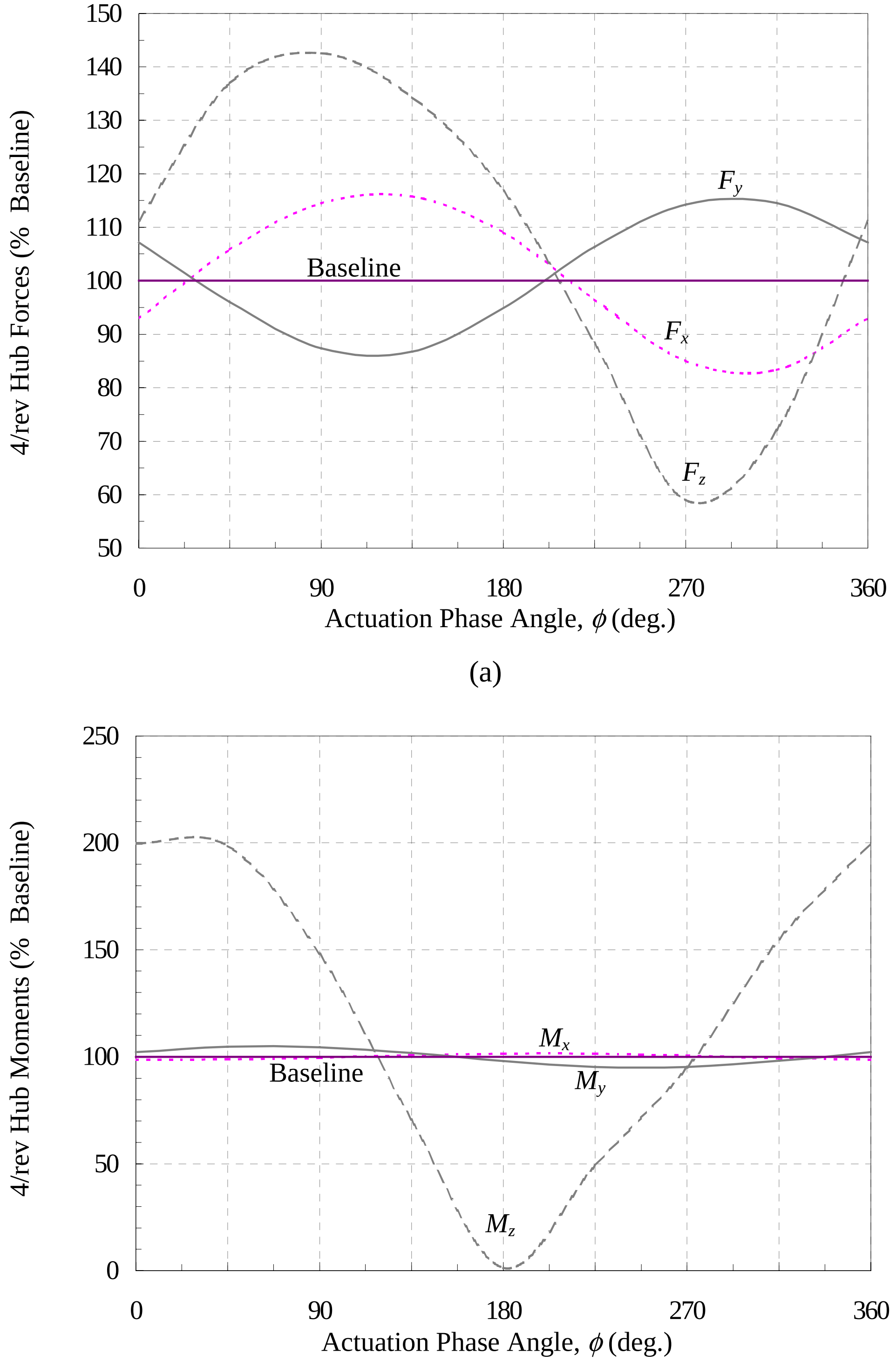

(a)

(b)

Figure 4.7: Influence of phase, ϕ, of 5/*rev* variation in lag stiffness on 4/*rev* hub forces (a) and moments (b), $\left\{ EI_\zeta = \overline{EI_\zeta} + \Delta EI_\zeta^{5p} \sin(5\psi + \phi), \ \ \Delta EI_\zeta^{5p} = 0.05\overline{EI_\zeta} \right\}$

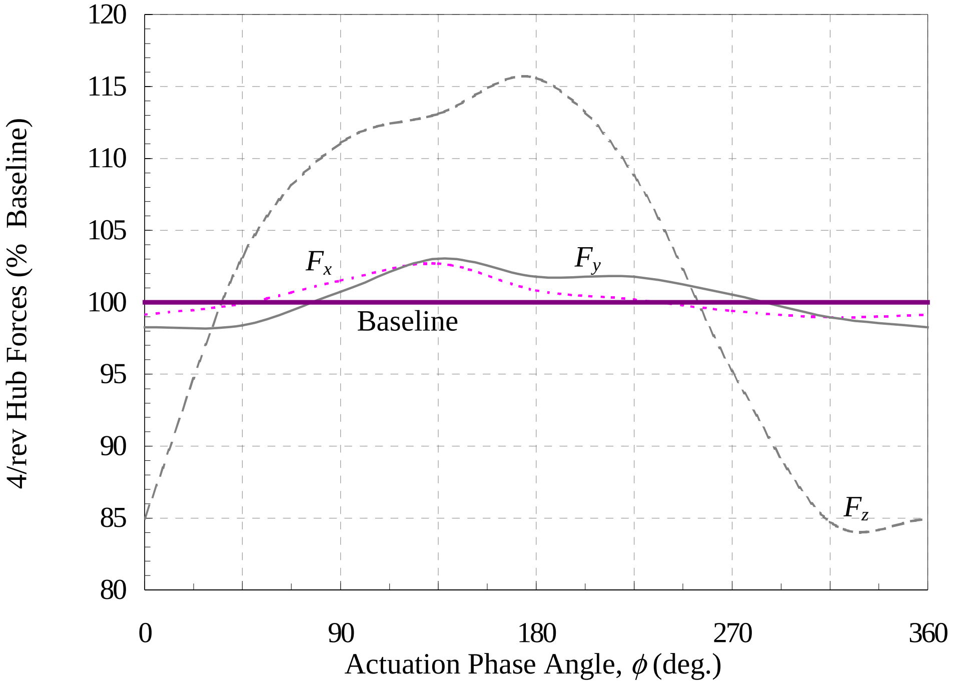

(a)

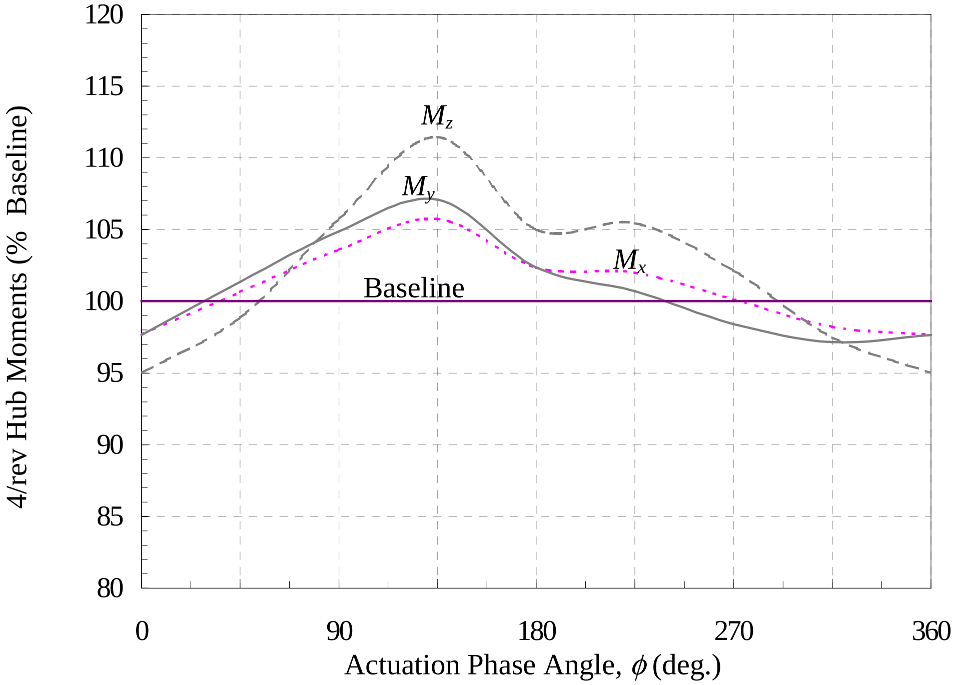

(b)

Figure 4.8: Influence of phase, ϕ, of 3*/rev* variation in torsion stiffness on 4/*rev* hub forces (a) and moments (b), $\left\{ GJ = \overline{GJ} + \Delta GJ^{3p}\sin(3\psi+\phi),\ \Delta GJ^{3p} = 0.15\overline{GJ} \right\}$

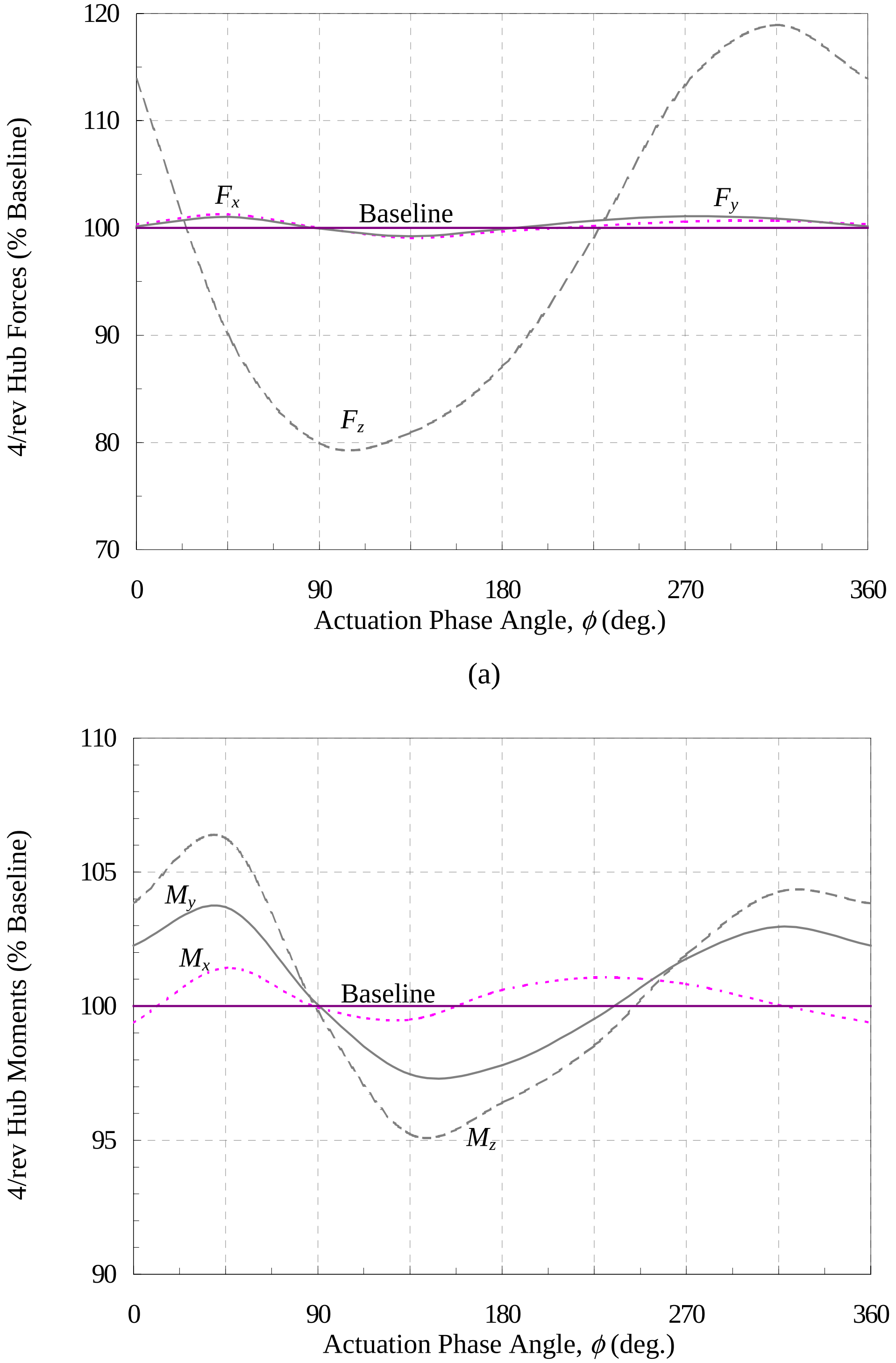

(a)

(b)

Figure 4.9: Influence of phase, ϕ, of 4/*rev* variation in torsion stiffness on 4/*rev* hub forces (a) and moments (b), $\left\{ GJ = \overline{GJ} + \Delta GJ^{4p} \sin(4\psi + \phi),\ \ \Delta GJ^{4p} = 0.15\overline{GJ} \right\}$

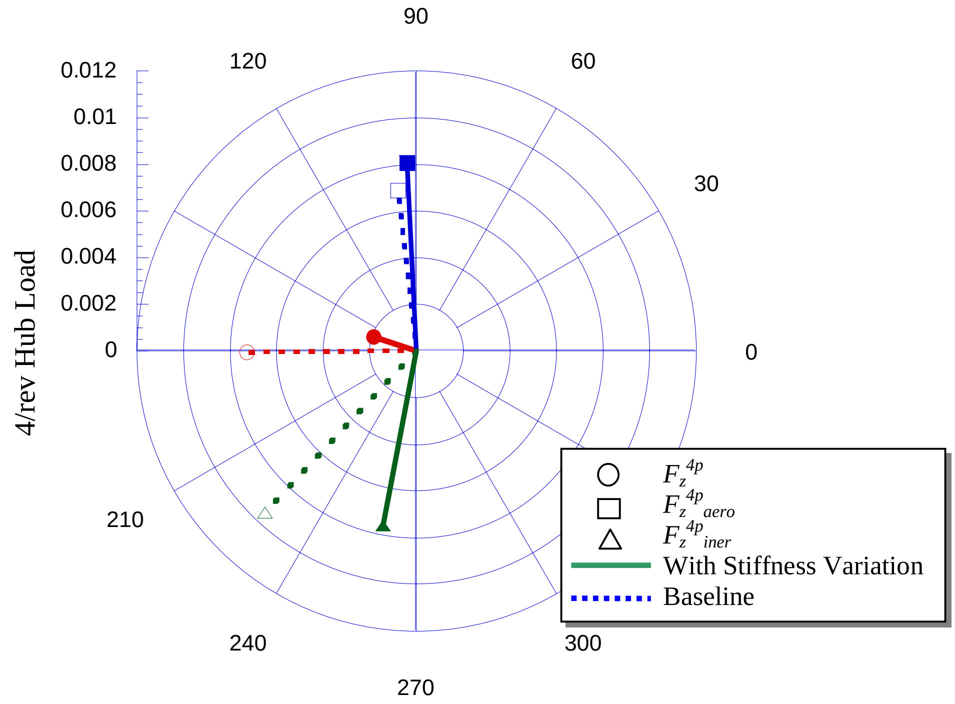

Figure 4.10: Change in 4/*rev* hub loads, F_z^{4p}, due to 2/*rev* variation in flap stiffness

$$\left\{ EI_\beta = \overline{EI}_\beta + \Delta EI_\beta^{2p}\sin(2\psi+\phi),\ \ \Delta EI_\beta^{2p} = 0.15\overline{EI}_\beta,\ \ \phi = 240^\circ \right\}$$

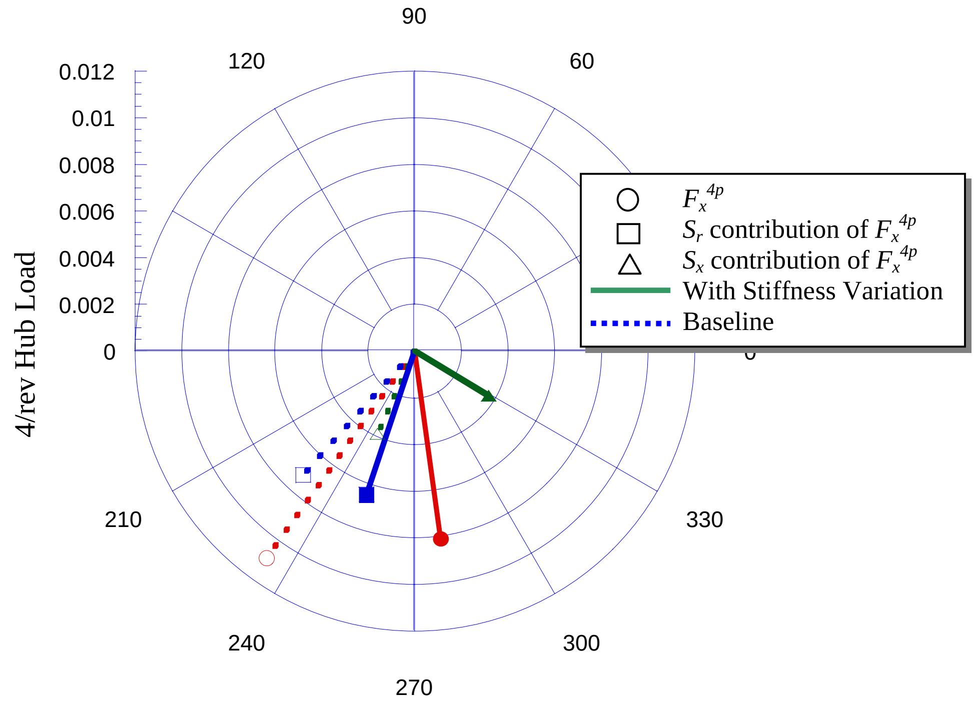

Figure 4.11: Change in contributions of hub load, F_x^{4p}, due to 3/*rev* variation in flap stiffness

$$\left\{ EI_\beta = \overline{EI}_\beta + \Delta EI_\beta^{3p}\sin(3\psi+\phi),\ \ \Delta EI_\beta^{3p} = 0.15\overline{EI}_\beta,\ \ \phi = 45^\circ \right\}$$

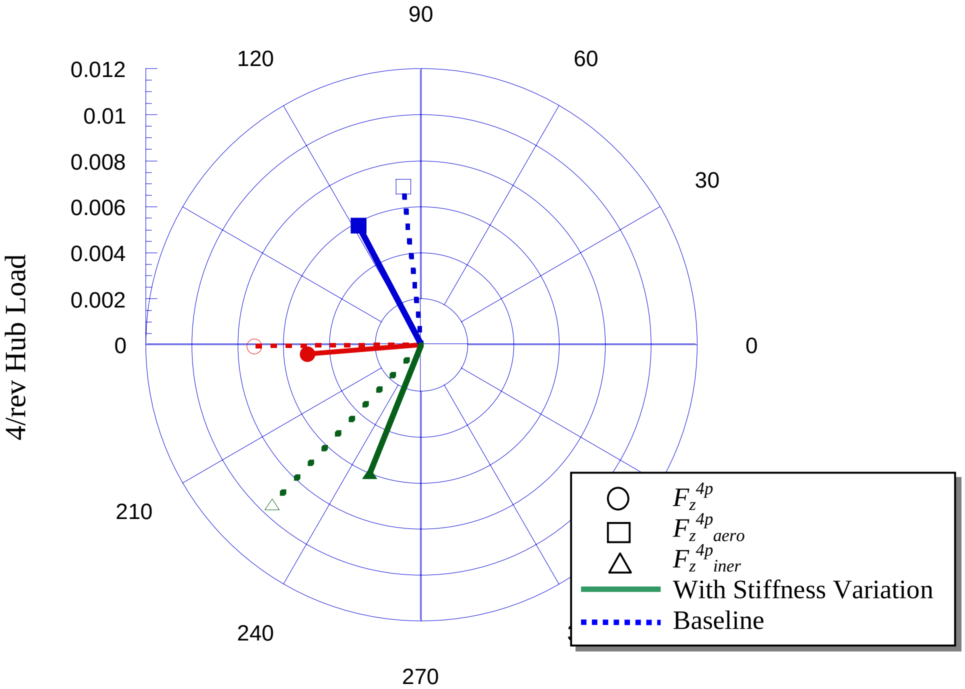

Figure 4.12: Change in 4/*rev* hub loads, F_z^{4p}, due to due to 3/*rev* variation in flap stiffness

$$\left\{ EI_\beta = \overline{EI_\beta} + \Delta EI_\beta^{3p}\sin(3\psi+\phi),\ \ \Delta EI_\beta^{3p} = 0.15\overline{EI_\beta},\ \ \phi = 45^\circ \right\}$$

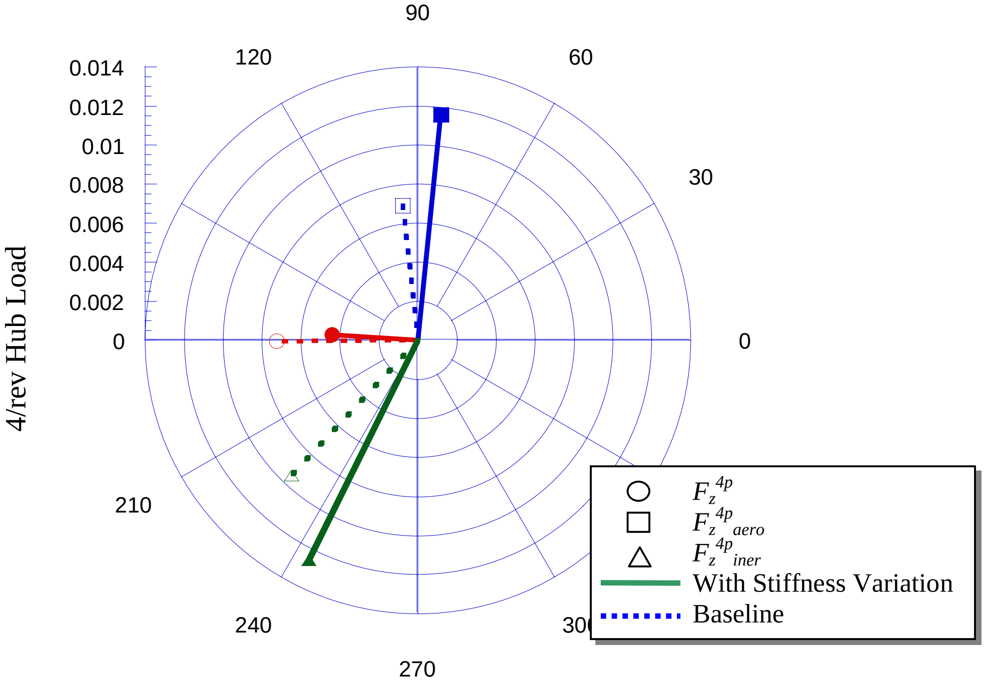

Figure 4.13: Change in 4/*rev* hub loads, F_z^{4p}, due to 3/*rev* variation in lag stiffness

$$\left\{ EI_\zeta = \overline{EI_\zeta} + \Delta EI_\zeta^{3p}\sin(3\psi+\phi),\ \ \Delta EI_\zeta^{3p} = 0.05\overline{EI_\zeta},\ \ \phi = 225^\circ \right\}$$

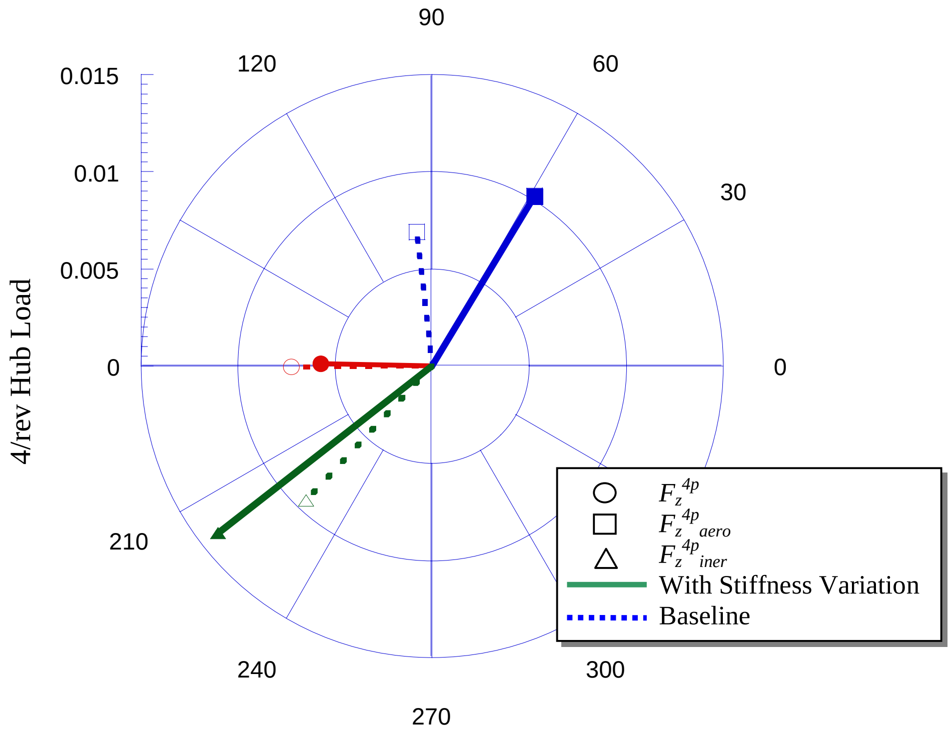

Figure 4.14: Change in 4/*rev* hub loads, F_z^{4p}, due to 4/*rev* variation in torsion stiffness

$$\left\{ GJ = \overline{GJ} + \Delta GJ^{4p}\sin(4\psi+\phi),\ \ \Delta GJ^{4p} = 0.15\overline{GJ},\ \ \phi = 100^{\circ} \right\}$$

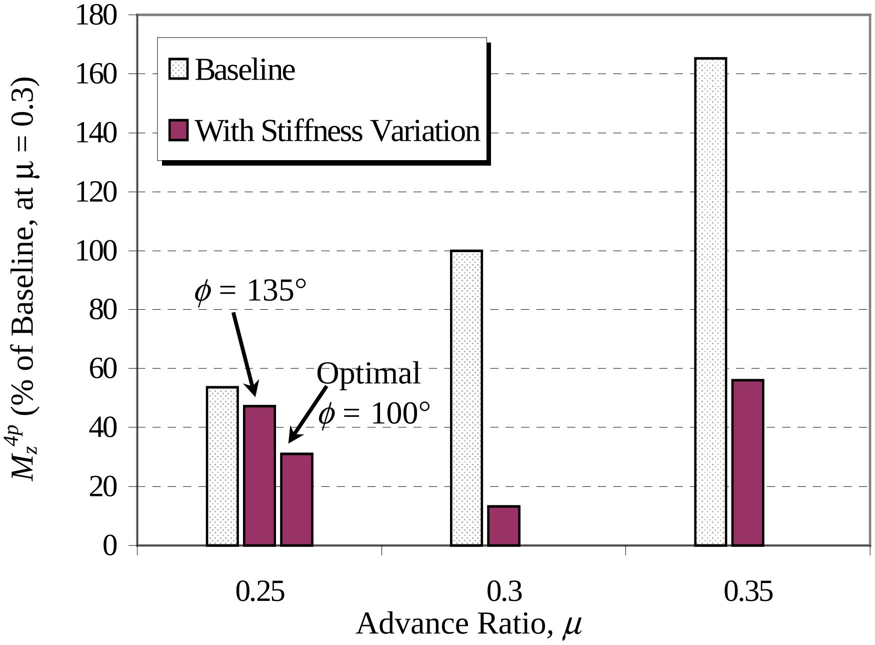

Figure 4.15: Reduction in M_z^{4p} at different advance ratios, due to 3/*rev* lag stiffness variation

$$\left\{ EI_{\zeta} = \overline{EI}_{\zeta} + \Delta EI_{\zeta}^{3p}\sin(3\psi+\phi),\ \Delta EI_{\zeta}^{3p} = 0.05\overline{EI}_{\zeta},\ \phi = 135^{\circ} \right\}$$

Vibratory Hub Loads[*]	
F_x^{4p}	1.0937
F_y^{4p}	1.0910
F_z^{4p}	0.7258
M_x^{4p}	8.3085
M_y^{4p}	8.6632
M_z^{4p}	6.5129

Table 4.1a: 4/*rev* vibratory hub loads for baseline rotor, no root element stiffness variation

Blade Root Loads	Harmonics[**]				
	1/*rev*	2/*rev*	3/*rev*	4/*rev*	5/*rev*
S_r	0.085114	0.008036	0.003606	0.001891	0.000092
S_x	0.072238	0.003599	0.001990	0.004815	0.000240
S_z	0.053513	0.039237	0.015058	0.001815	0.000483
M_ϕ	0.012710	0.004204	0.000335	0.000176	0.000029
M_β	0.192777	0.124387	0.042688	0.004195	0.001321
M_ζ	0.384243	0.018488	0.004317	0.016282	0.000898

Table 4.1b: Harmonics of blade root loads for baseline rotor, no root element stiffness variation

	Actuation Frequency (Magnitude)	Optimal Phase Angle, ϕ	Significant Changes in Vibratory hub loads	
			Decreases	Increases
Flap Stiffness Variation	2/*rev* (15%)	240°	F_z^{4p} (70%)	M_x^{4p} (20%), M_y^{4p} (10%)
	3/*rev* (15%)	0°	F_x^{4p}, F_y^{4p} (60%) F_z^{4p} (40%)	M_x^{4p} (20%)
		45°	M_x^{4p} (60%), M_y^{4p} (80%) F_x^{4p}, F_y^{4p} (30%) F_z^{4p} (30%)	M_z^{4p} (25%)
Lag Stiffness Variation	2/*rev* (15%)	90°	F_x^{4p}, F_y^{4p} (20-30%) M_z^{4p} (20%)	[***]
	3/*rev* (5%)	135°	M_z^{4p} (80%)	[***]
		225°	F_z^{4p} (40%)	[***]
	5/*rev* (5%)	200°	M_z^{4p} (80%)	[***]
Torsion Stiffness Variation	3/*rev* (15%)	320°	F_z^{4p} (15%)	[***]
	4/*rev* (15%)	100°	F_z^{4p} (20%)	[***]

Table 4.2: Summary of beneficial effects of stiffness variations on vibratory hub loads

---

[*] All vibratory hub forces are in % of F_z^0 (5940 lbs.), all vibratory hub moments are in % of M_z^0 (5244 ft-lbs.)

[**] Blade root shears are non-dimensionalized by $m_o\Omega^2R^2$, blade root moments are non-dimensionalized by $m_o\Omega^2R^3$

[***] Up to 10% increases in vibratory hub loads.

Blade Root Loads	Change in Harmonics (% Baseline)				
	1/*rev*	2/*rev*	3/*rev*	4/*rev*	5/*rev*
S_r	-0.28	-3.63	-1.52	-4.84	12.45
S_x	-0.24	8.86	-16.20	0.89	-11.67
S_z	1.44	8.31	12.69	-73.49	-63.48
M_ϕ	0.67	0.55	3.26	11.25	-22.11
M_β	-0.41	42.26	17.86	-34.22	-39.83
M_ζ	-0.26	-11.42	14.33	1.69	-5.75

Table 4.3a: Change in harmonics of blade root loads due to 2/*rev* variation in flap stiffness $\left\{ EI_\beta = \overline{EI_\beta} + \Delta EI_\beta^{2p} \sin(2\psi + \phi),\ \ \Delta EI_\beta^{2p} = 0.15\overline{EI_\beta},\ \ \phi = 240^\circ \right\}$

Blade Root Loads	Change in Harmonics (% Baseline)				
	1/*rev*	2/*rev*	3/*rev*	4/*rev*	5/*rev*
S_r	0.14	-5.52	-9.02	***87.89***	-64.65
S_x	0.00	-6.96	-6.46	36.37	30.09
S_z	1.29	-3.26	-23.66	-31.33	***133.68***
M_ϕ	0.14	-0.94	-20.60	22.62	18.05
M_β	-0.23	-6.25	-72.72	-2.86	***367.45***
M_ζ	0.00	7.33	18.65	24.02	***64.89***

Table 4.3b: Change in harmonics of blade root loads due to 3/*rev* variation in flap stiffness $\left\{ EI_\beta = \overline{EI_\beta} + \Delta EI_\beta^{3p} \sin(3\psi + \phi),\ \ \Delta EI_\beta^{3p} = 0.15\overline{EI_\beta},\ \ \phi = 45^\circ \right\}$

Blade Root Loads	Change in Harmonics (% Baseline)				
	1/*rev*	2/*rev*	3/*rev*	4/*rev*	5/*rev*
S_r	4.48	-1.26	-15.31	-20.98	***95.95***
S_x	5.31	-0.36	-43.88	-21.13	***98.19***
S_z	-1.16	0.21	-3.13	-3.31	-0.87
M_ϕ	-0.09	0.13	-59.47	-60.93	5.01
M_β	0.23	-0.15	-7.07	0.95	4.49
M_ζ	6.49	13.21	***207.14***	-19.34	***164.77***

Table 4.4a: Change in harmonics of blade root loads due to 2/*rev* variation in lag stiffness $\left\{ EI_\zeta = \overline{EI_\zeta} + \Delta EI_\zeta^{2p} \sin(2\psi + \phi),\ \ \Delta EI_\zeta^{2p} = 0.15\overline{EI_\zeta},\ \ \phi = 90^\circ \right\}$

Blade Root Loads	Change in Harmonics (% Baseline)				
	1/*rev*	2/*rev*	3/*rev*	4/*rev*	5/*rev*
S_r	-0.13	2.41	2.25	-38.37	40.71
S_x	-0.14	5.96	6.66	-72.63	-23.89
S_z	-0.06	-0.17	-0.04	6.03	-37.89
M_ϕ	-0.03	-0.04	-18.84	***99.69***	***276.22***
M_β	0.04	-0.58	0.27	11.96	-41.53
M_ζ	-0.18	9.96	-12.53	-86.70	-13.28

Table 4.4b: Change in harmonics of blade root loads due to 3/*rev* variation in lag stiffness

$$\left\{ EI_\zeta = \overline{EI_\zeta} + \Delta EI_\zeta^{3p}\sin(3\psi+\phi),\ \ \Delta EI_\zeta^{3p} = 0.05\overline{EI_\zeta},\ \ \phi = 135^\circ \right\}$$

Blade Root Loads	Change in Harmonics (% Baseline)				
	1/*rev*	2/*rev*	3/*rev*	4/*rev*	5/*rev*
S_r	0.13	2.74	0.21	***57.10***	***90.58***
S_x	0.16	8.64	-4.31	25.05	45.32
S_z	-0.09	0.38	-1.83	-39.29	-26.80
M_ϕ	-0.01	0.50	3.21	***75.73***	***64.85***
M_β	0.05	0.66	-1.50	-42.49	-26.06
M_ζ	0.20	31.78	33.99	7.66	***80.77***

Table 4.4c: Change in harmonics of blade root loads due to 3/*rev* variation in lag stiffness

$$\left\{ EI_\zeta = \overline{EI_\zeta} + \Delta EI_\zeta^{3p}\sin(3\psi+\phi),\ \ \Delta EI_\zeta^{3p} = 0.05\overline{EI_\zeta},\ \ \phi = 225^\circ \right\}$$

Blade Root Loads	Change in Harmonics (% Baseline)				
	1/*rev*	2/*rev*	3/*rev*	4/*rev*	5/*rev*
S_r	-0.01	0.14	0.20	-22.76	***563.21***
S_x	0.00	0.27	-0.50	-60.42	***579.04***
S_z	0.03	0.14	-0.96	5.56	-73.41
M_ϕ	0.00	0.10	-25.93	***111.85***	***304.38***
M_β	0.02	0.12	-1.08	16.78	-86.93
M_ζ	-0.01	-0.11	4.27	-75.04	***784.53***

Table 4.4d: Change in harmonics of blade root loads due to 5/*rev* variation in lag stiffness

$$\left\{ EI_\zeta = \overline{EI_\zeta} + \Delta EI_\zeta^{5p}\sin(5\psi+\phi),\ \ \Delta EI_\zeta^{5p} = 0.05\overline{EI_\zeta},\ \ \phi = 200^\circ \right\}$$

Blade Root Loads	Change in Harmonics of Blade Root Loads (% Baseline)				
	1/*rev*	2/*rev*	3/*rev*	4/*rev*	5/*rev*
S_r	0.00	0.26	-0.80	-1.84	32.47
S_x	0.00	0.57	-2.53	-2.88	-6.29
S_z	-0.05	0.19	-2.40	-15.83	6.78
M_ϕ	0.03	-0.54	-22.91	***258.13***	***586.79***
M_β	-0.05	0.14	-2.48	-18.77	9.80
M_ζ	0.00	0.27	-5.48	-2.97	-8.70

Table 4.5a: Change in harmonics of blade root loads due to 3/*rev* variation in torsion stiffness

$$\left\{ GJ = \overline{GJ} + \Delta GJ^{3p}\sin(3\psi + \phi),\ \Delta GJ^{3p} = 0.15\overline{GJ},\ \phi = 320^{\circ} \right\}$$

Blade Root Loads	Change in Harmonics of Blade Root Loads (% Baseline)				
	1/*rev*	2/*rev*	3/*rev*	4/*rev*	5/*rev*
S_r	0.04	0.18	-0.53	-0.14	-37.26
S_x	0.01	0.18	-0.64	-1.24	-11.76
S_z	0.08	0.20	-0.45	-20.88	-2.47
M_ϕ	0.17	0.41	-32.68	***295.43***	***1958.34***
M_β	0.07	0.35	-0.56	-25.26	-1.28
M_ζ	0.04	0.72	-4.02	-1.44	-12.35

Table 4.5b: Change in harmonics of blade root loads due to 4/*rev* variation in torsion stiffness

$$\left\{ GJ = \overline{GJ} + \Delta GJ^{4p}\sin(4\psi + \phi),\ \Delta GJ^{4p} = 0.15\overline{GJ},\ \phi = 100^{\circ} \right\}$$

Chapter 5

Optimal Control Study

The results presented in Chapter 4 clearly demonstrated that harmonic variations in root element stiffness could affect hub vibration levels. However, while a certain stiffness variation was most effective in reducing a particular component of hub load it often left other components unaffected, or even increased them. The present chapter applies the optimal semi-active control scheme developed in Chapter 3 to determine the amplitude and phase of multi-harmonic variation in flap, lag, and torsion stiffness for simultaneously reducing all components of hub vibration. Again, the effectiveness of optimal cyclic variations in blade root stiffness on hub vibration reduction is first examined at an advance ratio of 0.3, using Drees inflow model. Helicopter and rotor configurations are similar to that used in Chapter 4, with properties presented in Appendix H (Table H.1) and stiffness variations are achieved by varying root element stiffness cyclically (see Fig. 2.10 and Eq. 2.12). Five beam elements are used to model the rotor blade, and 6 modes (2 flap, 2 lag, and 2 torsion modes) are included in modal transformation. The baseline vibratory hub loads and blade root loads were already presented in Table 4.1a and 4.1b, respectively. The performance of the optimal control scheme is presented for; *(i)* a single harmonic case using 3/*rev* flap stiffness variation in Section 5.1, *(ii)* multi-harmonic cases using 2-3/*rev* flap and 3/*rev* lag stiffness variations in Section 5.2, and 2-3/*rev* variations of both flap and lag stiffness in Section 5.3. Both gradient and non-gradient based optimization methods are employed and the effect of penalty on semi-active inputs are examined as well. The effectiveness of the multi-harmonic stiffness variations is also evaluated for various rotor configurations (Section 5.4) and cruise speeds (Section 5.5). Section 5.6 summarizes the results presented in this chapter.

5.1 Optimal 3/*rev* flap stiffness variation

Using the gradient-based optimization method (presented in Section 3.1.1), optimal 3/*rev* flap stiffness variation is determined for maximum vibration reduction without any penalty on the semi-active input ($J = J_z$, $W_u = 0$). The amplitude of the optimal 3/*rev* flap stiffness variation is determined to be ΔEI_{β}^{3p} = 10.75% of the baseline flap stiffness, $\overline{EI}_{\beta}$, and the phase, $\phi = 22.5°$. Fig. 5.1 shows contours corresponding to constant values of the vibration index, J_z, versus cosine and sine components of the 3/*rev* flap stiffness variations. It is seen that the optimal solution yields a 65% reduction in vibration index, and the corresponding reductions in individual components of vibratory hub loads are shown in Fig. 5.2. From the figure it is seen that 40-60% reductions in the in-plane hub forces and moments, and 25-30% reductions in the vertical shear and hub torque are simultaneously achieved. Corresponding to the optimal 3/*rev* flap stiffness variation, the harmonics of blade root loads are calculated and summarized in Table 5.1. Small percentage increases in S_r^{4p} and M_{β}^{4p}, and larger percentage increases in S_z^{5p} and M_{β}^{5p} are observed. However, it should be noted that the baseline values for the 5th harmonic of all components of blade root loads are extremely small (see Table 4.1b).

5.2 Optimal 2,3/*rev* flap & 3/*rev* lag stiffness variations

Next, 2/*rev* and 3/*rev* flap stiffness variation and 3/*rev* lag stiffness variation is simultaneously considered for vibration reduction. Using the gradient-based minimization (described in Section 3.1.1) for maximum vibration reduction ($J = J_z$, $W_u = 0$), the optimal stiffness variations are presented in Table 5.2. For these optimal stiffness variations, the performance index, J_z, is reduced by a significant 91% (compared to the baseline). The reductions in individual components of vibratory hub loads are shown in Fig. 5.3 (55-65% reductions in F_x^{4p} and F_y^{4p}, a 70% reduction in F_z^{4p}, 75-80% reductions in M_x^{4p} and M_y^{4p}, and a 90% reduction in M_z^{4p} are observed). As expected, these reductions are significantly larger than those obtained using optimal 3/*rev* flap stiffness variations alone. However a large 2/*rev* flap stiffness variation was required (Table 5.2).

5.3 Optimal 2,3/*rev* Flap & Lag Stiffness Variations

Vibration reductions achieved using optimal flap (2/*rev* and 3/*rev*), and lag (2/*rev* and 3/*rev*) stiffness variations are presented in Fig. 5.4, now using both gradient (see Section 3.1.1) and non-gradient (see Section 3.1.2) based optimization methods. The objective function to be minimized, again, consists of only the components of vibratory hub loads, without any penalty on semi-active inputs ($J = J_z$, $W_u = 0$). The corresponding optimal stiffness variations are shown in Table 5.3a and Table 5.3b using gradient and non-gradient based optimizations, respectively.

Overall, the vibration reductions obtained are slightly larger than the corresponding reductions in the previous section without 2/*rev* lag stiffness variations (compare Fig. 5.3 to the results in Fig. 5.4 corresponding to gradient based optimization; and note also that J_z is reduced further from 8.92% to 7.34%). It is observed that the optimal stiffness variations obtained using non-gradient based optimization (Table 5.3b) are different from those determined through gradient-based optimization (Table 5.3a), and the optimal stiffness variations (from non-gradient based optimization) produces larger overall vibration reduction (evident from the lower value of performance index, J_z). This suggests that the gradient-based optimization located a local-minimum (as opposed to the global-minimum located using the non-gradient based approach). However, due to the nature of the non-gradient based optimization, the calculation time used is much longer than that of the gradient-based optimization. This would make it virtually unpractical to use the non-gradient based approach in an actual closed-loop adaptive controller. Both gradient as well as non-gradient based solutions yield large 2/*rev* flap stiffness variation, and the gradient-based approach further requires large 2/*rev* lag stiffness variation.

Due to large 2/*rev* stiffness variations requirement, the objective function is extended to include a penalty weighting on the semi-active inputs (W_u = I) in order to reduce the required semi-active inputs. As a result, the optimal stiffness variations are reduced significantly (Table 5.3c), without much of a penalty on the vibration reduction performance (see Fig. 5.5). Introduction of an input penalty reduces the optimal ΔEI_{ζ}^{2p} from 31% to 15% of the baseline lag stiffness (the vibration performance index is virtually unchanged). For many other cases similar results were obtained – significant reductions in required stiffness variations for relatively small reductions in performance, due to introduction of a penalty on control inputs (W_u = I). For the optimal stiffness variations of Table 5.3c with penalty on the input controls, the changes in harmonics of blade root loads (compared to the baseline) are summarized in Table 5.4. Although large percentage increases are seen in M_{ϕ}^{4p}, and most of the 5/*rev* components of blade root loads, the baseline values for harmonics of the blade root pitching moment, and the 5/*rev* components of all root loads are very small (Table 4.1b).

5.4 Influence of Baseline Stiffness on Effectiveness of Vibration Control

Sections 5.1-5.3 established the effectiveness of multi-cyclic variations in flap and lag stiffness for reduction of vibrations of the baseline configuration whose properties are given in Table H.1.

The present section examines the effectiveness of optimal 2, 3/*rev* flap and lag stiffness variations (determined using gradient based optimization with input penalty, W_u = I) for different rotor configurations. Specifically, the rotor flap, lag, and torsion stiffness (and correspondingly, the flap, lag, and torsion frequencies) are individually varied, and the effectiveness of cyclic stiffness variations to reduce vibration are re-examined.

Figure 5.6 shows the hub vibration index, J_z, for variation in fundamental flap stiffness (lag frequency). As the blade baseline flap stiffness, $\overline{EI}_\beta$, (and flap frequency) decreases, the vibration index (without cyclic stiffness variation) initially increases by 30% but then decreases once the first flap frequency is reduced below 1.125/*rev*. This peak vibration coincides with the second natural flap frequency passing through 3/*rev*. With optimal 2/*rev* and 3/*rev* flap and lag stiffness variations (determined using gradient based optimization, with input constraint) vibration levels are reduced significantly over the entire range of flap frequency variation (vibration index, J_z, seen to be less than 8% in Fig. 5.6). The stiffness variation (input effort) required does not show great sensitivity to flap frequency variation (as seen by the fact that J_u remains relatively unchanged).

For variation in blade lag stiffness (lag frequency), Figure 5.7 shows the effectiveness of the stiffness variations in reducing hub vibration. As the blade baseline lag stiffness, $\overline{EI}_\zeta$, (and lag frequency) decreases, the vibration index (with no cyclic stiffness variation) increases sharply when the first natural lag frequency is around 0.7/*rev*. This sharp vibration peak occurs due to the second natural lag frequency passing through 4/*rev*, and is exacerbated by the low damping in the lag mode. With optimal 2/*rev* and 3/*rev* flap and lag stiffness variations, it is seen in Fig. 5.7 that vibration levels are reduced significantly over the entire range of lag frequency (even around the aforementioned resonance). Furthermore, the stiffness variation (input effort) required does not show great sensitivity to lag frequency variation (J_u remains relatively uniform).

Figure 5.8 indicates that variation in the blade torsion stiffness, *GJ*, (corresponding to a torsion frequency variation between 3/*rev* and 5/*rev*) does not produce any significant changes in baseline vibration index (in the absence of stiffness variations). With optimal 2/*rev* and 3/*rev* flap and lag stiffness variations, vibration levels are reduced by over 90%, over the entire range, with the stiffness variation (input effort) required, once again showing little sensitivity to torsion frequency variation (J_u relatively uniform).

5.5 Effectiveness of Vibration Controller at Different Forward Speed

This section examines the effectiveness of optimal 2, 3/*rev* flap and lag stiffness variations, determined by gradient based optimization method with input penalty, on reducing vibration at different forward speeds. Figure 5.9 shows the hub vibration index, J_z, over forward speeds ranging from advance ratio 0.25 to 0.35. It is seen that as the advance ratio increases, the baseline vibrations (without cyclic stiffness variation) increase dramatically; with the index J_z increasing from 30% to 275% of the value at advance ratio 0.3. However, with optimal 2/*rev* and 3/*rev* flap and lag stiffness variations, the vibration index, J_z, is much smaller (well below 20%) and shows a much milder increase with advance ratio. It should be noted that in Fig. 5.9, the optimal stiffness variations are recomputed at different forward speeds. The input effort index, J_u, shows only a mild increase with advance ratio suggesting that there should be no actuator saturation problem at higher speeds.

5.6 Summary on optimal control of root element stiffness variation

The semi-active optimal control scheme (using gradient and non-gradient based optimization) is successful in producing optimal root element stiffness variation that significantly reduces all components of hub vibrations. The required stiffness variations can be reduced (without significantly compromising performance) by introducing a penalty on the semi-active input in the objective function. Reductions in the vibration performance index of over 90% are seen with optimal multi-cyclic 2/*rev* and 3/*rev* combined flap and lag stiffness variations. Multi-cyclic flap and lag stiffness variations are seen to be effective in reducing hub vibration even when the fundamental rotor properties (such as fundamental flap, lag, and torsion frequencies) are changed. Additionally, the multi-cyclic flap and lag stiffness variations are effective in reducing vibration at various forward speeds, without significant increase in the stiffness variation inputs.

However, it should be noted that while root element stiffness variation would be effective in reducing vibration , the only way to practically realize it would be through the introduction of discrete controllable stiffness devices in the blade root region.

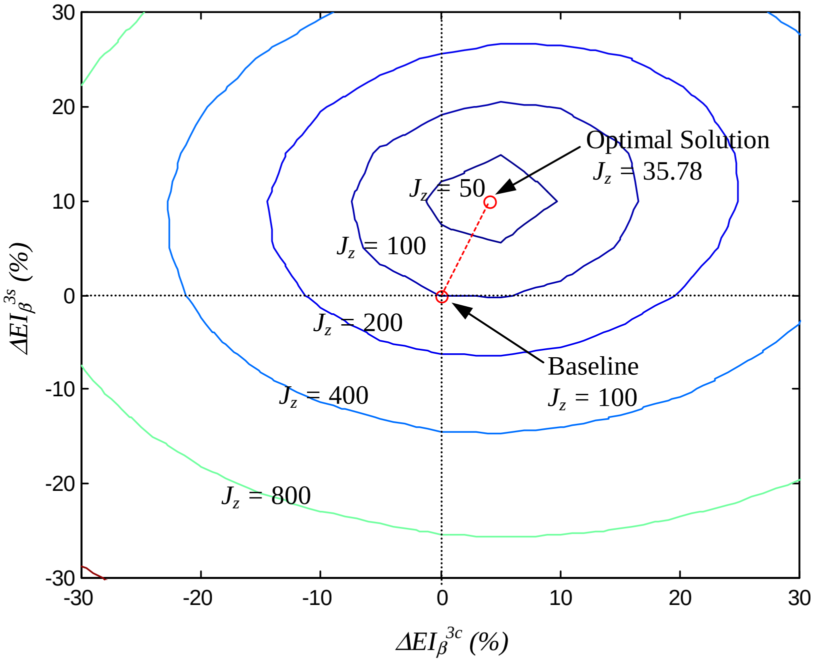

Figure 5.1: Contour plot of performance index, *J*, (% Baseline) due to 3/*rev* flap stiffness variation

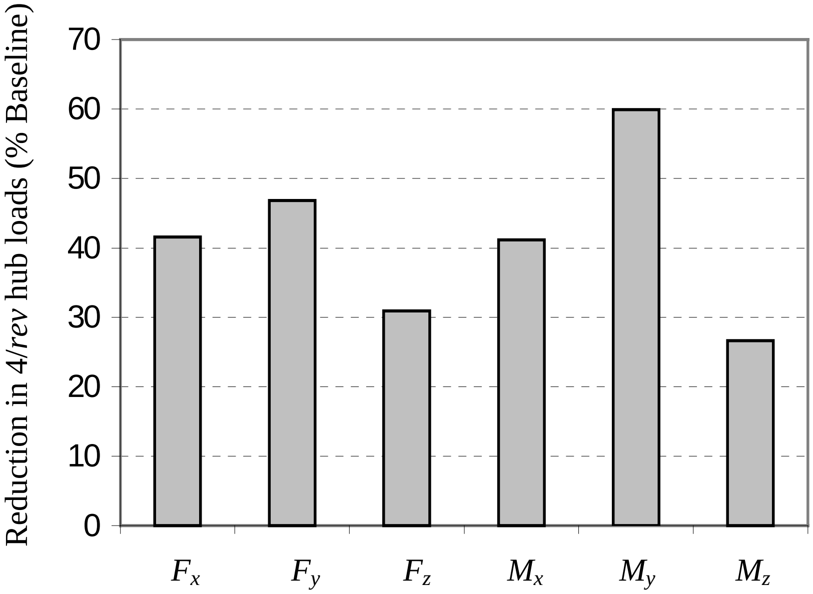

Figure 5.2: Hub vibration reduction due to optimal 3/*rev* flap stiffness variation

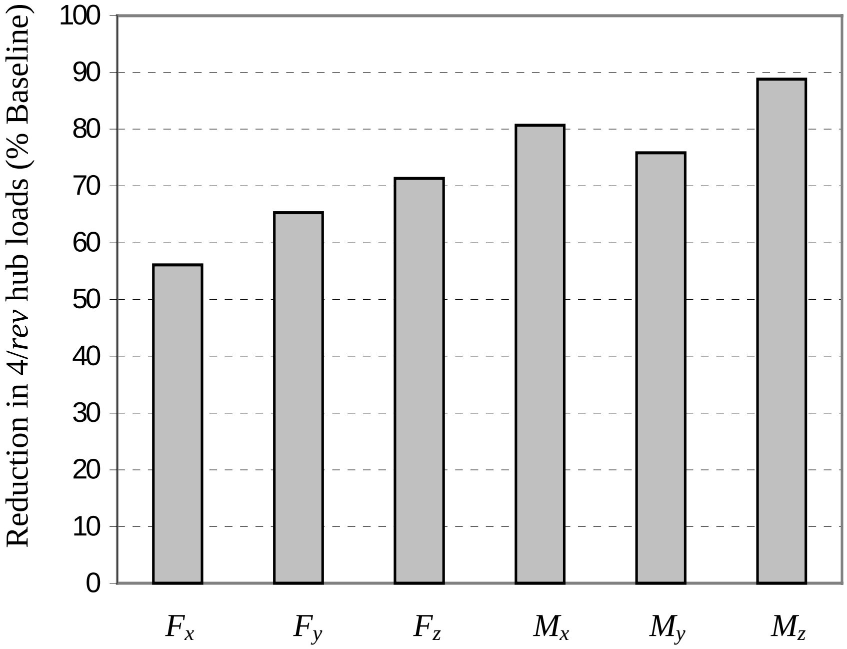

Figure 5.3: Hub vibration reduction due to optimal 2,3/*rev* flap and 3/*rev* lag stiffness variations

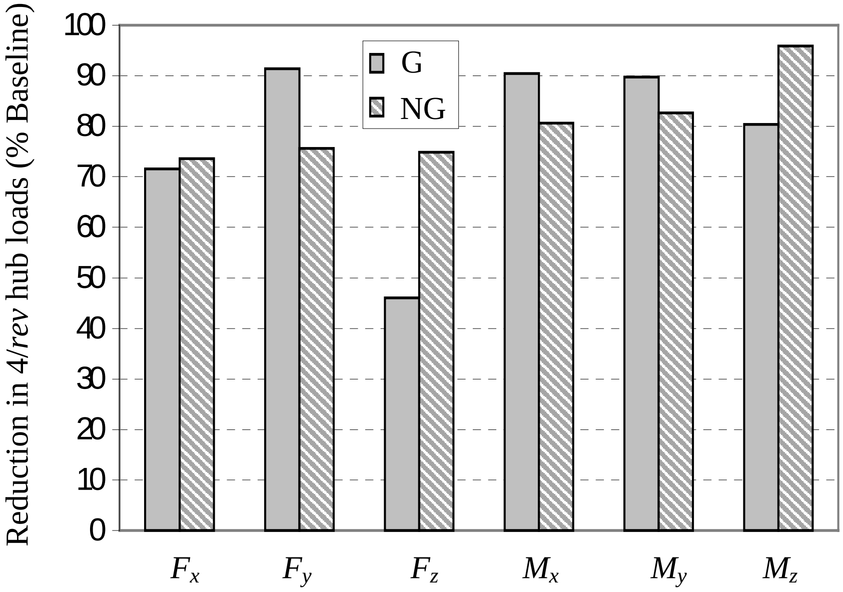

Figure 5.4: Hub vibration reduction due to optimal 2,3/*rev* flap and lag stiffness variations with gradient based (G) and non-gradient based (NG) optimizations

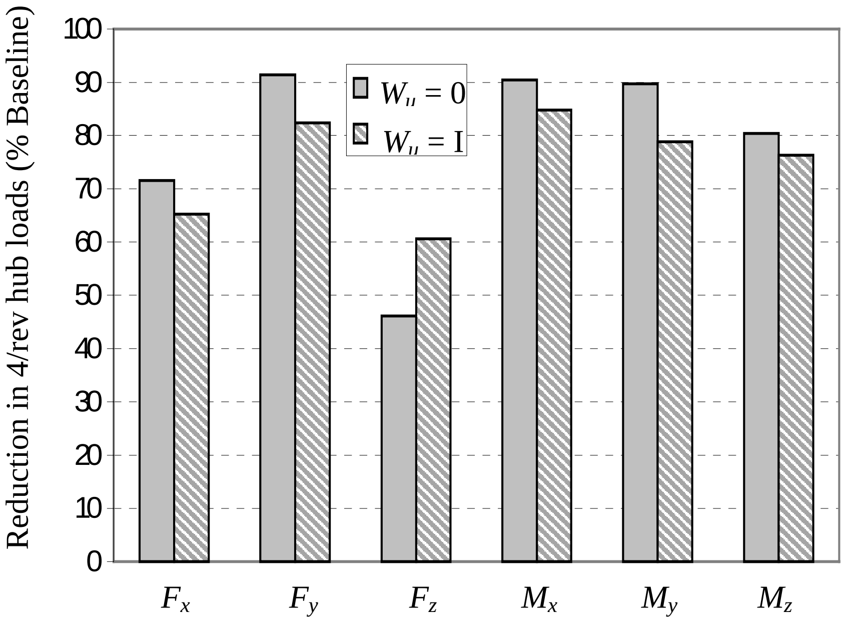

Figure 5.5: Hub vibration reduction due to optimal 2,3/*rev* flap and lag stiffness variations with (W_u = I) and without (W_u = 0) input penalty

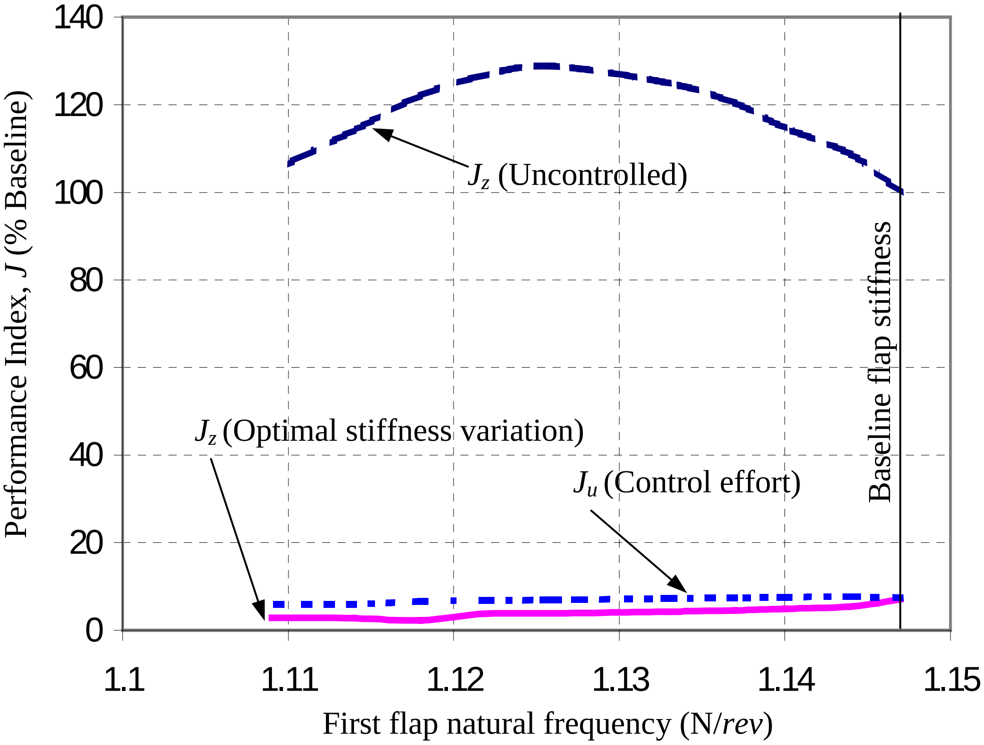

Figure 5.6: Effectiveness of optimal 2,3/*rev* flap and lag stiffness variations for different values of blade flap stiffness (flap natural frequency)

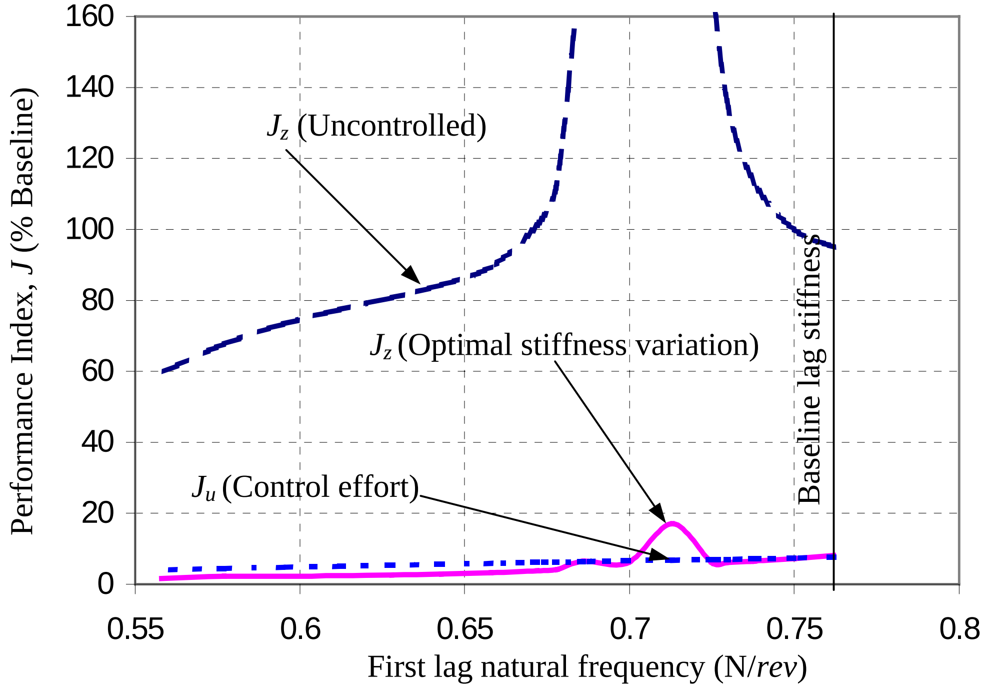

Figure 5.7: Effectiveness of optimal 2,3/*rev* flap and lag stiffness variations for different values of blade lag stiffness (lag natural frequency)

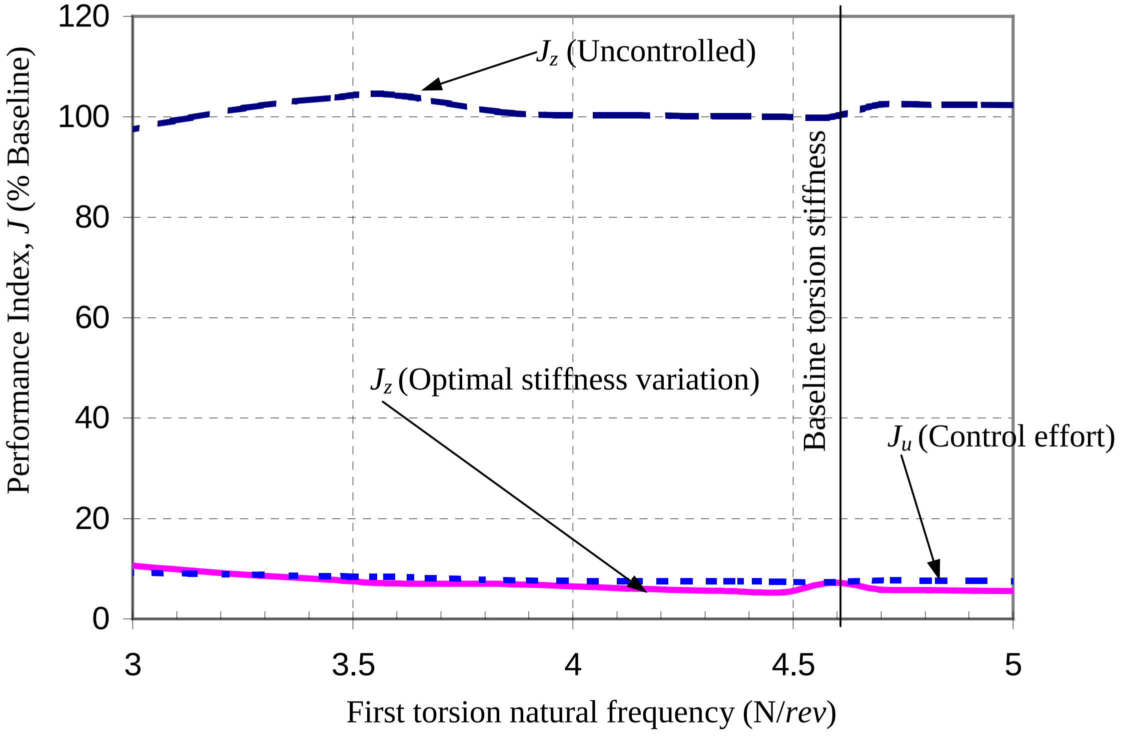

Figure 5.8: Effectiveness of optimal 2,3/*rev* flap and lag stiffness variations for different values of blade torsion stiffness (torsion natural frequency)

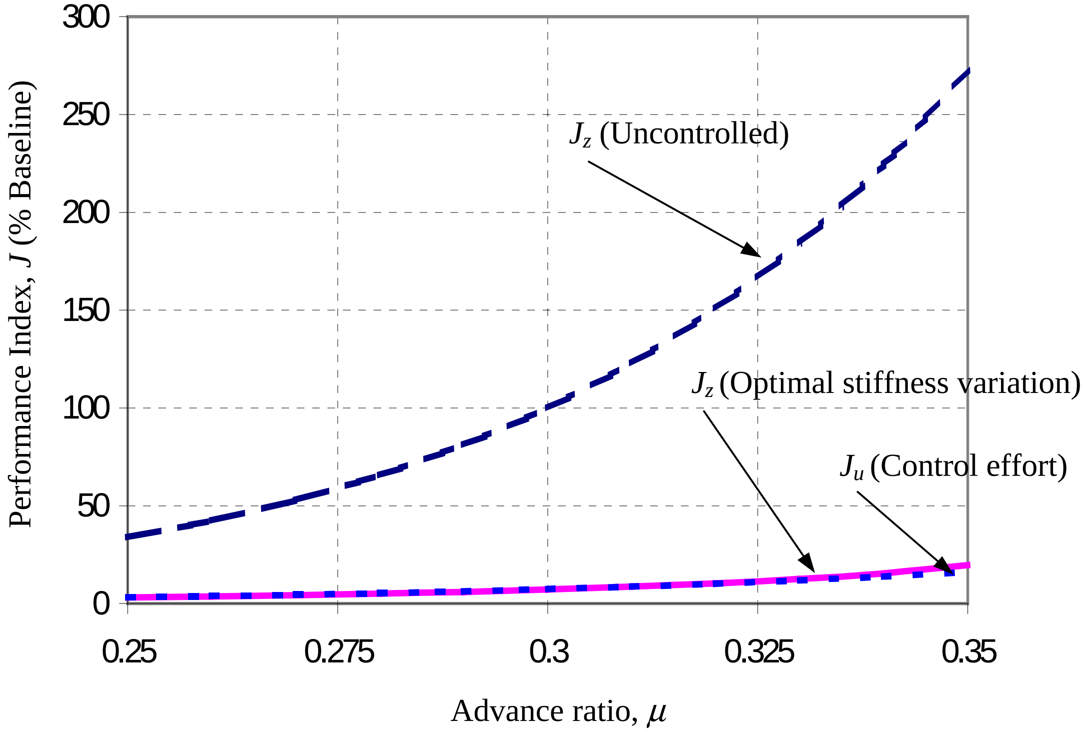

Figure 5.9: Effectiveness of optimal 2,3/*rev* flap and lag stiffness variations for different advance ratios

Blade Root Loads	Change in Harmonics (% Baseline)				
	1/*rev*	2/*rev*	3/*rev*	4/*rev*	5/*rev*
S_r	-0.03	-3.35	-19.73	24.45	-38.55
S_x	-0.12	-2.13	-62.01	-17.08	-33.41
S_z	0.70	-1.94	-61.32	-30.92	59.58
M_ϕ	0.09	-1.20	-12.75	-27.71	-14.74
M_β	-0.02	-3.83	-50.76	11.19	231.91
M_ζ	-0.11	4.72	-55.01	-26.62	-3.01

Table 5.1: Change in harmonics of blade root loads due to optimal 3/*rev* flap stiffness variation

Input		Amplitude	Phase
Flap stiffness variation	2/*rev*	$\Delta EI_\beta = 23\ \%\ \overline{EI}_\beta$	-111°
	3/*rev*	$\Delta EI_\beta = 15\ \%\ \overline{EI}_\beta$	31°
Lag stiffness variation	3/*rev*	$\Delta EI_\zeta = 8\ \%\ \overline{EI}_\zeta$	42°

Table 5.2: Optimal 2, 3/*rev* flap and 3/*rev* lag stiffness variations ($J_z = 8.92$)

Input		Amplitude	Phase
Flap stiffness variation	2/*rev*	$\Delta EI_\beta = 22\ \%\ \overline{EI}_\beta$	-102°
	3/*rev*	$\Delta EI_\beta = 14\ \%\ \overline{EI}_\beta$	48°
Lag stiffness variation	2/*rev*	$\Delta EI_\zeta = 31\ \%\ \overline{EI}_\zeta$	45°
	3/*rev*	$\Delta EI_\zeta = 8\ \%\ \overline{EI}_\zeta$	47°

Table 5.3a: Optimal 2, 3/*rev* flap and lag stiffness variations using gradient based optimization, without input penalty ($W_k = 0$), ($J_z = 7.34$)

Input		Amplitude	Phase
Flap stiffness variation	2/*rev*	$\Delta EI_\beta = 23\ \%\,\overline{EI}_\beta$	-125°
	3/*rev*	$\Delta EI_\beta = 14\ \%\,\overline{EI}_\beta$	27°
Lag stiffness variation	2/*rev*	$\Delta EI_\zeta = 9\ \%\,\overline{EI}_\zeta$	66°
	3/*rev*	$\Delta EI_\zeta = 7\ \%\,\overline{EI}_\zeta$	41°

Table 5.3b: Optimal 2, 3/*rev* flap and lag stiffness variations using non-gradient based optimization, without input penalty ($W_k = 0$), ($J_z = 3.55$)

Input		Amplitude	Phase
Flap stiffness variation	2/*rev*	$\Delta EI_\beta = 18\ \%\,\overline{EI}_\beta$	-108°
	3/*rev*	$\Delta EI_\beta = 13\ \%\,\overline{EI}_\beta$	37°
Lag stiffness variation	2/*rev*	$\Delta EI_\zeta = 15\ \%\,\overline{EI}_\zeta$	59°
	3/*rev*	$\Delta EI_\zeta = 6\ \%\,\overline{EI}_\zeta$	44°

Table 5.3c: Optimal 2, 3/*rev* flap and lag stiffness variations using gradient based optimization with input penalty ($W_k = I$)

Blade Root Loads	Change in Harmonics (% Baseline)				
	1/*rev*	2/*rev*	3/*rev*	4/*rev*	5/*rev*
S_r	1.62	-11.57	-34.60	-65.57	160.51
S_x	2.04	0.77	-22.39	-86.37	194.45
S_z	1.75	5.60	-26.26	-60.63	77.53
M_ϕ	0.58	-2.06	-50.34	112.65	66.93
M_β	-0.28	43.44	-83.15	25.06	167.71
M_ζ	2.12	-18.61	40.85	-76.33	254.16

Table 5.4: Change in harmonic of blade root loads due to the optimal 2,3/*rev* flap and lag stiffness variations ($W_k = I$)

Chapter 6

Discrete Controllable Stiffness Devices

The results in Chapters 4 and 5 illustrated that if the stiffness of the blade root region is cyclically varied, it will be effective in reducing helicopter hub vibration. The current chapter takes a step toward practical implementation of the concept by introducing discrete controllable stiffness devices (see Fig. 2.11) to control the effective stiffness of the blade root region. The rotor blade is modeled using five beam elements, with 6 modes (2 flap, 2 lag, and 2 torsion modes) included in modal transformation. Optimal device stiffness variations are calculated using the optimal semi-active control scheme developed in Chapter 3 through gradient based optimization method. The effectiveness of discrete controllable stiffness devices in reducing hub vibration is investigated first at a moderate advance ratio of 0.3, using Drees inflow model. The flap and lag controllable stiffness devices are modeled using the dual spring model (see Section 2.2.2.1, and Figs. 2.12a-2.12b), and the torsion discrete controllable stiffness device is modeled using the single spring model (see Section 2.2.2.2 and Fig. 2.13c). The stiffness variations are achieved by varying the stiffness of discrete devices cyclically (Eq. 2.15 and Eq. 2.16). Baseline configuration is presented in Section 6.1. The performance of optimal stiffness variation using flap, lag, and torsion controllable stiffness devices is examined individually in Sections 6.2, 6.3, and 6.4, respectively. Based on the performance of each individual device, Section 6.5 evaluates performance of optimal vibration control using combined controllable stiffness devices. Sections 6.6 and 6.7, respectively, demonstrate the effectiveness of the vibration control system for variations in baseline configuration and cruise speed. Summary of the results is presented in Section 6.8.

6.1 Baseline configuration

Helicopter and rotor configurations are similar to that used in Chapters 4 and 5, with properties presented in Appendix H (Table H.1). The only exception is that the stiffness of the flexure are reduced to compensate for the stiffness provided by the discrete controllable stiffness devices (see Table 6.1 for properties of flexure and the controllable stiffness devices). For this configuration, the baseline vibratory hub loads and blade root loads are given in Tables 6.2 (for advance ratios of 0.3 and 0.35). The baseline vibratory hub loads, shown in Table 6.2a, corresponds to the baseline vibration performance index, J_z = 100, to which all results in this chapter are compared.

6.2 Optimal 2,3/*rev* flap stiffness variations

Using only the controllable flap stiffness device (see Fig. 2.12a), 2/*rev* and 3/*rev* variations in translational flap spring stiffness, K_w, is considered through Eq. 2.15 (corresponding change in rotational flap spring stiffness, $K_{w'}$, are obtained through Eq. 2.16). The optimal amplitudes and phases of the 2,3/*rev* flap spring stiffness variations, calculated using the gradient based optimization procedure in Chapter 3, are summarized in Table 6.3. For these optimal stiffness variations, the output vibration index, J_z, is reduced by 76% as compared to its baseline value. The corresponding reductions in individual components of hub loads are shown in Fig. 6.1 (55-60% reduction in F_x^{4p} and F_y^{4p}, 75% reduction in F_z^{4p}, 45-50% reduction in M_x^{4p} and M_y^{4p}, and a 30% reduction in M_z^{4p} are observed).

6.3 Optimal 2,3/*rev* lag stiffness variations

Next, the controllable lag stiffness device is used (see Fig. 2.12b), and the 2/*rev* and 3/*rev* variations in translational and rotational lag spring stiffness, K_v and $K_{v'}$, are introduced using Eq. 2.15 and 2.16, respectively. The optimal lag spring stiffness variation inputs are shown in Table 6.4. For these spring stiffness variations, the vibration reduction achieved are presented in Fig. 6.2. 30% reductions in vibratory hub forces as well as a 40% reduction in M_z^{4p} are observed. The output vibration index, J_z, is decreased by 40%, however a large 2/*rev* lag stiffness variation is required.

6.4 Optimal 3,4/*rev* torsion stiffness variations

Optimal 3/*rev* and 4/*rev* variations in torsion spring stiffness are examined, using a controllable torsion stiffness device (Fig. 2.13c). Optimal torsion stiffness variation is presented in Table 6.5.

These stiffness variations produce only a 9% reduction in vibration index, J_z, which corresponds to individual reduction in components of hub loads shown in Fig. 6.3. Figure 6.3 shows that only F_z^{4p} is affected by the torsion stiffness variations and is reduced by 16%. This corroborates the observations in the sensitivity studies in Section 4.1.3. Due to the relative ineffectiveness of the torsion stiffness variation, it is not pursued further.

6.5 Optimal 2,3/*rev* flap and lag stiffness variations

Based on the promising performance of the flap and lag spring stiffness variations (presented in Sec. 6.2 - 6.3), they are examined in further vibration reduction studies. Hub vibration reduction achieved with optimal 2/*rev* and 3/*rev* flap, and 2/*rev* and 3/*rev* lag spring stiffness variations are presented in Fig. 6.4 and the corresponding optimal inputs are shown in Table 6.6. These optimal stiffness variations produce an 85% reduction in vibration index, which corresponds to 55-75% reductions in individual components of the vibratory hub loads. Corresponding changes in blade root loads are calculated and summarized in Table 6.7. A moderate percentage increase in M_β^{2p}, and large percentage increases in M_ϕ^{4p}, S_z^{5p}, and M_β^{5p} are observed. However, it should be noted that the baseline values for M_ϕ^{4p} and the 5th harmonic of all components of blade root loads are extremely small (see Table 6.2b).

6.6 Influence of flexure stiffness on effectiveness of vibration control

The effectiveness of the combined flap and lag spring stiffness variations for vibration reduction was demonstrated in Section 6.5 for the baseline configuration (properties are given in Table 6.1). The present section examines the effectiveness of the combined flap and lag spring stiffness variation in reducing vibration when blade structural properties change, especially the flexure stiffness. Without modifying the controllable device, the flap, lag, and torsion flexure stiffness are individually varied by ± 25% of their baseline values, and the effectiveness of the 2,3/*rev* flap and lag spring stiffness variations are re-examined.

Figures 6.5, 6.6, and 6.7 show effectiveness of the 2,3/*rev* flap and lag spring stiffness variations and uncontrolled vibration index when the flap, lag, and torsional flexure stiffness are varied, respectively. Overall, the multi-cyclic semi-active controller retains its effectiveness (producing over 80% reduction in vibration index, J_z) over the ranges of variations in root flap, lag, and torsion stiffness. Additionally, the control effort index, J_u, shows little sensitivity to the changes in the flexure stiffnesses.

6.7 Effectiveness of vibration controller at different forward speed

This section examines the effectiveness of the 2/*rev* and 3/*rev* flap and lag spring stiffness variation for vibration reduction at different forward speeds. Figure 6.8 shows the hub vibration index, J_z, over forward speed ranging from advance ratio of 0.25 to 0.35, with the optimal stiffness variations re-calculated based on operating condition. It is seen that as the advance ratio increases, the baseline vibration index (without device stiffness variation) increases dramatically; with the vibration index increasing from 30% to 275% of the nominal value at advance ratio 0.3. However, with optimal 2/*rev* and 3/*rev* flap and lag spring stiffness variations, the vibration index shows a much milder increase from 6% to 40% (of the value at advance ratio of 0.3) over the range of advance ratios considered. The control effort index, J_u, also increases moderately in the range of advance ratio.

6.8 Summary on discrete controllable stiffness device

It is demonstrated that discrete controllable stiffness devices could produce simultaneous reductions in all components of vibratory hub loads, using the gradient-based optimization. An 85% reduction in the vibration performance index was observed when optimal 2/*rev* and 3/*rev* flap and lag stiffness variation inputs were simultaneously employed. Cyclic torsion stiffness variations were much less effective (only influenced the vertical vibratory force). Multi-cyclic flap and lag stiffness variations were seen to be effective in reducing hub vibration even when the fundamental rotor properties (root element flexural flap, lag, and torsion stiffness) and the operating condition (forward speed) were changed.

In this chapter, however, the controllable stiffness devices were modeled using only the simple dual spring model, and rotor inflow was calculated by linear inflow model (which is an approximated version of the complicated rotor inflow). To increase the fidelity of vibration reduction prediction, more complicated device model and rotor inflow model are used in the following chapter.

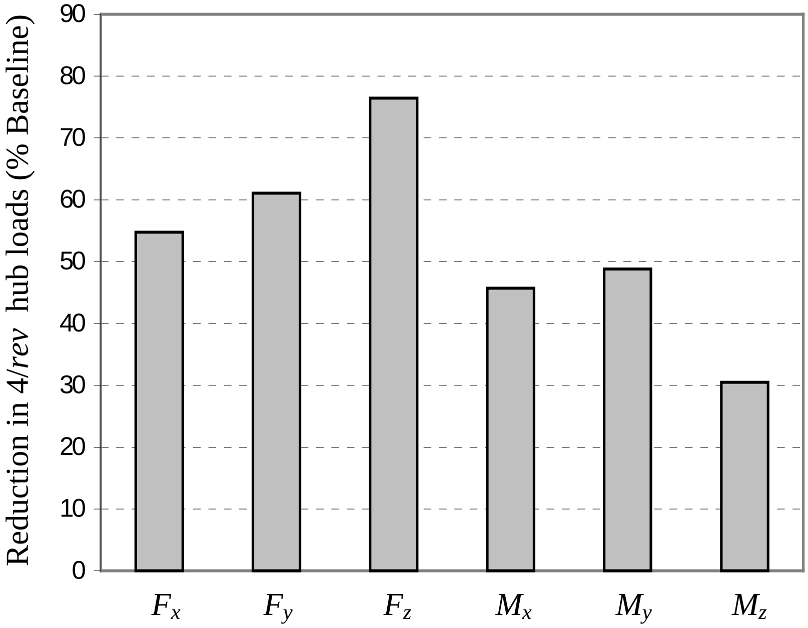

Figure 6.1: Hub vibration reduction due to optimal 2,3/*rev* discrete flap stiffness variations

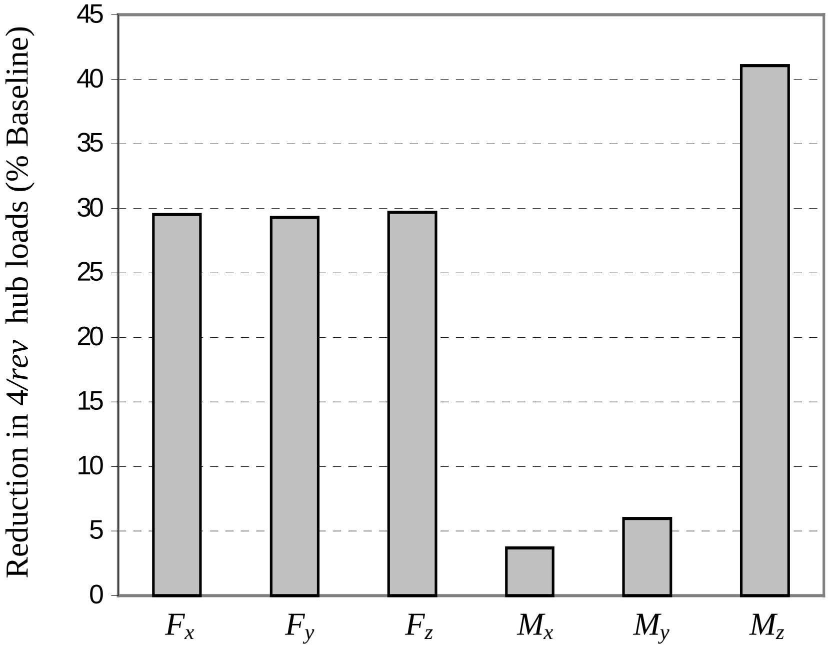

Figure 6.2: Hub vibration reduction due to optimal 2,3/*rev* discrete lag stiffness variations

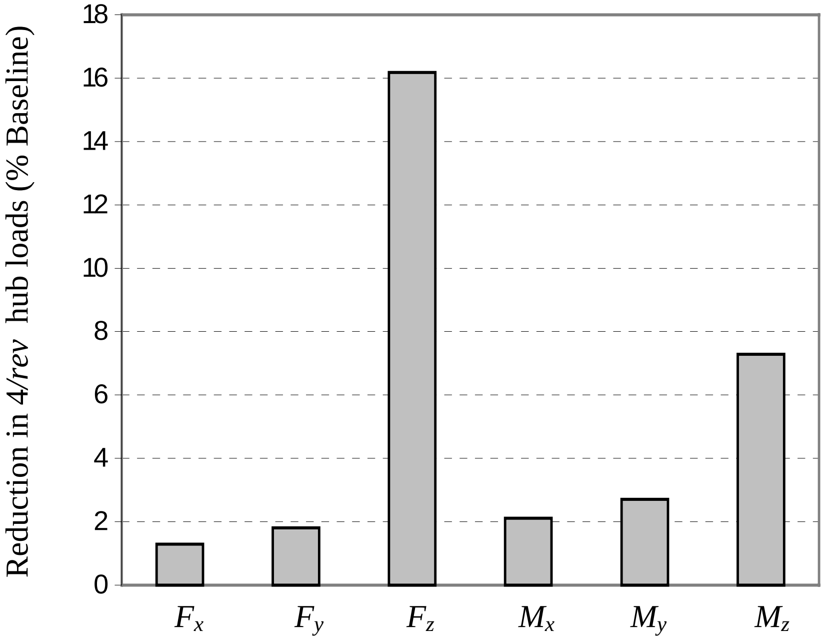

Figure 6.3: Hub vibration reduction due to the optimal 3,4/*rev* discrete torsion stiffness variations

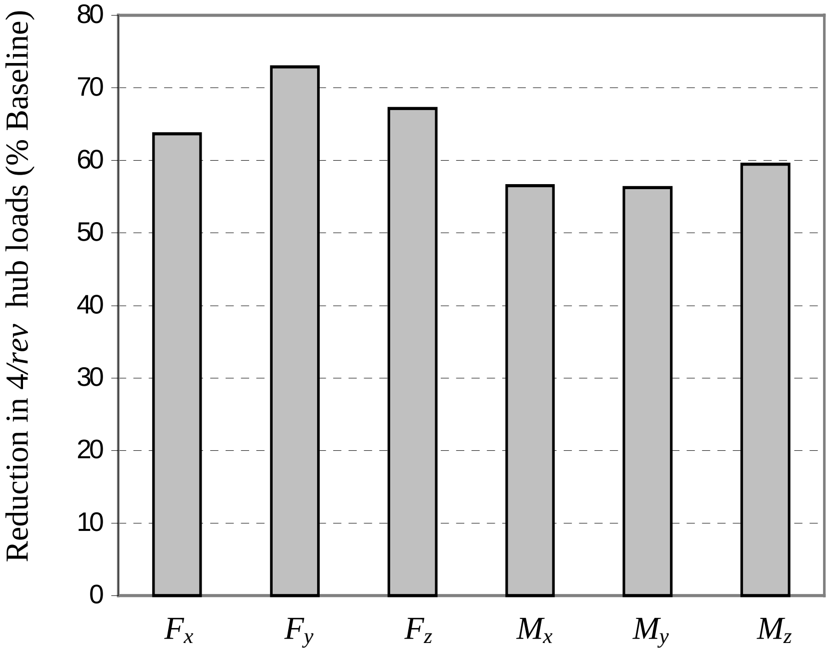

Figure 6.4: Hub vibration reduction due to the optimal 2,3/*rev* discrete flap and lag spring stiffness variations

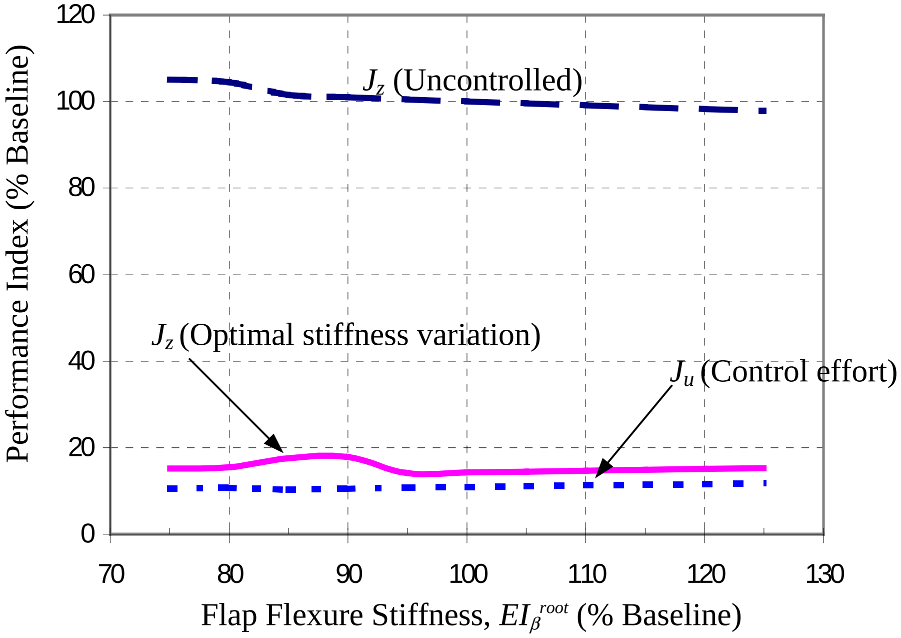

Figure 6.5: Effectiveness of optimal 2,3/*rev* discrete flap and lag spring stiffness variations for different value of flap flexure stiffness

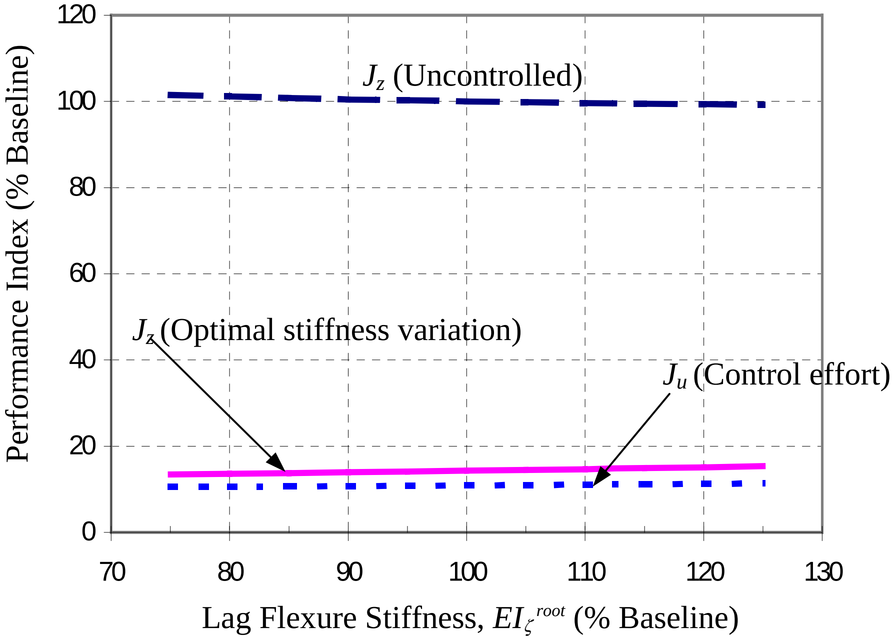

Figure 6.6: Effectiveness of optimal 2,3/*rev* discrete flap and lag spring stiffness variations for different value of lag flexure stiffness

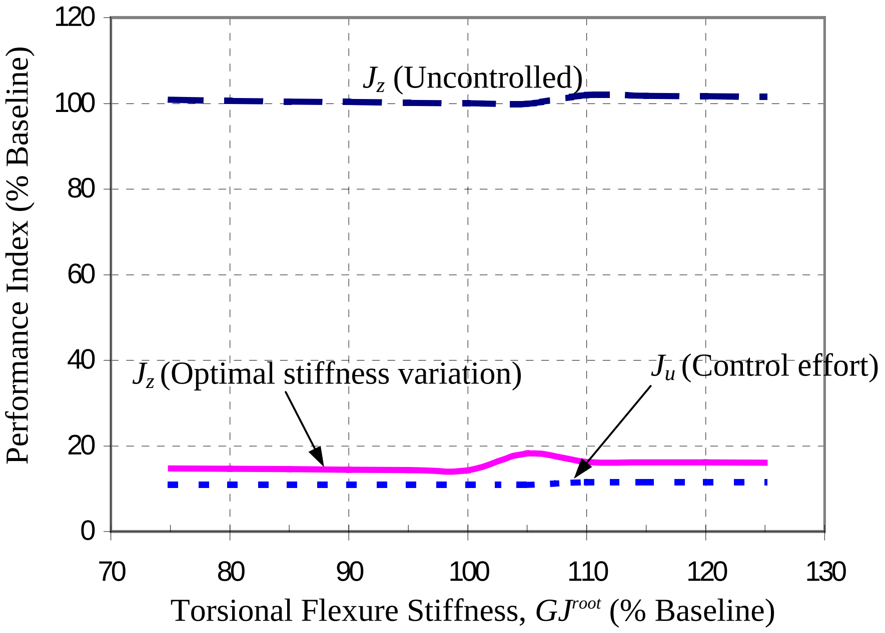

Figure 6.7: Effectiveness of optimal 2,3/*rev* discrete flap and lag spring stiffness variations for different value of torsional flexure stiffness

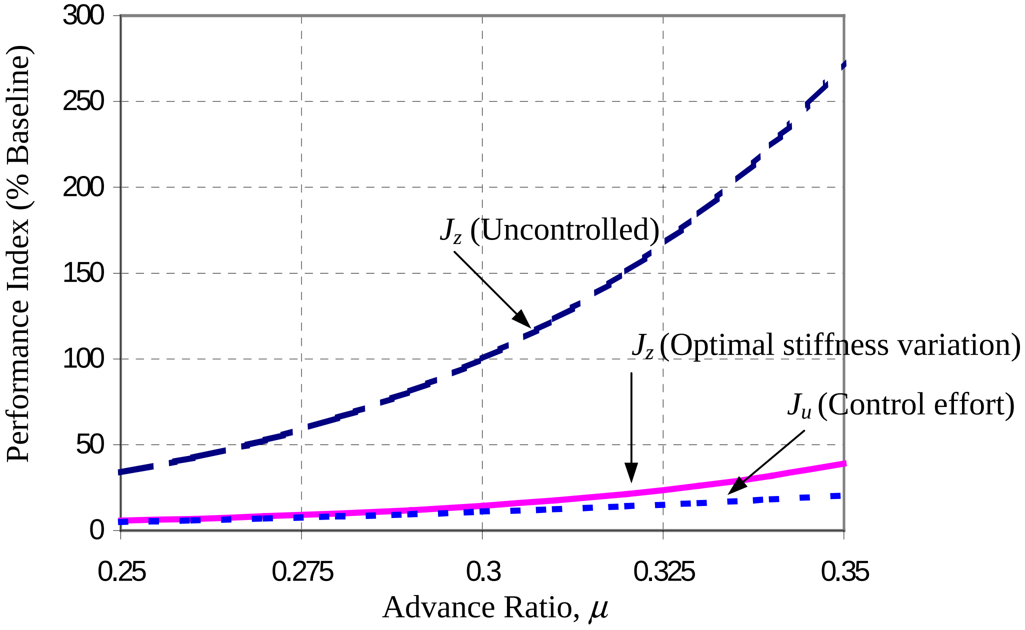

Figure 6.8: Effectiveness of the optimal 2,3/*rev* discrete flap and lag spring stiffness variations for different advance ratios

Flexure (Root Element) Properties	Flap bending stiffness $EI_{\beta}^{root}/EI_{\beta}$	0.70
	Lag bending stiffness $EI_{\zeta}^{root}/EI_{\zeta}$	0.60
	Torsional stiffness GJ^{root}/GJ	0.70
Controllable Stiffness Device Properties	$\overline{K}_w/(EI_{\beta}/R^3)$	0.2
	$\overline{K}_v/(EI_{\zeta}/R^3)$	0.1
	$\overline{K}_{\phi}/(GJ/R^2)$	0.2
	$\overline{K}_{w'}$	$\upsilon_w \overline{K}_w$
	$\overline{K}_{v'}$	$\upsilon_v \overline{K}_v$
	υ_w, υ_v	$(0.2R)^2/3$
Blade Natural Frequencies	Flap	1.199, 3.593, 7.825/*rev*
	Lag	0.802, 4.503, 11.174/*rev*
	Torsion	4.833, 13.742/*rev*

Table 6.1: Discrete controllable stiffness device and blade flexure properties

Vibratory Hub Loads*	
F_x^{4p}	0.8519
F_y^{4p}	0.8774
F_z^{4p}	0.7428
M_x^{4p}	9.9448
M_y^{4p}	10.1842
M_z^{4p}	3.6279

Table 6.2a: 4/*rev* vibratory hub loads for baseline rotor - no stiffness variation (Drees inflow, $\mu = 0.3$)

Blade Root Loads	Harmonics**				
	1/*rev*	2/*rev*	3/*rev*	4/*rev*	5/*rev*
S_r	0.09395	0.00770	0.00293	0.00077	0.00012
S_x	0.08132	0.00412	0.00144	0.00241	0.00024
S_z	0.04448	0.04007	0.01432	0.00186	0.00035
M_{ϕ}	-0.01259	-0.00406	-0.00038	-0.00012	-0.00005
M_{β}	-0.20101	-0.16374	-0.05066	-0.00582	-0.00096
M_{ζ}	-0.44682	-0.01932	-0.00419	-0.00907	-0.00091

Table 6.2b: Harmonics of blade root loads for baseline rotor - no stiffness variation (Drees inflow, $\mu = 0.3$)

---

* All vibratory hub forces are in % F_z^0 (5943 lbs.), all vibratory hub moments are in % M_z^0 (5222 ft-lbs.)

** Blade root shears are non-dimensionalized by $m_o\Omega^2R^2$, blade root moments are non-dimensionalized by $m_o\Omega^2R^3$

Vibratory Hub Loads[*]	
F_x^{4p}	1.6477
F_y^{4p}	1.7219
F_z^{4p}	1.2152
M_x^{4p}	12.8669
M_y^{4p}	13.1485
M_z^{4p}	6.0201

Table 6.2c: 4/*rev* vibratory hub loads for baseline rotor - no stiffness variation (Drees inflow, $\mu = 0.35$)

Blade Root Loads	Harmonics[**]				
	1/*rev*	2/*rev*	3/*rev*	4/*rev*	5/*rev*
S_r	0.11461	0.01138	0.00565	0.00156	0.00027
S_x	0.09883	0.00555	0.00286	0.00484	0.00054
S_z	0.07277	0.05577	0.02254	0.00304	0.00060
M_ϕ	-0.01283	-0.00490	-0.00055	-0.00020	-0.00009
M_β	-0.26453	-0.18860	-0.06550	-0.00770	-0.00139
M_ζ	-0.44750	-0.02161	-0.00719	-0.01505	-0.00167

Table 6.2d: Harmonics of blade root loads for baseline rotor - no stiffness variation (Drees inflow, $\mu = 0.35$)

Input		Amplitude $(\Delta K_w/\overline{K}_w)$	Phase
Flap device stiffness variation	2/*rev*	19 %	-101.3°
	3/*rev*	17 %	23.6°

Table 6.3: Optimal 2, 3/*rev* flap device stiffness variations ($J_z = 24.2$)

Input		Amplitude $(\Delta K_v/\overline{K}_v)$	Phase
Lag device stiffness variation	2/*rev*	34 %	141.4°
	3/*rev*	6 %	-135.5°

Table 6.4: Optimal 2, 3/*rev* lag device stiffness variations ($J_z = 60.8$)

---

[*] All vibratory hub forces are in % of F_z^0 (5943 lbs.), all vibratory hub moments are in % of M_z^0 (5222 ft-lbs.)

[**] Blade root shears are non-dimensionalized by $m_o\Omega^2R^2$, blade root moments are non-dimensionalized by $m_o\Omega^2R^3$

Input		Amplitude $(\Delta K_{\phi}/\overline{K}_{\phi})$	Phase
Torsion device stiffness variation	3/*rev*	15 %	-21.8°
	4/*rev*	19 %	102.5°

Table 6.5: Optimal 2, 3/*rev* torsion device stiffness variations (J_z = 91.3)

Input		Amplitude	Phase
Flap device stiffness variation	2/*rev*	$\Delta K_w = 23\,\%\,\overline{K}_w$	-103.6°
	3/*rev*	$\Delta K_w = 20\,\%\,\overline{K}_w$	26.1°
Lag device stiffness variation	2/*rev*	$\Delta K_v = 11\,\%\,\overline{K}_v$	101.6°
	3/*rev*	$\Delta K_v = 7\,\%\,\overline{K}_v$	42.8°

Table 6.6: Optimal 2, 3/*rev* flap and lag device stiffness variations (J_z = 14.28)

Blade Root Loads	Change in Harmonics (% Baseline)				
	1/*rev*	2/*rev*	3/*rev*	4/*rev*	5/*rev*
S_r	1.57	-14.95	-28.37	-0.03	-62.85
S_x	1.90	-3.57	-12.35	-75.73	-5.86
S_z	2.11	6.96	-43.96	-67.15	155.78
M_{ϕ}	0.38	-2.49	-0.21	209.88	21.26
M_{β}	-0.31	34.41	-56.79	6.37	360.60
M_{ζ}	2.67	-8.44	-38.54	-59.47	-6.03

Table 6.7: Change in harmonics of blade root loads due to the optimal 2,3/*rev* flap and lag spring stiffness variations

Chapter 7

Discrete Controllable Stiffness Device Results - Model Refinements

The results presented in Chapter 6 demonstrated that discrete controllable stiffness devices could produce significant hub vibration reduction. However, the simple rotor inflow model (Drees inflow) and controllable stiffness device model (dual spring model) were considered. This chapter evaluates vibration reductions achievable when a sophisticated rotor wake model (free wake model) along with more physical representations of discrete controllable stiffness devices (see Fig. 2.11 and description presented in Section 2.2.2.2) are considered. The stiffness of those discrete devices is varied cyclically (see Eq. 2.15) to reduce hub vibration at moderate flight speeds. Based on the convergence study presented in Appendix I, five finite elements and 10 modes (4 flap, 4 lag, and 2 torsion modes) are used to represent the rotor blade. The baseline configuration is summarized in Section 7.1. The effectiveness of individual discrete controllable stiffness devices (flap, lag, and torsion devices) is examined in Sections 7.2, 7.3, and 7.4, respectively. Section 7.5 examines the effectiveness of optimal vibration control using combined controllable stiffness devices (devices are chosen based on their individual performance). Sections 7.6 and 7.7 demonstrate the performance of the discrete controllable stiffness devices in reducing hub vibration for variations in configuration properties and cruise speed, respectively. Based on these results, Section 7.8 summarizes the effectiveness of the discrete controllable stiffness device on hub vibration reduction.

7.1 Baseline configuration

The baseline configuration is similar to that already presented in Chapter 6, except that the flexure stiffnesses are slightly modified, to compensate for the changed stiffness contributions from the single spring model of the discrete controllable stiffness devices (Section 2.2.2.2). Properties of blade flexure and discrete controllable stiffness devices are provided in Table 7.1. For this configuration, the baseline vibratory hub loads and blade root loads are given in Tables

7.2 (at an advance ratio of 0.30, using free wake analysis to obtain rotor inflow). The hub vibration levels in Table 7.2a corresponds to a vibration performance index $J_z = 100$, and are used as a point of reference to which vibration levels are compared when optimal stiffness variations are introduced.

7.2 Optimal 2,3/*rev* flap device stiffness variations

Multi-cyclic variations in the stiffness of only the flap device (see Fig. 2.13a) are considered first. The optimal 2/*rev* and 3/*rev* flap stiffness variations (amplitude and phase values) are determined using the approach described in Chapter 3, and are presented in Table 7.3. For these optimal stiffness variations, the output vibration index, J_z, is reduced by 31%, compared to the baseline value. The corresponding reductions in individual components of vibratory hub loads are shown in Fig. 7.1. An 80% reduction in in-plane hub drag force, F_x^{4p}, and a 45% reduction in in-plane hub side force, F_y^{4p}, are observed. Changes in the other components of vibratory hub loads are less than 10%. The variation in device stiffness over a single rotor revolution is shown in Fig. 7.2 and is bounded between 35% and 160% of the baseline value, $\overline{K}_w$.

7.3 Optimal 2,3/*rev* lag device stiffness variations

Next, variations in the stiffness of the lag device (see Fig. 2.13b) are examined. The optimal 2/*rev* and 3/*rev* stiffness variations of the lag device are presented in Table 7.4. These optimal lag device stiffness variations result in a 16% reduction in the vibration index, J_z, relative to the baseline, with changes in the individual components of vibratory hub loads shown in Fig. 7.3. From the figure, a 45% reduction in in-plane hub drag force, F_x^{4p}, and a 25% reduction in in-plane hub side force, F_y^{4p}, are observed; with the other components not showing any significant changes. The combination of the 2/*rev* and 3/*rev* inputs (amplitude and phase) implies that the lag device stiffness varies between 53% and 150% of the baseline value, $\overline{K}_v$, over a single rotor revolution (stiffness variation not shown).

7.4 Optimal 3,4/*rev* torsion device stiffness variations

Multi-cyclic variations in the spring coefficient of the controllable torsion stiffness device are considered next (see Fig. 2.13c). Optimal 3/*rev* and 4/*rev* torsion stiffness variations are presented in Table 7.5a and the corresponding reductions in individual components of vibratory hub loads are shown in Fig. 7.4. Only a very modest reduction (under 5%) in the vibratory vertical hub force, F_z^{4p}, is observed; and other components of hub vibratory loads have even lower sensitivity. These observations are qualitatively similar to those previously reported in the sensitivity study (Chapter 4), but the percentage reduction in F_z^{4p} is even smaller due to the higher baseline vibration levels associated with the inclusion of the free-wake in the present analysis. For the results in Table 7.5a and Fig. 7.4, a penalty weighting on the input of W_u = 0.02[I] was used, as the default value of $W_u = I$ (for results in Sections 7.2 and 7.3) produced torsion stiffness variations that were very small, and resulted in a negligible change in vibratory hub loads.

To examine whether any further reductions in hub vibration are possible using cyclic torsion stiffness variations, two additional cases are considered. In the first case, the penalty weighting W_u is reduced (from 0.02[I] to 0.015[I]), allowing for larger percentage variations in spring stiffness. In the second case, recognizing that the arbitrarily large percentage changes in spring coefficient are not permissible and yet it is the actual physical values of the stiffness changes that matter; $\overline{K}_\phi$ is itself increased to twice the baseline value. In this case, larger torsion stiffness variation can be introduced even while the change in spring coefficient, as a percentage of the baseline, is kept bounded (of course, the baseline rotor frequencies and vibration characteristics themselves undergo some change). The reductions in the vibratory vertical hub force, F_z^{4p}, for these two cases, shown in Fig. 7.5, suggest that only small improvements are possible. The corresponding optimal stiffness variations are given in Tables 7.5b and 7.5c. As seen in previous chapters, multi-cyclic torsion stiffness variations are again much less influential than flap and lag stiffness variations, and are not further considered for semi-active helicopter vibration reduction.

7.5 Optimal 2,3/*rev* flap and lag device stiffness variations

From the results in Sections 7.2–7.4, it is clearly established that multi-cyclic variations in either flap or lag device stiffness can significantly reduce some components of hub vibration, but variation in torsion stiffness is relatively ineffective. The present section examines the possible reductions in vibratory hub loads when optimal 2/*rev* and 3/*rev* flap, and 2/*rev* and 3/*rev* lag stiffness variations are simultaneously considered (these results are presented in Fig. 7.6, and the corresponding optimal inputs are shown in Table 7.6). The optimal stiffness variations produce a 33% reduction in the vibration index. It is seen that vibratory in-plane hub drag force, F_x^{4p}, is virtually eliminated, and the hub side force, F_y^{4p}, is reduced by 55%. Only minor changes in other components of hub loads are observed.

For the optimal flap and lag stiffness variations, Table 7.7 shows the percentage changes in the 1st through 5th harmonics of the various components of blade root loads (with reference to the baseline values given in Table 7.2b). None of the components of blade root loads show any significant increases. The 3rd through 5th harmonics of the blade root radial shear, S_r, show increases between 5-10%, the 4th harmonic of the blade root drag shear, S_x, shows an 8% increase, the 3rd through 5th harmonics of the blade root pitching moment, M_ϕ, show between 7-12% increases, and the 4th harmonic of the blade root lag moment, M_ζ, shows a 5% increase. Significant reductions seen were in the 3rd harmonic of S_x (40%), 2nd harmonic of M_ζ (30%), 3rd harmonic of the blade root vertical shear, S_z (23%), and 5th harmonic of the blade root flapping moment M_β (40%).

7.6 Influence of flexure stiffness on effectiveness of vibration reduction

In section 7.5, simultaneous multi-cyclic variations in spring stiffness of both the flap and lag devices were seen to significantly reduce the hub vibration levels for the baseline configuration whose properties are given in Table 7.1. The present section verifies that the concept of using multi-cyclic variations in spring coefficients of discrete controllable stiffness devices would be effective even if the baseline configuration changes. Keeping the discrete controllable devices unchanged from the baseline, the flap, lag, and torsion stiffness of the flexure (blade root element) is individually varied by upto ± 25% of its nominal value. The optimal 2,3/*rev* flap and lag device stiffness variations are re-evaluated, and their influence examined on the vibratory hub loads. Figures 7.7, 7.8, and 7.9 show reductions in vibration index, J_z, for variations in flap, lag, and torsion stiffness, of the flexure, respectively. Overall, the multi-cyclic controller retains its effectiveness (producing a 25%-35% reduction in vibration index, J_z, compared to the uncontrolled case) over the range of variations considered in the flap, lag, and torsion stiffness of the flexural element. The control effort index, J_u, shows a slight increase when the flap stiffness or lag stiffness of the flexural element is reduced.

7.7 Effectiveness of vibration controller at different forward speeds

This section examines the effectiveness of 2/*rev* and 3/*rev* flap and lag stiffness variations for vibration reduction at different cruise speeds. Figure 7.10 shows the vibration performance index, J_z, with and without the multi-cyclic stiffness variations, over forward speeds ranging from advance ratio of 0.25 to 0.35 (the optimal stiffness variations are re-calculated at different flight speeds). The vibration performance index is normalized with respect to the baseline (uncontrolled) vibrations at an advance ratio of 0.30 given in Table 7.2a, (corresponding to J_z = 100). It is seen that as the advance ratio increases from 0.30 to 0.35, the uncontrolled vibration index increases from 100 to 320. As the advance ratio decreases from 0.30 to 0.25, the uncontrolled vibration index again increases from 100 to 400, due to the dominant effect of the rotor wake at the lower advance ratio. With optimal 2/*rev* and 3/*rev* stiffness variations of the flap and lag devices, the vibration index shows reductions across the advance ratio range. The reductions in J_z, relative to the uncontrolled case, vary from 55% at an advance ratio of 0.25 to around 33% at advance ratios between 0.3 and 0.35. The control effort index, J_u, shows only mild variations over the range of forward speeds considered, despite the large differences in the uncontrolled vibration levels.

7.8 Summary on effectiveness of discrete controllable stiffness device

With more sophisticated rotor inflow and device modeling, the results in this chapter demonstrated that optimal multi-cyclic stiffness variations of discrete controllable stiffness devices could reduce the vibratory hub loads. Multi-cyclic stiffness variations of the flap and lag devices were most influential, and when optimal 2/*rev* and 3/*rev* stiffness variations of these devices were used in combination, the vibratory hub drag force was practically eliminated and the vibratory hub side force was reduced by 55%. No significant detrimental effects were observed on harmonics of the vibratory blade root loads. Multi-cyclic (3/*rev* and 4/*rev*) stiffness variations of the torsion device produced only small reductions in the 4/*rev* hub vertical force. Multi-cyclic stiffness variations of the flap and lag devices were seen to be effective in reducing hub vibration even when there were changes in fundamental rotor properties such as the flap, lag, and torsion stiffness of the root (flexure) element, and the cruise speed.

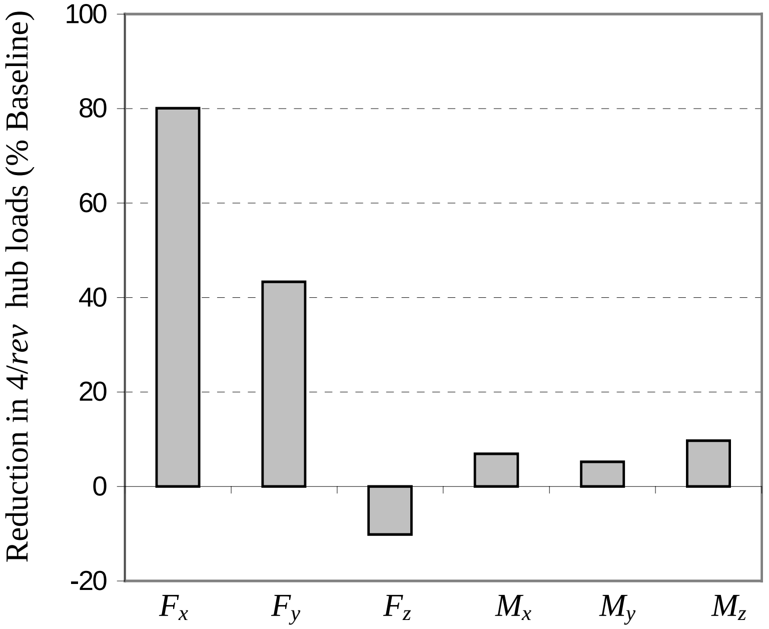

Figure 7.1: Hub vibration reduction due to optimal 2,3/*rev* flap device stiffness variations

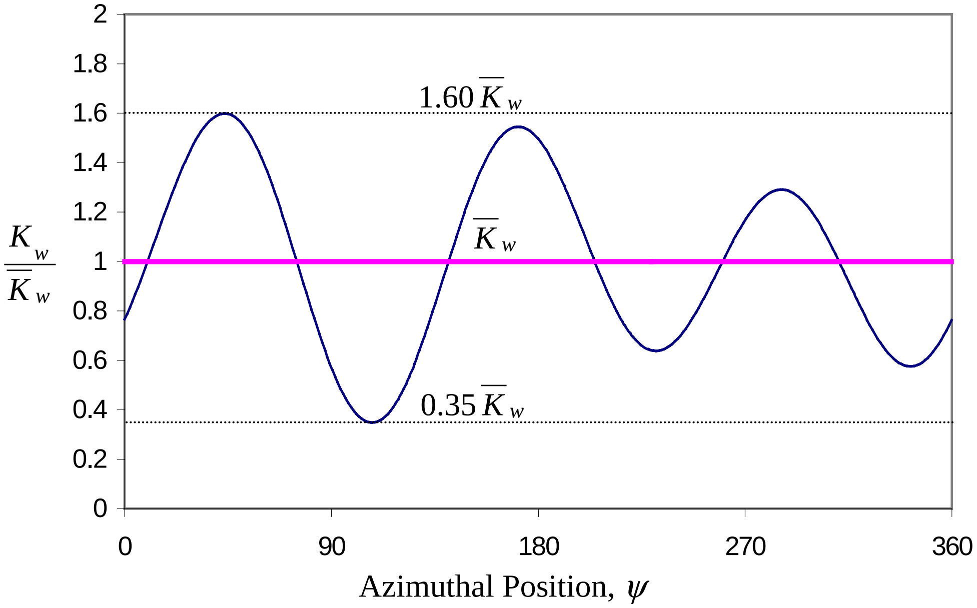

Figure 7.2: Optimal flap device stiffness variation over one rotor revolution, (with 2, 3/*rev* inputs from Table 7.3)

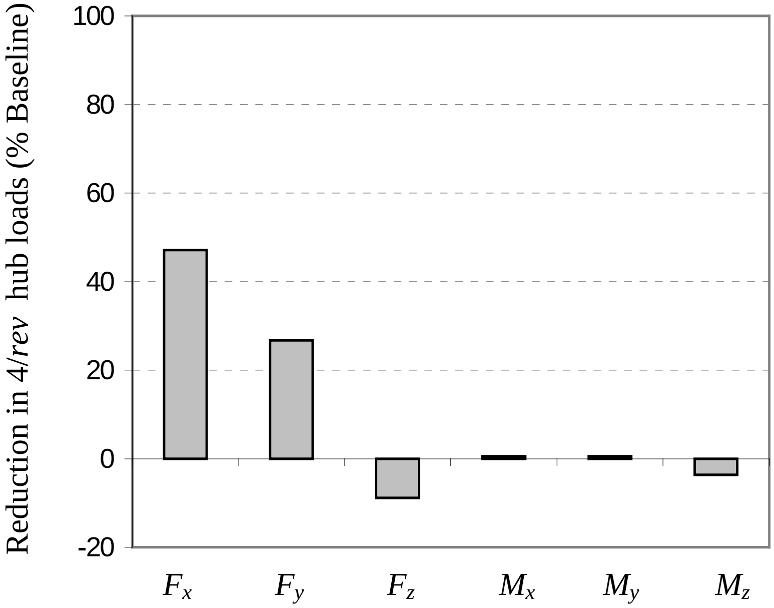

Figure 7.3: Hub vibration reduction due to optimal 2,3/*rev* lag device stiffness variations

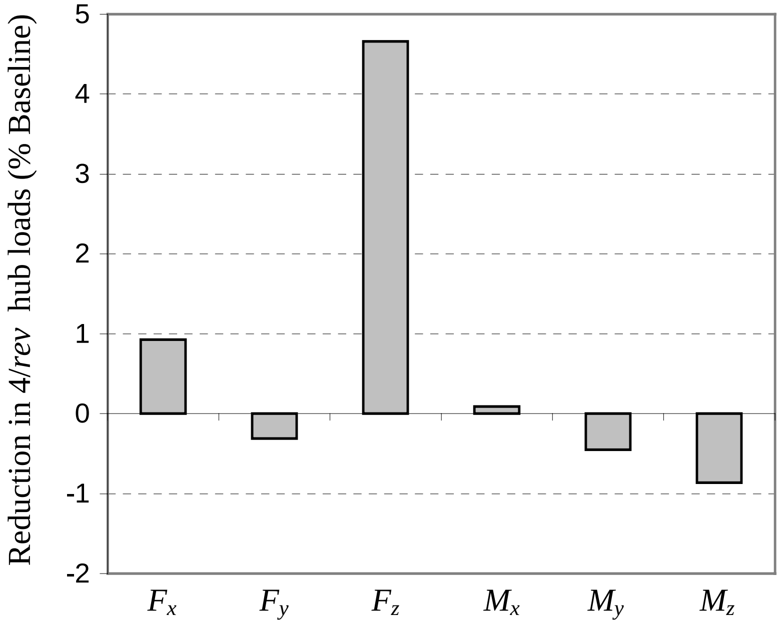

Figure 7.4: Hub vibration reduction due to optimal 3,4/*rev* torsion device stiffness variations (W_u = 0.02[I], baseline torsion device stiffness = $\overline{K}_\phi$)

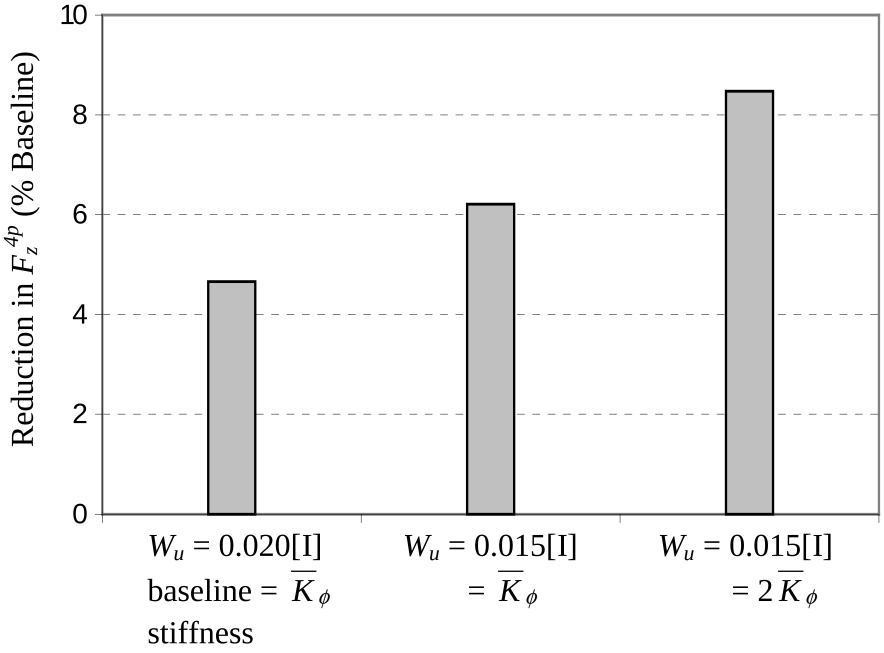

Figure 7.5: Hub vibration reduction due to the optimal 3,4/*rev* torsion device stiffness variations, with varying input weights (W_u) and baseline torsion spring stiffness ($\overline{K}_\phi$,2$\overline{K}_\phi$)

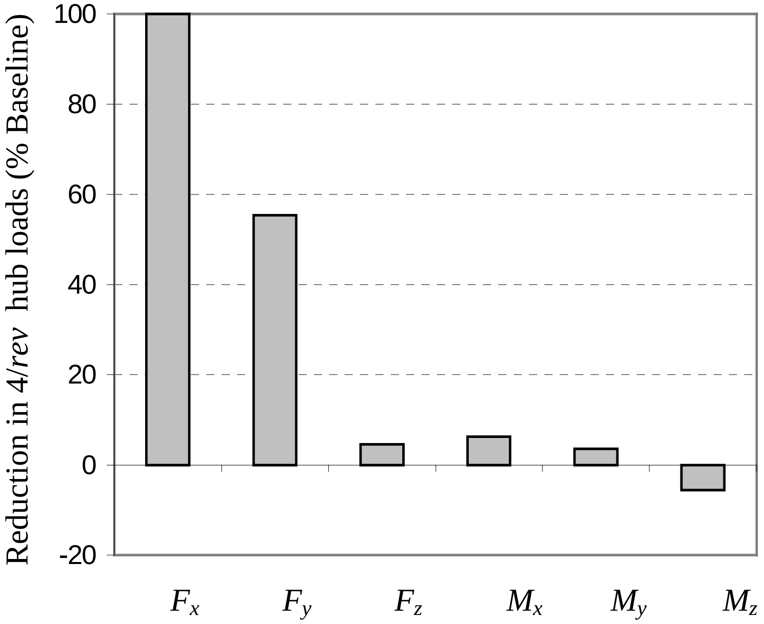

Figure 7.6: Hub vibration reduction due to optimal 2,3/*rev* flap and lag device stiffness variations

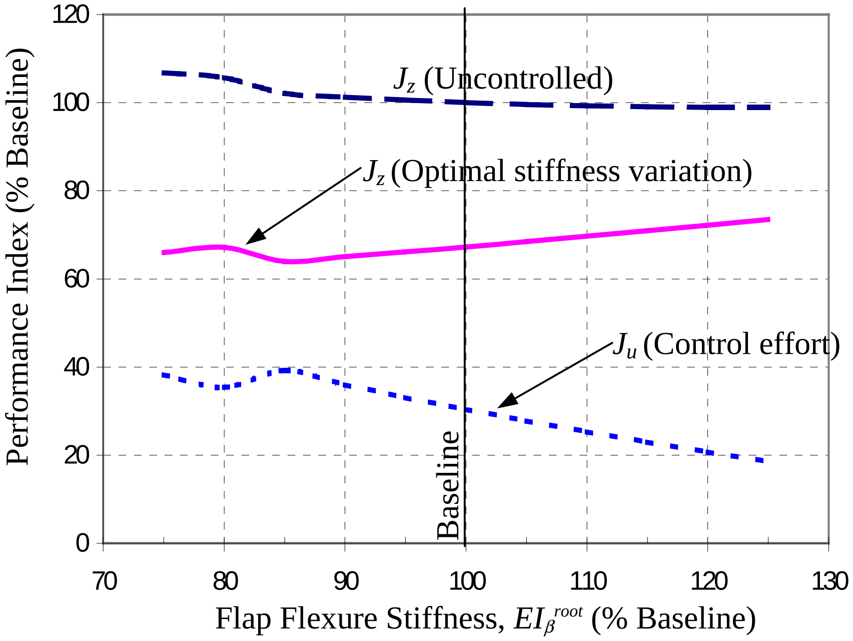

Figure 7.7: Effectiveness of optimal 2,3/*rev* flap and lag device stiffness variations for different values of flap flexure stiffness

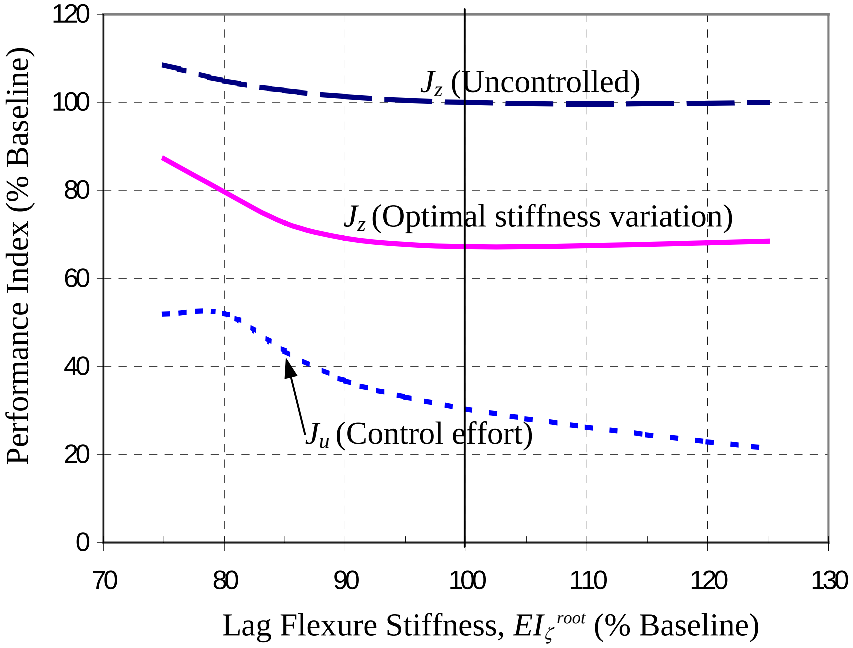

Figure 7.8: Effectiveness of optimal 2,3/*rev* flap and lag device stiffness variations for different values of lag flexure stiffness

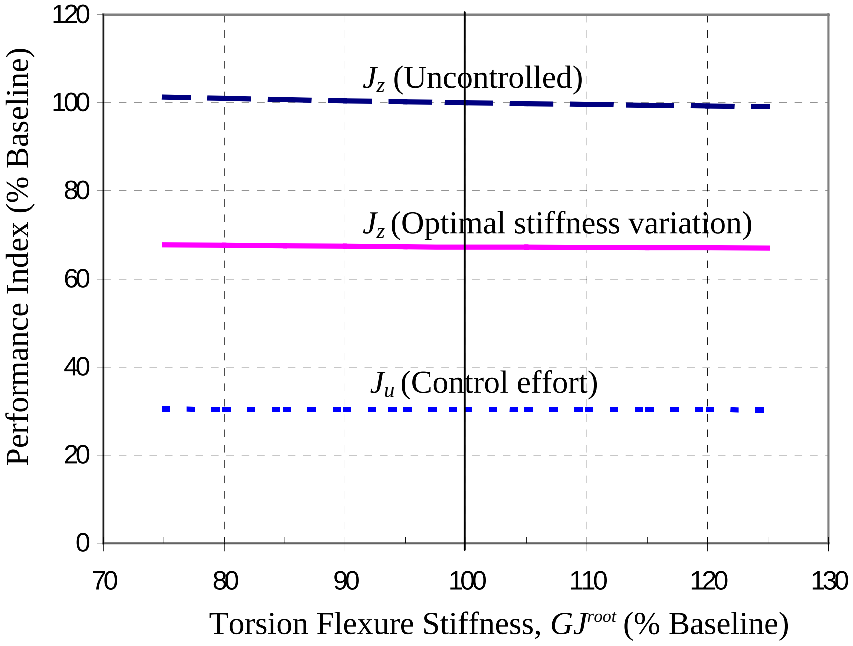

Figure 7.9: Effectiveness of optimal 2,3/*rev* flap and lag device stiffness variations for different values of torsion flexure stiffness

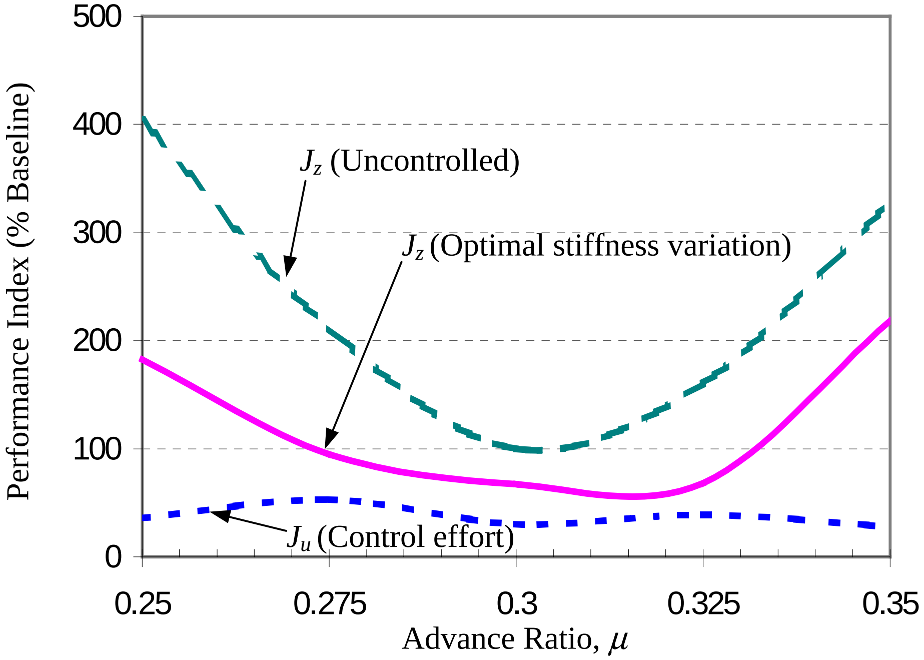

Figure 7.10: Effectiveness of optimal 2,3/*rev* flap and lag device stiffness variations for different advance ratios

Flexure (Root Element) Properties	Flap bending stiffness EI_β^{root}/EI_β	0.70
	Lag bending stiffness EI_ζ^{root}/EI_ζ	0.70
	Torsional stiffness GJ^{root}/GJ	0.70
Controllable Stiffness Device Properties	$\overline{K}_w/(EI_\beta/R^3)$	0.12231
	$\overline{K}_v/(EI_\zeta/R^3)$	0.11996
	$\overline{K}_\phi/(GJ/R^2)$	0.00716
	α_w, α_v	15°
	e_w, e_v	0.5c
Blade Natural Frequencies	Flap	1.147, 3.399, 7.447, 13.342/*rev*
	Lag	0.750, 4.364, 10.963, 20.653/*rev*
	Torsion	4.590, 13.595/*rev*

Table 7.1: Discrete controllable stiffness device and blade flexure properties

Vibratory Hub Loads[*]	
F_x^{4p}	1.1719
F_y^{4p}	2.2419
F_z^{4p}	2.6352
M_x^{4p}	37.7587
M_y^{4p}	40.2514
M_z^{4p}	54.8682

Table 7.2a: 4/*rev* vibratory hub loads for baseline rotor – no cyclic stiffness variation (Free-wake, $\mu = 0.3$)

Blade Root Loads	Harmonics[**]				
	1/*rev*	2/*rev*	3/*rev*	4/*rev*	5/*rev*
S_r	0.165412	0.01793	0.00348	0.015112	0.002833
S_x	0.135271	0.008518	0.009605	0.034555	0.005395
S_z	0.043921	0.013569	0.059717	0.006584	0.004924
M_ϕ	-0.01624	-0.0053	-0.00175	-0.00256	-0.00031
M_β	-0.20017	-0.04484	-0.19397	-0.01991	-0.01421
M_ζ	-0.77574	-0.03881	-0.03617	-0.13745	-0.0196

Table 7.2b: Harmonics of blade root loads for baseline rotor – no cyclic stiffness variation (Free-wake, $\mu = 0.3$)

---

[*] All vibratory hub forces are in % of F_z^0 (5914 lbs.), all vibratory hub moments are in % of M_z^0 (4878 ft-lbs.)

[**] Blade root shears are non-dimensionalized by $m_o\Omega^2R^2$, blade root moments are non-dimensionalized by $m_o\Omega^2R^3$

Input		Amplitude ($\Delta K_w/\overline{K}_w$)	Phase
Flap device stiffness variation	2/*rev*	18.4 %	44.4°
	3/*rev*	47.1 %	140.8°

Table 7.3: Optimal 2,3/*rev* flap device stiffness variations ($J_z = 69.25$)

Input		Amplitude ($\Delta K_v/\overline{K}_v$)	Phase
Lag device stiffness variation	2/*rev*	36.8 %	33.4°
	3/*rev*	14.3 %	-160.3°

Table 7.4: Optimal 2,3/*rev* lag device stiffness variations ($J_z = 84.23$)

Input		Amplitude ($\Delta K_\phi/\overline{K}_\phi$)	Phase
Torsion device stiffness variation	3/*rev*	18.7 %	-176.1°
	4/*rev*	46.8 %	151.9°

(a) $W_u = 0.020[I]$, baseline torsion device stiffness = $\overline{K}_\phi$

Input		Amplitude ($\Delta K_\phi/\overline{K}_\phi$)	Phase
Torsion device stiffness variation	3/*rev*	25.1 %	-179.3°
	4/*rev*	60.8 %	152.5°

(b) $W_u = 0.015[I]$, baseline torsion device stiffness = $\overline{K}_\phi$

Input		Amplitude ($\Delta K_\phi/2\overline{K}_\phi$)	Phase
Torsion device stiffness variation	3/*rev*	25.2 %	-175.5°
	4/*rev*	59.7 %	166.4°

(c) $W_u = 0.015[I]$, baseline torsion device stiffness = $2\overline{K}_\phi$

Table 7.5: Optimal 3,4/*rev* torsion spring stiffness variations, with varying input weights (W_u) and baseline torsion spring stiffness ($\overline{K}_\phi$ and $2\overline{K}_\phi$)

Input		Amplitude	Phase
Flap device stiffness variation	2/*rev*	$\Delta K_w = 5.5\ \%\,\overline{K}_w$	30.1°
	3/*rev*	$\Delta K_w = 43.5\ \%\,\overline{K}_w$	139.7°
Lag device stiffness variation	2/*rev*	$\Delta K_v = 32.2\ \%\,\overline{K}_v$	59.7°
	3/*rev*	$\Delta K_v = 8.9\ \%\,\overline{K}_v$	109.4°

Table 7.6: Optimal 2,3/*rev* flap and lag devices stiffness variations (J_z = 67.23)

Blade Root Loads	Change in Harmonics (% Baseline)				
	1/*rev*	2/*rev*	3/*rev*	4/*rev*	5/*rev*
S_r	-0.34	-4.20	9.46	10.27	5.03
S_x	-0.47	-8.23	-40.02	8.23	-0.14
S_z	-0.61	3.32	-23.42	-4.79	-10.87
M_ϕ	-0.36	-1.26	7.10	12.03	9.61
M_β	-0.32	0.67	-4.53	-14.70	-23.13
M_ζ	-0.83	-28.53	-11.18	5.60	0.30

Table 7.7: Change in harmonics of blade root loads due to the optimal 2,3/*rev* flap and lag device stiffness variations

Chapter 8

Discrete Controllable Orifice Dampers

It is demonstrated in previous chapters that the semi-active stiffness variation concept is a viable method for helicopter vibration reduction. However, availability of the controllable stiffness devices is limited, and the amount of stiffness variation authority may not be sufficient to produce satisfactory results. Thus, another alternative for vibration reduction is considered using controllable dampers, which are widely available as well as able to change damping coefficient by up to 80% (see Section 2.3.1). This present chapter examines the effectiveness of controllable orifice dampers on reducing vibratory hub loads in high-speed flight (advance ratio of 0.35), using rotor inflow calculated by free wake analysis. Damping variation is described in detail in Section 2.3 (see also Eq. 2.30). The rotor blade is modeled using five finite elements and 10 modes (4 flap, 4 lag, and 2 torsion modes) based on convergence study presented in Appendix I. The baseline configuration is described in Section 8.1. The effectiveness of using only the controllable lag damper is presented in Section 8.2. In addition to evaluating the reductions in hub vibration, the effects of changes in damper size and mounting configuration are also examined. In Section 8.3, a controllable flap damper is introduced in addition to the controllable lag damper to obtain further reductions in hub vibration. The ability of optimal semi-active cyclic damping variations in reducing the hub vibrations over a range of flight speeds is also demonstrated. A summary of the results in this chapter is presented in Section 8.4.

8.1 Baseline configuration

The baseline configuration consists of uniform blades (properties are given in Table H.1) with lag and flap dampers attached near the root (see Fig. 2.21). No modification on blade flexure is required since the introduction of the controllable dampers has insignificant effect on blade natural frequencies, unlike introduction of the discrete controllable stiffness devices (presented in

Chapters 6 and 7) which significantly influences blade natural frequencies. The dampers are selected so as to provide 11% and 8% critical damping in the fundamental lag and flap modes, respectively. Properties of the controllable dampers and damper attachment configuration are presented in Table 8.1. Without any cyclic variations in damping, the baseline vibratory hub loads, blade root loads, flexbeam root loads, damper loads, and blade tip responses, are presented in Tables 8.1a – 8.1e, respectively. The vibratory hub loads in Table 8.1a are used as a reference vibration level (corresponding to vibration index $J_z = 100$), against which all vibration reduction studies in this chapter are compared.

8.2 Lag Damping Variation

First, controllable lag damper is considered for hub vibration reduction. In addition to evaluating the reductions in hub vibration, changes in blade root loads, flexbeam root loads, damper loads, and blade response are also presented in Section 8.2.1. The effects of damper size and mounting configuration are also examined in Section 8.2.2.

8.2.1 Influence of optimal 2,3/*rev* lag damping variations

Multi-cyclic variations in the damping coefficient of only the lag damper are considered first. The optimal 2/*rev* and 3/*rev* lag damping variations (both cosine and sine components, or amplitude and phase values) are determined using the approach described in Chapter 3, and are presented in Table 8.3. The time history of the resulting damping variation, over a single rotor revolution, is shown in Fig. 8.1; and it is observed that the damping level varies between 20% and 175% of the baseline value, $\overline{C}_v$. For this optimal damping variation, the vibration index, J_z, is reduced by 35% as compared to its baseline value. The corresponding reductions in individual components of vibratory hub loads are shown in Fig. 8.2. It is observed that vibratory hub drag force, F_x^{4p}, and vibratory hub yawing moment, M_z^{4p}, can be virtually eliminated, while the vibratory hub side force, F_y^{4p}, is reduced by 15%. All other vibratory hub loads are almost unaffected.

Figure 8.3 shows the lag damper force over a rotor revolution, when the optimal multi-cyclic lag damping variations in Table 8.3 are used. Also shown in the figure is the reference damper force when no semi-active damping variations are introduced. With the 2/*rev* and 3/*rev* semi-active lag damping variations the peak damper force increases somewhat (from 700 lbs to 800 lbs), but more notably, there is a significant increase in the higher harmonic content of the damper force. While the baseline damper force had a predominant 1/*rev* component (also seen from Table 8.2d), the optimal semi-active input results in increases of 140%, 193%, 86%, and 57%, respectively, in the 2nd through 5th harmonics of the lag damper load (see Table 8.4). It is these higher harmonic loads, introduced by the controllable lag damper, that modify the blade response so as to reduce some of the hub vibrations. No significant change in harmonics of flap damper forces is observed (see Table 8.4), since the flap damper is not controlled in this case.

Table 8.5 shows variation in harmonics of blade root loads when the optimal 2/*rev* and 3/*rev* lag damping variations are used. It can be deduced from Section 2.3.2 that the semi-active control of the lag damper primarily influences the blade root drag shear, S_x, and the blade root lag moment, M_ζ, with a smaller effect on the blade root radial shear, S_r (due to coriolis effects, etc). It is interesting to note that there are large percentage increases in the 3/*rev* and 5/*rev* components of blade root drag shear, S_x. Intuitively, decreases in the 3rd and 5th harmonics of S_x and S_r would have been expected since the vibratory hub drag force, F_x^{4p}, has been eliminated. However, it should be recalled that

$$\begin{aligned} F_x^{4p} &= 2(S_r^{3c} - S_x^{3s})\cos 4\psi + 2(S_r^{3s} + S_x^{3c})\sin 4\psi \\ &\quad + 2(S_r^{5c} + S_x^{5s})\cos 4\psi + 2(S_r^{5s} - S_x^{5c})\sin 4\psi \end{aligned} \tag{8.1}$$

From Table 8.2b it is seen that for the baseline configuration the 3rd harmonic of S_r is an order of magnitude larger than that of S_x, and the 5th harmonic is twice as large. In essence, the blade root radial shear, S_r, is the dominant contributor to the in-plane vibratory hub drag force, F_x^{4p}, for the baseline rotor. The optimal lag damping variations appear to be increasing the 3rd and 5th harmonics of S_x such that (along with some modest reductions in the 3rd and 5th harmonics of S_r) the factors $(S_r^{3c} - S_x^{3s})$, $(S_r^{3s} + S_x^{3c})$, $(S_r^{5c} + S_x^{5s})$ and $(S_r^{5s} - S_x^{5c})$, in Eq. 8.1 are reduced, thereby reducing the vibratory hub drag force. In other words, increases in harmonics of blade root drag shear using cyclic variations in lag damping are producing the reductions in in-plane vibratory hub forces. Table 8.5 also indicates a 98% reduction in the 4th harmonic of the blade root lag moment, M_ζ, which is consistent with the reduction in the vibratory hub yawing moment seen in Fig. 8.2. Figures 8.4a and 8.4b show the variation in blade root drag shear, S_x, and radial shear, S_r, respectively, over one rotor revolution. It is seen that while the cyclic lag damping variation introduced small high-frequency oscillations in the blade root drag shear, relative to the baseline rotor, the overall changes are very small. Influence of the cyclic lag damping variation on the blade root radial shear is even less perceptible. Changes in other blade root loads are caused by secondary effects, and considered negligible.

Table 8.6 shows changes in the harmonics of flexbeam root loads using the optimal lag damping variations. Again, components of flexbeam loads that are directly effected by the semi-active lag damping variation are S_x^{flex}, S_r^{flex}, and M_ζ^{flex}. A reduction of around 50% is seen in the 2nd harmonic of S_x^{flex}, but the 3rd, 4th and 5th harmonics are seen to increase by around 350%, 200% and 100%, respectively. However, it should be noted that percentage increases appear excessively large because the higher harmonics of S_x^{flex} for the baseline rotor were very small (see Table 2c). The variation of S_x^{flex} over a rotor revolution (Fig. 8.5a) shows that despite the introduction of some high-frequency loading, relative to the baseline rotor, the overall changes are very small, so the flexbeam dynamic stresses will not be adversely affected. The variation of S_r^{flex} over a rotor revolution (Fig. 8.5b) shows that the peak-to-peak oscillations are actually reduced by about 300 lbs when cyclic lag damping variations are used. Some harmonics of M_ζ^{flex} are increased significantly by as much as 180% for the 3rd harmonic, but the increases are not perceptible since the corresponding baseline values are small to begin with. Changes in harmonics of other flexbeam root loads are again insignificant due to indirect effect of the damping variation.

Figure 8.6 shows the blade flap, lag, and torsion tip responses over one rotor revolution. Comparing with the response for the baseline rotor, the cyclic variation in lag damping does not appear to have had any significant influence. However, the higher harmonic damper loads do in fact introduce higher harmonics in the tip lag response, as seen in Table 8.7. The percentage increases in the 2nd through 5th harmonics appear a little exaggerated since the baseline values were very small (see Table 8.2e – baseline lag response was primarily at 1/*rev*). Changes in harmonics of flap and torsion response are much smaller.

8.2.2 Influence of lag damper sizing and configuration

From section 8.2.1 it is clear that multi-cyclic variations in lag damping coefficient can reduce the vibratory hub in-plane forces and yawing moment. However, the effectiveness of the controllable damper in reducing vibration can be expected to vary, depending on the damper configuration and size. For the results in section 8.2.1, nominal values of damper mounting angle, α_v = 20 deg, offset, e_v = *c*, and attachment point, L_v = 0.2*R*, were used. Further, the nominal damping coefficient, $\overline{C}_v$, related to the damper size, was selected to provide 11% damping in the fundamental lag mode. The present section examines the reductions in hub vibration levels that would be observed when these parameters are varied. It should be noted that when the parameters, α_v, e_v, L_v, and $\overline{C}_v$ are varied, the baseline vibration levels (without any semi-active inputs) may themselves change, and the optimal 2/*rev* and 3/*rev* variations in lag damping coefficient have to be re-evaluated.

Figure 8.7 shows the influence of the lag damper mounting angle, α_v, varied from 0 – 40 deg, on the vibration index, J_z, and the control effort index, J_u. For every value of α_v, the vibration levels are non-dimensionalized with respect to the uncontrolled vibration levels of the nominal configuration. From the figure, it is seen that the uncontrolled vibrations (no semi-active input) are relatively insensitive to changes in α_v. When optimal lag damping variations are introduced, slight additional reductions in vibration index (relative to the nominal) can be obtained for values of α_v in the 5 – 10 deg range. However, the control effort, J_u, increases substantially in this range. Conversely, the control effort can be reduced somewhat if α_v is increased beyond the nominal value of 20 deg, but the vibration index increases slightly. For values of α_v in the range of 15 – 40 deg the total performance index, *J*, the sum of J_z (with optimal damping variation) and J_u, shows little variation; which implies that any of these designs perform more-or-less comparably. However, as the mounting angle α_v increases, it may be difficult to install the device.

Figure 8.8 shows the influence of the lag damper offset, e_v, varied between 0.2*c* and 1.4*c* (nominal value is 1 *chord*). From the figure it is seen that for e_v varying between 0.7*c* and 1.4*c*, the uncontrolled vibrations (no semi-active input) are relatively unchanged. However, as the offset decreases below 0.7*c* – *(i)* the uncontrolled vibrations increase significantly, *(ii)* reductions in vibration index with optimal variations in lag damping coefficient are smaller, and *(iii)* the control effort, J_u, starts to decrease as well. The second and the third points suggest that the effectiveness of the semi-active inputs is diminishing when the offset becomes too small. From Eq. 2.34 it is deduced that since the nominal α_v is small, the controllable moments introduced by the damper on the blade would be quite important, and as e_v decreases, the damper is no longer able to effectively exert controllable lag bending moments on the blade. The total performance index, $J = J_z$ (with optimal damping variation) + J_u, is near its minimum for e_v ranging between *c* and 1.4*c*, so that any offset in this range would constitute a good choice. As e_v increases in this range, a slight increase in vibration index (relative to the nominal) is observed, but the control effort, J_u, decreases.

Figure 8.9 shows the influence of the lag damper attachment point on the blade, L_v, varying between 0.15*R* – 0.25*R* (nominal value is 0.2*R*). In general, as L_v increases, the uncontrolled vibrations, the vibration levels with optimal lag damping variations, and the control effort, all undergo very significant reductions. Of course larger values of L_v may be undesirable from a practical standpoint, which needs to be taken into consideration. It is also seen that as L_v decreases below 0.16*R*, the control effort index reduces, and the reductions in vibration index relative to the uncontrolled levels also diminish. An explanation for this is that the damper attachment point may be undergoing very limited motion, so that the effectiveness of the motion-dependent semi-active forces decreases. However, it should be noted that for articulated blades, or blades with a very soft flexure, this may not be the case and effectiveness of lag damping variations in reducing hub vibrations may be preserved even for low values of L_v.

Finally, the effect of varying the lag damper size from 70% to 150% of its nominal value, $\overline{C}_v$, is considered. In principle, larger reductions in vibration could potentially be obtained for larger cyclic variations in damping, ΔC_v. However, since the cyclic variations in damping coefficient are generally a fraction of $\overline{C}_v$, a larger $\overline{C}_v$ is required for greater semi-active authority. From Fig. 8.10, it is observed that the uncontrolled vibration levels (no semi-active inputs) are relatively insensitive to damper size. The vibration index with optimal lag damping variations also shows only mild changes with damper sizing. The control effort index, which depends on $\Delta C_v / \overline{C}_v$, reduces with increasing damper size, which suggests that the damper has not saturated, and would be unlikely to produce additional vibration reduction with larger cyclic variations in damping being possible. The limited reductions in vibration obtained may simply be due to the fact that the optimal inputs required to reduce F_y^{4p} may be conflicting with those reducing F_x^{4p} and M_z^{4p}.

8.3 Simultaneous flap and lag damping variations

The present section explores additional possible vibration reductions when 2/*rev* and 3/*rev* lag damping variations and 2/*rev* and 3/*rev* flap damping variations are introduced simultaneously. Changes in vibratory hub loads, blade root loads, flexbeam root loads, damper loads, and blade response due to optimal 2, 3/*rev* flap and lag damping variations are presented in Section 8.3.1. Section 8.3.2 examines the effectiveness of the flap and lag damping variations on hub vibration reduction for various forward speeds.

8.3.1 Influence of optimal 2,3/*rev* flap and lag damping variations

The effect of optimal 2, 3/*rev* flap and lag damping variations on hub vibration is examined in this section. The optimal lag and flap damping variations (amplitude and phase values) are presented in Table 8.8, and their time histories over one rotor revolution are shown in Fig. 8.11. From the figure, it is observed that the maximum variation in lag damping is 64% of the baseline value, $\overline{C}_v$, and the maximum variation in flap damping is 60% of the baseline value, $\overline{C}_w$ (well within the achievable range of controllable orifice dampers). For these optimal damping variations, the vibration index, J_z, is reduced by 47%, with corresponding reductions in individual components of vibratory hub loads shown in Fig. 8.12. As was the case when only lag damping variations were used, the vibratory hub drag force, F_x^{4p}, and vibratory hub yawing moment, M_z^{4p}, are basically eliminated, and a 10% reduction in the vibratory hub side force, F_y^{4p}, is seen. However, in addition, a 30% reduction in the vibratory hub vertical force, F_z^{4p}, is now observed, on account of the variations in flap damping coefficient. The vibratory hub pitching and rolling moments remain unaffected.

Figures 8.13 and 8.14 show the lag damper force and the flap damper force, respectively, over a rotor revolution, when the optimal multi-cyclic damping variations in Table 8.8 are used. Also shown in the figures is the reference damper force without any semi-active damping variations. From Fig. 8.13, the peak-to-peak lag damper force levels do not undergo any significant change, relative to the baseline, although some high-frequency content is now introduced in the damper force. Table 8.9 indicates that there are increases of approximately 90%, 150%, 30%, and 55%, respectively, in the 2nd through 5th harmonics of the lag damper force. As in section 8.2.1, the higher harmonic loads introduced by the lag damper will modify the blade lag response so as to reduce vibratory in-plane hub forces and yawing moment. From Fig. 8.14, the peak-to-peak flap damper force is seen to actually reduce by some 70 lbs, and Table 8.9 indicates that there are no increases in any of the flap damper force harmonics due to optimal damping variations. It is interesting to compare how the flap and the lag dampers reduce vibration. The lag damper actually generates higher harmonic semi-active forces, which increase the higher harmonics in blade lag response. The modified lag response, in turn, generates higher harmonic blade drag shear forces to cancel the vibratory radial shear contributions to the in-plane hub forces. The effect of the flap damper, in contrast, is to reduce the blade vertical shear forces (the only contributors to the hub vertical vibratory forces), thereby reducing the hub vertical vibrations.

Table 8.10 shows variation in harmonics of blade root loads when the optimal flap and lag damping variations in Table 8.8 are used. The controllable flap and lag dampers are expected to influence only specific components of blade root loads, particularly S_r, S_x, and M_ζ (by the lag damper) and S_z and M_β (by the flap damper). As in Section 8.2.1, large percentage increases in the 3/*rev* and 5/*rev* components of blade root drag shear, S_x, are observed, which (along with some modest reductions in the 3rd and 5th harmonics of S_r) contribute to the elimination of F_x^{4p}. Also seen in Table 8.10 are reductions of around 30% in the 4th harmonic of S_z and nearly 100%

in the 4th harmonic of M_{ζ}, which produce the corresponding reductions in F_z^{4p} and M_z^{4p} seen in Fig. 8.12. Small reductions in all harmonics of blade root flapping moment, M_{β}, are also observed, although the reductions in the 3rd harmonic are insignificant and therefore do not reduce the rotor hub vibratory rolling and pitching moments, M_x^{4p} and M_y^{4p}. Changes in harmonics of M_{ϕ} are primarily due to nonlinear coupling effect and are considered insignificant (since the corresponding baseline values are very small), but are presented for completeness.

Changes in harmonics of flexbeam root loads due to optimal flap and lag damping variation are presented in Table 8.11. Components of the flexbeam root loads that are directly affected by the lag damping variation are S_r^{flex}, S_x^{flex}, and M_{ζ}^{flex}, while the flap damping variation directly affects only S_z^{flex} and M_{β}^{flex}. The 2nd harmonic of S_x^{flex} reduces by around 55%, but large increases in the 3rd, 4th and 5th harmonics are observed, similar to the results presented previously in Section 8.2.1. It is interesting to note that even as the 4th harmonic of S_z reduces by 30% (Table 8.10), the 4th harmonic of S_z^{flex} is showing a 24% increase (Table 8.11). Clearly, the loads at the root of the flexbeam (Eq. 2.38) are being cancelled by the loads coming in at the damper (Eq. 2.39), so that the 4th harmonic of the "total" blade root vertical shear (Eq. 2.40) is reduced. Similarly, the 4th harmonic of the flexbeam root lag moment, M_{ζ}^{flex}, shows a reduction of only 38% and the additional lag moment introduced by the damper results in the elimination of the 4th harmonic of the "total" blade root lag moment, M_{ζ}, seen in Table 8.10.

Figure 8.15 shows the blade flap, lag, and torsion tip responses over one rotor revolution. Comparing with the response for the baseline rotor, the cyclic variations in flap and lag damping do not appear to have had any significant influence. However, the higher harmonic lag damper loads do in fact introduce higher harmonics in tip lag response, as seen in Table 8.12. The changes in the tip flap response are much more modest, consistent with the smaller changes in higher harmonic flap damper loads.

8.3.2 Effectiveness of flap and lag damping variations at different flight speeds

This section examines the effectiveness of 2/*rev* and 3/*rev* flap and lag damping variations for vibration reduction over a range of flight speeds. Figure 8.16 shows the vibration performance index, J_z, with and without the multi-cyclic damping variations, over forward speeds ranging from advance ratio of 0.30 to 0.375 (the optimal damping variations are re-calculated at different flight speeds). The vibration performance index is normalized with respect to the baseline (uncontrolled) vibrations at an advance ratio of 0.35 given in Table 8.2a, (corresponding to J_z = 100). It is seen that as the advance ratio increases from 0.35 to 0.375, the uncontrolled vibration index increases from 100 to 165. As the advance ratio decreases from 0.35 to 0.30, the uncontrolled vibration index again increases from 100 to 245, due to the dominant effect of the rotor wake at the lower speeds. With optimal 2/*rev* and 3/*rev* flap and lag damping variations, the vibration index shows reductions across the advance ratio range. The reductions in J_z, relative to the uncontrolled case, range from 45% at $\mu = 0.30$, to 32% $\mu = 0.325$, to 47% at $\mu = 0.35$ (nominal flight speed in this study), and to 43% at $\mu = 0.375$. The control effort index, J_u, shows only mild variations over the range of forward speeds considered, despite the large differences in the uncontrolled vibration levels.

8.4 Summary on controllable orifice dampers

Using the controllable orifice dampers, it was shown that cyclically varying the damping coefficient of controllable lag and flap dampers could reduce the 4/*rev* vibratory hub loads. The results showed that optimal 2/*rev* and 3/*rev* lag damping variations could virtually eliminate the vibratory hub drag force and yawing moments, and produce small reductions in the vibratory hub side force without detrimental effect on blade response, damper loads, and blade and flexbeam root loads. When optimal 2/*rev* and 3/*rev* variations in flap damping were introduced in conjunction with the optimal lag damping variations, 30% reductions in the hub vertical vibrations were obtained, in addition to the reductions in the vibratory in-plane forces and yawing moment. Reductions in hub vibration levels were obtained over a range of forward flight speeds.

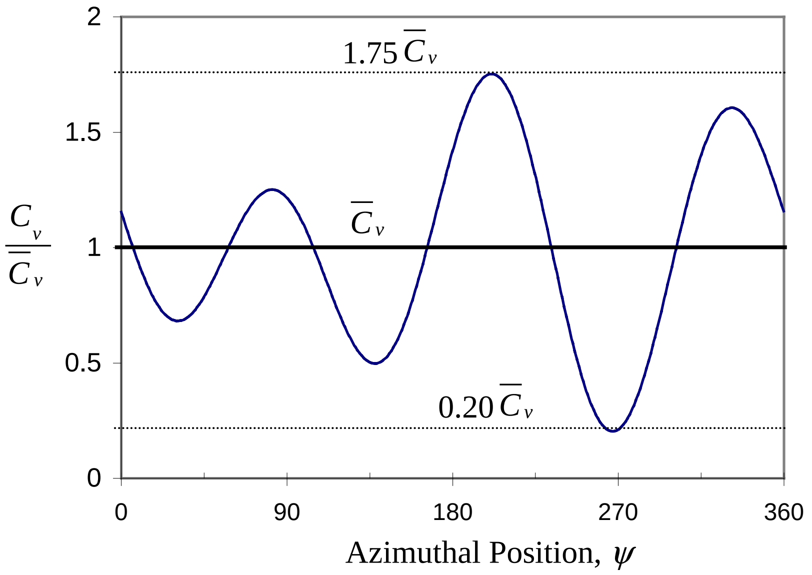

Figure 8.1: Optimal lag damping variation over one rotor revolution (with 2/*rev* and 3/*rev* inputs from Table 8.3)

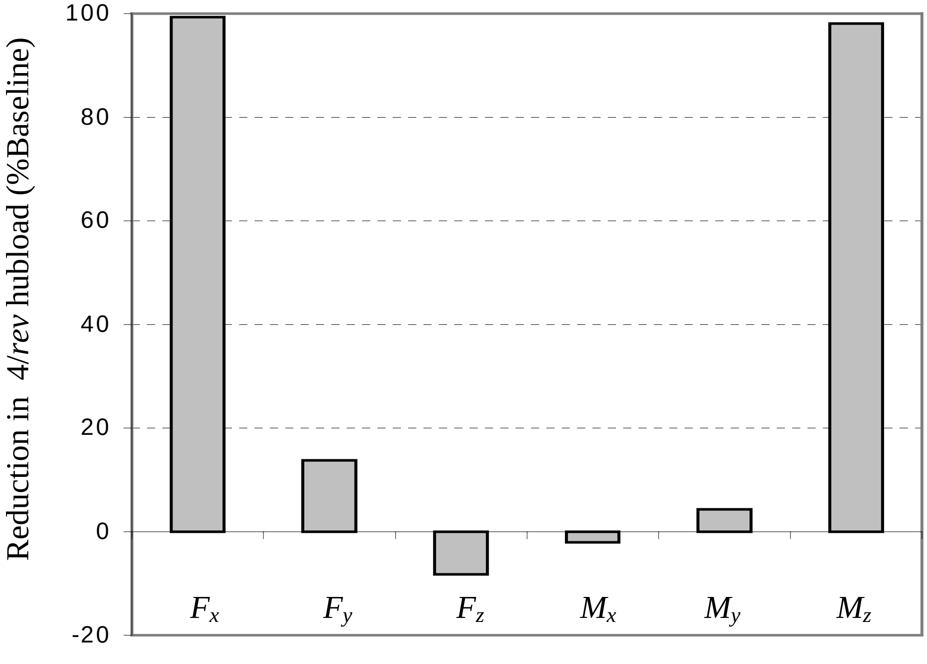

Figure 8.2: Hub vibration reduction due to optimal 2, 3/*rev* lag damping variation

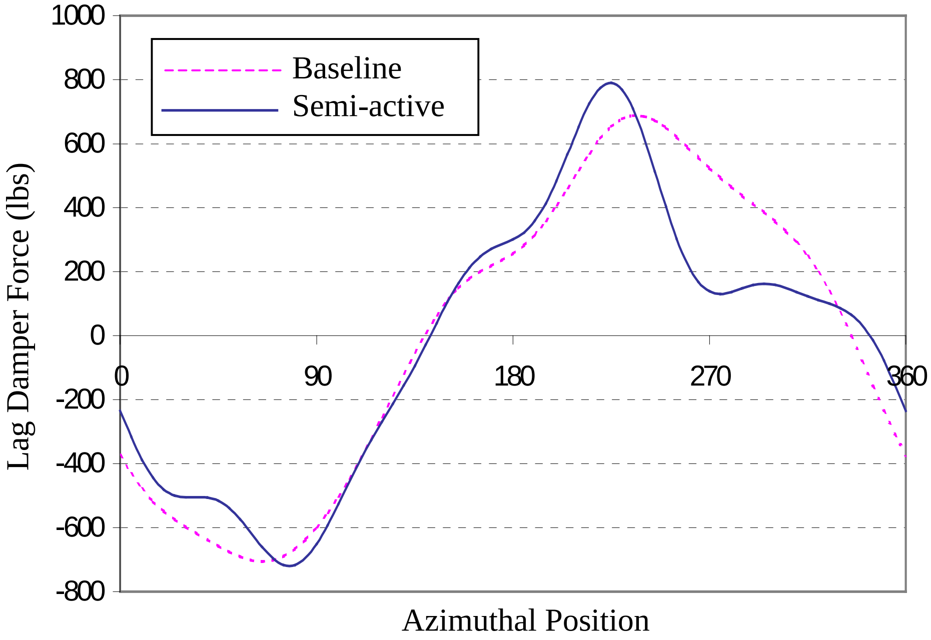

Figure 8.3: Lag damper force variation over one rotor revolution (with optimal semi-active lag damping variation from Table 8.3)

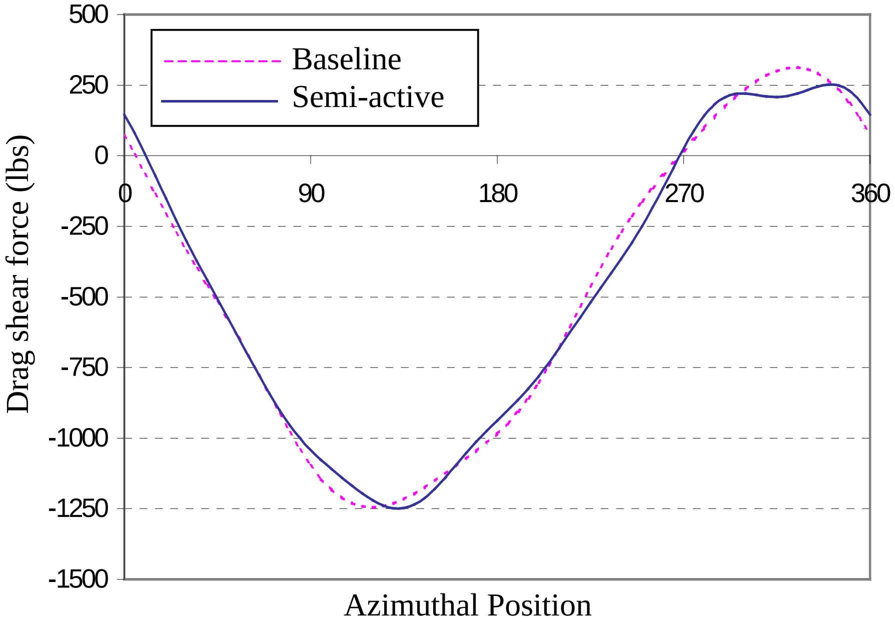

(a)

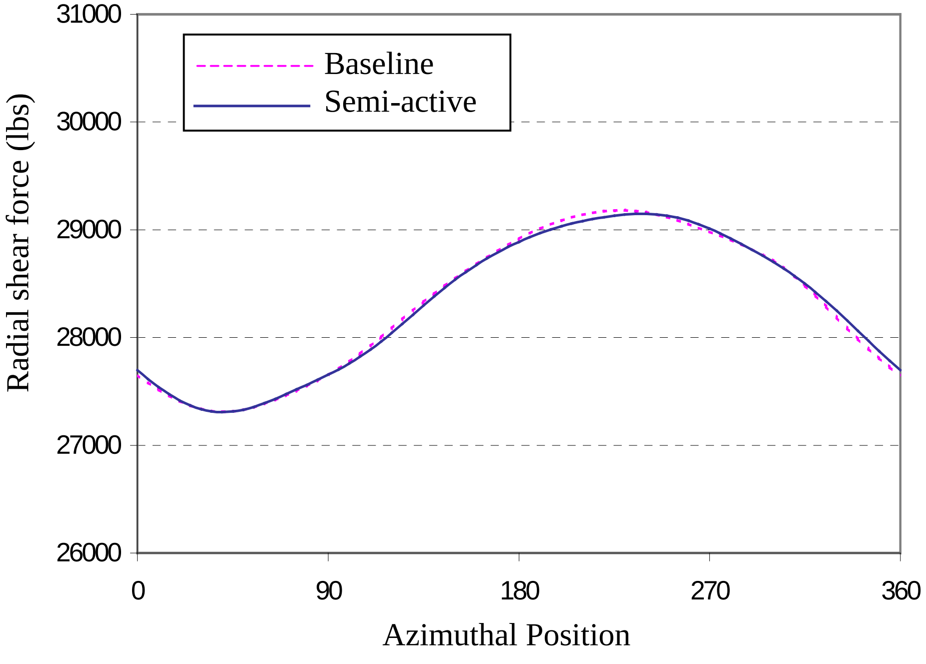

(b)

Figure 8.4: Blade root loads over one rotor revolution (with optimal semi-active lag damping variation from Table 3), (a) blade root drag shear, S_x, and (b) blade root radial shear, S_r

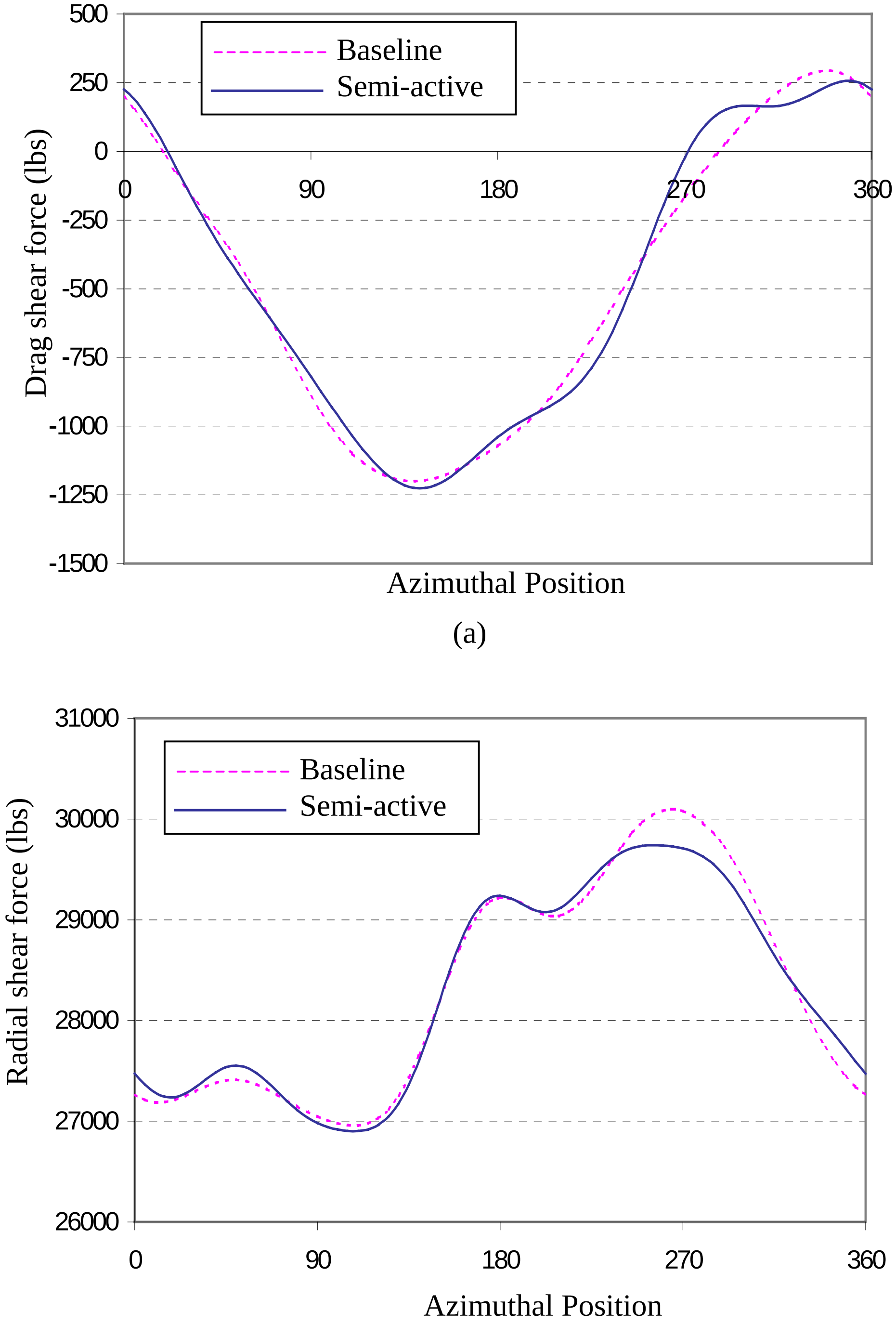

(a)

(b)

Figure 8.5: Flexbeam root loads over one rotor revolution (with optimal semi-active lag damping variation from Table 8.3), (a) flexbeam root drag shear, S_x^{flex}, and (b) flexbeam root radial shear, S_r^{flex}

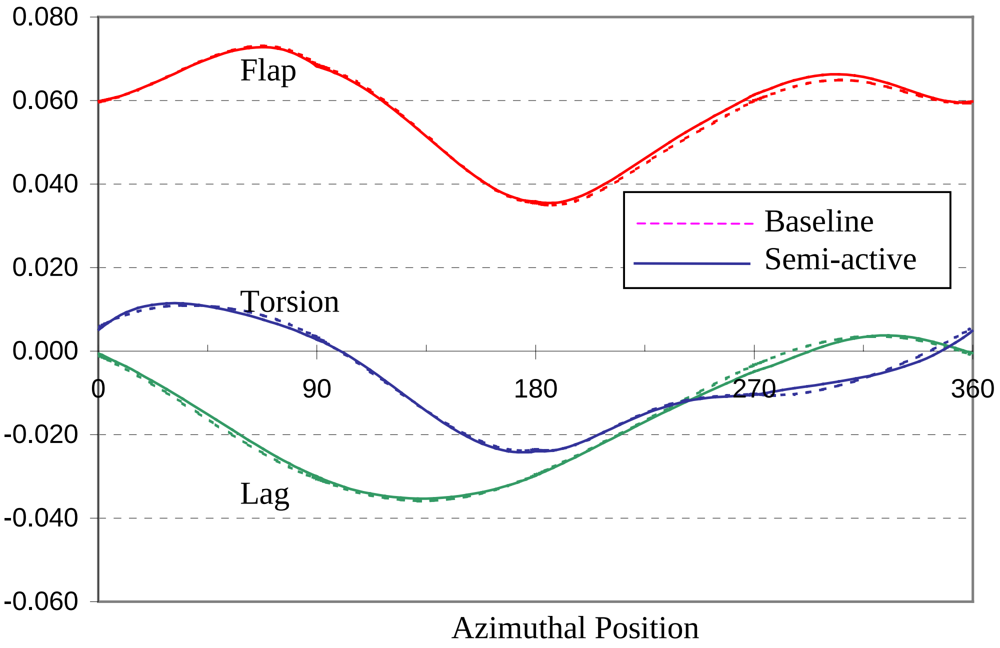

Figure 8.6: Blade flap, lag, and torsional tip responses over one rotor revolution (with optimal semi-active lag damping variation from Table 8.3)

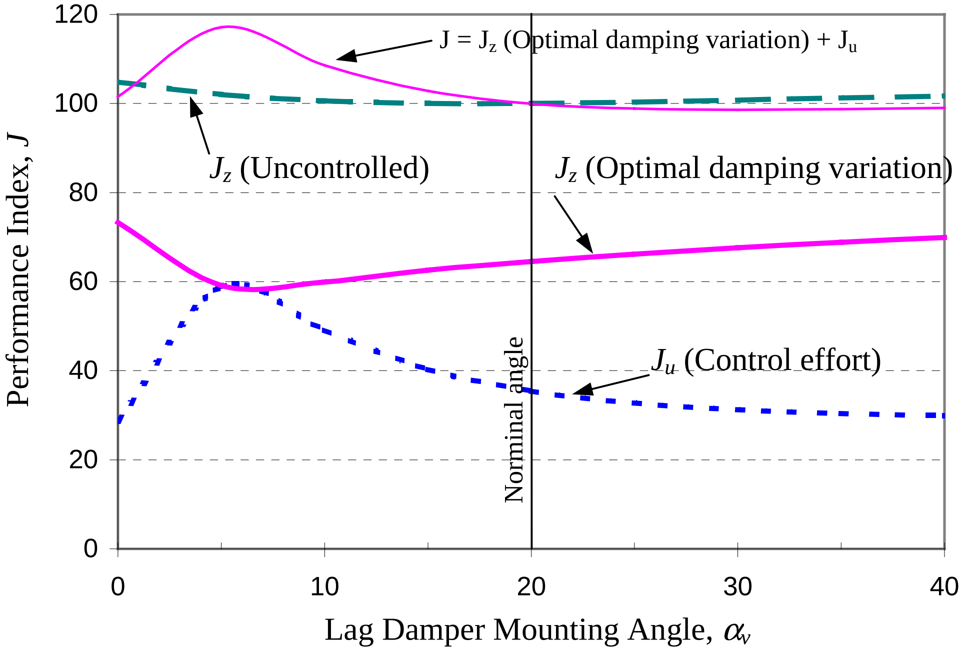

Figure 8.7: Effectiveness of lag damping variation in reducing vibration for different damper mounting angles

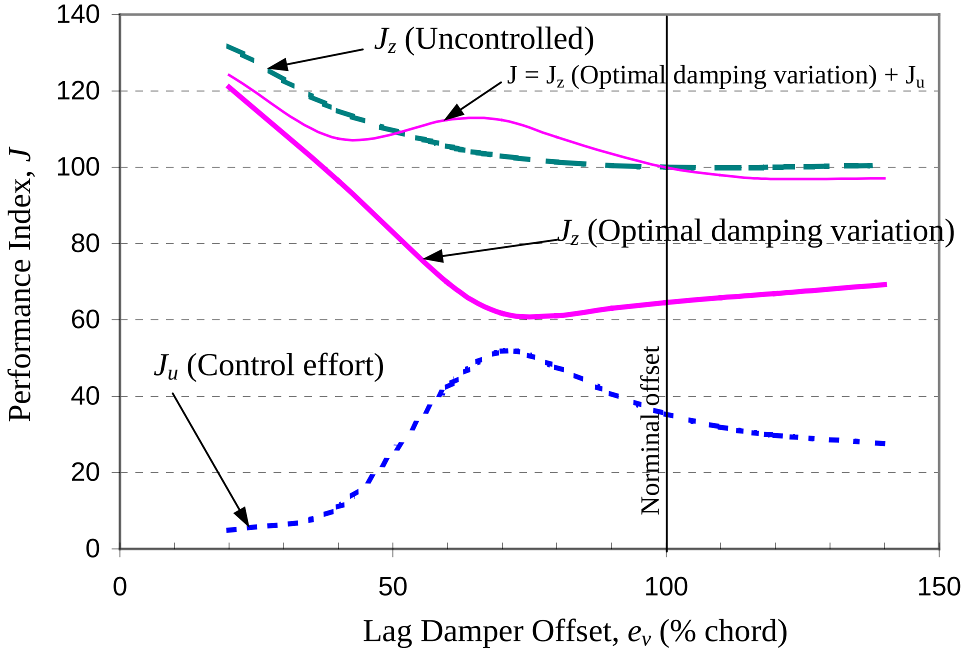

Figure 8.8: Effectiveness of lag damping variation in reducing vibration for different damper offsets

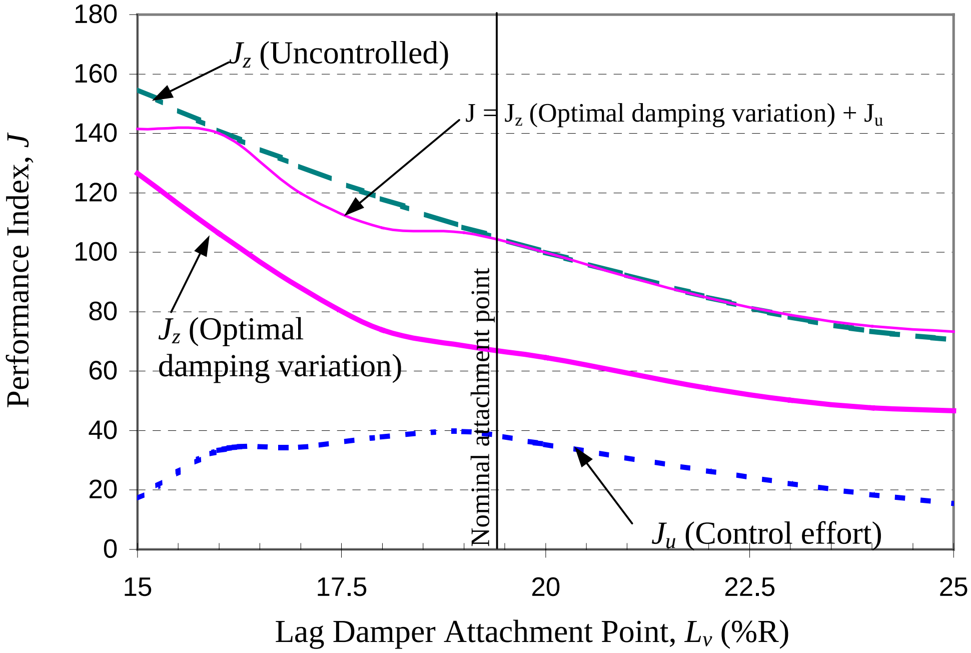

Figure 8.9: Effectiveness of lag damping variation in reducing vibration for different damper attachment points

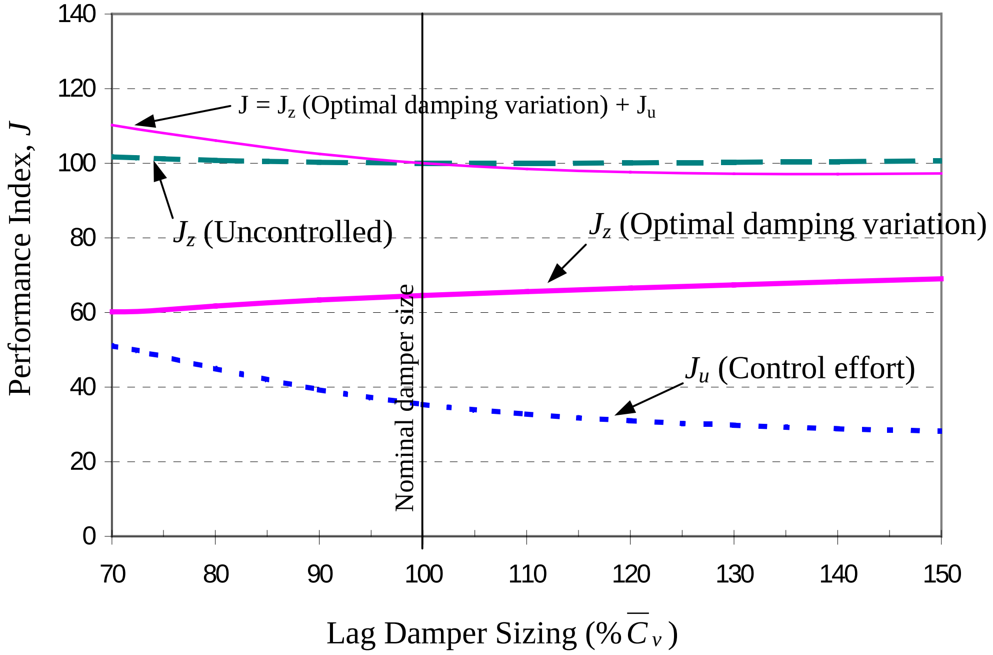

Figure 8.10: Effectiveness of lag damping variation in reducing vibration for different damper sizes

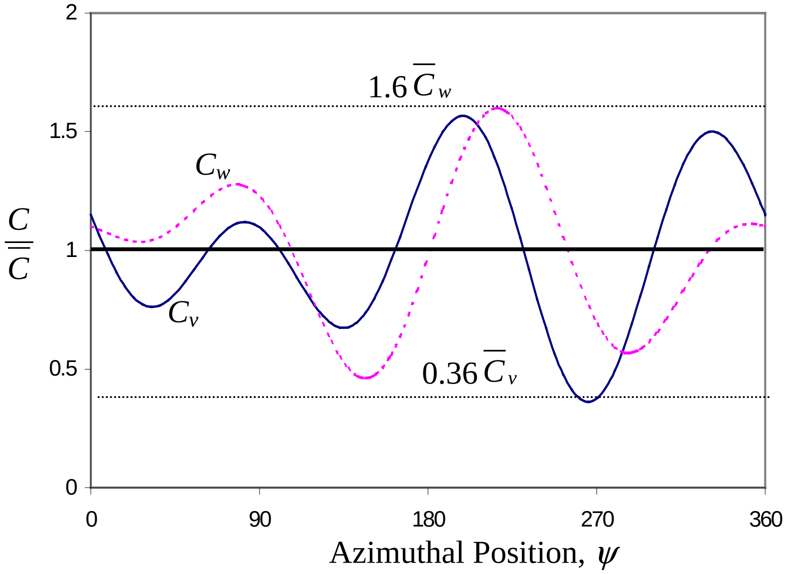

Figure 8.11: Optimal flap and lag damping variations over one rotor revolution (with 2/*rev* and 3/*rev* inputs from Table 8.8)

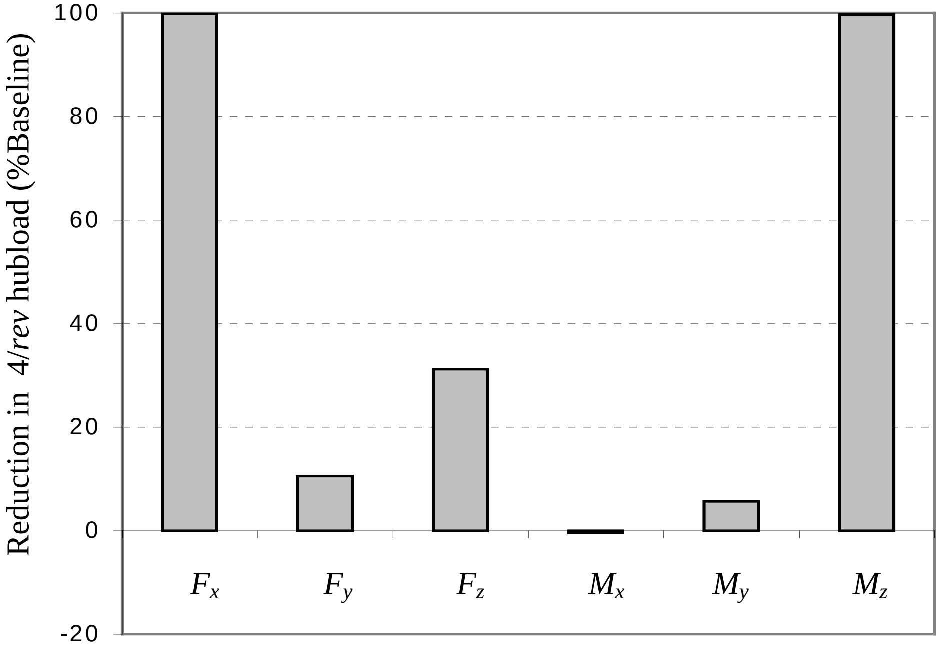

Figure 8.12: Hub vibration reduction due to optimal 2, 3/rev flap and lag damping variations

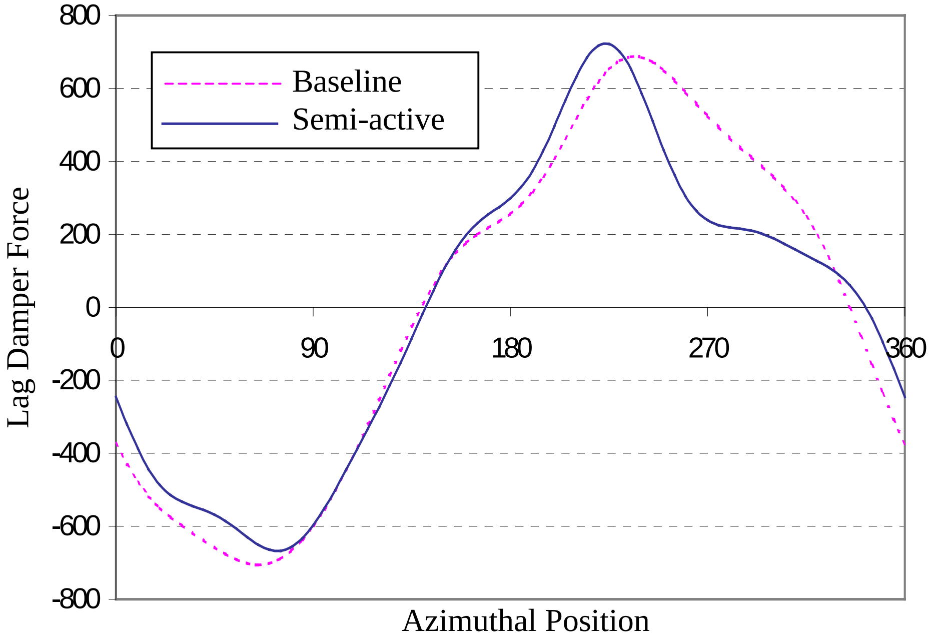

Figure 8.13: Lag damper force variation over one rotor revolution (with optimal semi-active flap and lag damping variations from Table 8.8)

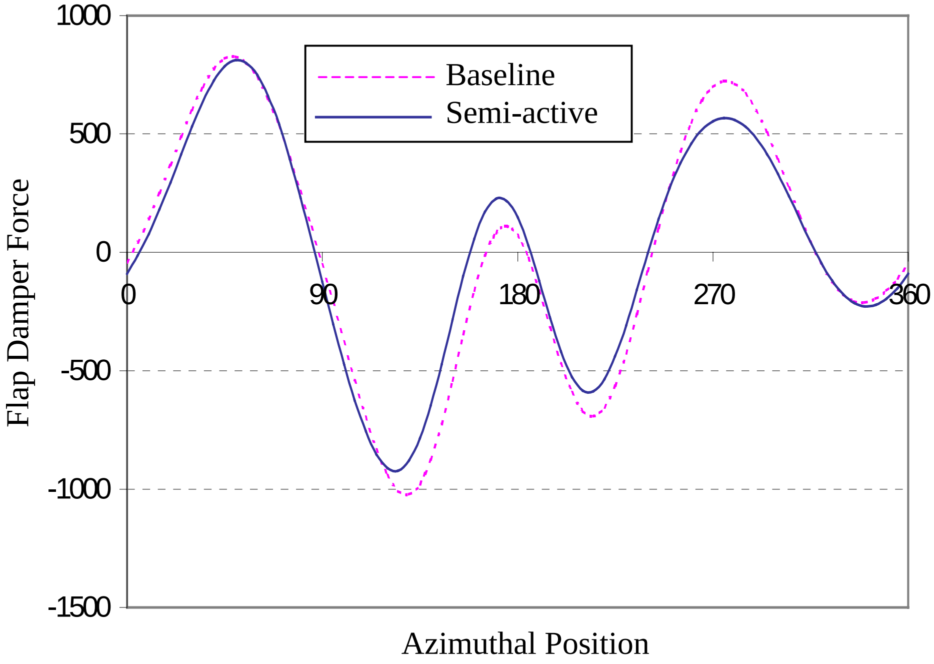

Figure 8.14: Flap damper force variation over one rotor revolution (with optimal semi-active flap and lag damping variations from Table 8.8)

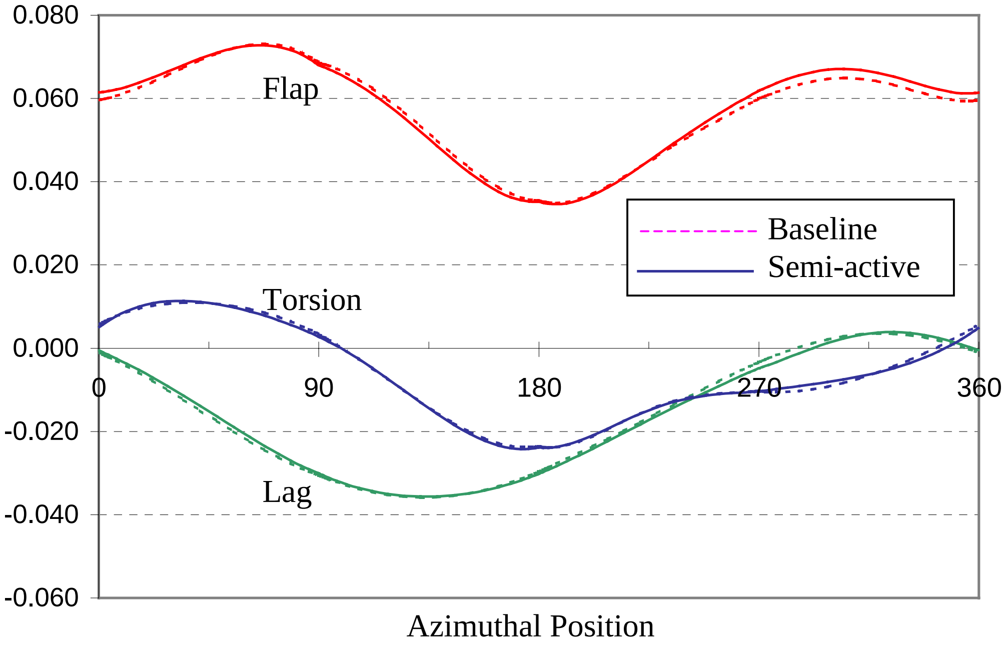

Figure 8.15: Blade flap, lag, and torsional tip responses over one rotor revolution (with optimal semi-active flap and lag damping variations from Table 8.8)

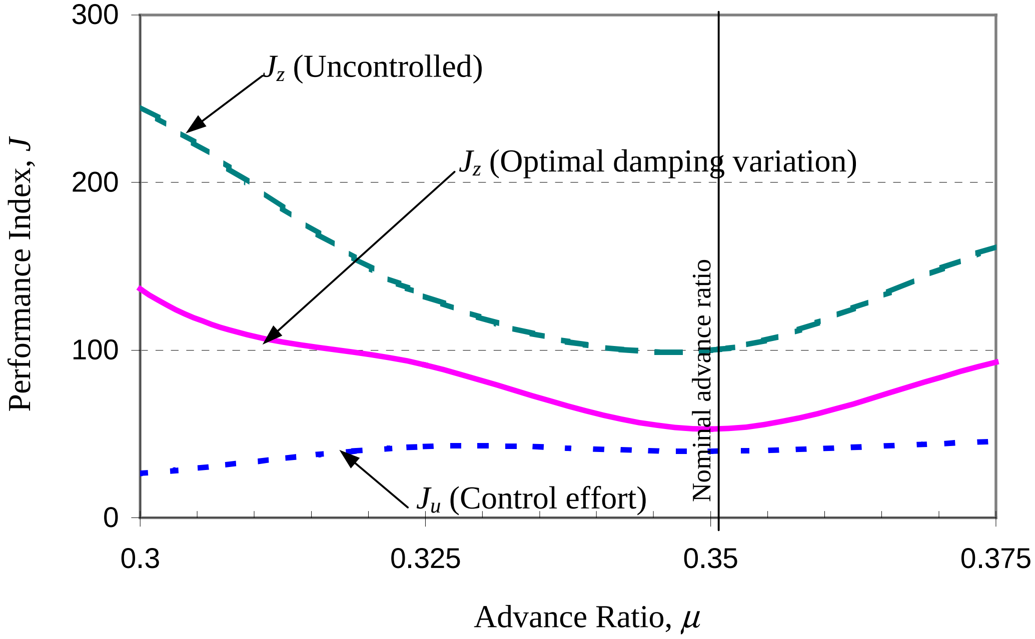

Figure 8.16: Effectiveness of optimal 2, 3/rev flap and lag damping variations for different advance ratios

Controllable Damper Properties	$\overline{C}_w$	8% (1st flap mode)
	$\overline{C}_v$	11% (1st lag mode)
	α_w, α_v	30°, 20°
	L_w, L_v	0.2R
	e_w, e_v	c
Blade Natural Frequencies	Flap	1.147, 3.405, 7.508, 13.601/*rev*
	Lag	0.750, 4.372, 11.073, 21.137/*rev*
	Torsion	4.590, 13.604/*rev*

Table 8.1: Discrete controllable damper properties and blade frequencies

Vibratory Hub Loads [*]	
F_x^{4p}	0.5960
F_y^{4p}	1.3484
F_z^{4p}	6.7270
M_x^{4p}	31.0628
M_y^{4p}	45.4364
M_z^{4p}	8.3403

Table 8.2a: 4/*rev* vibratory hub loads for baseline rotor, no cyclic damping variation

Blade Root Loads	Harmonics [**]				
	1/*rev*	2/*rev*	3/*rev*	4/*rev*	5/*rev*
S_r	0.0162315	0.0013585	0.0004744	0.0002330	0.0001373
S_x	0.0133722	0.0007594	0.0000419	0.0005449	0.0000679
S_z	0.0043653	0.0020158	0.0043754	0.0017716	0.0010215
M_ϕ	0.0000960	0.0000360	0.0000087	0.0000005	0.0000026
M_β	0.0015967	0.0007553	0.0013771	0.0005467	0.0002586
M_ζ	0.0040404	0.0001995	0.0000215	0.0001496	0.0000155

Table 8.2b: Harmonics of blade root loads for baseline rotor, no cyclic damping variation

Flexbeam Root Loads	Harmonics [**]				
	1/*rev*	2/*rev*	3/*rev*	4/*rev*	5/*rev*
S_r^{flex}	0.0254709	0.0036988	0.0069444	0.0022150	0.0012934
S_x^{flex}	0.0128488	0.0007105	0.0001206	0.0003878	0.0001240
S_z^{flex}	0.0024654	0.0012152	0.0015691	0.0008342	0.0003226
M_ϕ^{flex}	0.0000960	0.0000360	0.0000087	0.0000005	0.0000026
M_β^{flex}	0.0005831	0.0003394	0.0002595	0.0001058	0.0000222
M_ζ^{flex}	0.0049912	0.0002996	0.0000813	0.0002735	0.0000458

Table 8.2c: Harmonics of flexbeam root loads for baseline rotor, no cyclic damping variation

---

[*] All vibratory hub forces are in % of F_z^0 (6016 lbs.), all vibratory hub moments are in % of M_z^0 (6654 ft-lbs.)

[**] Root shear are non-dimensionalized by $m_o\Omega^2R^2$, root moments are non-dimensionalized by $m_o\Omega^2R^3$

Damper loads	Harmonics[*]				
	1/*rev*	2/*rev*	3/*rev*	4/*rev*	5/*rev*
Lag Damper Force	0.0115328	0.0009755	0.0004394	0.0009092	0.0002112
Flap Damper Force	0.0072865	0.0056419	0.0082052	0.0032957	0.0014002

Table 8.2d: Harmonics of damper loads for baseline rotor, no cyclic damping variation

Tip Responses	Harmonics				
	1/*rev*	2/*rev*	3/*rev*	4/*rev*	5/*rev*
Flap (w_{tip}/R)	0.0137415	0.0085815	0.0006332	0.0009103	0.0000420
Lag (v_{tip}/R)	0.0196645	0.0008083	0.0001069	0.0001341	0.0000135
Torsion (Rad.)	0.0148971	0.0050936	0.0014854	0.0001077	0.0002467

Table 8.2e: Harmonics of blade tip response for baseline rotor, no cyclic damping variation

Input		Amplitude ($\Delta C_v/\overline{C}_v$)	Phase
Lag damping variation	2/*rev*	29 %	80°
	3/*rev*	52 %	-165°

Table 8.3: Optimal 2,3/*rev* lag damping variation (J_z = 64.55)

	Change in harmonics (% Baseline)				
	1/*rev*	2/*rev*	3/*rev*	4/*rev*	5/*rev*
Lag Damper Force	-13.48	139.98	193.43	85.89	57.04
Flap Damper Force	-0.03	-4.24	-3.28	4.52	-14.69

Table 8.4: Change in harmonics of damper loads, due to optimal lag damping variation (from Table 8.3)

---

[*] Damper forces are non-dimensionalized by $m_o\Omega^2R^2$

Blade Root Loads	Change in Harmonics (% Baseline)				
	1/*rev*	2/*rev*	3/*rev*	4/*rev*	5/*rev*
S_r	-1.89	10.11	-16.43	77.52	-49.01
S_x	-2.49	19.77	154.15	5.03	275.36
S_z	-4.57	1.74	-1.42	8.37	-15.51
M_ϕ	0.50	0.00	-5.18	906.67	62.89
M_β	-3.72	-0.03	-1.39	7.70	-17.66
M_ζ	-4.34	75.85	95.54	-98.05	208.67

Table 8.5: Change in harmonics of blade root loads, due to optimal lag damping variation (from Table 8.3)

Flexbeam Root Loads	Change in harmonics (% Baseline)				
	1/*rev*	2/*rev*	3/*rev*	4/*rev*	5/*rev*
S_r^{flex}	-6.76	-24.43	-16.05	17.77	-32.11
S_x^{flex}	0.55	-51.08	350.08	196.39	97.09
S_z^{flex}	-20.78	-2.47	-9.27	18.14	-14.35
M_ϕ^{flex}	0.50	0.00	-5.18	906.67	62.89
M_β^{flex}	-22.12	-1.91	-13.33	30.79	-50.67
M_ζ^{flex}	-9.00	128.35	179.35	-10.33	93.14

Table 8.6: Change in harmonics of flexbeam root loads, due to optimal lag damping variation (from Table 8.3)

Tip Response	Change in Harmonics (% Baseline)				
	1/*rev*	2/*rev*	3/*rev*	4/*rev*	5/*rev*
Lag	-2.14	43.56	160.53	61.26	97.93

Table 8.7: Change in harmonics of blade tip lag response, due to optimal lag damping variation (from Table 8.3)

Input		Amplitude	Phase
Flap damping variation	2/*rev*	$\Delta C_w = 33\ \%\overline{C}_w$	7°
	3/*rev*	$\Delta C_w = 27\ \%\overline{C}_w$	167°
Lag damping variation	2/*rev*	$\Delta C_v = 26\ \%\overline{C}_v$	92°
	3/*rev*	$\Delta C_v = 38\ \%\overline{C}_v$	-163°

Table 8.8: Optimal 2, 3/*rev* flap and lag damping variations ($J_z = 52.87$)

	Change in harmonics (% Baseline)				
	1/*rev*	2/*rev*	3/*rev*	4/*rev*	5/*rev*
Lag Damper Force	-12.33	87.53	147.88	30.46	55.56
Flap Damper Force	-23.14	-13.95	-0.27	-8.52	-18.61

Table 8.9: Change in harmonics of damper loads, due to optimal flap and lag damping variations (from Table 8.8)

Blade Root Loads	Change in Harmonics (% Baseline)				
	1/*rev*	2/*rev*	3/*rev*	4/*rev*	5/*rev*
S_r	-0.67	8.88	-14.69	38.76	-32.13
S_x	-1.19	16.21	176.11	-21.87	296.68
S_z	8.01	-0.60	-6.00	-31.15	-13.21
M_ϕ	0.69	1.06	-8.75	671.11	21.48
M_β	-5.62	-9.51	-2.59	-20.75	-19.29
M_ζ	-2.67	58.48	36.80	-99.71	280.45

Table 8.10: Change in harmonics of blade root loads, due to optimal flap and lag damping variations (from Table 8.8)

Flexbeam Root Loads	Change in harmonics (% Baseline)				
	1/*rev*	2/*rev*	3/*rev*	4/*rev*	5/*rev*
S_r^{flex}	-4.21	-38.39	-10.81	22.92	-33.30
S_x^{flex}	1.64	-54.67	300.32	114.10	54.89
S_z^{flex}	1.73	8.88	-0.06	23.79	8.13
M_ϕ^{flex}	0.69	1.06	-8.75	671.11	21.48
M_β^{flex}	10.29	6.04	-1.73	42.25	42.00
M_ζ^{flex}	-7.32	92.77	128.37	-37.86	128.40

Table 8.11: Change in harmonics of flexbeam root loads, due to optimal flap and lag damping variations (from Table 8.8)

Tip Response	Change in Harmonics (% Baseline)				
	1/*rev*	2/*rev*	3/*rev*	4/*rev*	5/*rev*
Flap	5.64	0.33	10.65	-19.58	-9.90
Lag	-0.87	34.45	155.05	21.30	134.52

Table 8.12: Change in harmonics of blade tip flap and lag responses, due to optimal flap and lag damping variations (from Table 8.8)

Chapter 9

Semi-Active Isolator

The results presented in Chapters 4-8 showed that semi-active controllable stiffness and damping devices introduced in the rotor system were effective in reducing hub vibration, at the source. The current chapter examines another possible application of semi-active devices in reducing helicopter vibration – by introducing these devices in the fixed system, between the rotor hub and the fuselage (as semi-active isolators), so that the incoming vibratory loads transmitted to the fuselage are reduced. A simplified single degree of freedom system is used to represent the semi-active isolation system. The rotor (represented by a lumped mass under harmonic force excitation) is supported by a spring and a parallel damper on the fuselage (assumed to have infinite mass). Properties of the spring or damper could then be controlled to reduce transmission of the force into the fuselage or the support structure. Variations in the properties (stiffness or damping) of semi-active isolators are calculated using; *(i)* open loop, *(ii)* closed-loop, and *(iii)* closed-loop adaptive control schemes. Section 9.1 describes the basic configuration of the isolation system including the semi-active devices. Development of open-loop, closed-loop, and adaptive controllers are provided in Sections 9.2 and 9.3. Effectiveness of the controllers in reducing force transmission is examined in Section 9.4 using semi-active controllable stiffness and damping devices. Section 9.5 summarizes the results for this semi-active isolation technique.

9.1 System description

The effectiveness of the semi-active controller for vibration reduction is evaluated for a simple single-degree-of-freedom (SDOF) system shown in Fig. 9.1. The mass, m, supported on a spring and a parallel damper, is subjected to a harmonic vibratory force, F, at frequency, Ω. A mathematical model of the system with the controllable stiffness and damping devices is presented in Section 9.1.1 and 9.1.2, respectively.

9.1.1 System with controllable stiffness device

A mathematical model of the vibration control system using controllable stiffness device (see Fig. 9.1a) is developed in this section. Reduction of the support force F_s at frequency Ω is achieved by optimally modulating the stiffness of the semi-active controllable spring. The total stiffness of the semi-active spring is assumed to varied as follows:

$$K(t) = K_o + K_1 u(t) \tag{9.1}$$

where K_o represents the baseline (passive) stiffness, and $K_1 u(t)$ represents the variation in stiffness due to the command input u. Without any modulation of the stiffness (u = 0), the baseline spring, K_o, in parallel with the damper, C_o, provides a passive isolation treatment between the vibratory force and the support.

The equilibrium equation for the system in Fig. 9.1a, and the corresponding force at the support, can be expressed as:

$$m\ddot{x} + C_o\dot{x} + (K_o + K_1 u)x = F = F_o \sin(\Omega t) \tag{9.2a}$$

$$F_s = C_o\dot{x} + (K_o + K_1 u)x \tag{9.2b}$$

The bilinear term, ux, which appears in the above equations (such a bilinear term appears in most semi-active systems), makes it difficult to apply conventional linear control theories.

9.1.2 System with controllable damper

A model representing a vibration control system using a controllable damper (see Fig. 9.1b) is described in this section. The vibratory support force, F_s, will be reduced through optimal modulation of the damping coefficient of the controllable damper. It is assumed that the damping coefficient of the controllable damper can be varied as

$$C(t) = C_o + C_1 u(t) \tag{9.3}$$

where C_o is the baseline (passive) damping, and $C_1u(t)$ represents the damping variation due to command input u. In the absence of any modulation of the damping coefficient (zero command input, u), the spring, K_o, and the baseline damper, C_o, provide passive isolation.

From Fig. 9.1b, the equilibrium equation and the corresponding force at the support, can be derived as;

$$m\ddot{x} + (C_o + C_1 u)\dot{x} + K_o x = F = F_o \sin(\Omega t) \tag{9.4a}$$

$$F_s = (C_o + C_1 u)\dot{x} + K_o x \tag{9.4b}$$

In the above equations the bilinear term, $u\dot{x}$, complicates the control system design.

9.2 Fundamentals of Controller Design

This section describes basic components of the semi-active controller. The vibration reduction controller is derived using an optimal control scheme in the frequency-domain (see Section 9.2.1). Semi-active input saturation is also incorporated by scaling down the input whenever saturation limits are exceeded (Section 9.2.2). Selection of frequency content of the semi-active input, which provides vibration reduction, is described in detail in Section 9.2.3. System identification method, which is the key component of an adaptive controller, is described in Section 9.2.4.

9.2.1 Optimal semi-active control scheme

For vibration reduction using the semi-active devices (controllable stiffness device or damper), an optimal controller is developed in the frequency-domain, as an adaptation of an approach previously used in Ref. 117 for vibration reduction through pure active control. The basic approach is conceptually similar to that previously presented in Chapter 3, but is repeated here for the SDOF system; and thereafter extended to account for semi-active device, saturation concerns, and adaptive control implementation. The vibratory force at the support, F_s, and the command input, u, are expressed in the frequency-domain (as cosine and sine components of specified harmonics), and are denoted as z and u_c, respectively (defined later in Section 9.2.3).

The harmonics of u_c are carefully selected to reject the incoming vibration at frequency Ω (details provided in Section 9.2.3). The control algorithm is based on the minimization of a quadratic objective function, *J*, defined as:

$$J = z^T W_1 z + {u_c}^T W_2 u_c \tag{9.5}$$

In Eq. 9.5, W_1 and W_2 represent penalty weighting corresponding to the vibratory force at the support, *z*, and the input, u_c, respectively.

Due to the bilinear terms (see Eq. 9.2 or Eq. 9.4), the relationship between the input, u_c, and the support vibration, *z*, is not linear. However, it is assumed that the vibrations, *z*, are related to the frequency-domain inputs, u_c, as follows:

$$z = z_o + T u_c \tag{9.6}$$

where *T* is the system transfer matrix, and z_o represents the baseline support vibration levels without the input, u_c. The transfer matrix, *T*, can be calculated using both off-line and on-line approaches (detailed discussion is presented in Section 9.2.4). A gradient-based method is used to minimize *J* and determine the optimal inputs, u_c. By substituting Eq. 9.5 into Eq. 9.6 and setting $\partial J/\partial u_c = 0$, the resulting optimal input may be obtained as:

$$u_c = \overline{T} z_o \tag{9.7a}$$
$$\overline{T} = -\left(T^T W_1 T + W_2\right)^{-1} T^T W_1 \tag{9.7b}$$

A Frequency-to-Time domain conversion (F/T) unit is used to obtain the optimal time-domain input, *u(t)*, corresponding to the frequency-domain input, u_c (see Fig. 9.2)

9.2.2 Semi-active device saturation consideration

To ensure that maximum or minimum values of physically achievable device properties (stiffness or damping coefficient) are not exceeded, the input, u_c, will be modified if necessary. The semi-active controllable stiffness device has a baseline stiffness of K_o, and it is assumed that the maximum and minimum physically achievable values of stiffness are $K_o + K_1$ and $K_o - K_1$, respectively. Similarly, the semi-active controllable damper, which has a baseline damping coefficient, C_o, is assumed to vary between the maximum and minimum physically achievable values of damping coefficient of $C_o + C_1$ and $C_o - C_1$, respectively. Typically, the terms C_1 and K_1 could be expressed in term of fraction of K_o and C_o, and in this chapter they are assumed to be as follows:

$$K_1 = 0.7 K_o \tag{9.8a}$$

$$C_1 = 0.75 C_o \tag{9.8b}$$

From Eqs. 9.1 and 9.8a (for controllable stiffness device) and Eqs 9.3 and 9.8b (for controllable damper), it can be deduced that the range of the nondimensional semi-active input *u(t)* is:

$$-1 \le u \le 1 \tag{9.9}$$

The amplitude of optimal frequency-domain input, $u_{\max}$, is determined after u_c is determined using Eq. 9.7, and if $|u_{\max}|$ exceeds the maximum permissible value (of unity), then the semi-active input, u_c, will be “scaled down” as follows:

$$\bar{u}_c = \frac{u_c}{u_{\max}} \tag{9.10}$$

However, with such a scaling-down there is a question regarding the optimality of the input signal. Alternately, the input can be reduced by increasing the input penalty weight, W_2.

9.2.3 Frequency content of the semi-active input

In order to reduce vibration at frequency, Ω, higher harmonic semi-active inputs are required. This is different from a fully active system where the control input, u_c, would simply consist of cosine and sine components at the disturbance frequency, Ω, which would essentially minimize the support vibrations, z, at Ω. However, for a semi-active controller input at Ω (producing stiffness or damping variation at Ω), it is seen from Eqs. 9.2 and 9.4 that the resulting primary or dominant semi-active force would be at 2Ω, due to the bilinear terms, ux and $u\dot{x}$. Thus, there could be no vibration reduction at Ω, and additionally support vibrations would now be introduced at 2Ω. Instead, a semi-active controller input (stiffness or damping modulation) at 2Ω would directly result in semi-active forces (proportional to ux and $u\dot{x}$) at Ω and 3Ω, with the component at Ω then canceling the incoming vibration. Thus, for the present system the semi-active input, u_c, and output, z (used in minimization of objective function, *J*, Eq. 9.5), are selected as:

$$u_c = \begin{bmatrix} u^{2\Omega c} & u^{2\Omega s} \end{bmatrix}^T \tag{9.11a}$$

$$z = \begin{bmatrix} F_s^{\Omega c} & F_s^{\Omega s} \end{bmatrix}^T \tag{9.11b}$$

In the above equations, the superscripts "c" and "s" represents cosine and sine components, respectively, at frequencies Ω or 2Ω. It should be noted that while the selected inputs will reduce the incoming disturbance at Ω, the support will now experience additional forces at 3Ω. These could in principle be reduced by expanding z to include these components and introducing additional harmonics in the input u_c.

9.2.4 Identification of the system transfer matrix, *T*

The system transfer matrix, *T* (defined in Eq. 9.6), can be identified using both off-line and on-line approaches. Off-line identification of the *T* matrix is achieved by perturbation of individual component of the input, u_c. The first column of *T* matrix, which corresponds to the first input of u_c, is obtained by setting the first input $u^{2\Omega c}$ to a non-zero value (while the other input $u^{2\Omega s}$ is set to zero), and the column is calculated as:

$$\begin{bmatrix} t_{11} \\ \vdots \\ t_{1n} \end{bmatrix} = \frac{z - z_o}{u_c^1} \tag{9.12}$$

This process is repeated for $u^{2\Omega s}$ to obtain the second column of the *T* matrix.

For the on-line identification of the *T* matrix, an initial estimate is obtained using the batch least square method [119], and it is updated using the recursive least square method (with variable forgetting factors) [120]. The on-line batch least square method yields an initial estimate of the

T matrix from an array of inputs, u_c, and corresponding vibration measurements, *z*, at $m+1$ time steps, as follows:

$$\begin{aligned} &T = Z\Phi^T\left(\Phi\Phi^T\right)^{-1} \\ &\Phi = \left[u_c(k) \quad u_c(k-1) \quad \cdots \quad u_c(k-m)\right] \\ &Z = \left[z(k) \quad z(k-1) \quad \cdots \quad z(k-m)\right] \end{aligned} \tag{9.13}$$

where $u_c(k)$ and $z(k)$ represents the input and the corresponding vibration level at the kth time step. It should be noted that the number of time steps used has to be greater than or equal to the number of parameters to be identified, which is equal to 4 in this case (*T* is a 2×2 matrix). In this chapter, the number of time steps used for the batch least square identification is 5 time steps with each time step covering an interval of six disturbance cycles to avoid transient response.

An on-line recursive least square method is implemented for introducing updates to the *T* matrix. A variable forgetting factor, λ, is used to prevent parameter estimation 'blow-up', which can occur when the estimation is running continuously for a long time without any change in parameters being estimated. The recursive least square identification is summarized as follows:

$$\begin{aligned} &T(k) = T(k-1) + \varepsilon(k)K(k) \\ &\varepsilon(k) = z(k) - T(k-1)u_c(k) \\ &K(k) = \left[I + u_c^T(k)P(k-1)u_c(k)\right]^{-1} u_c^T(k)P(k-1) \\ &P(k) = \frac{P(k-1)}{\lambda(k)}\left[I - u_c(k)K(k)\right] \\ &\lambda(k) = 1 - \left[1 - K(k)u_c(k)\right]\frac{\varepsilon^T(k)\varepsilon(k)}{\Sigma_o} \end{aligned} \tag{9.14}$$

where Σ_o was chosen to be 0.0025, and lower limit of λ was set at 0.15. Updates to $T(k)$ are carried out at every time step with each time step covering an interval of four disturbance cycles. It should be noted that the recursive least square method uses shorter time steps than the batch least square identification. The shorter time step is introduced to expedite the rate of adaptation of the adaptive controller.

9.3 Semi-active controller schemes

Using the fundamental components presented in Section 9.2, this section explains how those components are linked together in different types of controllers (open-loop, closed-loop, and closed-loop adaptive).

9.3.1 Open-loop controller

An open-loop control scheme can in principle be effective for vibration reduction if the excitation force and the system are not changing with time. In such a situation, the optimal control input in the frequency-domain, u_c, is based only on the *baseline (uncontrolled) support vibration levels*, z_o, as seen in Eq. 9.7, (and not on any measurements of "current" vibration levels). Once the uncontrolled support vibration, z_o, is determined, and the transfer matrix, *T,* is obtained using the off-line identification, the open-loop control scheme can be implemented following a block diagram shown in Fig. 9.3. Input scaling is introduced to ensure that the semi-active input is well within physical limits.

9.3.2 Closed-loop controller

If the excitation force changes during the course of operation, an open-loop algorithm is in general no longer suitable and a closed-loop algorithm has to be employed instead. Using an approach adapted from Ref. 121, previously applied to the active vibration reduction problem, the closed-loop control scheme for the present semi-active vibration reduction problem is implemented in the discrete-time domain. The idea is to calculate adjustments in input, Δu_c, based on "current" support vibration levels, $z(k)$, such that vibration levels in the next time step are minimized. In such a case,

$$\Delta u_c(k) = \overline{T} z(k) \qquad (9.15)$$

with $\overline{T}$ identical to that in Eq. 9.7, and the *T* matrix identified off-line, a priori. The total semi-active input is then expressed as

$$u_c(k) = u_c(k-1) + \Delta u_c(k) \qquad (9.16)$$

The block diagram corresponding to such a closed-loop control scheme is shown in Fig. 9.4. Updates to the inputs, $\Delta u_c(k)$, are carried out at intervals of every two disturbance cycles, based on calculated support vibration levels, $z(k)$, at these times.

9.3.3 Closed-loop adaptive controller

In addition to basing control inputs on currently measured vibration levels to allow for variations in excitation force, the system transfer matrix, *T*, would require identification and updating on-line if the system is undergoing changes (making it a closed-loop adaptive control scheme). However, the current semi-active system is non-linear (bi-linear), and the results in sections 9.4.3 and 9.4.4 will show that *on-line identification of the transfer matrix is required for effective vibration reduction even when the system properties are not changing (and only the disturbance changes) during operation*. A detailed explanation of this phenomenon is provided in section 9.4.4. The closed-loop adaptive control algorithm is simply the closed-loop scheme described in the previous section with the controller gain, $\overline{T}$ (in Eqs. 9.7 and 9.15), updated using on-line identification of the transfer matrix, *T*, (as described earlier in Section 9.2.4). The block diagram for this closed-loop adaptive controller is shown in Fig. 9.5.

9.4 Effectiveness of semi-active controllers for vibration reduction

Numerical simulations are carried out to evaluate the effectiveness of semi-active controllers (using either a controllable stiffness device or a controllable damper) for reducing force transmitted to the support structure due to harmonic excitation. The system parameters used in the simulations are given in Table 9.1. Without any semi-active input, Section 9.4.1 presents the baseline vibration produced by passive isolation characteristics of the system. Additional vibration reduction achieved using open-loop, closed-loop, and closed-loop adaptive controllers are presented in Section 9.4.2-9.4.4, respectively. The effect of change in excitation force on controller performance is evaluated and compared for all types of controllers.

9.4.1 Baseline System

The baseline support force, F_s (z_o in the frequency domain), due to a disturbance force, $F_o \sin(\Omega t)$, is first calculated in the absence of any semi-active input (see Figs. 9.6). From Fig.

9.6b, the amplitude of the support force is seen to be 41% of the excitation force, this attenuation being due to the passive isolation characteristics of K_o and C_o in parallel. In the following simulations, further reductions in the support vibrations due to semi-active modulation in stiffness or damping are compared to this baseline vibration level (due to pure passive isolation).

9.4.2 Vibration reduction using open-loop controller

In this section, additional reductions in the vibration transmitted to the support are examined when an open-loop control scheme is used with controllable stiffness device and controllable damper.

9.4.2.1 Controllable stiffness device

The effectiveness of the open-loop controller for vibration reduction using controllable stiffness device is evaluated in this section. The semi-active inputs are calculated using Eq. 9.7, which specifies stiffness modulation required to minimize the support vibration at frequency Ω. The first set of simulations used a penalty weighting of $W_1 = I$ (identity matrix), and $W_2 = 0$. For the mathematically optimal inputs determined directly from Eq. 9.7 (no "scaling down"), $u^{2\Omega c} =$ 1.8186 and $u^{2\Omega s}$ = -2.1271, Fig. 9.7 shows the frequency content of the steady state vibrations transmitted to the support. Although the amplitude of the support force at the disturbance frequency, Ω, is seen to be reduced to 9% of the excitation force amplitude (compared to 41% in the absence of any stiffness modulations), a higher harmonic component at 3Ω (with an amplitude of 26% of the excitation force) is now observed. This, of course, is expected due to the $K_1 xu$ term as discussed in Section 9.2.3. From this perspective, some of the disturbance energy can effectively be thought of as being transferred to higher harmonics. This may be advantageous in certain conditions when it is important to avoid specific frequencies due to resonances, or to exploit the improved effectiveness of viscous and viscoelastic damping mechanisms at higher frequencies. However, it should be noted that the amplitude of the control input, $\left|u^{2\Omega}\right| = \sqrt{\left(u^{2\Omega c}\right)^2 + \left(u^{2\Omega s}\right)^2}$, exceeds unity, so the condition on the maximum permissible input, specified in Eq. 9.9, is violated. For the system considered, it is clear that the mathematically optimal control input, or stiffness variation, is not practically realizable. Since the stiffness variations required are larger than those that can be physically achieved by modulations of the variable stiffness device, it implies that to achieve the levels of disturbance rejection at Ω seen in Fig. 9.7, energy input would be actually required, and the system would no longer be semi-active.

In the next set of simulations, the control inputs were "scaled down" (as described in Section 9.2.2), so that the stiffness variation inputs ($u^{2\Omega c}$ = 0.6498 and $u^{2\Omega s}$ = -0.7601) never exceeded the maximum permissible values. In this case, Fig. 9.8 shows that the amplitude of the transmitted force at the disturbance frequency, Ω, is 28% of the disturbance force amplitude. Compared to a corresponding value of 41% in the absence of stiffness variation (recall Fig. 9.6b), this represents an additional 32% reduction in transmitted vibration over that achieved due to the pure passive isolation characteristics. The amplitude of the higher harmonic component at 3Ω is now 10% of the disturbance force amplitude.

Figure 9.9 shows the force transmitted to the support (both at the disturbance frequency, Ω, as well as the higher harmonic component at 3Ω), corresponding to different amplitudes of control input, u_c. Vibration levels corresponding to control inputs greater than unity represent only a mathematical solution not practically achievable by the variable stiffness device. In fact, for $\left|u_c\right|$ > 1.43, the total stiffness would actually be *negative* over parts of the cycle. Since energy input would be required to realize the solutions corresponding to $\left|u_c\right| \geq 1$, this region has been marked as "active" on Fig. 9.9. Examining the support vibrations corresponding to different "semi-active" stiffness variation inputs, it can be observed that as the control input increases, the support force at the excitation frequency decreases linearly (producing up to an additional 32% reduction over the passive isolation case for the present system), and the 3Ω component increases linearly. The control input levels were varied using two different methods – *(i)* the "scaling down" approach; and *(ii)* using different values of the input penalty weighting, W_2 (which produces an optimal solution). Since the results produced by both methods were identical, it is concluded that the "scaling down" approach, also, essentially provides optimal inputs when considering physical limits in stiffness variation. Since scaling-down is simple and convenient, it is used in all subsequent simulations.

9.4.2.2 Controllable damper

This section presents vibration reduction achieved using an open-loop control scheme with controllable damper for vibration reduction. The optimal damping variation determined using Eq. 9.7 is $u^{2\Omega c}$ = -2.4527 and $u^{2\Omega s}$ = -2.1057. Since the required damping variation exceed allowable limit (|u| > 1), input scaling is employed to adjust the semi-active input. With the scaled down semi-active input, Fig. 9.10 shows the steady-state support force (both the Ω and 3Ω components) corresponding to various level of semi-active damping variation inputs. As the semi-active damping variation input increases, the support force at the excitation frequency decreases linearly producing up to 29% reduction over the passive case. As expected the 3Ω component of the support force increases as the semi-active damping variation input increases.

The vibration reduction achieved using semi-active damping variation is comparable to that obtained using semi-active stiffness variation (see Section 9.4.2.1). The achievable reduction is roughly 30% over the passive case using maximum allowable stiffness and damping variations presented in Eq. 9.8. For increasing semi-active authority, the achievable vibration reduction is increased, and vice versa.

9.4.3 Vibration reduction using closed-loop controller

Benefits to using a closed-loop controller are expected when the disturbance changes during operation. In this section, the performance of both open-loop as well as closed-loop controllers are examined *when the disturbance phase changes during the simulation.* For the closed-loop controller, the semi-active control inputs (stiffness or damping variations) are updated based on Eqs. 9.15 and 9.16 at intervals of every two disturbance cycles. The change in disturbance phase, ϕ, is introduced at t = 10π s, as described below:

$$F(t) = \begin{cases} F_o \sin(\Omega t) & 0 \le t < 10\pi \\ F_o \sin(\Omega t + \phi) & t \ge 10\pi \end{cases} \tag{9.17}$$

The influence of this change in excitation force on performance of the closed-loop controller is evaluated using both a controllable stiffness device and a controllable damper.

9.4.3.1 Closed-loop controller with controllable stiffness device

This section examines effectiveness of the controllable stiffness device in reducing vibration when there are changes in excitation force. For a phase change of ϕ = 45° (Eq. 9.17), Fig. 9.11 shows the time history of the excitation force, as well as the force transmitted to the support, when the closed-loop controller is operational. It is seen that even after the change in disturbance phase occurs, the closed-loop controller is once again able to reduce the support vibration levels, in a short duration. Figure 9.12 shows the amplitude of the support force at the disturbance frequency, Ω, using both open- and closed-loop controllers. As expected the open-loop controller is no longer effective in reducing vibration after the phase of excitation force changes (since the control inputs, which are based only on the initial vibration levels, become non-optimal after the phase of excitation force, and therefore the phase of the support vibrations, changes). However, with the closed-loop controller, after a transition period, the vibration transmitted to the support is once again reduced. When a phase change of ϕ = 90° is introduced, Fig. 9.13 once again shows that the closed-loop controller performs better than the open-loop controller. For the 45° change in phase angle, the closed-loop control inputs (stiffness variation) are changed to $u^{2\Omega c}$= -0.3097 and $u^{2\Omega s}$ = -0.9508, and the corresponding inputs for the 90° phase change are $u^{2\Omega c}$= -0.9265 and $u^{2\Omega s}$ = -0.3762. It should be noted that although the closed-loop controller is more effective than the open-loop controller, the steady state vibration levels transmitted to the support are not as low as those prior to change in disturbance phase (as would have been expected if an active force-generator type actuator had been used).

Figure 9.14 shows the steady-state support vibrations at the disturbance frequency, Ω, as a function of phase change (varying between -90° and 90°). It is observed that as the phase change increases, the effectiveness of the open-loop control scheme is degraded significantly, to the extent that the support vibration levels are larger than those for the uncontrolled case when the phase change exceeds ±40°. Performance degradation is also observed for the closed-loop scheme, but is milder. The reason that the closed-loop controller is not able to track phase changes perfectly (as would have been expected if an active force-generator type actuator) can be explained as follows: For a *pure active controller*, the control force can be written as Au (where A is some *constant* coefficient). When the disturbance phase changes during operation, the phase of the response and the support vibrations will correspondingly change, and since the input, u, is based on the current support vibrations, its phase is appropriately adjusted and comparable reductions in vibration are obtained. For the *semi-active controller*, the control force is K_1xu. Thus, when the closed-loop controller adjusts the input u proportional to the change in phase of the response (and the support vibration levels), the bi-linear semi-active force generated, K_1xu, is no longer simply proportional to this change in response phase. This suggests that an adaptive controller (recalculating the system transfer matrix, *T*, online) may be required for the semi-active vibration reduction if the excitation force is likely to change during operation, even when the system parameters are unchanged.

9.4.3.2 Closed-loop controller with controllable damper

The effectiveness of the controllable damper in reducing vibration is evaluated when the phase of excitation force changes during simulation (Eq. 9.17). Figure 9.15 shows the steady state support force after the change in excitation phase, as a function of excitation phase change. The results are very similar to those obtained for a controllable stiffness device. The performance of the open-loop controller is again degraded considerably (the vibration is above passive level) for phase changes over ±40°. For the closed-loop control scheme, a mild degradation in performance is observed when the phase changes between ±90°. The reason for the performance deterioration presented in Section 9.4.3.1 is also applicable for the case of the controllable damper. Once again, this suggests the necessity of using an adaptive control scheme when the excitation force can change.

9.4.4 Closed-Loop Adaptive Control Scheme

The effectiveness of the closed-loop adaptive controller with controllable stiffness device is evaluated in this section when the disturbance phase changes during operation. Online identification of the transfer matrix, *T*, using batch least square approach (Eq. 9.13) for initial estimates and recursive least square identification (Eq. 9.14), for updates is carried out, as described in section 9.2.4. For the present simulations, updates of the transfer matrix (in the recursive least squares approach) were carried out every four disturbance cycles. The disturbance phase changes as described in Eq. 9.17, except that it is introduced at t = 32π s (instead of 10π s). The first 24π seconds is used for batch least square identification of the *T* matrix by inputting a sequence of small input signals, at the end of which period the controller is switched on. Figures 9.16 and 9.17, respectively, show the variation of the support force amplitude at the disturbance frequency, Ω, for disturbance phase changes of 45° and 90°. It is seen from both figures that when the adaptive controller is operational, after a transition period, the support vibration levels are reduced to those prior to the change in disturbance phase (unlike the "non-adaptive" closed-loop controller that did not retain its effectiveness; recall Figs. 9.11-13).

Figure 9.18 shows the steady-state support vibrations at the excitation frequency, Ω, as a function of phase change (varying between -90° and 90°). It is observed that even as there is an increase in disturbance phase change, unlike the open- and closed-loop controllers, the closed-loop adaptive controller completely retains its effectiveness in reducing support vibrations. Thus, for a semi-active (bi-linear) system, a closed-loop adaptive controller (continuous on-line identification of system transfer matrix) is required even when there is only a disturbance change, and not a "direct" change in system properties. Although, it could be said that for a non-linear semi-active system, the "system", as such, is dependent on the excitation, so a change in the disturbance changes the system itself.

9.5 Summary of semi-active isolator

The results in this chapter demonstrated that the semi-active isolation system was effective in reducing vibration of a single degree of freedom system. The vibration reduction controller could be applied to use with both a controllable stiffness device and a controllable damper. The effectiveness of open-loop, closed-loop, and adaptive controllers in reducing the transmitted force was evaluated and compared. The results of the study indicated that for physically achievable stiffness and damping coefficient variations, the support force could be reduced by about an additional 30%, beyond the levels due to the passive isolation characteristics (no stiffness/damping variations), but higher harmonic loads were generated. When the phase of excitation force changed during the simulation, the effectiveness of the open-loop controller rapidly degraded. While the closed-loop controller (with inputs based on current support vibration levels) performed better, there was still some degradation in performance, and support vibrations were not reduced to levels prior to the phase change. The results showed that for the semi-active isolation system to retain its effectiveness in rejecting disturbances, a closed-loop, adaptive controller (with on-line system identification) is required; even when there is only a change in disturbance, and no change in basic system properties.

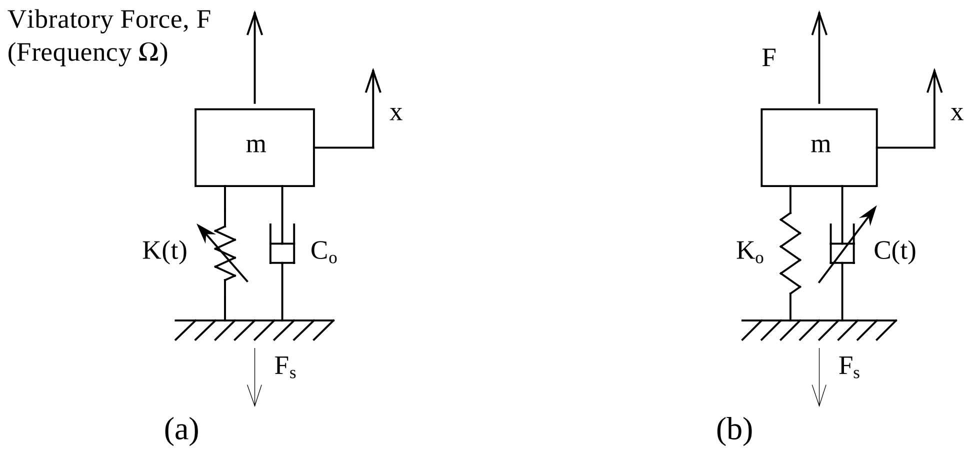

Vibratory Force, F
(Frequency Ω)
m
x
K(t)
Co
Fs
(a)
F
m
x
Ko
C(t)
Fs
(b)

Figure 9.1: Schematics of single-degree-of-freedom system for vibration reduction using (a) semi-active controllable stiffness device, and (b) controllable damper

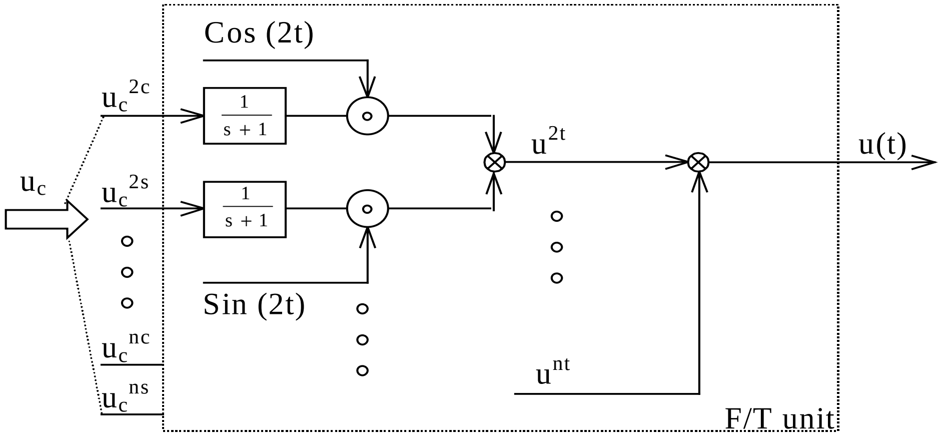

Cos (2t)
uc2c
1 / s + 1
u2t
u(t)
uc
uc2s
1 / s + 1
Sin (2t)
ucnc
ucns
unt
F/T unit

Figure 9.2: Frequency-to-Time domain conversion (F/T) unit

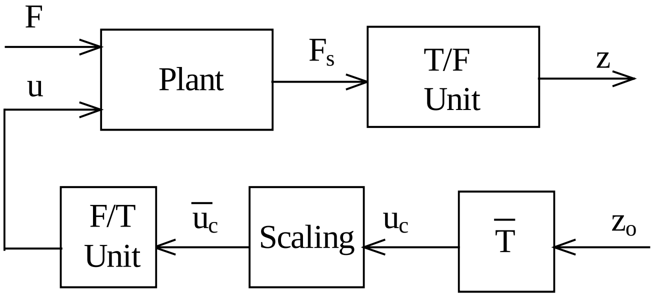

F
u
Plant
Fs
T/F Unit
z
F/T Unit
ūc
Scaling
uc
T̄
zo

Figure 9.3: Block diagram of open-loop control system

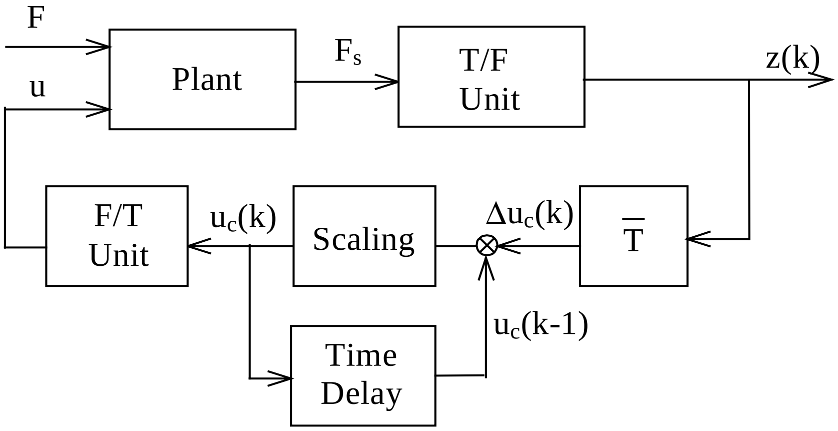
F
u
Plant
F_s
T/F Unit
z(k)
F/T Unit
u_c(k)
Scaling
Δu_c(k)
T̄
u_c(k-1)
Time Delay

Figure 9.4: Block diagram of closed-loop control system

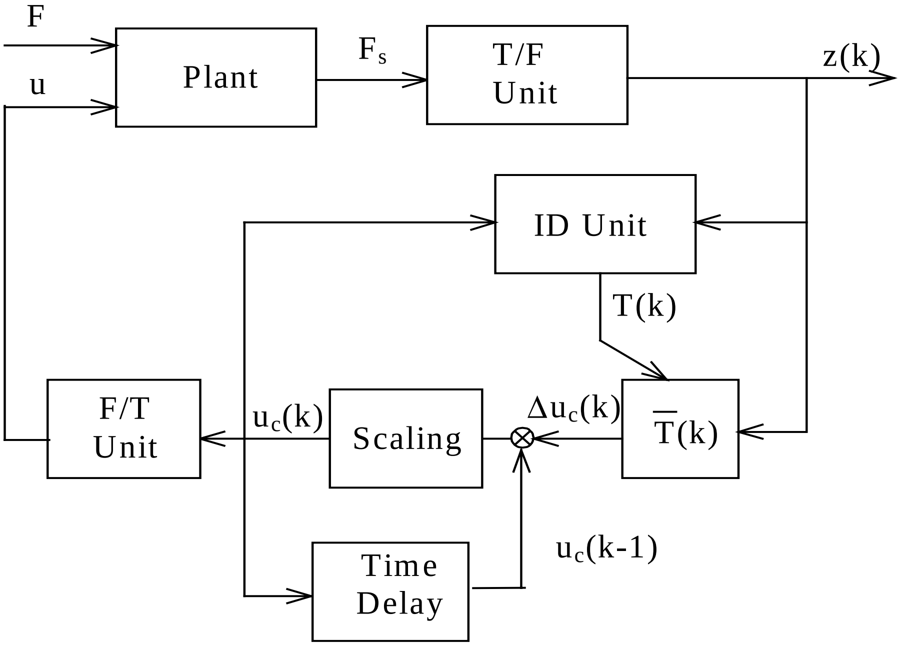
F
u
Plant
F_s
T/F Unit
z(k)
ID Unit
T(k)
F/T Unit
u_c(k)
Scaling
Δu_c(k)
T̄(k)
u_c(k-1)
Time Delay

Figure 9.5: Block diagram of closed-loop adaptive control system

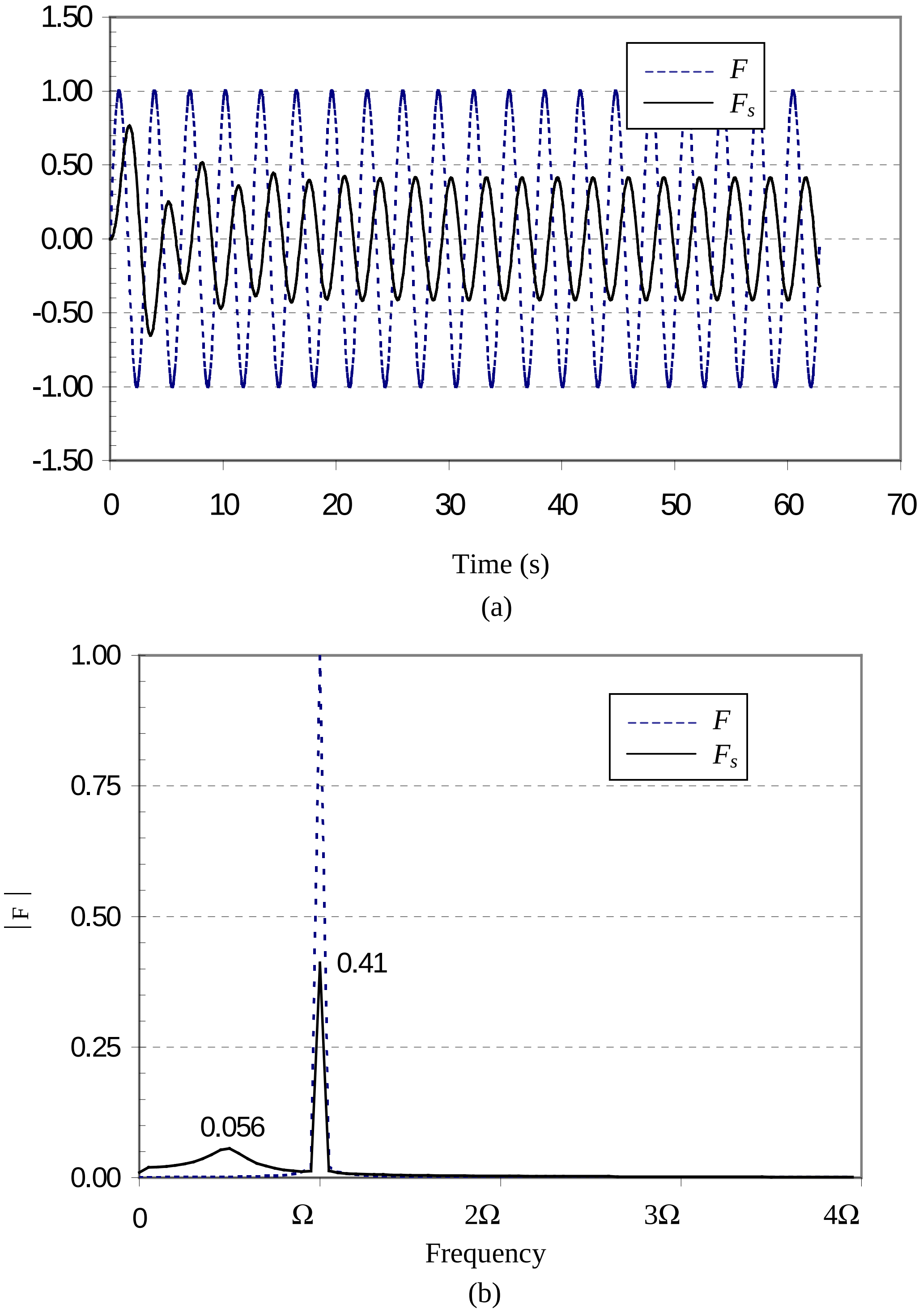

Figure 9.6: (a) Time history and (b) corresponding frequency content of disturbance force, *F*, and support force, F_s, of the baseline uncontrolled system

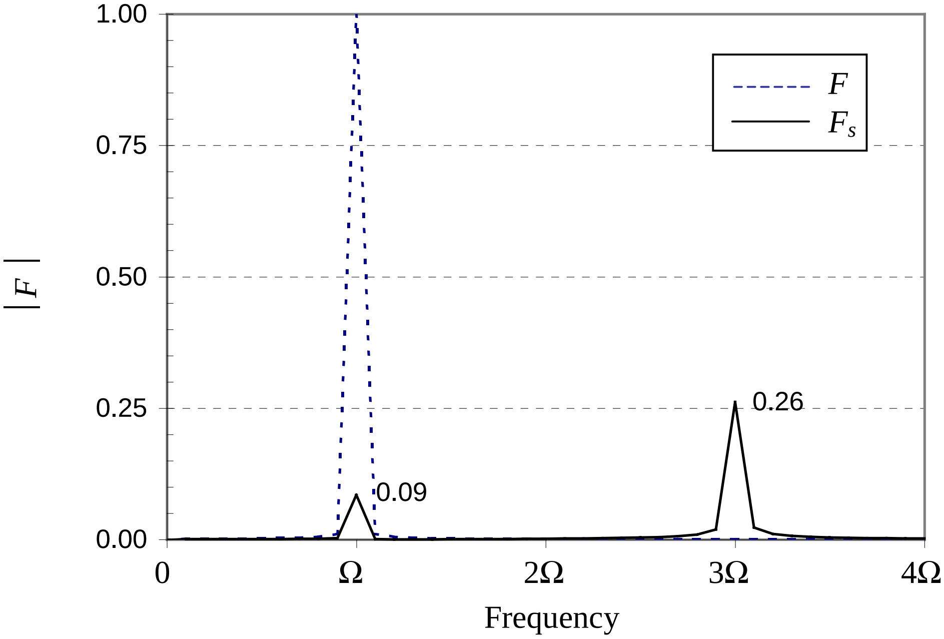

Figure 9.7: Frequency content of disturbance force, F, and support force, F_s, due to optimal stiffness variation input (no input limits)

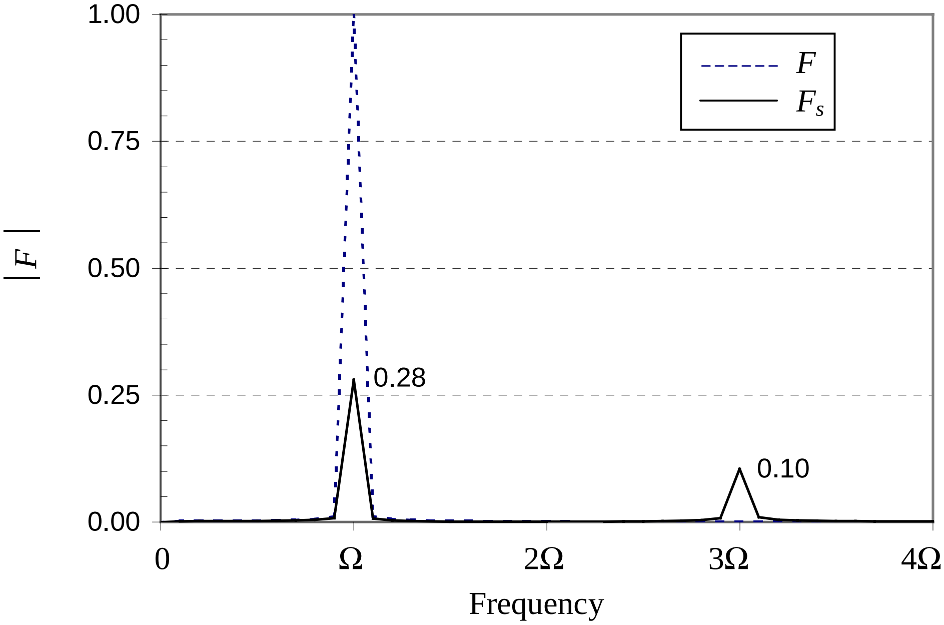

Figure 9.8: Frequency content of disturbance force, F, and support force, F_s, due to optimal semi-active stiffness variation (input "scaled-down")

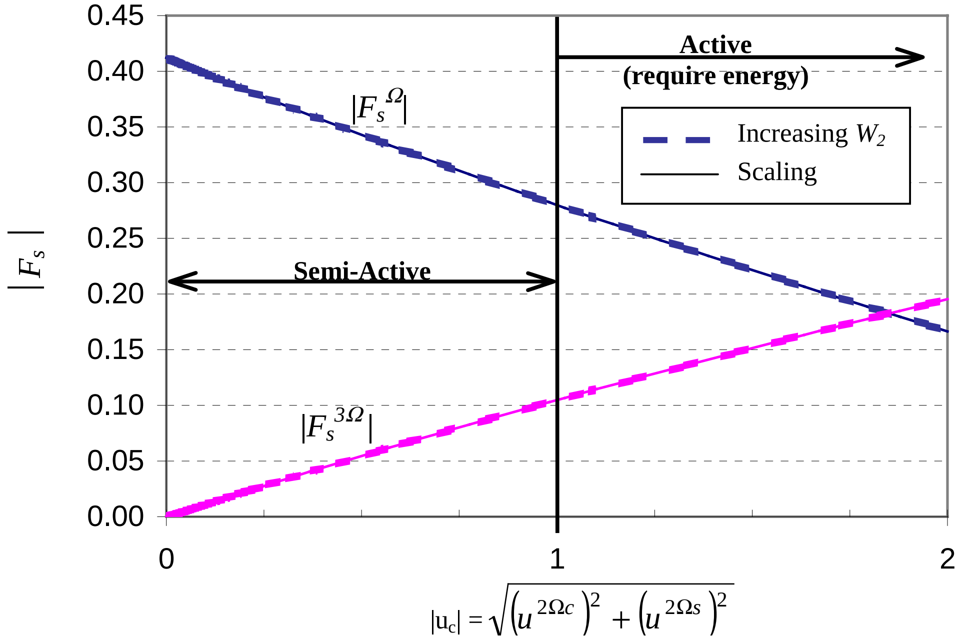

Figure 9.9: Frequency contents of support force, F_s, for increasing stiffness variation input amplitudes.

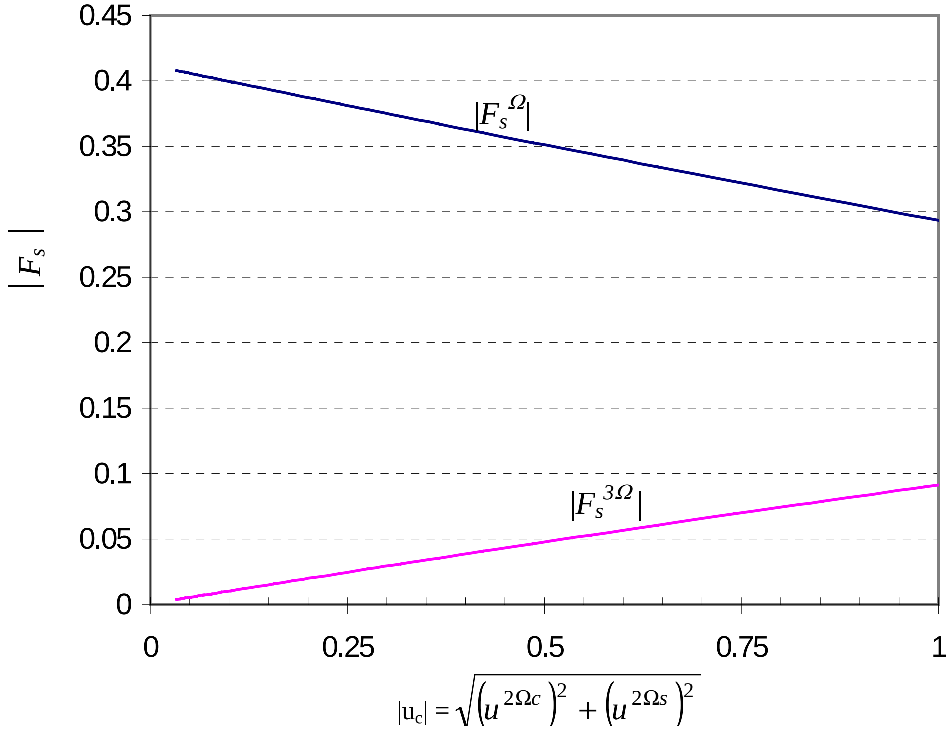

Figure 9.10: Frequency contents of support force, F_s, for increasing semi-active damping variation input amplitudes (with “input scaling”).

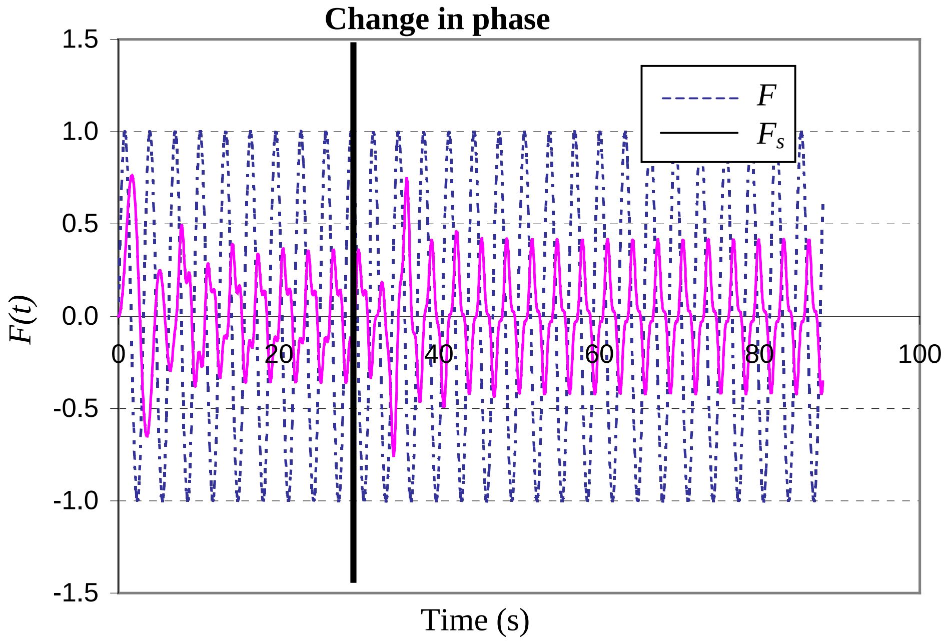

Figure 9.11: Time history of disturbance force, *F*, and support force, F_s, for closed-loop controller with controllable stiffness device, with change in phase of excitation force (ϕ = 45°)

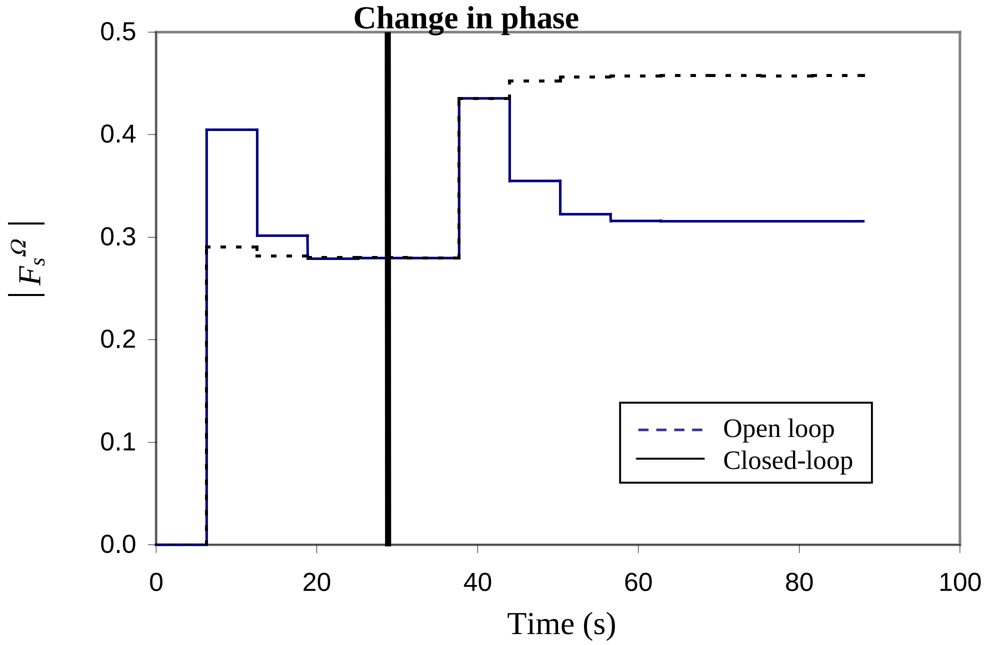

Figure 9.12: Amplitude of support force, F_s, at disturbance frequency, Ω, for open-loop and closed-loop controller with controllable stiffness device, with change in phase of excitation force (ϕ = 45°)

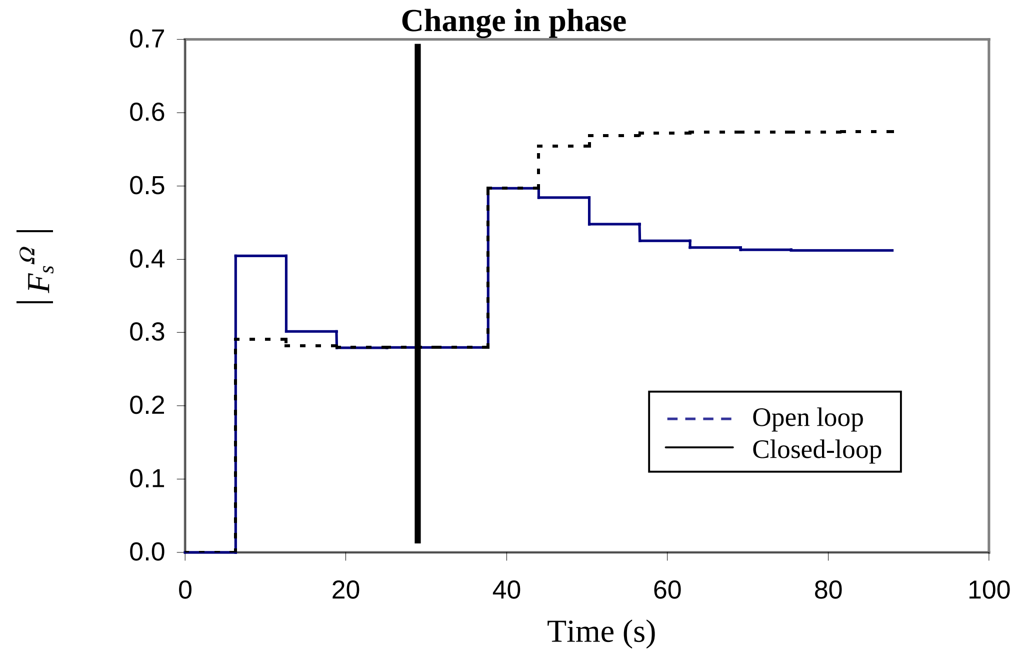

Figure 9.13: Amplitude of support force, F_s, at excitation frequency, Ω, for open-loop and closed-loop controllers with controllable stiffness device, with change in phase of excitation force (ϕ = 90°)

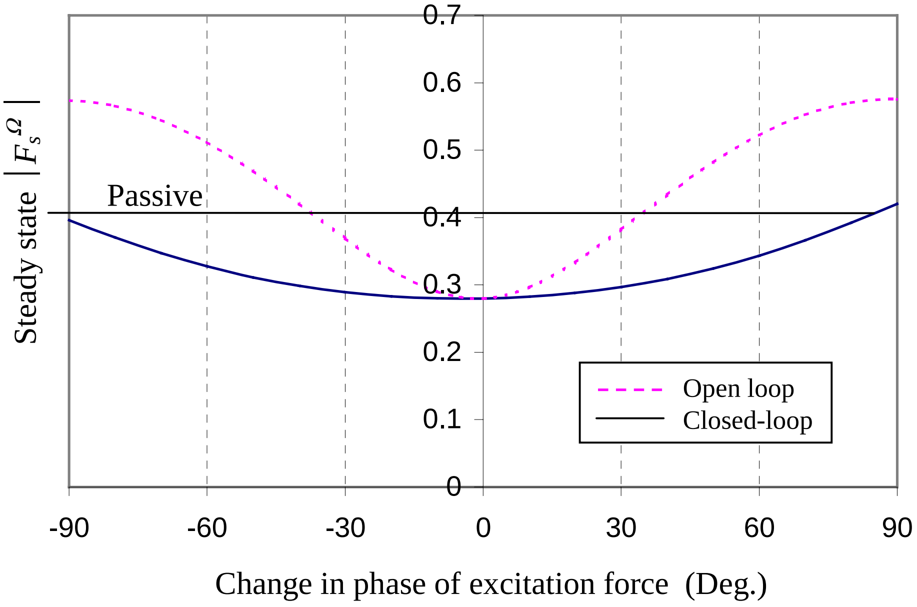

Figure 9.14: Variation in steady state support force, F_s, at Ω for closed-loop and open-loop controllers with controllable stiffness device as a function of change in phase of excitation force

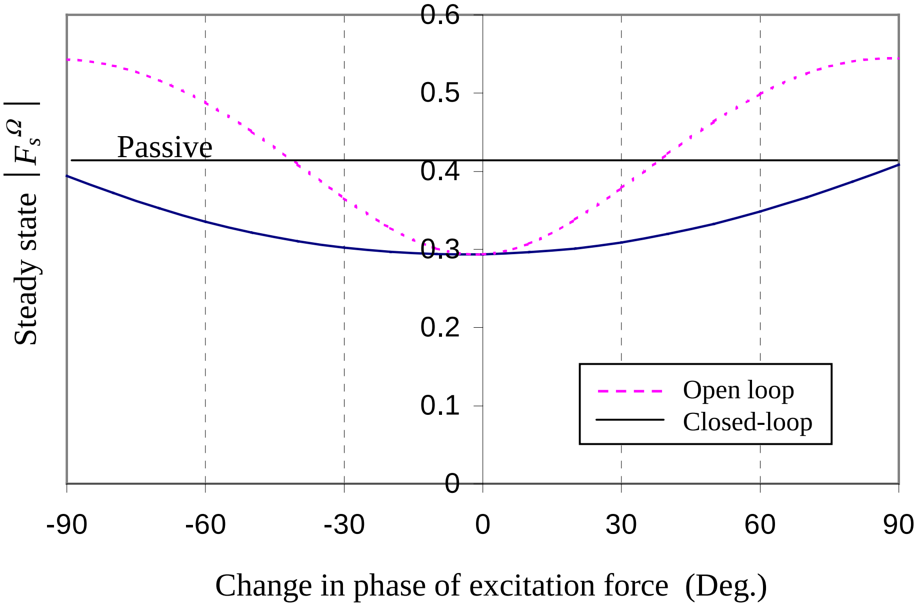

Figure 9.15: Variation in steady state support force, F_s, at Ω for closed-loop and open-loop controllers with controllable damper as a function of change in phase of excitation force

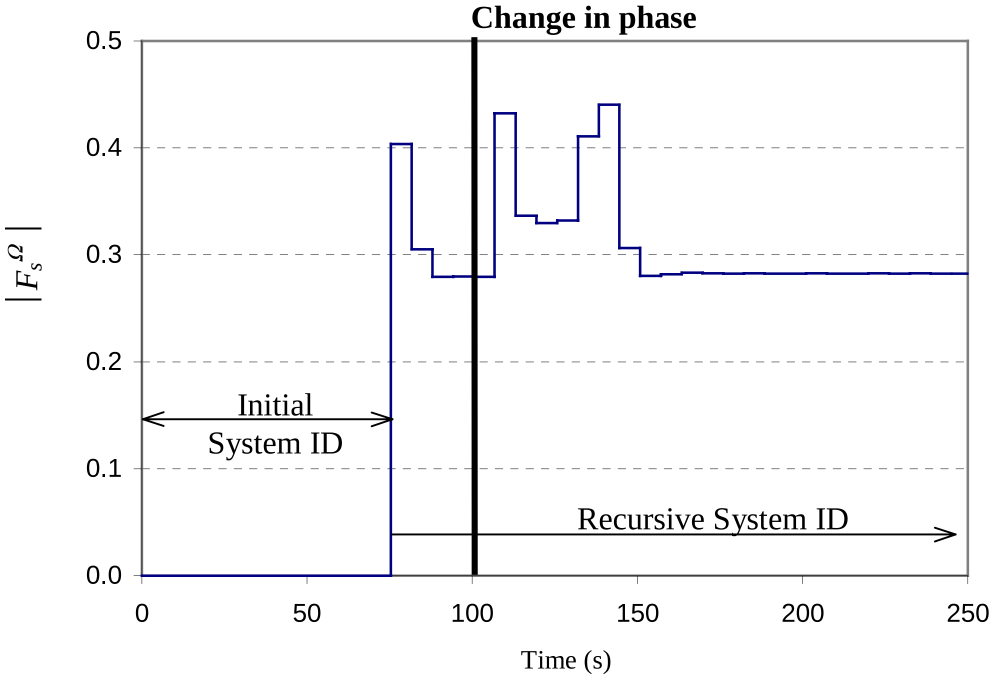

Figure 9.16: Amplitude of support force, F_s, at excitation frequency, Ω, for closed-loop adaptive controller using controllable stiffness device, with change in phase of excitation force ($\phi = 45°$)

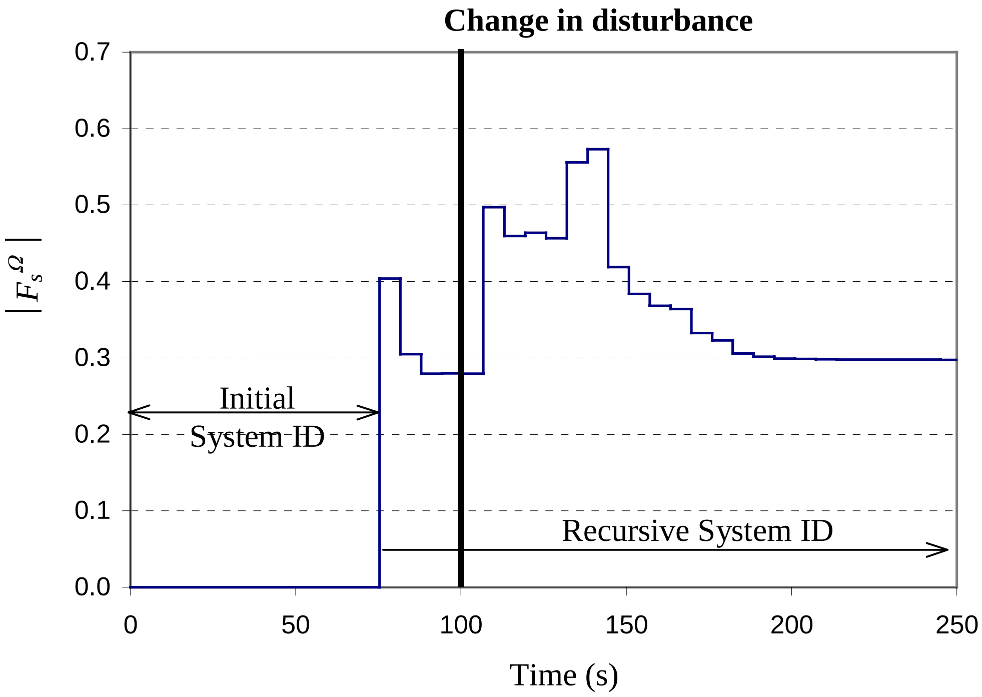

Figure 9.17: Amplitude of support force, F_s, at excitation frequency, Ω, for closed-loop adaptive controller using controllable stiffness device, with change in phase of excitation force (ϕ = 90°)

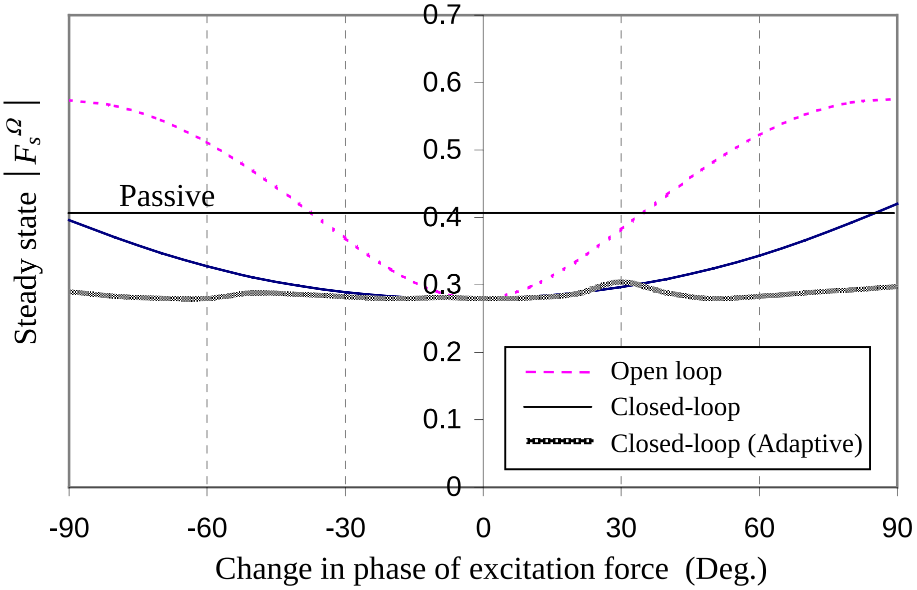

Figure 9.18: Variation in steady state support force, F_s, at Ω for open-loop, closed-loop and closed-loop adaptive controllers with controllable stiffness device as a function of change in phase of excitation force

Parameter	Value
m	1
C_o/m	0.4
K_o/m	1
K_1/ K_o	0.7
C_1/ C_o	0.75
F_o/m	1
Ω	2 rad/s

Table 9.1: Numerical values of system parameters for single degree of freedom system

Chapter 10

Concluding Remarks and Recommendations

The results presented in this dissertation showed viability of using semi-active concepts for helicopter vibration reduction. Semi-active devices, controllable stiffness devices or controllable orifice dampers, were introduced; *(i)* in the blade root region (rotor-based concept) and *(ii)* conceptually, between the rotor and the fuselage as semi-active isolators (in non-rotating frame). The corresponding semi-active controllers for vibration reduction were also developed and evaluated. This final chapter presents major concluding remarks from this dissertation and recommendations for future work.

10.1 Concluding remarks

The initial phase of this research focused on examining whether hub vibration could be influenced by modulating the stiffness of the blade in the root region. This sensitivity study was conducted for a 4 bladed hingeless rotor helicopter in moderate- to high-speed flight. It was observed that the hub vibration could be modified using specific harmonic variations in root element stiffness (flap, lag, and torsion). With proper harmonics, amplitudes, and phase angles, flap stiffness variation could produce significant reduction in vibratory hub pitching and rolling moments and all vibratory hub forces, while lag stiffness variation could reduce vibratory hub yawing moment and all vibratory hub forces considerably. Torsion stiffness variation, on the other hand, could produce only modest reductions in vibratory hub vertical force. It was noted that the stiffness variations could actually create vibration, instead of reducing it, if the amplitude was larger than an optimal value. For a single harmonic stiffness variation input (even with proper phase and amplitude), it could produce only vibration reduction in some components of hub vibration, not all components simultaneously, and other components of hub vibration might even increase. The vibration reductions were achieved by one of two mechanisms, *(i)* reduction in magnitude and *(ii)* change in relative phase, of blade root load components contributing to hub vibrations.

Since the sensitivity study showed that single harmonic stiffness variation did not produce simultaneous reduction in all components of vibratory hub loads, the effort shifted toward introducing multi-harmonic stiffness variations to simultaneously reduce all vibratory hub loads. To calculate the proper (optimal) multi-harmonic variation in root element stiffness, an optimal semi-active control scheme was developed using gradient based and non-gradient based optimizations. The effectiveness of this control scheme to calculate semi-active input (root element stiffness variations) that could produce simultaneous reduction in all components of hub vibration was evaluated. Using a multi-cyclic stiffness variation (2/*rev* and 3/*rev* for both flap and lag stiffness variations), the developed control scheme could produce significant reduction in all components of hub vibration, which resulted in a 90% reduction in hub vibration index. Despite the effectiveness of this multi-cyclic stiffness variation of the root element, the only practical way to realize it would be through the introduction of discrete controllable stiffness devices in the blade root region.

The discrete controllable stiffness devices were introduced in the blade root region to modify effective root stiffness of the blade for vibration reduction. These devices were mathematically modeled using controllable springs (translational and rotational). Two separate spring models were considered; *(i)* dual spring model and *(ii)* single spring model. The single spring model could be used to represent the controllable stiffness devices more accurately than the dual spring model, since the single spring model could reflect coupling effect between translational and rotational springs. The effectiveness of these discrete controllable stiffness devices was examined using, first, the dual spring model. The multi-cyclic stiffness variations of the flap and lag controllable stiffness devices (2/*rev* and 3/*rev*) could produce significant reduction in all components of hub vibration (55-75%). Next, the single spring model was used to represent the discrete controllable stiffness devices (free wake analysis was used to calculated rotor inflow in this case). Significant reductions in vibratory hub forces were still achieved, although the reduction in vibration index was smaller, because of the increased baseline hub vibrations associated with the inclusion of the rotor wake. Additional results demonstrated that there were no detrimental effects of the discrete controllable stiffness devices on lower harmonics of blade root loads, and the devices were effective in reducing hub vibration over a range of cruise speeds and for variations in fundamental rotor properties. Even though, the discrete controllable stiffness devices were effective in reducing hub vibration, availability of the devices is limited and the amount of stiffness variation might not be sufficient to produce satisfactory results. Thus, an alternative was considered - using discrete controllable dampers, which were commonly available and whose damping properties could be varied significantly.

The controllable flap and lag dampers were introduced in the blade root region for vibration reduction. The effectiveness of the controllable dampers was examined in high-speed flights, using rotor inflow calculated from free wake analysis. A reduced order controllable damper model was developed and validated with a fluid dynamic model. The reduced order damper model was then included in rotor blade analysis, and the damper force was determined using damper mounting kinematics. The inclusion of these dampers created multiple paths for transferring loads to the rotor hub. However, direct contributions from damper loads were canceled out. The effect of the dampers was to modify blade response and thus blade loads (which were dependent on the blade response). Hub vibrations, particularly the vibratory hub drag force and yawing moment, were reduced significantly using the controllable lag damper (2/*rev* and 3/*rev*), and the addition of controllable flap damper could produce an additional 30% reduction in hub vertical vibration. No detrimental effects on lower harmonics of blade response, damper loads, and blade and flexbeam root loads were noted. In addition, the vibration reduction was achieved over a range of forward speeds.

It was demonstrated so far that the semi-active devices (controllable stiffness devices or controllable dampers) introduced in the rotor system were effective in reducing hub vibration. As an alternative, these devices could be introduced in the fixed system, conceptually, between the hub and the fuselage as semi-active isolators, that reduced vibratory loads transmitted to the fuselage.

The effectiveness of the semi-active isolators was examined using a simplified single degree of freedom isolation system. A lumped mass (representing the rotor under harmonic force excitation) was supported by a spring and a parallel damper on a fixed support (representing the fuselage). Properties of the spring or damper could then be controlled to reduce transmission of the vibratory force into the support structure (or fuselage). Variations in the properties (stiffness or damping) of semi-active isolators were calculated using; *(i)* open loop, *(ii)* closed-loop, and *(iii)* closed-loop adaptive control schemes. Using the semi-active isolation concept, the vibratory support force could be reduced by 30%, beyond the levels achieved using passive isolation (no stiffness/damping variations), but higher harmonic loads were generated. It was also shown that a closed-loop adaptive control scheme was required to maintain isolation effectiveness if the phase of excitation force was changed.

10.2 Recommendations for future work

Despite this comprehensive study on semi-active helicopter vibration reduction using controllable stiffness and damping concepts, further investigation on these semi-active concepts can be conducted. Suggestions for further investigation on these semi-active concepts are described below;

The adaptive vibration reduction control scheme (developed for the semi-active isolation system) can also be applied to the rotor-based semi-active vibration reduction concept. No modification on the controller structure and its components is needed. The effectiveness of the adaptive controller should be evaluated for various flight conditions, such as for different cruise speeds or payloads.

The rotor-based semi-active concept should also be applied to articulated rotors. More vibration reduction is possible since blade deformation (which produces semi-active force) in articulated rotor blades is generally more than that in hingeless rotor blades. Similar semi-active devices and controllers can also be used for the articulated rotors.

A comprehensive analysis of the semi-active isolator concept should be conducted using detailed fuselage structure. This will include the influence of fuselage dynamic response into consideration. The effectiveness of the semi-active isolator should be examined for various flight speeds, rotor RPM, payloads, and C.G. offsets. This future research is quite complicated, since it involves detailed analysis of fuselage, which can be represented by a complex finite element model (100,000 nodes or more). The semi-active isolation system may be designed as an integrated unit to mount the rotor/transmission assembly to the fuselage.

An improvement can be made to the adaptive controller for semi-active vibration reduction to cope with possible variation in rotor RPM. A frequency identification scheme will be required in this research to determine the frequency of the rotor. Once the rotor RPM is identified, it will be used in the adaptive controller to produce harmonic inputs to the semi-active devices at appropriate frequencies.

Before the semi-active vibration reduction concepts can be applied to any production helicopters, stability and failure analysis of the semi-active vibration reduction systems must be conducted. Stability of the vibration control system may be determined using for example Floquet theory. In the event of any failure (such as, controller failure, power shortage, and jammed orifice valve), it is crucial to evaluate whether the helicopter still can be operated safely.

Experimental verifications of these semi-active concepts are also necessary to reaffirm (or to disprove) the effectiveness of the concepts. Experimental setup of semi-active isolator system is simpler to build and evaluate, since it involves only single degree of freedom system with a controllable damper or a controllable stiffness device. To show the effectiveness of the rotor-based semi-active vibration reduction system, it requires that the tests be conducted in a wind tunnel.

References

[1] Bielawa, R. L., "Rotary Wing Structural Dynamics and Aeroelasticity," American Institute of Aeronautics and Astronautics, Washington DC, 1992.

[2] Ellis, C. W. and Jones, R., "Application of an Absorber to Reduce Helicopter Vibration Levels," *Journal of the American Helicopter Society,* Vol. 8 (3), July 1963, pp. 30-42.

[3] Amer, K. B. and Neff, J. R., "Vertical-Plane Pendulum Absorbers for Minimizing Helicopter Vibratory Loads," *Journal of the American Helicopter Society,* Vol. 19 (4), October 1974, pp. 44-48.

[4] Milgram, J. H., "Analysis of $3\Omega/5\Omega$ Pendulum absorber Flight test Results," Technical Report TN 132-3/85, Messerschmitt-Boelkow-Blohm GmhH, June 10,1985.

[5] Miao, W. L. and Mouzakis, T., "Nonlinear Dynamic Characteristics of Rotor Bifilar Absorber," *Proceedings of the 37th American Helicopter society,* New Orleans, May 1981.

[6] Mouzakis, T., "Monofilar – A Dual Frequency Rotorhead Absorber," *Proceedings of the American Helicopter society Northeast Region National Specialists Meeting on Helicopter Vibration,* Hartford, CT, November 1981.

[7] Hawrylecki, W. and Klimkowsky, J., "Roller Vibration Absorber for Helicopter Main Rotor Hub," *Proceedings of the Nineteenth European Rotorcraft Forum,* Cernobbio, Italy, September 1993.

[8] Schuett, E., "Application of Passive Rotor Isolator for alleviation of Rotor Induced Vibration," *Journal of the American Helicopter Society,* Vol. 14 (2), April 1969, pp. 34-48.

[9] Viswanathan , S. P. and Myers, A. W., "Reduction of Helicopter Vibration Through Control of Hub Impedence," *Journal of the American Helicopter Society,* Vol. 25 (4), October 1980, pp. 3-12.

[10] Shipman, D. P., White, J. A., and Cronkhite, J. D., "Fuselage Nodalization," *Proceedings of the 28th Annual Forum of the American Helicopter society,* May 1972.

[11] Loewy, R. G., "Helicopter Vibrations: A Technological Perspective," *Journal of the American Helicopter Society,* Vol. 29, October 1984, pp. 4-30.

[12] Tarzanin, F., Young, D. K., and Panda, B., "Advanced Aeroelastic Optimization Applied to an Improved Performance, Low Vibration Rotor," *Proceedings of the 55th Annual Forum of the American Helicopter society,* Montreal, Canada, May 1999, pp. 184-194.

[13] Ganguli, R. and Chopra, I., “Aeroelastic Optimization of an Advance Geometry Helicopter Rotor,” *Journal of the American Helicopter Society,* Vol. 41 (1), January 1996, pp. 18-28.

[14] Leconte, P. and Geoffroy, P., “Dynamic Optimization of a Rotor Blade,” *Proceedings of the Aeromechanics Specialists Conf. on Aerodynamics, Acoustics and Dynamics,* San Francisco, January 1994, pp. 5.2-1 to 5.2-9.

[15] Friedmann, P. P., “Helicopter Vibration Reduction Using Structural Optimization With Aeroelastic/Multidisciplinary Constrains – A Survey,” *Journal of Aircraft,* Vol. 28, No. 1, January 1991, pp. 8-21.

[16] Weller, W. H. and Davis, M. W., “Experimental Verification of Helicopter Blade Designs Optimized for Minimum Vibration,” *Proceedings of the 44th Annual Forum of the American Helicopter society,* Washington, DC, June 1988, pp. 263-279.

[17] Milgram, J. H. and Chopra, I., “Dynamically Tuned Blade Pitch Links for Vibration Reduction,” *Proceedings of the 50th Annual National Forum of the American Helicopter society,* Washington DC, May 1994.

[18] Taylor, R., Fried, J., and MacDonald, H. I. Jr., “Reduction of Helicopter Control System Loads with Fixed System Damping,” *Proceedings of the 29th Annual National Forum of the American Helicopter Society,* 1973.

[19] Drees, J. M. and Wernicke, R. K., “An Experimental Investigation of a Second Harmonic Feathering Device on the UH-1A Helicopter,” *U.S. Army Transportation Research Command,* TR-62-109, Fort Eustis, Virginia, June 1963.

[20] Daughaday, H., “Suppression of Transmitted Harmonic Rotor Hob Loads by Blade Pitch Control,” *U.S. Army Aviation Material laboratories,* TR-67-14, Fort Eustis, Virginia, November 1967.

[21] McHugh, F. J. and Shaw, J., “Helicopter Vibration Reduction with Higher Harmonic Blade Pitch,” *Journal of the American Helicopter Society,* Vol. 23 (4), October 1978, pp. 26-35.

[22] Shaw, J. “Higher Harmonic Blade Pitch Control: A System for Helicopter Vibration Reduction,” Ph.D. Thesis, Massachusetts Institute of Technology, May 1980.

[23] Nguyen, K., “Higher Harmonic Control Analysis for Vibration Reduction of Helicopter Rotor Systems,” Ph.D. Thesis, University of Maryland, 1989.

[24] Robinson, L. H., “Aeroelastic simulation of Higher Harmonic Control,” Ph.D. Thesis, University of California, Los Angeles, 1989.

[25] Nguyen, K. and Chopra, I., “Effects of Higher Harmonics Control on Rotor Performance and Control Loads,” *Journal of Aircraft,* Vol. 29, No.3, May-June 1992, pp. 336-342.

[26] Hall, S. R. and Wereley N. M., “Performance of Higher Harmonic Control Algorithms for Helicopter Vibration Reduction,” *Journal of Guidance*, Vol. 16, No.4, 1993 pp. 793-797.

[27] Robinson, L. H., Lawson, H. and Friedmann, P. P., “Aeroelastic Simulation of Higher Harmonic Control,” NASA-CR-4623, 1994.

[28] Kube, R., Wall, B. V. D., and Schultz, K. J., “Mechanisms of Vibration and BVI noise Reduction by Higher Harmonic Control,” *Proceedings of the 20th European Rotorcraft Forum*, Amsterdams, The Netherlands, 1994, pp. 27.1-27.23.

[29] Hammond, C. E., “Wind Tunnel Results Showing Rotor Vibratory Loads Reduction Using Higher Harmonic Blade Pitch,” *Journal of the American Helicopter Society,* Vol. 28 (1), January 1983, pp 10-15.

[30] Shaw, J., Albion, N., Hanker, E. J. and Teal, R. S., “Higher Harmonic Control: Wind Tunnel Demonstration of Fully Effective Vibratory Hub Force Suppression,” *Journal of the American Helicopter Society*, Vol. 34 (1), January 1989, pp. 14-29.

[31] Jacklin, S. A., Lau, B. H., Nguyen, K. Q., Smith, R. L., and McNulty, M. J., “Full-scale Wind Tunnel Tests of the McDonnell Douglas Five-bladed Advanced Bearingless Rotor - Performance, Stability, Loads, Control Power, Vibration and HHC Data,” *Proceedings of the Aeromechanics Specialists Conf. on Aerodynamics, Acoustics and Dynamics,* San Francisco, January 1994, pp. 4.3-1 to 4.3-14.

[32] Kube, R. et al., “HHC Aeroacoustic Rotor Tests in the German-Dutch Wind Tunnel - Improving Physical understanding and Prediction Codes,” *Aerospace Science and Technology*, Vol. 2, No. 3, 1998, pp. 177-190.

[33] Kitaplioglu, C., Betzina, M., and Nguyen, K. Q., “ Full-Scale Demonstratation of Higher Harmonic Control for Noise and Vibration Reduction on the XV-15 Rotor,” *Proceedings of the 56th Annual Forum of the American Helicopter Society*, Virginia Beach, VA, 2000.

[34] Wood, E. R., Powers, R. W., and Cline, J. H., “On the Developing and Flight Testing a Higher Harmonic Control System,” *Proceedings of the 39th Annual Forum of the American Helicopter Society,* St. Louis, May 1983.

[35] Straub, F. K. and Byrns, E. V., Jr., “Application of Higher Harmonic Blade Feathering on the OH-6A Helicopter for Vibration Reduction,” NASA CR-4031, December 1986.

[36] Walsh, D. M., " Flight Tests of an Open Loop Higher Harmonic Control system of an S-76A Helicopter," *Proceedings of the 42nd Annual Forum of the American Helicopter Society,* Alexandria, VA, 1986, pp. 831-843.

[37] Ham, N. D., "Helicopter Individual-Blade-Control Research at MIT 1977-1985," *Vertica,* Vol. 11, No. 1/2, 1987, pp. 109-122.

[38] Jacklin, S. A., Nguyen K. Q., Blass, A., and Richter, P., "Full-Scale Wind Tunnel Test of a Helicopter Individual Blade Control System," *Proceedings of the 50th Annual Forum of the American Helicopter Society,* Washington, DC, 1994, pp. 579-596.

[39] Jacklin, S. A., Blass, A., Teves, D., and Kube, R., "Reduction of Helicopter BVI Noise, Vibration and Power Consumption through Individual Blade Control," *Proceedings of the 51st Annual Forum of the American Helicopter Society,* Fort Worth, TX, 1995, pp. 662-680.

[40] Jacklin, S. A., Blass, A., Swanson, S. M., and Teves, D., "Second Test of a Helicopter Individual Blade Control System in the NASA Ames 40- by 80-foot Wind Tunnel," *Proceedings of the International Aeromechanics Specialists' Conference,* Bridgeport, CT, October 1995, pp. 7.9-7.26.

[41] Kube, R., Van Der Wall, B. G., "IBC Effects on BVI noise and Vibrations –A Combined numerical and Experimental Investigation," *Proceedings of the 55th International Annual Forum of the American Helicopter Society,* Montreal, Canada, 1999, pp. 2282-2291.

[42] Mueller, M., Arnold U. T. P., and Morbitzer, D., "On the Importance and Effectiveness of 2/rev IBC for Noise, Vibration and Pitch Link Load Reduction," *Proceedings of the 25th European Rotorcraft Forum,* Rome, Italy, 1999.

[43] Ham, N. D., "Helicopter Individual-Blade-Control: Promising Technology for the Future Helicopter," *Proceeding the American Helicopter Society Aeromechanics conference, Bridgeport, CT,* Oct. 1995, pp. 7-1 to 7-8.

[44] Millott, T. A., "Vibration Reduction in Helicopter Rotors Using an Actively Controlled Partial Span Trailing Edge Flap Located on the Blade," Ph.D. Thesis, University of California, Los Angeles, 1993.

[45] Friedmann P. P. and Millott T. A., "Vibration Reduction in Rotorcraft Using Active Control: A Comparison of Various Approaches," *Journal of Guidance, Control, and Dynamics,* Vol. 18, No. 4, July-August 1995.

[46] Milgram, J. H., "A Comprehensive Aeroelastic Analysis of Helicopter Main Rotors with Trailing Edge Flaps for Vibration Reduction," Ph.D. Thesis, University of Maryland, January 1997.

[47] Kaman, C. H., "Aircraft of Rotary Wing Type," U.S. Patent 2,455,866, filed August 19, 1946, issued December 7, 1948.

[48] Lee, T. and Chopra, I., "Design of piezostack-driven trailing-edge flap actuator for helicopter rotors," *Smart Materials and Structures*, Vol. 10, No. 1, February 2001, p. 15-24

[49] Centolanza, L. R. and Smith, E. C., "Design and Experimental Testing of an Induced-Shear Piezoelectric Actuator for Rotor Blade Trailing Edge Flaps," *Proceedings of the 41st AIAA/ASME/ASCE/AHS/ASC Structures, Structural Dynamics, and Materials Conference,* Atlanta, GA, April, 2000.

[50] Koratkar, N. and Chopra, I., "Analysis and Testing of Mach-Scaled Rotor with Trailing-edge Flaps," *Journal of the AIAA*, Vol. 38, No. 7, July 2000, pp. 1113-1124.

[51] Bernhard, A. and Chopra, I., "Trailing Edge Flap Activated by a Piezo-Induced Bending-Torsion Coupled Beam," *Journal of the American Helicopter Society*, Vol. 44, No. 1, January 1999, pp. 3-15.

[52] Straub, F. K., Ngo, H. T., Anand, V., and Domzalski, D. B., "Development of a Piezoelectric Actuator for Trailing Edge Flap Control of Rotor Blades," *Proceedings of the Smart Structures and Integrated Systems Meeting*, Newport Beach, CA, SPIE Vol. 3668, 1999, pp. 2-13.

[53] Ben-Zeev, O. and Chopra, I., "Continued Development of a Helicopter Rotor Model Employing Smart Trailing-Edge Flaps for Vibration Suppression," *Proceedings of the Smart Structures and Integrated Systems Conference*, San Diego, CA, SPIE Vol. 3668, 1999, pp. 2-13.

[54] Prechtl, E. F., Hall, S. R., "An X-Frame Actuator Servo-Flap Actuation System for Rotor Control," *Proceedings of the Smart structures and integrated systems Meeting,* San Diego, CA, March, 1998, SPIE Vol. 3329, pp. 309-320.

[55] Spencer, B. T. and Chopra, I., "Design and testing of a helicopter trailing edge flap with piezoelectric stack actuators," *Proceedings of the Smart structures and integrated systems Meeting*, San Diego, CA, February 1996, (SPIE Vol. 2717), pp. 120-131.

[56] Seeley, C. E., Chattopadhyay, A., and Mitchell, L. "Design of a Smart Flap Using C-Block Actuators and a Hybrid Optimization Technique," *Proceedings of the Smart structures and integrated systems Meeting*, San Diego, CA, February 1996, SPIE Vol. 2717, pp. 132-145.

[57] Millott, T. A. and Friedmann, P. P., "Vibration Reduction in Hingeless Rotors Using an Actively Controlled Flap and Its Implementation Using Magnetostrictive Actuation," *Proceedings of the 20th European Rotorcraft Forum*, Amsterdam, 1994, pp. 60.1-60.26.

[58] Bothwell, C. M., Chandra, R., and Chopra, I., "Torsional Actuation with Extension-Torsion Composite Coupling and a Magnetostrictive Actuator," Proceedings of the AIAA/ASME Adaptive Structures Forum, Hilton Head, SC, April 1994, pp. 241-252.

[59] Fenn, R. C., Downer, J. R., Bushko, D. A., Gondhalekar, V., and Ham, N. D., "Terfenol-D Driven Flaps for Helicopter Vibration Reduction," *Journal of Smart Materials and Structures*, Vol. 5, No. 1, 1996, pp. 49-57.

[60] Prechtl, E. F., Hall, S. R., "Closed-loop vibration control experiments on a rotor with blade mounted actuation," *Proceedings of the 41st AIAA/ASME/ASCE/AHS/ASC Structures, Structural Dynamics, and Materials Conference,* Atlanta, GA, April, 2000.

[61] Dowson, S. et al., "Wind Tunnel Test of An Active Flap Rotor - BVI noise and Vibration Reduction," *Proceedings of the 51st Annual Forum of the American Helicopter Society,* Fort worth, TX, 1995, pp. 631-648.

[62] Schimke, D., Jaenker, P., Wendt, V., and Junker, B., "Wind Tunnel Evaluation of a Full Scale Piezoelectric Flap Control Unit," *Proceedings of the 24th European Rotorcraft Forum*, Marseilles, France, 1998, pp. TE02.1-TE02.12.

[63] Koratkar, N. A. and Chopra, I., "Wind Tunnel Testing of a Mach-Scaled Rotor Model with Trailing-Edge Flaps," *Proceedings of the 56th International Annual Forum of the American Helicopter Society,* Virginia Beach, VA, 2000.

[64] Straub, F. K. et al., "Smart Material Actuated Rotor Technology - SMART," *Proceedings of the 41st AIAA/ASME/ACSE/AHS/ASC Structures, Structural Dynamics, and Materials Conference,* Atlanta, GA, April, 2000.

[65] Bernhard, A. and Chopra, I., "Analysis of a Bending-Torsion Coupled Actuator for a Smart Rotor with Active Blade Tips," *Smart Materials and Structures,* Vol. 10, No. 1, February 2001, pp. 35-52.

[66] Wilkie, W. K., Wilbur, M. L., Mirick, P. H., Cesnik, C. E. S., and Shin, S., "Aeroelastic Analysis of the NASA/ARMY/MIT Active Twist Rotor," *Proceedings of the 55th Annual Forum of the American Helicopter Society,* Montreal, Canada, 1999, pp. 545-557.

[67] Cesnik, C. E. S., Shin, S., Wilkie, W. K., Wilbur, M. L., and Mirick, P. H., "Modeling, Design, and Testing of the NASA/ARMY/MIT Active Twist Rotor Prototype Blade," *Proceedings of the 55th International Annual Forum of the American Helicopter Society,* Montreal, Canada, 1999, pp. 533-544.

[68] Wilbur, M. L., Yeager, W. T. Jr., Wilkie, W. K., Cesnik, C. E. S., and Shin, S., "Hover Testing of the NASA/ARMY/MIT Active Twist Rotor," *Proceedings of the 56th Annual Forum of the American Helicopter Society,* Virginia Beach, VA, 2000.

[69] Wilbur, M. L. *et. al.*, "Vibratory Loads Reduction Testing of the NASA/ARMY/MIT Active Twist Rotor," *Proceedings of the 57th International Annual Forum of the American Helicopter Society,* Washington, D.C., 2001, pp. 1050-1068.

[70] Chen, P. C. and Chopra, I., "Wind Tunnel Test of a Smart Rotor Model With Individual Blade Twist Control," *Journal of Intelligent Material Systems and Structures*, Vol. 8, No. 5, May 1997, pp. 414-425.

[71] Chen, P. C. and Chopra, I., "Hover Testing of Smart Rotor with Induced-Strain Actuation of Blade Twist," *AIAA Journal*, Vol. 35, No. 1, January 1997, pp. 6-16.

[72] Cribbs, R. and Friedmann, P. P., "Vibration Reduction in Rotorcraft Using an Enhanced ACSR Model," *Proceedings of the 41st AIAA/ASME/ACSE/AHS/ASC Structures, Structural Dynamics, and Materials Conference*, Atlanta, GA, April, 2000.

[73] Chiu, T. and Friedmann, P. P., "An Analytical Model for ACSR Approach to Vibration Reduction in a Helicopter Rotor-Flexible Fuselage System," *The Aeronautical Journal*, Vol. 101, No. 1009, November, 1997, pp. 399-408.

[74] Chiu, T. and Friedmann, P. P., "Vibration Suppression in Helicopter Rotor/Flexible Fuselage System Using the ACSR Approach with Disturbance Rejection," *Proceedings of the 52nd Forum of the American Helicopter Society,* Washington, DC, 1996, pp. 736-757.

[75] Staple, A. E., "The Development and Testing of Active Control Techniques to Minimized Helicopter Vibration," *Environmental Engineering*, Vol. 3, December, 1990, pp. 16-17.

[76] Staple, A. E. and Wells, D. M., “The development and Testing of an Active Control of Structural Response System for the EH101 Helicopter,” *Proceedings of the 16th European Rotorcraft Forum*, Glasgow, Scotland, 1990, pp. 12.1.

[77] Welsh, W. A., Von Hardenberg, P. C., Von Hardenberg, P. W., and Staple, A. E., “Test and Evaluation of Fuselage Vibration Utilizing Active Control of Structural Response (ACSR) Optimized to ADS-27,” *Proceedings of the 46th Annual Forum of the American Helicopter society*, Washington DC, 1990, pp. 21-37.

[78] Heverly, D. E., “Optimal Actuator Placement and Active Structural Design of Control of Helicopter Airframe Vibration,” Ph.D. Thesis, The Pennsylvania State University, 2002.

[79] Staple, A. E., “An Evaluation of Active Control of Structural Response and a Means of Reducing Helicopter Vibration,” *Proceedings of the 46th Annual Forum of the American Helicopter society*, Washington DC, 1990, pp. 3-17.

[80] Welsh, W. A., Fredrickson, C., Rauch, C., and Lyndon, I., “Flight Test of an Active Vibration Control System on the UH-60 Black Hawk Helicopter,” *Proceedings of the 51st Annual Forum of the American Helicopter society*, Fort Worth, TX, 1995, pp. 393-400.

[81] Hackett, N., “EH101 Active Control of Structural Response Development, Productionisation and Certification,” *Proceedings of the EH101 Avionics- Civil and Military Conf.*, London, United Kingdom, November 1995, pp. 5.1-5.10.

[82] Goodman, R. K. and Millott, T. A., “Design, Development, and Flight Testing of the Active Vibration Control System for the Sikorsky S-92,” *Proceedings of the 56th Annual Forum of the American Helicopter society,* Virginia Beach, Virginia, 2000.

[83] Symans, M. D. and Constantinou, M. C., “Semi-Active Control Systems for Seismic Protection of Structures: A State-of-the-Art Review,” *Engineering Structures*, Vol. 21, 1999, pp. 469-487.

[84] Wang, K. W. et al., “Semi-Active Vibration Controls of Flexible Structures via Adaptive Materials [Final Report],” NASA Report, NIPS-96-94822, 1996.

[85] Iver, D. E. and Miller L. R., “Semi-Active Suspension Technology: An Evolutionary View,” *ASME, Design Engineering Division*, DE Vol. 40, December 1991, pp. 327-346.

[86] Karnopp, D., “Active Damping in Road Vehicle Suspension systems,” *Vehicle System Dynamics*, Vol. 12, No. 6, December 1983, pp. 291-316.

[87] Redfield, R. C., “Performance of Low-Bandwitdh, Semi-Active Damping Concepts for Suspension Control,” *Vehicle System Dynamics,* Vol. 20, No. 5, 1991, pp. 245-267.

[88] Yi, K., Wargelin, M., and Hedrick, K., “Dynamic Tire Force Control by Semi-Active Suspensions,” *ASME, Dynamic Systems and Control Division*, DSC Vol. 44, November 1992, pp. 299-310.

[89] Tseng, H. E. and Hedrick, J. K., “Performance of a Semi-Active Suspension with Leading System Information,” *ASME, Dynamic Systems and Control Division*, DSC Vol. 54, November 1994, pp. 115-126.

[90] Karnopp, D., “Active and Semi-Active Vibration Isolation,” *Journal of Mechanical Design, Transaction of the ASME,* Vol. 117B, June 1995, pp. 177-185.

[91] El-Tawwab, A. M. A. and Abou-El-Seoud, S. A., “Theoretical Study of the Hydro-Pneumatic Semi-Active Suspension System with Preview,” *Heavy Vehicle Systems,* Vol. 5, No. 2, 1998, pp. 167-180.

[92] Yoshida, K. and Okamoto, B. “Bilinear Disturbance-Accommodating Optimal Control of Semi-Active Suspension for Automobiles,” *Proceedings of the IEEE conference on Control Applications*, August 1999, pp. 1496-1501.

[93] Rajamani, R. and Hedrick J. K., “Semi-Active Suspensions – Comparison between theory and experiments,” *Vehicle System Dynamics,* Vol. 20, August 1991, pp. 504-518.

[94] Crolla, D. A. and Abdel-Hady, M. B. A., “Semi-Active Suspension Control for a Full Vehicle Model,” *SAE Special Publications*, No. 878, September 1991, pp. 45-51.

[95] Fodor, M. and Redfield, R. C., “ Experimental Verification of Resistance Control, Semi-Active Damping,” *Vehicle System Dynamics,* Vol. 26, 1996, pp. 143-159.

[96] Cebon, D., Besinger, F. H., and Cole, D. J., “Control Strategies for Semi-Active Lorry Suspensions,” *ImechE, Part D: Journal of Automobile Engineering*, Vol. 210, 1996, pp. 161-178.

[97] Kitching, K. J., Cebon, D., and Cole, D. J., “Experimental Investigation of Preview Control,” *Vehicle System Dynamics*, Vol. 32, 1999, pp. 459-478.

[98] Fodor, M. and Redfield, R. C., “Resistance Control, Semi-Active Damping Performance,” *ASME, Dynamic Systems and Control Division*, DSC Vol 56, November 1995, p. 161-169.

[99] Ohsaku, S., Nakayama, T., Kamimura, I., and Motozono, Y., “Nonlinear $H_{infinity}$ Control for Semi-Active Suspension,” *JSAE Review,* Vol. 20, No. 4, 1999, pp. 447-452.

[100] Kawabe, T., Isobe, O., Watanabe, Y., Hanba, S., and Miyasato, Y., “New Semi-Active Suspension Controller Design Using Quasi-Linearization and Frequency Shaping,” *Control Engineering Practice*, Vol. 6, No. 10, October 1998, pp. 1183-1191.

[101] Onoda, J., and Watanabe, N., “Vibration Suppression by Variable-Stiffness Members,” *AIAA Journal*, Vol. 29, No. 6, June 1991, pp. 977-983.

[102] Kawashima, K., and Unjoh, S., “Seismic Response Control of Bridges by Variable Dampers,” *Journal of Structure Engineering*, Vol 120, No 9, Sept. 1994, p 2583-2601.

[103] Yang, J. N., Wu, J. C., and Li, Z., “ Control of Seismic-Excited Buildings Using Active Variable Stiffness Systems,” *Proceedings of the American Control Conference*, Vol. 1, 1994, pp. 1083-1088.

[104] Symans, M. D., Constantinou, M., “Semi-Active Fluid Damping Control Systems for Seismic Hazard Mitigation,” *Proceedings of the 15th Structures Congress*, Vol. 2, 1997, pp. 1353-1357.

[105] Gavin, H. P. and Doke, N. S., “Resonance Suppression through Variable Stiffness and Damping Mechanisms,” *Proceedings of the SPIE Conference on Smart System for Bridges, Structures and Highways*, SPIE Vol. 3671, March 1999, pp. 43-53.

[106] Madden, G., Wongprasert, N., and Symans, M. D., “Analytical and Numerical Study of a Smart Sliding Base Isolation System for Seismic Protection of Buildings,” *Proceedings of SPIE Conference on Smart System for Bridges, Structures and Highways*, March 2000.

[107] Symans, M. D., “Development and Experimental Study of Semi-Active Fluid Damping Devices for Seismic Protection of Structures,” Ph.D. Thesis, State University of New York at Buffalo, 1995.

[108] Symans, M. D. and Constantinou, M. C., “Experimental Study of Seismic Response of Structures with Semi-Active Damping Control System,” *Journal of Intelligent Material Systems and Structures*, Vol. 8, No. 8, August 1997, pp. 644-657.

[109] Symans, M. D. and Constantinou, M. C., “Seismic Testing of a Building Structure with a Semi-Active Fluid Damper Control System,” *Earthquake Engineering and Structural Dynamics*, Vol. 26, 1997, pp. 759-777.

[110] Dyke, S. J., and Spencer, B. F. Jr., Sain, M. K., and Carlson J. D., “An Experimental Study of MR Dampers for Seismic Protection,” *Smart Materials and Structures*, Vol. 7, No. 5, October 1998, pp. 693-703.

[111] Nitzsche, F., "Tailoring the Dynamic Response of Helicopter Rotors Using Smart Materials," *Proceedings of the AIAA/ASME Adaptive Structures Forum*, April 1995, (AIAA 95-1083)

[112] Nitzsche, F., "Smart Spring-Type Actuation for Helicopter Individual Blade Control," *Sixth International Conference on Adaptive Structures*, Technomic, Lancaster-Basel, 1996, pp. 230-240.

[113] Nitzsche, F., "Smart-Spring Actuation for Helicopter Individual Blade Control: A Frequency Domain Analysis," *Seventh International Conference on Adaptive Structures*, Technomic, 1997, pp. 331-341.

[114] Bir, G., Chopra, I., *et al*, "University of Maryland Advanced Rotorcraft Code (UMARC) Theory Manual," UM-AERO Report 92-02, Aug. 1992.

[115] Drees, J. M., "A Theory of Airflow through Rotors and Its Application to Some Helicopter Problems," *Journal of the Helicopter Association of Great Britain*, Vol. 3, 1949.

[116] Tauszig, L., "Numerical Detection and Characterization of Blade-Vortex Interactions Using a Free Wake Analysis," MS Thesis, Department of Aerospace Engineering, the Pennsylvania State University, 1998.

[117] Johnson, W., "Self-tuning regulators for multicyclic control of helicopter vibration," NASA Technical Paper 1996, March 1982.

[118] Carroll, D. L., "Fortran Genetic Algorithm Driver version 1.7," Talbot Lab, University of Illinois, Urbana, Illinois, Dec 1998.

[119] Astrom, K. J. and Wittenmark, B. "Adaptive Control," 2nd Ed., *Addison-Wesley Publishing Company Inc.*, Reading, MA, 1995.

[120] Fortescue, T. R., Kershenbaum, L. S., and Ydstie, B. E., "Implementation of Self-Tuning Regulators with Variable Forgetting Factors," *Automatica*, Vol 17, No 6, 1981, p 831-835.

[121] Hall, S. R. and Wereley, N. M., "Linear Control Issues in the Higher Harmonic Control of Helicopter Vibrations," *Proceedings of the American Helicopter Society 45th Annual Forum*, Boston, MA, May 1989.

Appendix A

Loads on Helicopter Fuselage

A.1 Loads from fuselage

The fuselage itself can generate both inertial and aerodynamic loads on the helicopter. The inertial contribution of fuselage load is only the weight of the helicopter, since the helicopter is assumed to be in level flight for all instants (see Fig. 2.1). The aerodynamic contribution of fuselage loads is given below as functions of advance ratio, μ:

$$\begin{aligned} D_f &= \frac{\gamma N}{6a\sigma}\frac{f}{A}\mu^2 \\ Y_f &= \frac{\gamma N}{6a\sigma}C_{yf}\mu^2 \\ M_{xf} &= \frac{\gamma N}{6a\sigma}C_{mxf}\mu^2 \\ M_{yf} &= \frac{\gamma N}{6a\sigma}C_{myf}\mu^2 \\ M_{zf} &= \frac{\gamma N}{6a\sigma}C_{mzf}\mu^2 \end{aligned} \tag{A.1}$$

where, $\frac{f}{A}$ is fuselage equivalent flat plat area (A is disk area, πR^2), C_{yf} is fuselage side force coefficient, C_{mxf} is fuselage rolling moment coefficient, C_{myf} is fuselage pitching moment coefficient, and C_{mzf} is fuselage yawing moment coefficient.

A.2 Lift from horizontal tail

Lift produced by the horizontal tail is calculated using simple lifting line theory as follows;

$$L_{ht} = \frac{1}{2}\rho V^2 S_{ht} a_{ht} \alpha_s \tag{A.2}$$

Where S_{ht}, a_{ht}, and V, are horizontal tail area, lift curve slope, and free stream velocity respectively.

A.3 Thrust from tail rotor

Thrust produce by the tail rotor T_{tr}, can be calculated as follows;

$$T_{tr} = \frac{N_{tr}\rho c_{tr} a_{tr} R_{tr}^3 \Omega_{tr}^2}{4}\left[\theta_{tr}\left(\frac{2}{3}+\mu_{tr}^2\right)-\lambda_{tr}\right] \qquad \text{(A.3).}$$

The tail rotor inflow, λ_{tr}, can be estimated by solving Eq. A.4, iteratively using Newton's method for nonlinear equations.

$$\lambda_{tr} = \frac{N_{tr} c_{tr} a_{tr} \Omega_{tr}^2}{8\pi R_{tr}\sqrt{\lambda_{tr}^2+\mu_{tr}^2}}\left[\theta_{tr}\left(\frac{2}{3}+\mu_{tr}^2\right)-\lambda_{tr}\right] \qquad \text{(A.4)}$$

Appendix B

Elemental Structural Matrices and Load Vector

B.1 Elemental structural mass matrix

The structural mass matrix of the ith element can be expressed as

$$[M]_i = \begin{bmatrix} M_{vv} & M_{vw} & M_{v\phi} \\ M_{wv} & M_{ww} & M_{v\phi} \\ M_{\phi v} & M_{\phi w} & M_{\phi\phi} \end{bmatrix} \tag{B.1}$$

where

$$[M_{vv}] = \int_0^1 m H^T H ds$$

$$[M_{ww}] = \int_0^1 m H^T H ds$$

$$[M_{\phi\phi}] = \int_0^1 m k_m{}^2 H_{\hat{\phi}}{}^T H_{\hat{\phi}} ds$$

$$[M_{v\phi}] = [M_{\phi v}]^T = \int_0^1 m e_g \sin\theta_0 H^T H_{\hat{\phi}} ds$$

$$[M_{w\phi}] = [M_{\phi w}]^T = \int_0^1 m e_g \cos\theta_0 H^T H_{\hat{\phi}} ds$$

$$[M_{vw}] = [M_{wv}] = 0$$

$$H^T = \begin{Bmatrix} 2s^3 - 3s^2 + 1 \\ l_i(s^3 - 2s^2 + s) \\ -2s^3 + 3s^2 \\ l_i(s^3 - s^2) \end{Bmatrix}$$

$$H_{\hat{\phi}}{}^T = \begin{Bmatrix} 2s^2 - 3s + 1 \\ -4s^2 + 4s \\ 2s^2 - s \end{Bmatrix}$$

B.2 Elemental structural stiffness matrix

The structural stiffness matrix of the ith element can be written as

$$[K]_i = \begin{bmatrix} K_{vv} & K_{vw} & K_{v\phi} \\ K_{wv} & K_{ww} & K_{v\phi} \\ K_{\phi v} & K_{\phi w} & K_{\phi\phi} \end{bmatrix} \tag{B.2}$$

where

$$
\begin{aligned}
[K_{vv}] &= \int_0^1 F_A H'^T H' ds + \int_0^1 \left(EI_y \sin^2\theta_0 + EI_z \cos^2\theta_0\right) H''^T H'' ds - \int_0^1 m\Omega^2 H^T H ds \\
[K_{ww}] &= \int_0^1 F_A H'^T H' ds + \int_0^1 \left(EI_z \sin^2\theta_0 + EI_y \cos^2\theta_0\right) H''^T H'' ds \\
[K_{\phi\phi}] &= \int_0^1 m\Omega^2 \left(k_{m2}{}^2 - k_{m1}{}^2\right) \cos 2\theta_0 H_{\hat{\phi}}{}^T H_{\hat{\phi}} ds + \int_0^1 \left(GJ - EB_1 \theta_0'^2\right) H_{\hat{\phi}}'^T H_{\hat{\phi}}' ds \\
&\quad + \int_0^1 EC_1 H_{\hat{\phi}}''^T H_{\hat{\phi}}'' ds \\
[K_{v\phi}] = [K_{\phi v}]^T &= \int_0^1 m\Omega^2 e_g \sin\theta_0 H^T H_{\hat{\phi}} ds - \int_0^1 xm\Omega^2 e_g \sin\theta_0 H'^T H_{\hat{\phi}} ds \\
&\quad - \int_0^1 EB_2 \theta_0' \cos\theta_0 H''^T H_{\hat{\phi}}' ds - \int_0^1 EC_2 \sin\theta_0 H''^T H_{\hat{\phi}}'' ds \\
[K_{w\phi}] = [K_{\phi w}]^T &= \int_0^1 xm\Omega^2 e_g \cos\theta_0 H'^T H_{\hat{\phi}} ds \\
&\quad - \int_0^1 EB_2 \theta_0' \sin\theta_0 H''^T H_{\hat{\phi}}' ds + \int_0^1 EC_2 \cos\theta_0 H''^T H_{\hat{\phi}}'' ds \\
[K_{vw}] = [K_{wv}]^T &= \int_0^1 \left(EI_z - EI_y\right) \sin\theta_0 \cos\theta_0 H''^T H'' ds \\
F_A &= \int_x^1 mx d\xi
\end{aligned}
$$

B.3 Elemental structural damping matrix

The structural damping matrix of the ith element is defined as

$$
[C]_i = \begin{bmatrix} C_{vv} & C_{vw} & C_{v\phi} \\ C_{wv} & C_{ww} & C_{v\phi} \\ C_{\phi v} & C_{\phi w} & C_{\phi\phi} \end{bmatrix} \tag{B.3}
$$

where

$$
\begin{aligned}
[C_{vv}] &= \int_0^1 2me_g \Omega \cos\theta_0 H'^T H ds - \int_0^1 2me_g \Omega \cos\theta_0 H^T H' ds \\
[C_{vw}] &= -\int_0^1 2m\Omega\beta_p H^T H ds - \int_0^1 2me_g \Omega \sin\theta_0 H^T H' ds \\
[C_{wv}] &= -[C_{vw}] \\
\lfloor C_{\phi\phi} \rfloor &= [C_{ww}] = \lfloor C_{\phi w} \rfloor = \lfloor C_{w\phi} \rfloor = \lfloor C_{\phi v} \rfloor = \lfloor C_{v\phi} \rfloor = 0
\end{aligned}
$$

B.4 Elemental structural force vector

The structural load vector of the ith element is given as

$$
\{F\}_i = \begin{Bmatrix} F_v \\ F_w \\ F_\phi \end{Bmatrix} \tag{B.4}
$$

where

$$
\begin{aligned}
\{F_v\} = {} & \int_0^1 m\left(\Omega^2 e_g \cos\theta_0 + \ddot{\theta}_0 e_g \sin\theta_0\right) H^T ds - \int_0^1 m\Omega^2 e_g \cos\theta_0 x H'^T ds \\
& + \int_0^1 \left[\left(EI_z - EI_y\right) v''\hat{\phi} \sin 2\theta_0 - \left(EI_z - EI_y\right) w''\hat{\phi} \cos 2\theta_0\right] H''^T ds \\
& + \int_0^1 2m\left(\int_0^x \left(v'\dot{v}' + w'\dot{w}'\right) d\xi\right) H^T ds - \int_0^1 2v'\left(\int_x^1 m\dot{v}\, d\xi\right) H'^T ds \\
\{F_w\} = {} & -\int_0^1 m\ddot{\theta}_0 e_g \cos\theta_0 H^T ds - \int_0^1 m\Omega^2 e_g \sin\theta_0 x H'^T ds \\
& - \int_0^1 \left[\left(EI_z - EI_y\right) w''\hat{\phi} \sin 2\theta_0 + \left(EI_z - EI_y\right) v''\hat{\phi} \cos 2\theta_0\right] H''^T ds \\
& - \int_0^1 GJ\hat{\phi}' v'' H'^T ds - \int_0^1 2w'\left(\int_x^1 m\dot{v}\, d\xi\right) H'^T ds \\
\{F_\phi\} = {} & -\int_0^1 m k_m{}^2 \ddot{\theta}_0 + m\Omega^2 \left(k_{m2}{}^2 - k_{m1}{}^2\right) \sin\theta_0 \cos\theta_0 H_{\hat{\phi}}{}^T ds \\
& - \int_0^1 \left(EI_z - EI_y\right) w''^2 \sin\theta_0 \cos\theta_0 + \left(EI_z - EI_y\right) v'' w'' \cos 2\theta_0 H_{\hat{\phi}}{}^T ds \\
& + \int_0^1 \left(EI_z - EI_y\right) v''^2 \sin\theta_0 \cos\theta_0 H_{\hat{\phi}}{}^T ds - \int_0^1 GJ w' v'' H'_{\hat{\phi}}{}^T ds
\end{aligned}
$$

Appendix C

Rotor Inflow Models

C.1 Linear inflow model

In this inflow model, the rotor inflow is assumed to vary as a function of radial location, *x*, and azimuthal position, ψ, as

$$\lambda = \lambda_o + \lambda_{1c} x \cos\psi + \lambda_{1s} x \sin\psi \qquad \text{(C.1)}$$

where

$$\lambda_o = \frac{C_T}{2\sqrt{\lambda_o^2 + \mu^2}} + \mu \tan\alpha_s$$

$$\lambda_{1c} = \frac{C_T}{2\sqrt{\lambda_o^2 + \mu^2}} \frac{4}{3}\left[\left(1 - 1.8\mu^2\right)\sqrt{1 + \left(\frac{\lambda_o}{\mu}\right)^2} - \frac{\lambda_o}{\mu}\right]$$

$$\lambda_{1s} = \frac{C_T}{2\sqrt{\lambda_o^2 + \mu^2}}\left(-2\mu\right)$$

C.2 Rotor inflow using free wake analysis

Using a free wake analysis, rotor inflow can be calculated more accurately since the rotor inflow is dominated by the induced inflow from vortices released by the rotor blades. The vortices are approximated using vortex lattice method. The rotor wake is modeled using two different parts; near wake and far wake. The near wake is represented by horseshoe vortex filaments to approximate both trailed and bound vorticity. In the far wake portion (beyond some distance behind the blade, usually around 30°), the trailed vortices are assumed to roll up to form a single tip vortex, which is represented by a series of connected vortex elements. The geometry of the vortex elements is changed due to complex interactions between all other vortex elements in the rotor wake. Rotor induced inflow is then calculated using Biot-Savart Law (for a straight vortex element with finite length). Details of this analysis can be found in Ref. [116].

Appendix D

Elemental Aerodynamic Load Vector

The elemental aerodynamic load vector is described in this section. The formulation of the load vector begins with calculation of blade sectional velocity. Sectional blade loads due to the velocity are calculated using quasi-steady aerodynamic. Blade loads due to non-circulatory effect are also included. The elemental aerodynamic load vector is obtained by integrating these blade loads within the element.

D.1 Resultant incident velocity

Resultant velocity of a blade section can be summarized as

$$\begin{Bmatrix} U_R \\ U_T \\ U_P \end{Bmatrix} = T_{DU} \begin{Bmatrix} U_x \\ U_y \\ U_z \end{Bmatrix} \tag{D.1}$$

where

$$\begin{aligned}
U_x &= \dot{u} - \left(\dot{v}' + w'\dot{\theta}_1\right)\eta_r \cos\theta_1 - \left(\dot{w}' - v'\dot{\theta}_1\right)\eta_r \sin\theta_1 - \Omega\left(v + \eta_r \cos\theta_1\right) \\
&\quad - \mu\Omega R \cos\psi \\
U_y &= \dot{v} - \dot{\theta}_1\eta_r \sin\theta_1 + \Omega\left(x + u - v'\eta_r \cos\theta_1 - w'\eta_r \sin\theta_1\right) + \mu\Omega R \sin\psi \\
U_z &= \dot{w} + \dot{\theta}_1\eta_r \cos\theta_1 + \lambda\Omega R \\
\theta_1 &= \theta_0 + \hat{\phi} \\
\dot{u} &= -\int_0^x \left(v'\dot{v}' + w'\dot{w}'\right) d\xi \\
T_{DU} &= \begin{bmatrix} 1 - \frac{v'^2}{2} - \frac{w'^2}{2} & v' & w' \\ -\left(v'\cos\theta_1 + w'\sin\theta_1\right) & \left(1 - \frac{v'^2}{2}\right)\cos\theta_1 - v'w'\sin\theta_1 & \sin\theta_1\left(1 - \frac{w'^2}{2}\right) \\ v'\sin\theta_1 - w'\cos\theta_1 & -\left(1 - \frac{v'^2}{2}\right)\sin\theta_1 - v'w'\cos\theta_1 & \cos\theta_1\left(1 - \frac{w'^2}{2}\right) \end{bmatrix}
\end{aligned}$$

D.2 Blade sectional loads from circulatory effects

Blade aerodynamic loading due to circulatory effects is calculated using a quasi-steady aerodynamic model. The aerodynamic loads are functions of blade velocity, and are described in Eq. D.2.

$$\begin{Bmatrix} L_u \\ L_v \\ L_w \end{Bmatrix} = {T_{DU}}^T \begin{Bmatrix} \overline{L}_u \\ \overline{L}_v \\ \overline{L}_w \end{Bmatrix} \tag{D.2a}$$

where
$$\overline{L}_u = \frac{\gamma}{6a} d_o U_R U_T$$
$$\overline{L}_v = \frac{\gamma}{6a}\left(-d_o U_T^2 + (d_1 + c_o) U_T U_P + (c_1 + d_2) U_P^2\right)$$
$$\overline{L}_w = \frac{\gamma}{6a}\left(c_o U_T^2 - (c_1 + d_o) U_T U_P + d_1 U_P^2\right)$$
$$M_{\hat{\phi}} = \frac{\gamma}{6a}\frac{c}{R}\left(f_o (U_T^2 + U_P^2) - f_1 U_T U_P\right) - e_d \overline{L}_w \tag{D.2b}$$

D.3 Blade sectional loads from non-circulatory effects

The effect of non-circulatory airloads is incorporated into sectional blade loads as follow

$$\begin{aligned} L_u^A &= L_u \\ L_v^A &= L_v \\ L_w^A &= L_w + L_w^{NC} \\ M_{\hat{\phi}}^A &= M_{\hat{\phi}} + M_{\hat{\phi}}^{NC} \end{aligned} \tag{D.3}$$

where
$$L_w^{NC} = \frac{\gamma\pi\frac{c}{R}}{12a}\left(-\frac{\ddot{w}}{R} + \frac{\frac{c}{4} + e_d}{R}\ddot{\theta}_1 + (x + \mu \sin\psi)\dot{\theta}_1\right)$$
$$M_{\hat{\phi}}^{NC} = \frac{\gamma\pi\frac{c}{R}}{12a}\left(\frac{\frac{c}{4} + e_d}{R}\frac{\ddot{w}}{R} - \left(\frac{\frac{c}{4} + e_d}{R}\right)^2 \ddot{\theta}_1 - \frac{\frac{c}{2} + e_d}{R}(x + \mu \sin\psi)\dot{\theta}_1 - \frac{c^2}{32R^2}\ddot{\theta}_1\right)$$

D.4 Elemental aerodynamic force vector

The aerodynamic load vector of the ith element is given as

$$\left\{F^A\right\}_i = \begin{Bmatrix} F_v^A \\ F_w^A \\ F_\phi^A \end{Bmatrix} \tag{D.4}$$

where
$$\left\{F_v^A\right\} = \int_0^1 L_v^A H^T ds$$
$$\left\{F_w^A\right\} = \int_0^1 L_w^A H^T ds$$
$$\left\{F_\phi^A\right\} = \int_0^1 M_{\hat{\phi}}^A {H_\phi}^T ds$$

Appendix E

Blade Response Calculation

Rotor blade response is obtained using Finite Element in time method. The blade equations of motion in modal space (Eq. 2.8) can also be written in a Hamiltonian form

$$\int_0^{2\pi} \delta p^T \left(\overline{M}\ddot{p} + \overline{C}\dot{p} + \overline{K}p - \overline{F}\right) d\psi = 0 \tag{E.1}$$

In order to use the temporal Finite Element method, Eq. E.1 are integrated by parts to yield blade equations in first order form as

$$\int_0^{2\pi} \begin{Bmatrix} \delta p \\ \delta \dot{p} \end{Bmatrix}^T \begin{Bmatrix} -\overline{C}\dot{p} - \overline{K}p + \overline{F} \\ \overline{M}\dot{p} \end{Bmatrix} d\psi = \begin{Bmatrix} \delta p \\ \delta \dot{p} \end{Bmatrix}^T \begin{Bmatrix} \overline{M}\dot{p} \\ 0 \end{Bmatrix} \Bigg|_0^{2\pi} \tag{E.2}$$

The right hand side of the above equation is zero due to the periodicity condition of the response, $\dot{p}(2\pi) = \dot{p}(0)$. Then Eq. E.2 can be rewritten as

$$\int_0^{2\pi} \delta y^T Q(y) d\psi = 0 \tag{E.3}$$

where $y = \begin{Bmatrix} p \\ \dot{p} \end{Bmatrix}$ and $Q(y) = \begin{Bmatrix} -\overline{C}\dot{p} - \overline{K}p + \overline{F} \\ \overline{M}\dot{p} \end{Bmatrix}$.

Using the Finite Element in time method, one revolution of the azimuth position, ψ, is discretized into a number of time elements (see Fig. 2.4). Eq. E.3 then can be represented by summation over a number of time elements, N_t, as

$$\sum_{j=1}^{N_t} \int_{\psi_j}^{\psi_{j+1}} \delta y_j^T Q_j d\psi = 0 \tag{E.4}$$

To determine the blade response, a first order Taylor series expansion of Eq. E.4 is performed with the result presented in Eq. E.5.

$$\sum_{j=1}^{N_t} \int_{\psi_j}^{\psi_{j+1}} \delta y_j^T Q_j (y_o + \Delta y) d\psi = \sum_{j=1}^{N_t} \int_{\psi_j}^{\psi_{j+1}} \delta y_j^T (Q_j(y_o) + T_j(y_o)\Delta y) d\psi = 0 \qquad \text{(E.5)}$$

where $T_j = \begin{bmatrix} \frac{\partial \overline{F}}{\partial p} - \overline{K} & \frac{\partial \overline{F}}{\partial \dot{p}} - \overline{C} \\ 0 & \overline{M} \end{bmatrix}_j$. Within the jth time element, the modal response, p, is expressed in term of time shape functions, H_t, and temporal nodal response vector, ξ, as

$$p_j = H_t \xi_j \qquad \text{(E.6).}$$

where $H_t = \left\{ \begin{matrix} \frac{32}{3}t^4 - \frac{80}{3}t^3 + \frac{70}{3}t^2 - \frac{25}{3}t + 1 \\ \frac{-128}{3}t^4 + \frac{228}{3}t^3 - \frac{208}{3}t^2 + 16t \\ 64t^4 - 128t^3 + 76t^2 - 12t \\ \frac{-128}{3}t^4 + \frac{224}{3}t^3 - \frac{112}{3}t^2 + \frac{16}{3}t \\ \frac{32}{3}t^4 - 16t^3 + \frac{22}{3}t^2 - t \end{matrix} \right\}^T$ for a five node element shown in Fig. 2.4

This also yields

$$y_j = \Phi_t \xi_j \qquad \text{(E.7)}$$

where $\Phi_t = \begin{Bmatrix} H_t \\ \dot{H}_t \end{Bmatrix}$. Using this transformation, Eq. E.5 can be rewritten as

$$\sum_{j=1}^{N_t} \int_{\psi_j}^{\psi_{j+1}} \delta \xi_j^T \Phi_t^T (Q_j + T_j \Phi_t \Delta \xi_j) d\psi = 0 \qquad \text{(E.8)}$$

For arbitrary $\delta\xi$, the integrand must be zero and the blade equations are presented as

$$\overline{Q} + \overline{T} \Delta \xi = 0 \qquad \text{(E.9)}$$

where $\overline{Q} = \sum_{j=1}^{N_t} \int_{\psi_j}^{\psi_{j+1}} \Phi_t^T Q_j d\psi$, $\overline{T} = \sum_{j=1}^{N_t} \int_{\psi_j}^{\psi_{j+1}} \Phi_t^T T_j \Phi_t d\psi$, and $\Delta\xi = \sum_{j=1}^{N_j} \Delta \xi_j$. Eq. E.9, which is a simple algebraic equation, can be easily solved for the required changes in the nodal response vector, $\Delta\xi$, such that the nodal response, ξ, satisfies the blade equation of motion Eq. 2.8. The nodal response vector is updated using Eq. E.10.

$$\xi^{new} = \xi^{old} + 0.5\Delta\xi \qquad \text{(E.10)}$$

Using the new set of nodal response, ξ^{new}, Eq. E.9 is updated and solved again. The process is repeated until the nodal response converges, or $\Delta\xi$ is closed to zero.

Appendix F

Vehicle Trim Calculation

The vehicle pitch control settings and vehicle orientations or vehicle trim can be obtained through vehicle equilibrium relations, since the sum of forces and moments in Eq. (2.1) must equal zero or

$$\overline{F} = 0 \tag{F.1}$$

where $\overline{F} = \lfloor F_x^H \quad F_y^H \quad F_z^H \quad M_x^H \quad M_y^H \quad M_z^H \rfloor^T$, and $\overline{F}$ is a function of the vehicle trim setting, $\eta = \lfloor \alpha_s \quad \phi_s \quad \theta_o \quad \theta_{1c} \quad \theta_{1s} \quad \theta_{tr} \rfloor^T$. To determine the vehicle trim that satisfies equilibrium, a first order Taylor series expansion of $\overline{F}$ is obtained with the result presented in Eq. F.2.

$$\overline{F}(\eta_o + \Delta\eta) = \overline{F}(\eta_o) + \Delta\eta \left. \frac{\partial \overline{F}(\eta)}{\partial \eta} \right|_{\eta=\eta_o} = 0 \tag{F.2}$$

where η_o is the initial guess of vehicle trim. The trim jacobian matrix, $J = \left[\left. \frac{\partial \overline{F}(\eta)}{\partial \eta} \right|_{\eta=\eta_o} \right]$, is calculated using numerical perturbation method. The required correction in vehicle trim, $\Delta\eta$, can be obtained easily by solving algebraic Eq. F.3

$$\Delta\eta = -\left[\left. \frac{\partial \overline{F}(\eta)}{\partial \eta} \right|_{\eta=\eta_o} \right]^{-1} \overline{F}(\eta_o) \tag{F.3}$$

The vehicle trim is updated using the correction as

$$\eta_o^{NEW} = \eta_o + 0.5\Delta\eta \tag{F.4}$$

Using the new set of vehicle trim, η_o^{NEW}, Eq. F.3 is updated and solved again. The procedure repeats until vehicle equilibrium is satisfied or $\Delta\eta$ is close to zero.

Appendix G

Fluid Dynamic Model of Controllable Damper

The fluid dynamic based model is developed using incompressible flow through small orifice opening [107]. Differential equations governing the pressures developed in each chamber of the damper are summarized below:

$$\frac{dP_1}{dt} = \frac{\left\{ A_p \dot{u} - k_{pri} A_{pri} \delta \left[\frac{2(P_1 - P_2)}{\rho} \right] - k_{con} A_{con} \left[\frac{2\left| P_1 - P_2 \right|}{\rho} \right]^{\frac{1}{2}} \operatorname{sgn}(P_1 - P_2) \right\}}{\left[\left(L_1 - u + \frac{P_1 A_f}{K_a} \right) \frac{A_p}{\beta_1} + \frac{A_f A_p}{K_a} \right]} \tag{G.1}$$

$$\frac{dP_2}{dt} = \frac{\left\{ (A_r - A_p)\dot{u} + k_{pri} A_{pri} \delta \left[\frac{2(P_1 - P_2)}{\rho} \right] + k_{con} A_{con} \left[\frac{2\left| P_1 - P_2 \right|}{\rho} \right]^{\frac{1}{2}} \operatorname{sgn}(P_1 - P_2) \right\}}{\frac{(A_p - A_r)(L_2 - u)}{\beta_2}} \tag{G.2}$$

where A_p is the piston area, A_r is the rod area, A_f is the accumulator piston area (see Fig. 2.16), K_a is the equivalent accumulator stiffness, and β is the fluid bulk modulus (the value of which is dependent on the fluid pressure and thus varies in the two chambers). A_{pri} and A_{con} are the primary and controllable orifice areas, k_{pri} and k_{con} are the primary and controllable orifice discharge coefficients, δ is a dimensional correction constant, and ρ is the mean fluid density. $\dot{u}$ is the piston velocity, and L_1 and L_2 are the chamber lengths (which depend on piston position, u).

Appendix H

Helicopter and Rotor Properties

Main Rotor Properties	Number of blades	4
	Lock number, γ	6.34
	Solidity ratio,σ	0.1
	Rotational speed, Ω	40.1234 rad/s
	C_T/σ	0.07
Rotor Blade Properties	Blade radius, R	16.2 ft.
	Blade chord, c/R	0.08
	Mass per unit length, m_o	0.135 slug/ft
	Flap bending stiffness $EI_y/m_o\Omega^2R^4$	0.008345
	Lag bending stiffness $EI_z/m_o\Omega^2R^4$	0.023198
	Torsional stiffness $GJ/m_o\Omega^2R^4$	0.003822
	Lift curve slope, a	5.73
	Skin friction drag coefficient, C_{d0}	0.0095
	Induced drag coefficient, C_{d2}	0.2
	Pitching moment coefficient, C_m	0.0
	Flap natural frequencies	1.147, 3.399/*rev*
	Lag natural frequencies	0.750, 4.364/*rev*
	Torsion natural frequencies	4.590, 13.595/*rev*
Tail Rotor Properties	Number of blades, N_{tr}	4
	Tail rotor radius, R_{tr}	3.24 ft.
	Solidity ratio, σ_{tr}	0.15
	Rotor speed, Ω_{tr}	5Ω
	Lift curve slope, a_{tr}	6.0
	Tail rotor location, $(x_{tr}/R, z_{tr}/R)$	(1.2, 0.2)
Horizontal Tail Properties	Horizontal tail area, $S_{ht}/\pi R^2$	0.011
	Horizontal tail lift curve slope, a_{ht}	6.0
	Horizontal tail location, x_{ht}/R	0.95
Fuselage Properties	C.G. location, (x_{cg}, y_{cg})	(0, 0)
	Hub location, h/R	0.2
	Net weight, W	5800 Lbs.

Table H.1: Rotor and fuselage properties

Appendix I

Convergence Study: Numbers of Finite Elements and Modal Representation

The introduction of discrete controllable stiffness (damping) devices near the blade root raises questions about the required finite element discretization along the span, and the number of modes required to represent the blade. Since it is possible that a finer finite element mesh may be required, especially in the root region, or a larger number of modes may be required in the modal transformation; a convergence study is conducted. The convergence study is conducted using the same blade configuration as the one implemented in Chapter 7 (discrete controllable stiffness device study).

I.1 Number of finite elements along the blade span

A nominal number of five equal spanwise finite elements is used to capture the elastic flap-bending, lag-bending, and torsion deformations of the blade (Fig. 2.2), with the discrete devices connected between the two innermost elements (at around 20% span). Variation in blade frequencies (up to 20/*rev*) and the corresponding mode shapes is examined when increasing numbers of spanwise elements are used (as shown in Figs. I.1a – I.1d), with a finer concentration of elements near the root region where the discrete devices are attached. The variation in blade natural frequencies with increasing numbers of elements is shown in Fig. I.2. From the figure it is seen that starting with a nominal five spanwise elements, and going up to 19 spanwise elements, the first ten modal frequencies (up to 20/*rev*) are virtually unchanged. Figures I.3, I.4, and I.5, respectively, show the flap, lag, and torsion mode shapes, when increasing numbers of spanwise elements are used. From the figures it is seen that when an increasing number of elements is used, the first four flap, the first four lag, and the first two torsion mode shapes show little variation. From the above results, it is concluded that five spanwise finite elements (30 degrees of freedom – 10 flap bending, 10 lag bending, and 10 torsion) are sufficient to capture the lowest ten modes (up to 20/*rev*); and even in the presence of discrete devices in the blade root region, increasing the number of elements does not improve accuracy of modal frequencies or mode shapes. Consequently, a total of five spanwise elements can be used to model the blade.

I.2 Number of blade modes in modal transformation

In helicopter aeroelastic analyses it is common to transform the blade finite element equations of motion to a few modal equations, to calculate the blade periodic response in forward flight in a computationally efficient manner. The number of modes used in the transformation, however, has to be sufficient to accurately capture the hub vibrations. In the present study, even greater care is required since the discrete devices are cyclically changing their stiffness or damping coefficients around the azimuth, and it is not known, *a priori*, how many modes would be required to accurately predict the hub vibrations. This section examines the effect of using increasing numbers of flap, lag, and torsion modes on the vibratory hub load predictions. Simulations are carried out at an advance ratio of 0.35, and the Drees inflow model is used to obtain rotor inflow. Although it is recognized that this could lead to under-prediction in hub vibration levels, the emphasis in this section is to establish the number of modes required to predict hub vibrations with cyclic stiffness variations of discrete devices, rather than predicting the “correct” vibration levels using a more sophisticated aerodynamic model.

Using, nominally, 2 flap, 2 lag, and 2 torsion modes (along with the Drees inflow model, at an advance ratio of 0.35), optimal 2/*rev* and 3/*rev* stiffness variations of the flap device, 2/*rev* and 3/*rev* stiffness variations of the lag device, and 3/*rev* and 4/*rev* stiffness variations of the torsion device were first determined (see Table I.1). The baseline vibration levels (no cyclic stiffness variations), and the reduced vibration levels obtained when using the flap device, lag device, or torsion device (with inputs in Table I.1) were also recorded (see Table I.2). Next, for the optimal 2/*rev* and 3/*rev* stiffness variations of the flap device, the hub vibration levels were calculated using increasing number of flap modes (inputs were held constant, *not* recalculated for increasing number of modes), and these results are shown in Fig. I.6. The figure clearly indicates that for a given optimal cyclic stiffness variation of the flap device, when the number of flap modes is greater than four, no change in any component of the predicted 4/*rev* vibratory hub loads is observed. This process was then repeated using optimal stiffness variations of the lag device and progressively increasing the number of lag modes; and using optimal stiffness variations of the torsion device and progressively increasing the number of torsion modes (results are presented in Figs I.7 and I.8, respectively). Examining the effects of increasing number of lag and torsion modes on predicted 4/*rev* hub vibrations suggests that 4 lag modes and 2 torsion modes are sufficient for hub vibration prediction in the presence of the discrete controllable springs. The conclusion of this modal convergence study was that 4 flap modes, 4 lag modes, and 2 torsion modes were required to predict the 4/*rev* hub vibration levels, when the discrete controllable stiffness devices are introduced. These are the number of modes used in the vibration reduction studies in Chapter 7 (discrete controllable stiffness device study). Also, the same number of modes can be used in Chapter 8, since discrete controllable damping devices are introduced in a similar manner as the discrete controllable stiffness devices here.

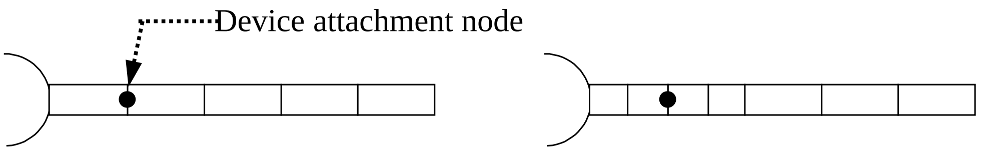

(a) 5 elements (b) 7 elements

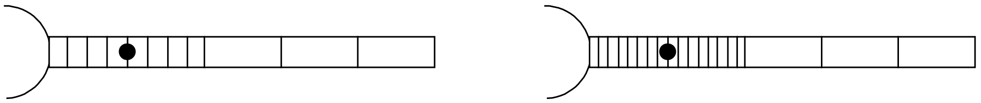

(c) 11 elements (d) 19 elements

Figure I.1: Rotor blade finite element discretization used in the convergence study

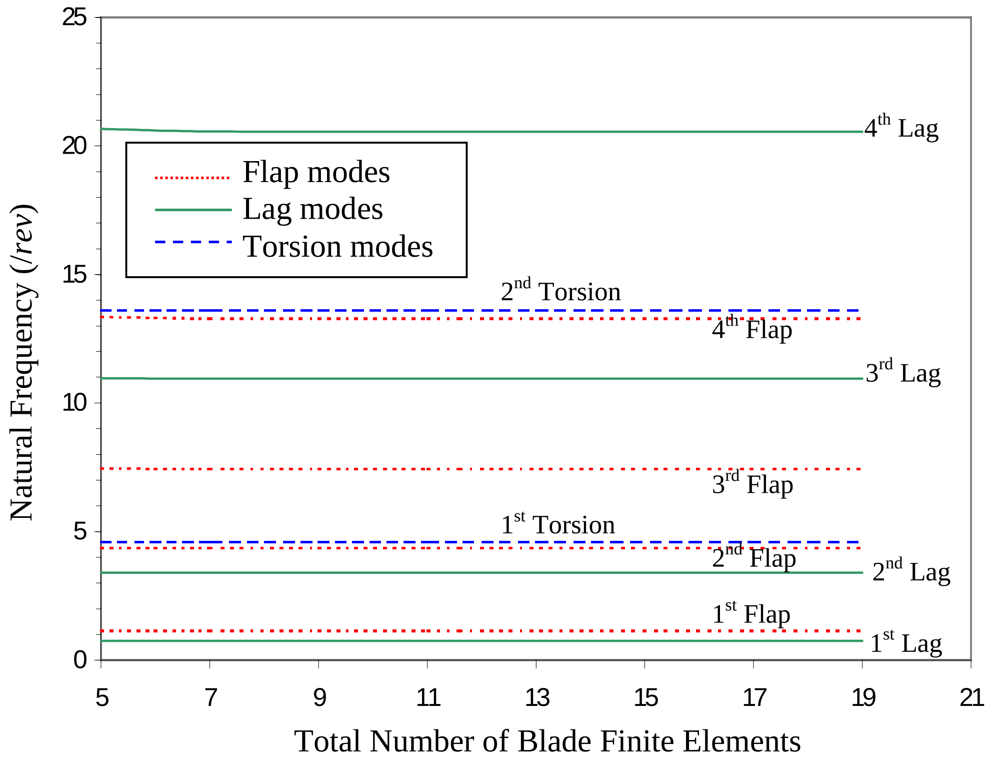

Figure I.2: Blade rotating natural frequencies for increasing number of finite elements

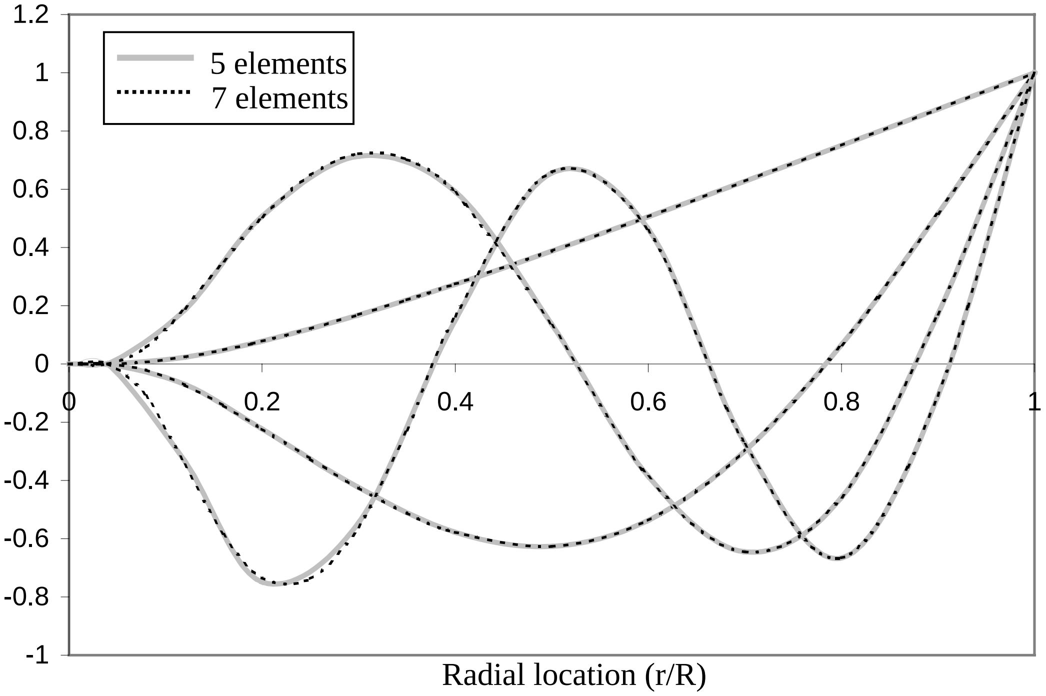

Figure I.3: Blade flap mode shapes for increasing number of finite elements

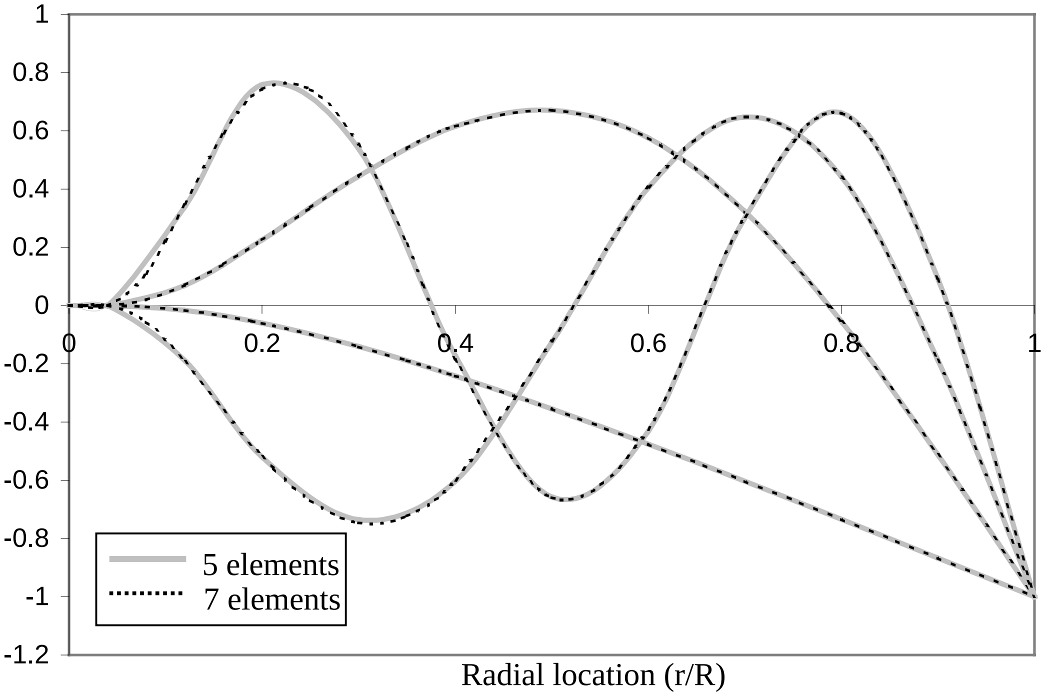

Figure I.4: Blade lag mode shapes for increasing number of finite elements

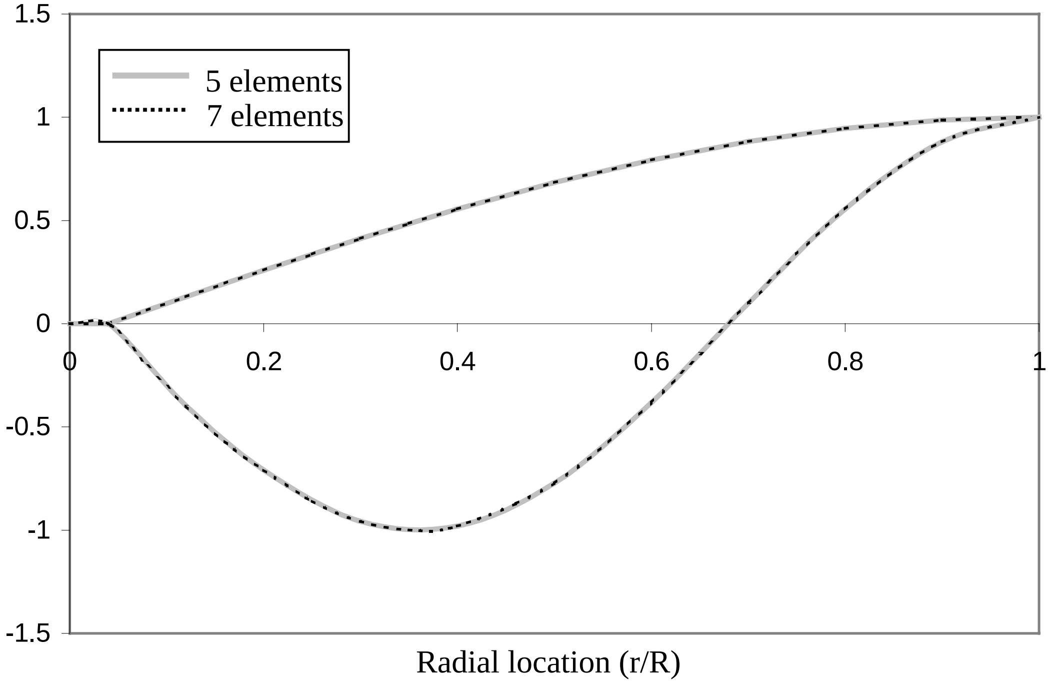

Figure I.5: Blade torsional mode shapes for increasing number of finite elements

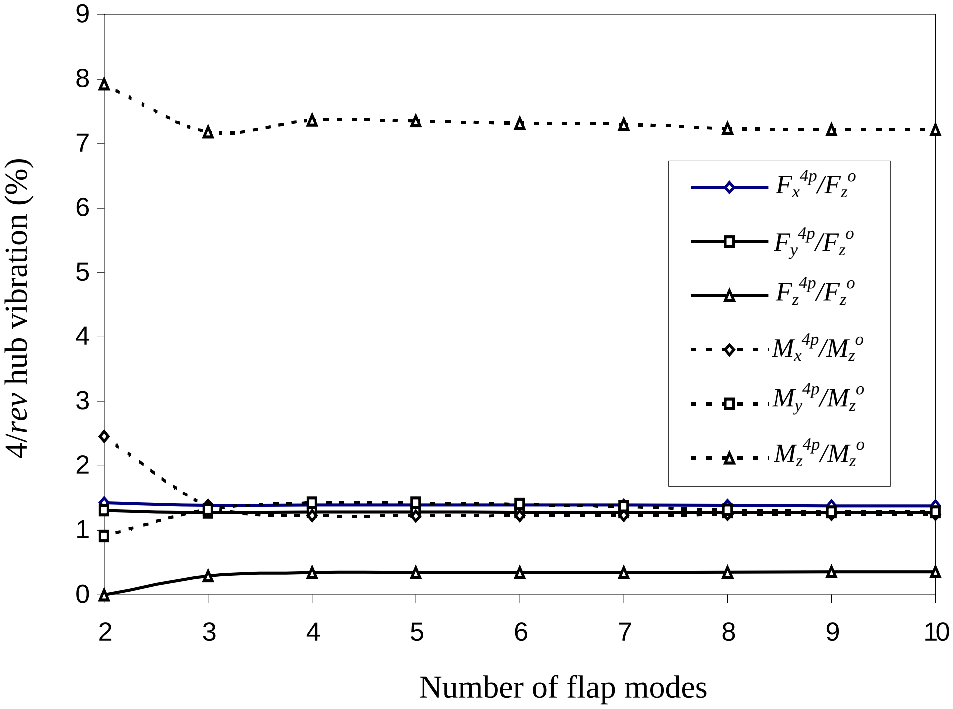

Figure I.6: Variation in 4/*rev* vibratory hub load predictions with increasing number of flap modes, when a 2,3/*rev* flap stiffness variation is used (Drees inflow, $\mu = 0.35$)

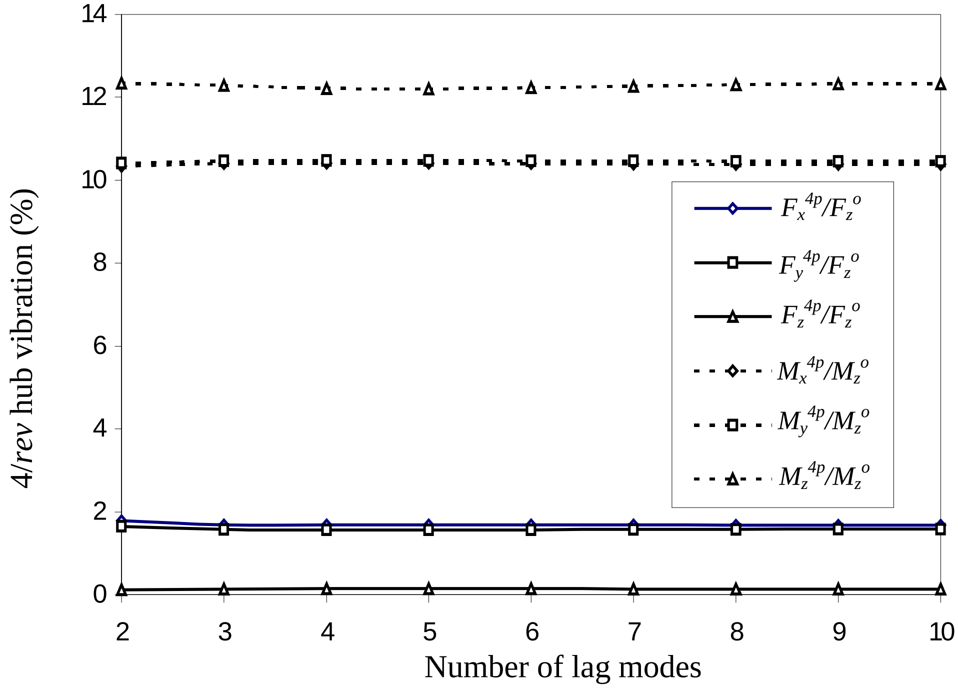

Figure I.7: Variation in 4/*rev* vibratory hub load predictions with increasing number of lag modes, when a 2,3/*rev* lag stiffness variation is used (Drees inflow, μ = 0.35)

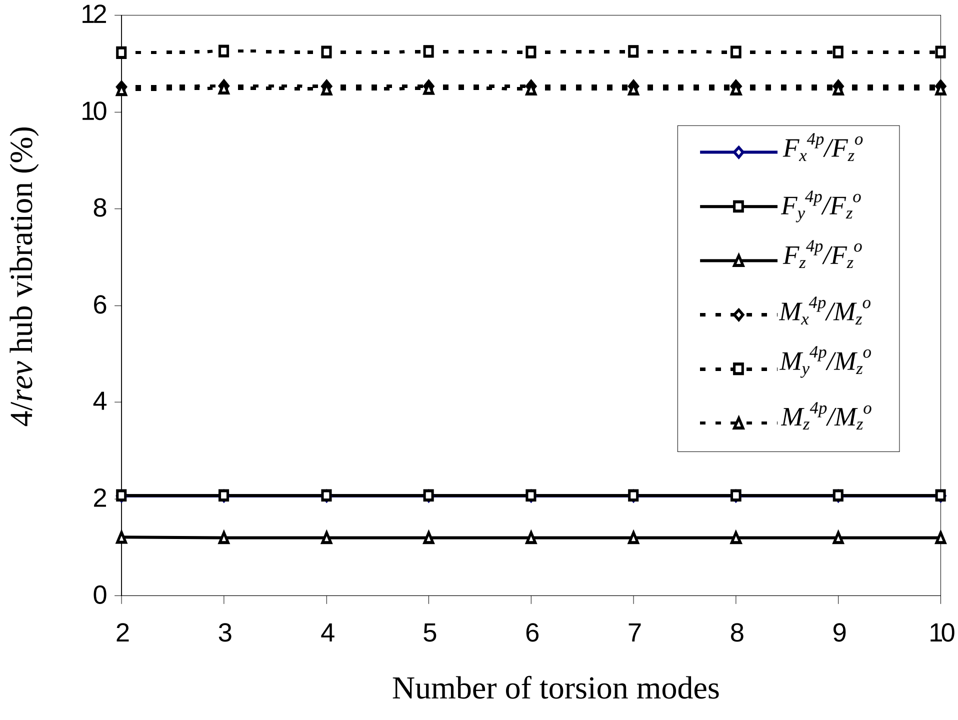

Figure I.8: Variation in 4/*rev* vibratory hub load predictions with increasing number of torsion modes, when a 3,4/*rev* torsion stiffness variation is used (Drees inflow, μ = 0.35)

Input		Amplitude	Phase
Flap device stiffness variation	2/*rev*	$\Delta K_w = 29.3\% \overline{K}_w$	143.6°
	3/*rev*	$\Delta K_w = 68.3\% \overline{K}_w$	36.9°
Lag device stiffness variation	2/*rev*	$\Delta K_v = 25.1\% \overline{K}_v$	-74.4°
	3/*rev*	$\Delta K_v = 49.8\% \overline{K}_v$	-167.1°
Torsion device stiffness variation	3/*rev*	$\Delta K_\phi = 48.1\% \overline{K}_\phi$	-8.3°
	4/*rev*	$\Delta K_\phi = 42.0\% \overline{K}_\phi$	134.9°

Table I.1: Optimal stiffness variations predicted using 2 flap, 2 lag, and 2 torsion modes (Drees inflow, $\mu = 0.35$)

Hub loads*	No Stiffness Variation	With 2, 3/rev flap stiffness variation	With 2, 3/rev lag stiffness variation	With 3, 4/rev torsion stiffness variation
F_x^{4p}	2.06	1.43	1.79	2.06
F_y^{4p}	2.08	1.31	1.65	2.07
F_z^{4p}	1.23	0.002	0.12	1.21
M_x^{4p}	10.52	2.46	10.33	10.51
M_y^{4p}	11.26	0.91	10.41	11.22
M_z^{4p}	10.52	7.92	12.34	10.46

Table I.2: 4/*rev* vibratory hub loads (predicted using 2 flap, 2 lag, and 2 torsion modes), with and without stiffness variations (Drees inflow, $\mu = 0.35$)

---

[*] All forces are % of F_z^0 (6042 lbs.), all moments are % of M_z^0 (6556 ft-lbs.)

Vita

Phuriwat Anusonti-Inthra

Education: Doctor of Philosophy in Aerospace Engineering, August 2002
The Pennsylvania State University, University Park, PA

Master of Science in Aerospace Engineering, August 1998
The Pennsylvania State University, University Park, PA

Bachelor of Science in Electrical Engineering, March 1993
King Mongkut's Institute of Technology, Bangkok, Thailand

Journal Publications:

- Anusonti-Inthra, P. and Gandhi, F., "Helicopter Vibration Reduction through Cyclic Variations in Blade Root Stiffness," *Journal of Intelligent Material Systems and Structures*, Vol. 11, No. 2, February 2000, pp.153-166.
- Anusonti-Inthra, P. and Gandhi, F., "Optimal Control of Helicopter Vibration Through Cyclic Variations in Blade Root Stiffness," *Smart Materials and Structures*, Special Issue on Rotorcraft Application, Vol. 10, No. 1, February 2001, pp.86-95.
- Gandhi, F. and Anusonti-Inthra, P., "Helicopter Vibration Reduction using Discrete Controllable-Stiffness Devices at the Rotor Hub," Accepted for publication in the *AIAA Journal of Aircraft*.

Selected Conference Proceedings:

- Anusonti-Inthra, P. and Gandhi, F., "Adaptive control of Semi-Active Variable Stiffness Devices for Narrow-Band Disturbance Rejection," *Proceedings of the 12th International Conference on Adaptive Structures and Technologies (ICAST)*, College Park, MD, October 2001.
- Anusonti-Inthra, P. and Gandhi, F., "Narrow-Band Disturbance Rejection using Semi-Active Control," Proceedings of the Adaptive Structures and Material Systems Symposium, International Mechanical Engineering Congress and Exposition (Winter Annual Meeting of the ASME), New York, NY, November, 2001.
- Anusonti-Inthra, P., Gandhi, F., and Miller, L., "Reduction of Helicopter Vibration through Cyclic Control of Variable Orifice Dampers," *Proceedings of the 58th American Helicopter Society Forum*, Montreal, Canada, May 2002.

Professional Position:

Project Engineer, OTIS Elevator Company, Bangkok, Thailand (1993-1994)